Ingenieurfakultät Bau Geo Umwelt
Technische Universität München

Sparse Recovery in Spaceborne SAR Tomography

Nan Ge

Vollständiger Abdruck der von der Ingenieurfakultät Bau Geo Umwelt der Technischen Universität München zur Erlangung des akademischen Grades eines

Doktor-Ingenieurs (Dr.-Ing.)

genehmigten Dissertation.

Vorsitzende:

Prof. Dr. rer. pol. habil. Bing Zhu

Prüfende der Dissertation:

1. Prof. Dr.-Ing. habil. Xiaoxiang Zhu
2. Prof. Dr.-Ing. habil. Richard Hans Georg Bamler
3. Prof. Dr.-Ing. habil. Laurent Ferro-Famil,
   Université de Rennes 1

Die Dissertation wurde am 28.11.2019 bei der Technischen Universität München eingereicht und durch die Ingenieurfakultät Bau Geo Umwelt am 06.03.2020 angenommen.

Abstract

Synthetic aperture radar (SAR) tomography is a technique for reconstructing three-dimensional far field from two-dimensional measurements of radar echoes. As a result of a doctoral study, this dissertation addresses mainly several sparse recovery problems in spaceborne SAR tomography.

Single-master SAR tomography uses a common acquisition for interferogram generation. In the *single-look* or single-snapshot case, each look or snapshot is processed independently. Under the assumption of a compressible far field in urban scenarios, this typically involves solving a complex-valued ℓ_1-regularized least squares (L1RLS) problem. From a bi-criterion optimization point of view, each L1RLS solution associated with a fixed regularization parameter is Pareto optimal, and therefore its solution path can be sampled in order to achieve automatic tuning. Besides, we show empirically that a simple diagonal preconditioning can substantially improve the convergence of this notoriously ill-posed problem as applied to spaceborne SAR tomography. On the other hand, the far fields of various looks or snapshots are jointly reconstructed in the *multi-look* case. We show that the prior knowledge of scatterers sharing the same elevation position among different looks leads in general to a joint tensor mode recovery problem for repeat-pass acquisitions.

Single-look multi-master SAR tomography is a relatively new research topic that is primarily inspired by prospective spaceborne SAR missions in bi- or multistatic configurations (i.e., with one transmitter and multiple receivers). We establish the single-look multi-master data model, and propose a generic inversion framework comprised of nonconvex sparse recovery, model-order selection and off-grid correction. Two algorithm are developed vis-à-vis nonconvex sparse recovery: one extends the conventional nonlinear least squares (NLS) to the single-look multi-master data model, and the other is based on bi-convex relaxation and alternating minimization. In addition, we prove two theorems regarding the critical points of the objective function of any NLS subproblem. We show empirically that the conventional *single-look single-master* approach, if applied to a *single-look multi-master* stack, can be insufficient for layover separation, even when the elevation distance between two scatterers is significantly larger than the Rayleigh resolution.

In the end, we develop a hybrid approach for *single-look* pursuit monostatic acquisitions. This approach estimates first scatterers' elevation from solely pursuit monostatic interferograms, and subsequently their motion parameters from all acquisitions by exploiting the previous elevation estimates as deterministic prior. The former is a special case of *single-look multi-master* tomography, while the latter is a variant of *single-look single-master* tomography. This approach is directly applicable to bistatic acquisitions.

Zusammenfassung

Radar mit synthetischer Apertur (englisch: Synthetic Aperture Radar, abgekürzt als SAR)-Tomografie ist eine Technik zur Rekonstruierung eines dreidimensionalen Fernfeldes mit zweidimensionalen Messungen der Radarechos. Bei dieser Dissertation handelt es sich hauptsächlich um Optimierungsprobleme zur Schätzung dünnbesetzter Signale in der satellitengestützten SAR-Tomografie sowie ihre Löser.

Bei der *Einzelmaster-SAR-Tomografie* verwendet man eine gemeinsame Aufnahme für die Interferogramerzeugung. Im Falle der *Einzellook-Einzelmaster-SAR-Tomografie* wird jeder Look unabhängig voneinder prozessiert. Unter der Annahme eines komprimierbares Fernfeldes in urbanen Gebieten, steht es im Mittelpunkt der tomografischen Prozessierung ein komplexwertiges ℓ_1-regularisiertes Problem der kleinsten Quadrate zu lösen. Aus dem Gesichtspunkt der Bikriterien-Optimierung ist jede mit einem fixen Regularisierungsparameter verbundene Lösung Pareto-optimal. Daher könnte man den Lösungspfad des Optimierungsproblems abtasten, um das Tuning des Regularisierungsparameters zu automatisieren. Außerdem zeigen wir empirisch mit echten SAR-Daten, dass eine einfache diagonale Präkonditionierung die Konvergenz dieses schlecht konditioniertes Problems in der SAR-Tomografie wesentlich verbessern kann. Andererseits bei der *Multilook-SAR-Tomografie* werden die Fernfelder mehrerer Looks gemeinsam rekonstruiert. Die a priori Kenntnisse, dass sich die Rückstreuer in verschiedenen Looks in derselben Elevationsposition befinden, führt im Allgemeinen zu einem Optimierungsproblem zur Schätzung eines dünnbesetzten Tensors, in dem die Rückstreuer mit einem Regularisierungsterm gefordert werden, sich nach dem ersten, der Elevationsrichtung entsprechenden, Tensormodus auszurichten.

Die *Einzellook-Multimaster-SAR-Tomografie* ist ein relativ neues Forschungsthema. Dies ist vor allem durch künftige satellitengestützte SAR-Missionen in bi- oder multistatischen Konfigurationen (d.h., mit einem Sender und mehreren Empfängern) inspiriert. Wir etablieren zuerst das Einzellook-Multimaster-Datenmodell. Darauf basierend entwickeln wir ein allgemeines Verfahren für die tomografische Inversion. Dieses Verfahren setzt sich aus drei Teilen zusammen, nämlich die nichtkonvexe Schätzung eines dünnbesetzten Signals, die Auswahl der Modellordnung, sowie die Korrektur des Gitterfehlers. Für den ersten Teil werden zwei Algorithmen entwickelt. Der Eine passt die konventionelle nichtlineare Methode der kleinsten Quadrate (englisch: Nonlinear Least Squares, abgekürzt als NLS) an das Einzellook-Multimaster-Datenmodell. Der Andere basiert auf bi-konvexer Relaxation und alternierender Minimierung. Des Weiteren beweisen wir zwei Theoreme hinsichtlich der kritischen Punkte der Objetivfunktion jedes NLS-Unterproblems. Mit echten SAR-Daten zeigen wir empirisch, dass das konventionelle *Einzellook-Einzelmaster-Verfahren*, falls für eine tomografische Prozessierung mit einem *Einzellook-Einzelmaster-Datensatz* eingesetzt, das Layover-Trennungsproblem

möglicherweise nicht lösen kann, selbst wenn die Distanz zwischen zwei Rückstreuern in der Elevationsrichtung deutlich größer als die Rayleigh-Auflösung ist.

Letztendlich entwickeln wir ein Mischverfahren zur tomografischen Prozessierung von SAR-Aufnahmen im pursuit-monostatischen Modus. Dieses Verfahren schätzt zuerst die Elevationspositionen der Rückstreuer aus lediglich pursuit-monostatischen Interferogrammen, und anschließend ihre Bewegungsparameter aus allen Aufnahmen, wobei die zuvor geschätzten Elevationspositionen als deterministische a priori Kenntnisse verwendet werden. Der erstere Schritt ist im Grunde genommen ein Sonderfall der *Einzellook-Multimaster-SAR-Tomografie*, während sich der letztere Schritt als eine Variante der *Einzellook-Einzelmaster-SAR-Tomografie* darstellt. Dieses Verfahren ist unmittelbar auf bistatische SAR-Aufnamen anwendbar.

Acknowledgements

I would like to thank my "Doktoreltern" Prof. X. Zhu and Prof. R. Bamler for granting me the opportunity to pursue a doctor's degree in the fascinating field of SAR tomography, for kindly sharing their expertise in SAR, for suggesting interesting and substantial research topics, for showing their great patience and understanding when listening to my occasionally controversial arguments, and for offering their precious time for discussions, which lead me all the way from being an absolute novice to what I am today.

I would like to thank Prof. L. Ferro-Famil for his willingness to be my third examiner, for his encouragement and for many fruitful discussions.

I would like to thank Prof. B. Zhu for agreeing to act as the chairwoman of my examining committee on short notice.

This dissertation would not have been possible without the kind and, in several cases, selfless help from many people. N. Adam brought me to DLR when I was a master student at TUM, taught me numerous things about IWAP, and consistently offered his advice during my doctoral study. Dr. H. Ansari was always ready for scientific discussions. Dr. S. Auer, who is my role model of how to become an honest, just, caring and supportive supervisor, never gave up on me when I failed several times to find a proper application of his RaySAR simulations. I am glad that our joint work has finally paid off. Dr. G. Baier attended to my each and every IT consultancy request and helped me a lot to polish up my German, for which I am truly grateful. B. Bierkamp-Michalak scheduled many of my meetings with Prof. R. Bamler, which undoubtedly accelerated my doctoral study. H. Breit kept me updated on TerraSAR-X and future missions. Dr. R. Brcic taught me a few things about split-band interferometry. Dr. F. De Zan never hesitated to share his massive expertise in InSAR and in particular SAR tomography in forested scenarios. Prof. M. Eineder warmly welcomed me back at the SAR department meetings, and gave me valuable advice about presentation style. Dr. G. Fornaro was always encouraging and supportive of my work. Dr. T. Fritz clarified many things regarding the TerraSAR-X annotation components. Dr. S. Gernhardt was ready to share his expertise in PSI processing all the time. Dr. P. Ghamisi had many heated discussions with me about publication ethics and career planning. Dr. C. Gisinger took over the geodetic corrections, and lectured me about SAR imaging geodesy. Dr. Y. Hao trained me to be a better TEXer by AMS standards. Dr. D. Hong gave me loads of assignments, which brought many headaches but also broadened my understanding of nonconvex optimization. Dr. T. Ji taught me a few optimization tricks. Dr. M. Lachaise patiently explained to me in details the different height accuracies adopted by the TanDEM-X mission. Dr. S. Li offered plenty of insight into my work from an algebraic geometric point of view, and never shied away from showing his amazing skills of constructing (counter)examples. S. Luo urged me to improve my mathematical thinking and reasoning. L. Krieger con-

stantly updated me on his own progress, which forced me to compromise the quality of this dissertation. Dr. S. Montazeri always lent me a helping hand whenever in need. Without his assistance I would not have survived many project deadlines. A. Parizzi taught me many things about backscattering mechanism, side lobe detection, L-band interferometry, etc. Dr. S. Peter gave me an excellent overview of sparse recovery algorithms, and was always ready to discuss my optimization problems. F. Rodriguez Gonzalez, who is practically my "shadow mentor", taught me countless things ranging from SAR focusing, PSI processing, numerical optimization, to software engineering, and aided me persistently in data processing whenever he was able to, despite the heavy workloads that he had already undertaken. The quality of this dissertation would have been much inferior without his contributions, for which I am forever indebted. Dr. M. Schmitt kindly gave me his code at the very beginning, which I viewed as a welcome message from this community. Dr. R. Shau offered his IT expertise whenever needed, and helped me a lot with my German. The TerraSAR-X Science Coordination, in particular U. Marschalk, and the DFD Orderdesk supported me consistently throughout the whole doctoral study, without which there would not have been any tomographic point cloud in this dissertation. Dr. Y. Wang allowed me to use his predecessor during the first half of my doctoral study. Dr. N. Yokoya showed me the beauty and power of ADMM, which underlies many algorithms in this dissertation.

I dedicate this dissertation to my natural stupidity, without which my doctoral study would have been finished two years earlier.

Contents

List of Figures

List of Tables

Acronyms

1-D	one-dimensional
2-D	two-dimensional
3-D	three-dimensional
ADMM	Alternating Direction Method of Multipliers
APS	Atmospheric Phase Screen
BFGS	Broyden-Fletcher-Goldfarb-Shanno
BIC	Bayesian Information Criterion
BiCRAM	Bi-Convex Relaxation and Alternating Minimization
CRLB	Cramér-Rao Lower Bound
DLR	Deutsches Zentrum für Luft- und Raumfahrt
GPS	Global Positioning System
GSRLS	Group Sparsity-Regularized Least Squares
HRWS	High Resolution Wide Swath
InSAR	Interferometric SAR
IWAP	Integrated Wide Area Processor
JSRLS	Joint Sparsity-Regularized Least Squares
JTMRLS	Joint Tensor Mode-Regularized Least Squares
KKT	Karush-Kuhn-Tucker
L1RLS	ℓ_1-Regularized Least Squares
M-RELAX	Multi-look Relaxation
MAD	Median Absolute Deviation
MUSIC	Multiple Signal Classification
NLS	Nonlinear Least Squares

PS	Persistent Scatterer
PSI	Persistent Scatterer Interferometry
SAR	Synthetic Aperture Radar
SD	Standard Deviation
SESAME	Sentinel-1 SAR Companion Multistatic Explorer
SLC	Single-Look Complex
SNR	Signal-to-Noise Ratio
TanDEM-X	TerraSAR-X add-on for Digital Elevation Measurements
TUM	Technical University of Munich
UTM	Universal Transverse Mercator

1 Introduction

This chapter provides a very short introduction to spaceborne Synthetic Aperture Radar (SAR) tomography in urban scenarios, a review of the state of the art, and the motivation for the work to be elucidated in the following chapters.

First of all, we introduce the mathematical notations adopted throughout this dissertation.

Notation. We denote scalars as lower- or uppercase letters (e.g., m, N, λ), vectors as bold lowercase letters (e.g., $\mathbf{g}$, $\boldsymbol{\gamma}$), matrices, sets and ordered pairs as bold uppercase letters (e.g., $\mathbf{R}$, $\boldsymbol{\Omega}$), tensors as calligraphic bold uppercase letters (e.g., $\boldsymbol{\mathcal{X}}$), and number fields as blackboard bold uppercase letters (e.g., $\mathbb{Z}$, $\mathbb{R}$, $\mathbb{C}$) with the following conventions:

- g_n denotes the nth entry of $\mathbf{g}$.
- $\mathbf{a}^m$ and $\mathbf{a}_n$ denote the mth row and nth column of $\mathbf{A}$, respectively.
- $\operatorname{Diag}(\mathbf{a})$ denotes a square diagonal matrix whose entries on the main diagonal are equal to $\mathbf{a}$, and $\operatorname{Diag}(\mathbf{A})$ denotes a vector whose entries are equal to those on the main diagonal of $\mathbf{A}$.
- $\operatorname{Supp}(\mathbf{x})$ denotes the index set of the nonzero entries or support of $\mathbf{x}$.
- $\overline{\mathbf{A}}$, $\mathbf{A}^T$ and $\mathbf{A}^H$ denote the (elementwise) complex conjugate, transpose and conjugate transpose of $\mathbf{A}$, respectively.
- $\mathbf{A}_R$ and $\Re(\mathbf{A})$ denote the real part of $\mathbf{A}$.
- $\mathbf{A}_I$ and $\Im(\mathbf{A})$ denote the imaginary part of $\mathbf{A}$.
- $\mathbf{A} \circ \mathbf{B}$ and $\mathbf{A} \otimes \mathbf{B}$ denote the Hadamard and Kronecker products of $\mathbf{A}$ and $\mathbf{B}$, respectively.
- $\mathbf{A} \succ \mathbf{0}$ means that $\mathbf{A}$ is positive definite. $\mathbf{B} \prec \mathbf{0}$ means that $\mathbf{B}$ is negative definite.
- $\mathbf{A}_{\boldsymbol{\Omega}}$ denotes the matrix formed by extracting the columns of $\mathbf{A}$ indexed by $\boldsymbol{\Omega}$.
- $(\mathbf{A}, \mathbf{B})$ denotes the vertically concatenated matrix $\begin{pmatrix} \mathbf{A} \\ \mathbf{B} \end{pmatrix}$.
- $\|\mathbf{A}\|_{1,2}$ denotes the $\ell_{1,2}$ norm of $\mathbf{A}$, i.e., the sum of the ℓ_2 norms of its rows.
- $\mathbf{I}$ denotes the identity matrix.
- $[N]$ denotes the set $\{1, \ldots, N\}$.

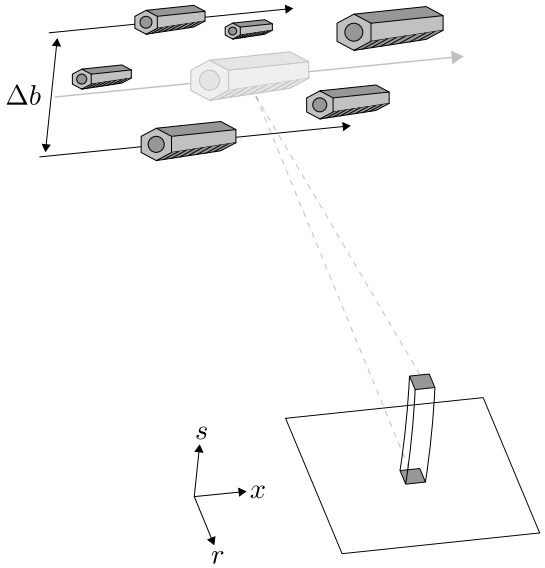

Figure 1.1: SAR imaging geometry. The azimuth, range and elevation axes are denoted as x, r and s, respectively. The spread of repeat-pass sensor positions forms an elevation aperture Δb for reconstructing the 3-D far field.

- $|\mathbf{\Omega}|$ denotes the cardinality of the set $\mathbf{\Omega}$.
- The nonnegative and positive subsets of a number field $\mathbb{F}$ are denoted as $\mathbb{F}_+$ and $\mathbb{F}_{++}$, respectively.

1.1 Fundamentals of Spaceborne SAR Tomography

SAR tomography is an Interferometric SAR (InSAR) technique for reconstructing three-dimensional (3-D) sensor far field from two-dimensional (2-D) range-azimuth measurements of radar echoes [2–4]. It is occasionally deemed a multi-scatterer extension of Persistent Scatterer Interferometry (PSI) [5–7], although the latter is based on the inversion of phase double-differences of neighboring Persistent Scatterers (PSs).

Denote the azimuth, range and elevation axes as x, r and s, respectively, where s is perpendicular to the x-r plane (see Fig. 1.1). Suppose there are a total of N repeat-pass acquisitions by a spaceborne sensor. After deramping, each Single-Look Complex (SLC) SAR measurement at some x-r positions can be approximated by the Fourier transform $\Gamma : \mathbb{R} \to \mathbb{C}$ of the elevation-dependent reflectivity profile $\gamma : \mathbb{R} \to \mathbb{C}$ at the corresponding wavenumber k [8]:

$$g_n = \Gamma(k_n) \coloneqq \int \gamma(s) \exp(-jk_n s) \mathrm{d}s, \quad n \in [N], \tag{1.1}$$

where $k_n \coloneqq -4\pi b_n/(\lambda r_0)$ is the nth wavenumber dependent on the nth sensor position b_n relative to an arbitrary reference position along an axis $b \parallel s$, λ is the radar wavelength,

and r_0 is the slant range distance relative to a ground reference point. For the sake of simplicity, we assume here that the scatterers in the far field are not subject to any motion. An extension to the differential case, in which scatterers' motion is typically modeled as a linear combination of basis functions, is revisited in Sec. 3.1.

Discretizing the elevation axis as $s_1, \ldots, s_L$ and replacing the integral in (1.1) by a finite sum result in a linear model:

$$\mathbf{g} \approx \mathbf{R}\boldsymbol{\gamma}, \tag{1.2}$$

where $\mathbf{g} \in \mathbb{C}^N$ is the SLC measurement vector, $\mathbf{R} \in \mathbb{C}^{N \times L}$ is the tomographic sensing matrix given by $r_{nl} \coloneqq \exp(-jk_n s_l)$, and $\boldsymbol{\gamma} \in \mathbb{C}^L$ is the discrete reflectivity vector. This leads to an inverse problem of estimating $\boldsymbol{\gamma}$ with known $\mathbf{R}$ and $\mathbf{g}$.

Now we briefly revisit some theoretical bounds on the performance of elevation reconstruction. The spread of repeat-pass sensor positions builds an elevation aperture Δb (i.e., the range of b_n, see Fig. 1.1), which determines the Rayleigh resolution:

$$\rho_s \coloneqq \frac{\lambda r_0}{\Delta b} = \frac{4\pi}{\Delta k}, \tag{1.3}$$

where Δk is the range of k_n. In the case of TerraSAR-X [9–11], ρ_s is typically 20–30 m, which is much coarser than the azimuth and range resolutions at meter or sub-meter levels in the spotlight modes. This is a consequence of confining the sensor positions into a 250-m orbit tube [12]. Nevertheless, the actual performance of any tomographic SAR algorithm is not limited by ρ_s, but rather by the Cramér-Rao Lower Bound (CRLB) of elevation estimates [13]:

$$\sigma_{\hat{s}} \coloneqq \frac{1}{\sqrt{N}\sqrt{2SNR}\,\sigma_k}, \tag{1.4}$$

where SNR is the scatterer's Signal-to-Noise Ratio (SNR), σ_k is the uncorrected sample standard deviation of k_n. Suppose the sensor positions are independent and identically distributed random variables with some fixed standard deviation, we have $\sigma_{\hat{s}} \propto 1/\sqrt{N \cdot SNR}$, i.e., N and SNR are to some extent interchangeable.

In the case of double scatterers, their mutual interference may lead to a degradation of the quality of elevation estimates. The CRLB of elevation estimates is in addition dependent on their elevation distance δs and phase difference $\delta\phi$ [14, 15]:

$$\sigma_{\hat{s}_i} \coloneqq \frac{1}{\sqrt{N}\sqrt{2SNR_i}\,\tau(k_1, \ldots, k_N, \delta s, \delta\phi)}, \quad i \in [2], \tag{1.5}$$

where SNR_i is the SNR of the ith scatterer, and $\tau : \mathbb{R}^{N+2} \to \mathbb{R}_{++}$ is a nonlinear function that is periodic in $\delta\phi$ (with a period of π) if all the other parameters are fixed [14]:

$$\tau(k_1, \ldots, k_N, \delta s, \delta\phi) \coloneqq \sqrt{\Upsilon_1 + \Upsilon_2 \cos(2\delta\phi) + \Upsilon_3 \sin(2\delta\phi)}, \tag{1.6}$$

where

$$\Upsilon_1 \coloneqq \Phi_1 - \frac{\Phi_2^2 + \Phi_3^2}{2\Phi_1}, \quad \Upsilon_2 \coloneqq -\frac{\Phi_2^2 - \Phi_3^2}{2\Phi_1}, \quad \Upsilon_3 \coloneqq -\frac{\Phi_2\Phi_3}{\Phi_1}, \tag{1.7}$$

$$\begin{aligned}
\Phi_1 &:= \frac{X_2(X_0^2 - \Psi_0^2 - \Omega_0^2) - X_0(X_1^2 + \Psi_1^2 + \Omega_1^2) + 2X_1(\Psi_0\Psi_1 + \Omega_0\Omega_1)}{X_0^2 - \Psi_0^2 - \Omega_0^2}, \\
\Phi_2 &:= \frac{-\Psi_2(X_0^2 - \Psi_0^2 - \Omega_0^2) - \Psi_0(X_1^2 + \Psi_1^2 - \Omega_1^2) + 2\Psi_1(X_0X_1 - \Omega_0\Omega_1)}{X_0^2 - \Psi_0^2 - \Omega_0^2}, \\
\Phi_3 &:= \frac{-\Omega_2(X_0^2 - \Psi_0^2 - \Omega_0^2) - \Omega_0(X_1^2 - \Psi_1^2 + \Omega_1^2) + 2\Omega_1(X_0X_1 - \Psi_0\Psi_1)}{X_0^2 - \Psi_0^2 - \Omega_0^2},
\end{aligned} \tag{1.8}$$

and

$$X_p := \frac{1}{N^{p-1}} \sum_{n\in[N]} k_n^p, \quad \Psi_p := \frac{1}{N^{p-1}} \sum_{n\in[N]}^{N} k_n^p \cos(k_n \delta s), \quad \Omega_p := \frac{1}{N^{p-1}} \sum_{n\in[N]} k_n^p \sin(k_n \delta s), \tag{1.9}$$

$p = 0, 1, 2$.

In the next section, we review the state of the art as a result of a literature research, and justify the motivation for the work to be introduced in the following chapters.

1.2 State of the Art and Motivation

As shown in Tab. 1.1, tomographic SAR algorithms can be roughly classified into four categories:

- *Single-look single-master*
  Reigber & Moreira (2000) accomplished the avant-garde work on airborne SAR tomography by sampling densification via the integer interferogram combination technique and subsequently discrete Fourier transform on an interpolated linear

Table 1.1: A classification of tomographic SAR algorithms with examples

	Single-Master	Multi-Master
Single-Look	Reigber & Moreira (2000) Fornaro et al. (2003, 2005, 2008) Budillon et al. (2010) Zhu & Bamler (2010a, 2010b, 2011) Etc.	Zhu & Bamler (2012)†
Multi-Look	Aguilera et al. (2012) Schmitt & Stilla (2012) Liang et al. (2018) Shi et al. (2019) Etc.	Gini et al. (2002) Lombardini (2005) Duque et al. (2009, 2010, 2014) Fornaro et al. (2014) Etc.

† Uses the single-look single-master data model

array of baselines [2]. Fornaro et al. (2003, 2005, 2008) paved the way for spaceborne SAR tomography with repeat-pass acquisitions over a long period of time and proposed to use more advanced inversion techniques such as truncated singular value decomposition [4,8,16]. Zhu & Bamler (2010a) made the first demonstration of SAR tomography with very high resolution spaceborne SAR data by employing Tikhonov regularization and Nonlinear Least Squares (NLS) [17]. Budillon et al. (2010) and Zhu & Bamler (2010b) married compressive sensing techniques with tomographic inversion by assuming that the sensor far field is compressible. Zhu & Bamler (2011) proposed a generic algorithm (named SL1MMER) consisting of spectral estimation, model-order selection and debiasing [15].

- *Single-look multi-master*
  As far as we know, there is hardly any publication in this category. Zhu & Bamler (2012) extended the Tikhonov regularization, NLS and compressive sensing approaches to a mixed TerraSAR-X and TerraSAR-X add-on for Digital Elevation Measurements (TanDEM-X) stack by exploiting a pre-estimated covariance matrix [18]. Still, these algorithms are based on the single-look single-master data model.

- *Multi-look single-master*
  Aguilera et al. (2012) utilized the joint sparsity among multiple polarimetric channels by means of distributed compressive sensing [19]. Schmitt & Stilla (2012) also used distributed compressive sensing to reconstruct an adaptively chosen neighborhood of looks in a collective manner [20]. Liang et al. (2018) employed compressive sensing for joint 2-D range-elevation focusing in an azimuth line [21]. Shi et al. (2019) performed nonlocal filtering of interferograms before tomographic reconstruction [22].

- *Multi-look multi-master*
  As a rule of thumb, any algorithm based on an estimation of the auto-correlation matrix belongs to this category. This is closely related to state-of-the-art adaptive multi-looking techniques that exploit all possible interferometric combinations [23–27]. Gini et al. (2002) studied the performance of different spectral estimators such as Capon, Multiple Signal Classification (MUSIC) and the Multi-look Relaxation (M-RELAX) algorithm [3]. Lombardini (2005) extended SAR tomography to the differential case by reformulating it as a multi-dimensional spectral estimation problem and proposed to solve it with higher-order Capon [28]. Duque et al. (2009, 2010) carried out the first investigation of bistatic SAR tomography by using ground-based receivers and spectral estimators such as Capon and MUSIC [29, 30]. Duque et al. (2014) analyzed the feasibility of SAR tomography using only a single pass of alternating bistatic acquisitions, in which the hypothesis test on the number of scatterers is based on the eigendecomposed empirical covariance matrix [31]. Fornaro et al. (2014) proposed an algorithm (named CAESAR) using principal component analysis of the eigendecomposed empirical covariance matrix in an adaptively chosen neighborhood [32]. Naturally, SAR tomography in forested

scenarios (e.g., [33–40]), where random volume scattering in canopy is generally expected, also falls in this category.

In the *single-master* configuration, one SLC, typically near the center of joint orbital and temporal distribution, is selected as the common master for interferogram generation. Suppose the master is indexed by $i \in [N]$. Each interferogram is usually normalized by the master magnitude, i.e., $g_n\overline{g_i}/|g_i|$, $\forall n \in [N]$. This phase calibration step converts k_n into the wavenumber baseline $\Delta k_n \coloneqq k_n - k_i$, $\forall n \in [N]$. Consequently, the zero position of wavenumber baseline is fixed, i.e., $\Delta k_i = 0$. The rationale behind this is, e.g., to facilitate 2-D phase unwrapping for Atmospheric Phase Screen (APS) compensation by smoothing out interferometric phase in the x-r plane. In the *single-look* case, it is deemed plausible to assume that the discrete reflectivity vector $\boldsymbol{\gamma}$ in (1.2) is compressible in urban scenarios, since roof, facade and ground appear to be the major sources of layover phenomena [41]. Exploiting this compressibility prior typically involves solving an ℓ_1-Regularized Least Squares (L1RLS) problem. In the common case of differential SAR tomography using repeat-pass acquisitions, this problem is both large-scale and ill-posed. First-order methods, although preferred for solving large-scale problems due to their efficiency, are typically subject to convergence issues due to the fact that the tomographic sensing matrix $\mathbf{R}$ is ill-conditioned. Besides, the choice of regularization parameter may be crucial for obtaining reasonable elevation estimates. In the *multi-look* case, Zhu et al. (2015) demonstrated that the prior knowledge of motion-free scatterers among different looks sharing the same elevation position can be incorporated into tomographic inversion by means of joint sparsity recovery [42]. However, it is often necessary to consider scatterers' motion in long-term repeat-pass acquisitions, and the joint sparsity prior can be too strong since it tends to enforce scatterers to share the same motion.

In the *multi-master* setting, the data model is similar to (1.1) in forested scenarios, where multi-looking is required for the underlying random volume scattering. Suppose $\gamma(s)$ is a white random signal. For any master and slave sampled at k and $k + \Delta k$, respectively, the Van Cittert–Zernike theorem implies that the expectation (due to multi-looking) of the interferogram, which is at the same time the autocorrelation function $R_{\Gamma\Gamma}$ of Γ, is the Fourier transform of the elevation-dependent backscatter coefficient $\sigma_0 : \mathbb{R} \to \mathbb{R}$ at Δk:

$$\mathrm{E}[\Gamma(k + \Delta k)\overline{\Gamma(k)}] = R_{\Gamma\Gamma}(\Delta k) = \int \sigma_0(s) \exp(-j\Delta k s)\mathrm{d}s, \tag{1.10}$$

where the white property of $\gamma(s)$, i.e., $\mathrm{E}[\gamma(s)\overline{\gamma(s')}] = \sigma_0(s)\delta(s - s')$, is used. This leads to an inverse problem similar to the one in the *single-look single-master* configuration. On the contrary, the data model in the *single-look* setting has not been investigated yet.

A study of *single-look multi-master* SAR tomography is interesting on its own. Moreover, it is also partially motivated by the special case of single-look bi- or multistatic SAR tomography that is relevant for future spaceborne SAR missions such as:

- Tandem-L, a German satellite mission concept with a principal goal to observe the dynamics of the earth's surface in high resolution with an unprecedented ac-

curacy [43]. It consists of two satellites, and each will be equipped with a high-resolution wide-swath L-band SAR sensor. In general, these two satellites will fly in close formation and operate in bistatic mode. This mode employs one sensor as a transmitter to illuminate a common radar footprint, while both receive radar echoes from the earth's surface. The requirement of a highly accurate mutual time and phase referencing will be easily fulfilled by means of the heritage of the TanDEM-X mission [44]. Due to limited temporal decorrelation and APS, single-pass bistatic interferograms are characterized by better phase quality as compared to conventional repeat-pass ones and thus are more suitable for generating a global consistent digital elevation model in high resolution [45].

- SAOCOM-CS, a bistatic mission concept adding to SAOCOM a passive companion SAR satellite operating in L-band [46].

- Sentinel-1 SAR Companion Multistatic Explorer (SESAME), a bistatic mission concept attaching to Sentinel-1 two passive companion SAR satellites operating in C-band [47].

- Sentinel-1 "tandem" (i.e., one-day separation) or bistatic mission concept employing the prospective Sentinel-1C and another satellite from the series [48].

- High Resolution Wide Swath (HRWS), the successor of TerraSAR-X comprising one or two SAR satellites operating in X-band [49, 50], and several additional passive companion transponder satellites without bidirectional phase synchronization link (known as MirrorSAR) [51–53].

Above all, Tandem-L is the most fascinating one, not only because it has already undergone extremely comprehensive and intensive studies (see for example [53–57] and the references therein), but it is also highly promising for a large variety of geophysical applications. Therefore, we need to develop tomographic SAR algorithms dedicated to bistatic acquisitions.

This dissertation addresses the following scientific questions:

Q1 In the *single-look single-master* case, how can we improve the convergence of first-order methods for solving the L1RLS problem, and achieve automatic tuning of its regularization parameter?

Q2 In the *multi-look single-master* case, given the looks where scatterers are located at the same elevation position, how can we exploit this prior knowledge in the repeat-pass acquisitions, while still taking scatterers' different motion patterns into account?

Q3 How does *single-look multi-master* SAR tomography work?

Q4 Given a stack of bistatic or multistatic acquisitions, how can we effectively estimate both scatterers' elevation and motion?

The rest of the dissertation is organized as follows. The SAR and auxiliary data sets underlying the numerical experiments in the subsequent chapters are described in Chp. 2. Chp. 3 is dedicated to Q1 and Q2. An answer to Q3 is provided in Chp. 4. Chp. 5 addresses Q4. Chp. 6 summarizes this dissertation and provides some outlook.

2 Data Sets

This chapter provides a brief description of two data sets: the first one is comprised of conventional repeat-pass SAR acquisitions of Munich and the height ground truth of a building facade (see also Chp. 3 and 4), and the second one consists of pursuit monostatic SAR acquisitions of the city of Las Vegas (see also Chp. 5).

2.1 Munich Data Set

The first data set contains 31 TerraSAR-X repeat-pass acquisitions of the central Munich area in the staring spotlight mode from a descending track. These scenes were acquired from March 31, 2016 to December 7, 2017, and processed with Deutsches Zentrum für Luft- und Raumfahrt (DLR)'s Integrated Wide Area Processor (IWAP) [58,59]. Besides side lobe detection, every non-peak look inside a main lobe was also removed, since it could otherwise result in a "ghost" scatterer after tomographic reconstruction, like any side lobe. The vertical wavenumbers of a single-master stack with the master from December 20, 2016 are shown in Fig. 2.1. Since the IWAP-PSI results show no obvious linear motion, a sinusoidal basis function will be employed to model periodical motion induced by temperature change. The vertical Rayleigh resolution (1.3) at scene center is approximately 12.66 m. Given a nominal SNR of 2 dB, the CRLB of height estimates (1.4) is approximately 1.02 m.

Our region of interest comprises mainly a six-story building ("Nordbau") of the Technical University of Munich (TUM), which is shown in Fig. 2.2 (left). The building signature in the SAR intensity image can be observed in Fig. 2.2 (right). The regular grid of salient points within the building footprint results from triple reflections on three orthogonal surfaces: metal plate (behind window glass), window ledge and brick wall [1]. After main and side lobe detection, a total of 594 looks, whose azimuth-range positions are illustrated in Fig. 2.3 (right), were obtained for tomographic reconstruction.

The Munich data set also consists of height ground truth made available via a SAR imaging geodesy and simulation framework [1]. The starting point was to create a 3-D facade model from terrestrial measurements via (drone-borne) camera, tachymeter,

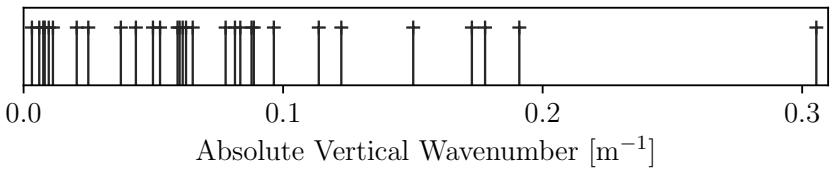

Figure 2.1: Absolute vertical wavenumbers. The largest one is approximately 0.31 m^{-1}.

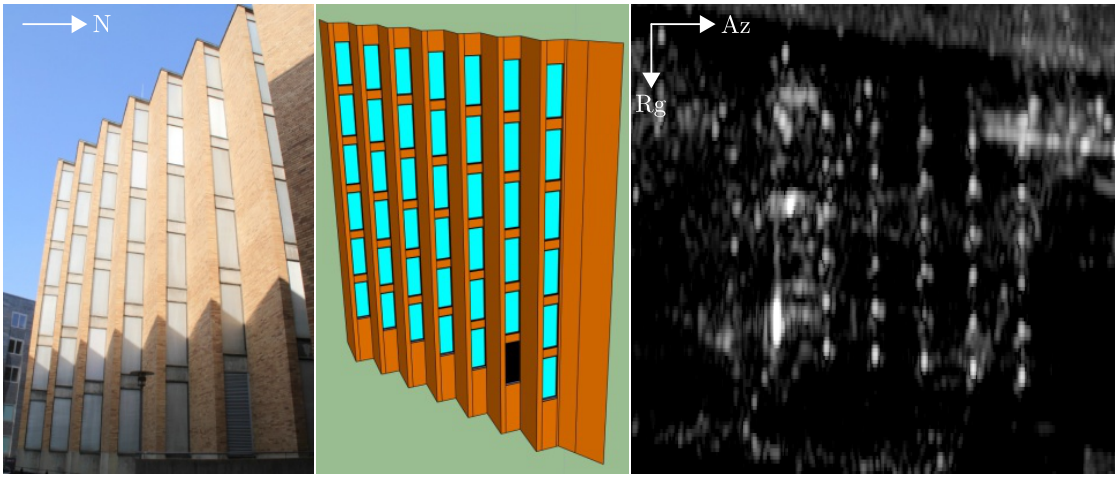

Figure 2.2: Eastern facade of the six-story TUM-Nordbau building in our region of interest [1]. Left: in-situ photo. Middle: 3-D facade model (the black shape corresponds to a metallic window). Right: SAR intensity image.

measuring rod and differential Global Positioning System (GPS). This facade model has an overall accuracy better than 2 cm and a very high level of details [1]. Ground control points were employed for referencing it to an international terrestrial reference frame. Fig. 2.2 (middle) provides a visualization of this 3-D facade model. The RaySAR simulator [60] was used to simulate dominant scatterers that correspond to the aforementioned triple reflections on the building facade. By means of atmospheric and geodynamic corrections from DLR's SAR Geodetic Processor [61, 62], and the recently enhanced TerraSAR-X orbit products [63], scatterers' absolute coordinates were converted into azimuth timing, range timing and height, which we refer to as *Level 0* ground truth data.

Level 1 ground truth data is comprised of the height of 30 simulated PSs that are matched with real ones. The matching was conducted in the range-azimuth geometry, so as not to be affected by any height estimate error [64]. Fig. 2.3 (left) shows the height simulations at the sub-pixel range-azimuth positions of the corresponding 30 PSs. This height is relative to a corner reflector located next to a permanent GPS station on top of a neighboring TUM building [1].

Level 2 ground truth data consists of the interpolated height of a total of 594 looks. The interpolation was performed in the following way. First, the height of each simulated PS was converted into topographic phase. Subsequently, the distance to the polyline representing the furthest-range cross-section of the building facade was used as the independent variable to construct a one-dimensional (1-D) interpolator. Lastly, topographic phase was interpolated at the previously mentioned 594 looks and converted back into height. This interpolated height is shown in Fig. 2.3 (right). Naturally, the underlying assumption of this interpolation is that each scatterer, if it does exist, should be located on the building facade. A cross-validation of the 1-D interpolator was per-

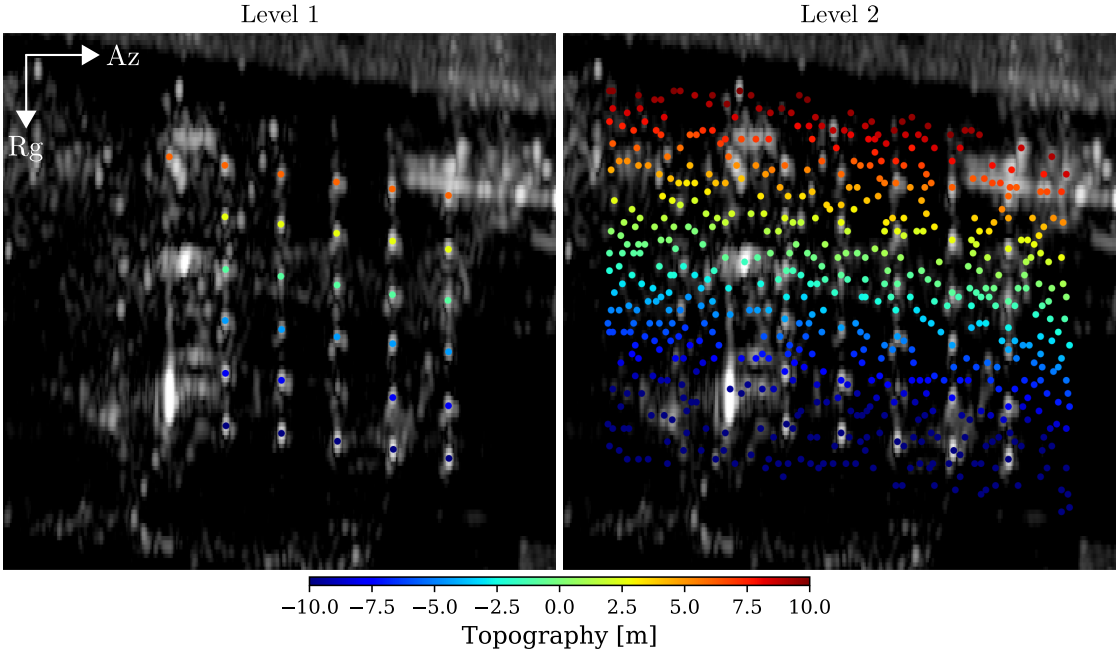

Figure 2.3: Height ground truth of the TUM-Nordbau facade in our region of interest. Left: RaySAR height simulations at 30 matched PS coordinates (Level 1). Right: interpolated height at 594 facade looks (Level 2).

formed in [1], in which the Standard Deviation (SD) and Median Absolute Deviation (MAD) were reported to be 0.004 and 0.002 m, respectively.

2.2 Las Vegas Data Set

The second data set comprises 12 TanDEM-X pursuit monostatic acquisitions of the City of Las Vegas in the staring spotlight mode from an ascending track. Contrary to the bistatic mode, the pursuit monostatic counterpart utilizes two satellites in a close formation to operate independently from each other [44]. It can be considered as a backup solution of the bistatic mode for the case where pulse or phase synchronization fails. The pursuit monostatic mode was temporarily employed from October 2014 to February 2015 during the TanDEM-X Science Phase [65]. In order to rule out any radio frequency interference between radar signals, the along-track distance was programmed to be circa 76 km, which corresponds to a time interval of approximately 10 s. Given moderate wind speed, the temporal decorrelation is still small for vegetated terrain types, and APS is largely eliminated by interferogram generation [65]. During these five months, the cross-track perpendicular baselines were set to slowly drift from 0 to 750 m, so as to favor tomographic and other applications in polar regions [65]. The vertical wavenumbers are illustrated in Fig. 2.4. The vertical Rayleigh resolution (1.3) is

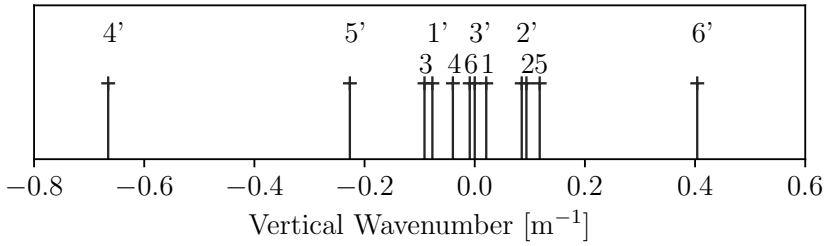

Figure 2.4: Vertical wavenumbers of 12 acquisitions. The numbers on top of the crosses are the master and slave indices of pursuit monostatic interferograms, i.e., (i, i') represents the ith interferogram, $\forall i \in [6]$.

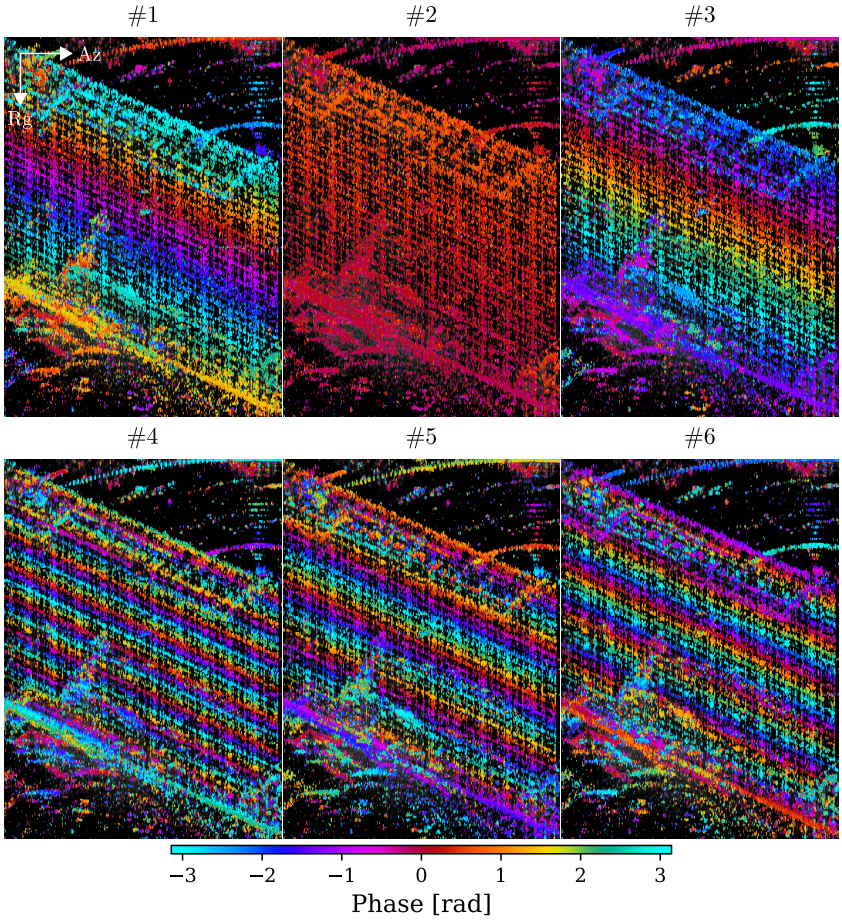

Figure 2.5: Six pursuit monostatic interferograms generated from 12 acquisitions (see also Fig. 2.4).

approximately 5.88 m at scene center, while the CRLB of height estimates (1.4), given a nominal SNR of 2 dB, is circa 0.68 m.

Our region of interest comprises mainly a thirty-story high-rise building and its surroundings. Fig. 2.5 shows the six pursuit monostatic interferograms of this region, where the fringes in the building footprint appear to be highly coherent.

3 Single-Master SAR Tomography

This chapter is divided into two sections. Sec. 3.1 introduces an algorithm for solving the L1RLS problem in the *single-look* case. Another algorithm for jointly reconstructing scatterers at the same elevation position, but possibly subject to different motion, is developed in Sec. 3.2.

3.1 Single-Look Case

If scatterers are subject to any motion, which is likely the case for repeat-pass acquisitions over a long period of time, (1.1) becomes

$$g_n = \int \gamma(s) \exp\left(-j\left(k_n s + (4\pi/\lambda) d(s,t_n)\right)\right) \mathrm{d}s, \quad n \in [N], \tag{3.1}$$

where $d(s,t_n)$ denotes the motion of the scatterer with elevation position s at time t_n. Without loss of generality, suppose $d(s,t_n)$ can be decomposed into a linear combination of basis functions:

$$d(s,t_n) = \frac{\lambda}{4\pi} \sum_{m\in[M]} c_m(s)\psi_m(t_n), \tag{3.2}$$

where the elevation-dependent c_m denotes the unknown parameter of the mth basis function $\psi : \mathbb{R} \to \mathbb{R}$. Thereby (3.1) becomes

$$g_n = \int \gamma(s) \exp\left(-j\left(k_n s + \sum_{m\in[M]} c_m(s)\psi_m(t_n)\right)\right) \mathrm{d}s, \quad n \in [N], \tag{3.3}$$

which can be shown to be equivalent to a multi-dimensional Fourier transform [66].

Likewise, let $\mathbf{s}$ be the discretization of s, and $\mathbf{c}_m$ be that of c_m, $\forall m \in [M]$. This leads again to the linear model

$$\mathbf{g} \approx \mathbf{R}\boldsymbol{\gamma}, \tag{1.2}$$

where the tomographic sensing matrix $\mathbf{R} \in \mathbb{C}^{N\times L}$ is given by $\mathbf{r}^n \coloneqq \exp(-j\psi_n^M \mathbf{c}_M) \otimes \cdots \otimes \exp(-j\psi_n^1 \mathbf{c}_1) \otimes \exp(-jk_n\mathbf{s})$, $\psi_n^m \coloneqq \psi_m(t_n)$, and $\boldsymbol{\gamma} \in \mathbb{C}^L$ is the discrete reflectivity vector along elevation and motion parameters. Since $L = |\mathbf{s}| \prod_{m=1}^{M} |\mathbf{c}_m|$, the dimension of the inverse problem increases multiplicatively with the complexity of the motion model.

In the case of one single motion basis function, i.e., $M = 1$, the CRLB of the elevation estimates of a single scatter is

$$\sigma_{\hat{s}} \coloneqq \frac{1}{\sqrt{N}\sqrt{2SNR}\sqrt{1 - r_{k\psi}^2}\,\sigma_k}, \tag{3.4}$$

where $r_{k\psi}$ is the sample correlation coefficient between k_n and $\psi_n \coloneqq \psi(t_n)$. This can be interpreted as a degradation of σ_k by taking motion into account.

As already mentioned in Sec. 1.2, the discrete reflectivity vector $\boldsymbol{\gamma}$ in (1.2) can be assumed to be compressible in urban scenarios, since roof, facade and ground appear to be the major sources of layover phenomena. Under this assumption, a popular choice is to solve the L1RLS problem [67] [68, §3.4.2]:

$$\underset{\boldsymbol{\gamma}}{\text{minimize}}\, \frac{1}{2}\|\mathbf{R}\boldsymbol{\gamma} - \mathbf{g}\|_2^2 + \lambda\|\boldsymbol{\gamma}\|_1, \tag{3.5}$$

where the regularization parameter $\lambda \in \mathbb{R}_{++}$ (not to be confused with the radar wavelength) controls the balance between the model goodness of fit and the sparsity of $\boldsymbol{\gamma}$.

Since L1RLS solutions are prone to spike-like artifacts [69], it is customary to perform subsequently model-order selection in order to reduce false positive rate [15]. Based on the Bayesian Information Criterion (BIC) [70], model-order selection can be formulated as the following constrained minimization problem:

$$\begin{aligned} \hat{\boldsymbol{\Omega}} \coloneqq \underset{\boldsymbol{\Omega}(,\boldsymbol{\delta})}{\arg\min} \quad & 2N \ln\left(\|\mathbf{R}_{\boldsymbol{\Omega}}\boldsymbol{\delta}_{\boldsymbol{\Omega}} - \mathbf{g}\|_2^2/N\right) + (5|\boldsymbol{\Omega}| + 1)\ln(N) \\ \text{subject to} \quad & \text{Supp}(\boldsymbol{\delta}) = \boldsymbol{\Omega} \subset \text{Supp}(\hat{\boldsymbol{\gamma}}), \end{aligned} \tag{3.6}$$

where $\hat{\boldsymbol{\gamma}}$ is the solution of (3.5), and the second term in the objective function penalizes model complexity. This involves solving a sequence of subset least squares problems in the form of

$$\underset{\boldsymbol{\epsilon}}{\text{minimize}}\, \frac{1}{2}\|\mathbf{R}_{\boldsymbol{\Omega}}\boldsymbol{\epsilon} - \mathbf{g}\|_2^2, \tag{3.7}$$

whose solution is known analytically.

Let $\hat{K} \coloneqq |\hat{\Omega}|$ denote the number of selected scatterers. Since their elevation positions and motion parameters are unlikely to be located on the previously defined grids, we propose to correct the consequential off-grid errors by solving the following nonlinear and nonconvex minimization problem:

$$\underset{\gamma_l^R,\gamma_l^I,s_l,c_l^m}{\text{minimize}} \sum_{n\in[N]} \left| g_n - \sum_{l\in[\hat{K}]} (\gamma_l^R + j\gamma_l^I) \exp\left(-j\left(k_n s_l + \sum_{m\in[M]} \psi_n^m c_l^m\right)\right)\right|^2, \tag{3.8}$$

where γ_l^R, γ_l^I, s_l and c_l^m denote the real and imaginary parts of the lth scatterer's complex reflectivity, its elevation and its motion parameter associated with the mth basis function, respectively. Since its objective function is differentiable w.r.t. γ_l^R, γ_l^I, s_l and c_l^m, $\forall l \in [\hat{K}]$, $m \in [M]$, (3.8) can be solved effectively by using, e.g., the Broyden-Fletcher-Goldfarb-Shanno (BFGS) algorithm [71, §6.1].

The next two subsections are dedicated to the sparse recovery problem (3.5).

3.1.1 Accelerated Sparse Recovery

In this subsection, we develop an algorithm for solving (3.5), or equivalently

$$\underset{\mathbf{x}}{\text{minimize}}\, \frac{1}{2}\|\mathbf{A}\mathbf{x} - \mathbf{b}\|_2^2 + \lambda\|\mathbf{x}\|_1, \tag{3.9}$$

Algorithm 3.1 An ADMM-based algorithm for solving (3.9)

1: **Input:** $\mathbf{A}$, $\mathbf{b}$, $\mathbf{z}^{(0)}$, λ, ρ
2: **Initialize** $\mathbf{z} \leftarrow \mathbf{z}^{(0)}$
3: **Until** stopping criterion is satisfied, **Do**
4: $\quad \mathbf{x} \leftarrow (\mathbf{A}^H\mathbf{A} + \rho\mathbf{I})^{-1}(\mathbf{A}^H\mathbf{b} + \rho\mathbf{z} - \mathbf{y})$
5: $\quad \mathbf{z} \leftarrow \mathrm{Prox}_{\ell_1,\lambda/\rho}\left(\mathbf{x} + (1/\rho)\mathbf{y}\right)$
6: $\quad \mathbf{y} \leftarrow \mathbf{y} + \rho\left(\mathbf{x} - \mathbf{z}\right)$
7: **Output:** $\mathbf{z}$

based on the Alternating Direction Method of Multipliers (ADMM) [72]. ADMM solves a minimization problem by alternatively minimizing its augmented Lagrangian [73, p. 509], in which the augmentation term is scaled by a penalty parameter $\rho \in \mathbb{R}_{++}$. It converges under very general conditions with medium accuracy [72, §3.2].

The minimization problem (3.9) is equivalent to

$$\begin{aligned} \underset{\mathbf{x},\mathbf{z}}{\text{minimize}} \quad & \frac{1}{2}\|\mathbf{A}\mathbf{x} - \mathbf{b}\|_2^2 + \lambda\|\mathbf{z}\|_1 \\ \text{subject to} \quad & \mathbf{x} - \mathbf{z} = \mathbf{0}. \end{aligned} \tag{3.10}$$

Applying the ADMM update rules results in Alg. 3.1, where $\mathrm{Prox}_{\ell_1,\lambda} : \mathbb{C}^L \to \mathbb{C}^L$ is the proximal operator of the ℓ_1 norm scaled by λ (also known as the soft thresholding operator [74]):

$$\mathrm{Prox}_{\ell_1,\lambda}(\mathbf{x}) \coloneqq \arg\min_{\mathbf{z}} \lambda\|\mathbf{z}\|_1 + \frac{1}{2}\|\mathbf{x} - \mathbf{z}\|_2^2, \tag{3.11}$$

whose i-th entry is given by [75, §6.5.2]

$$\mathrm{Prox}_{\ell_1,\lambda}(\mathbf{x})_i = (1 - \lambda/|x_i|)_+ \, x_i, \tag{3.12}$$

where $(x)_+ \coloneqq \max(x, 0)$.

In the case of differential SAR tomography, Alg. 3.1 may be slow due to the fact that (3.9) is both large-scale and ill-posed. In order to resolve this issue, we employ several acceleration techniques.

The first one provides a more efficient way for the $\mathbf{x}$-update.

1) *Matrix inversion lemma:* In Alg. 3.1, an L-by-L matrix has to be inverted. In the case of large L, a direct exact approach is tedious. Instead, we utilize the following lemma.

   Lemma 3.1 (Matrix inversion lemma [76])**.** For any $\mathbf{A} \in \mathbb{C}^{n\times m}$, $\mathbf{B} \in \mathbb{C}^{m\times n}$ and nonsingular $\mathbf{C} \in \mathbb{C}^{n\times n}$, the following equation holds:

   $$(\mathbf{A}\mathbf{B} + \mathbf{C})^{-1} = \mathbf{C}^{-1} - \mathbf{C}^{-1}\mathbf{A}(\mathbf{I} + \mathbf{B}\mathbf{C}^{-1}\mathbf{A})^{-1}\mathbf{B}\mathbf{C}^{-1}. \tag{3.13}$$

   The right-hand side of (3.13) is more efficient if inverting $\mathbf{C}$ is straightforward. This condition is satisfied for $\mathbf{A}^H\mathbf{A} + \rho\mathbf{I}$, and applying Lemma 3.1 leads to

   $$(\mathbf{A}^H\mathbf{A} + \rho\mathbf{I})^{-1} = \frac{1}{\rho}\mathbf{I} - \frac{1}{\rho^2}\mathbf{A}^H\left(\mathbf{I} + \frac{1}{\rho}\mathbf{A}\mathbf{A}^H\right)^{-1}\mathbf{A}. \tag{3.14}$$

As a result, instead of the original L-by-L matrix, only an N-by-N matrix needs to be inverted. Since $\mathbf{I} + (1/\rho)\mathbf{A}\mathbf{A}^H \succ \mathbf{0}$, the Cholesky factorization, which takes $(1/3)N^3$ [76, §C.3.2] flops, can be used.

Alternatively, the least squares subproblem in the $\mathbf{x}$-update can be solved approximately in an iterative manner [77]. This is also known as inexact minimization [72, §3.4.4].

The following techniques can be applied in order to improve convergence.

2) *Varying penalty parameter:* The principal idea is to update the penalty parameter ρ at each iteration. In addition to the convergence aspect, this also makes Alg. 3.1 less dependent on the initial choice of ρ. At the $(k+1)$th iteration, a common approach is to set [72, §3.4.1]

$$\rho^{(k+1)} := \begin{cases} \tau\rho^{(k)} & \text{if } \|\mathbf{r}^{(k)}\|_2 > \mu\|\mathbf{s}^{(k)}\|_2 \\ \rho^{(k)}/\tau & \text{if } \|\mathbf{s}^{(k)}\|_2 > \mu\|\mathbf{r}^{(k)}\|_2 \\ \rho^{(k)} & \text{otherwise} \end{cases}, \tag{3.15}$$

where $\tau, \mu > 1$ are parameters, $\mathbf{r}^{(k)} := \mathbf{x}^{(k)} - \mathbf{z}^{(k)}$ denotes the primal residual, and $\mathbf{s}^{(k)} := \rho^{(k)}(\mathbf{z}^{(k)} - \mathbf{z}^{(k-1)})$ denotes the dual residual. Both $\mathbf{r}^{(k)}$ and $\mathbf{s}^{(k)}$ converge to $\mathbf{0}$ as $k \to \infty$. Intuitively, increasing ρ tends to impose a larger penalty on the augmenting term $(\rho/2)\|\mathbf{x} - \mathbf{z}\|_2^2$ in the augmented Lagrangian [73, p. 509] and therefore decrease $\|\mathbf{r}^{(k)}\|_2$ on the one hand, and to increase $\|\mathbf{s}^{(k)}\|_2$ by definition on the other, and vice versa. The motivation is to keep $\mathbf{r}^{(k)}$ and $\mathbf{s}^{(k)}$ approximately of the same order. As a matter of course, (3.14) needs to be recomputed whenever ρ changes, which can be viewed as a downside of this technique.

3) *Diagonal preconditioning:* In the augmented Lagrangian, the augmenting term $(\rho/2)\|\mathbf{x} - \mathbf{z}\|_2^2$ can be replaced by

$$(1/2)\langle \mathbf{P}(\mathbf{x} - \mathbf{z}), \mathbf{x} - \mathbf{z} \rangle, \tag{3.16}$$

where $\mathbf{P} \in \mathbb{R}^{L \times L}$ is diagonal and positive definite. Note that this falls under the category of more general augmenting terms [72, §3.4.2]. By means of this, Alg. 3.1 is freed from the choice of ρ, and the ADMM updates become

$$\begin{aligned} \mathbf{x} &\leftarrow (\mathbf{A}^H\mathbf{A} + \mathbf{P})^{-1}(\mathbf{A}^H\mathbf{b} + \mathbf{P}\mathbf{z} - \mathbf{y}) \\ \mathbf{z} &\leftarrow \mathrm{Prox}_{\ell_1, \lambda/\mathbf{p}}\left(\mathbf{x} + \mathbf{P}^{-1}\mathbf{y}\right) \\ \mathbf{y} &\leftarrow \mathbf{y} + \mathbf{P}\left(\mathbf{x} - \mathbf{z}\right), \end{aligned} \tag{3.17}$$

where $\mathbf{p} := \mathrm{Diag}(\mathbf{P})$, and $\mathrm{Prox}_{\ell_1, \mathbf{w}} : \mathbb{C}^L \to \mathbb{C}^L$ is the proximal operator of the weighted ℓ_1 norm with weights $\mathbf{w} \in \mathbb{R}_{++}^L$:

$$\mathrm{Prox}_{\ell_1, \mathbf{w}}(\mathbf{x}) := \arg\min_{\mathbf{z}} \ \|\mathbf{z}\|_{\mathbf{w},1} + \frac{1}{2}\|\mathbf{x} - \mathbf{z}\|_2^2, \tag{3.18}$$

whose i-th entry is given by

$$\mathrm{Prox}_{\ell_1, \mathbf{w}}(\mathbf{x})_i = (1 - w_i/|x_i|)_+ \, x_i. \tag{3.19}$$

Table 3.1: Number of iterations using different acceleration techniques

	#1	#2	#3	#4	#5	#6
Baseline	20289	14250	15752	19571	23920	16983
Vary	1445	1101	1780	1958	2005	1033
Precondition	679	480	504	1074	840	805
Relax	11272	7916	8750	10866	13288	9446
Vary+Relax	767	625	871	821	834	1051
Precondition+Relax	377	260	288	595	467	447

If $\mathbf{A}^H\mathbf{A}$ is ill-conditioned, which is typically the case in spaceborne SAR tomography, $\mathbf{P}$ can be interpreted as a preconditioner. Naturally, Lemma 3.1 can also be utilized to invert $\mathbf{A}^H\mathbf{A} + \mathbf{P}$.

Pock and Chambolle (2011) proposed a simple and elegant approach to construct diagonal preconditioners for a primal-dual algorithm [78] [73, §15.2] with guaranteed convergence:

$$p_i \coloneqq \frac{1}{\|\mathbf{a}_i\|_\alpha^\alpha}, \quad \forall l \in [L], \tag{3.20}$$

where $\alpha \in [0, 2]$ is a parameter.

4) *Over-relaxation:* An additional step is added to Alg. 3.1 between the $\mathbf{x}$- and $\mathbf{z}$-updates:

$$\mathbf{x} \leftarrow \beta\mathbf{x} + (1 - \beta)\mathbf{z}, \tag{3.21}$$

where $\beta \in [1.5, 1.8]$ is a parameter (see for example [72, §3.4.3] and the references therein).

Fig. 3.1 illustrates the convergence curves of Alg. 3.1 using different acceleration techniques, as applied to real tomographic SAR data (#6 in Tab. 3.1, see also Sec. 4.4.2). In order to generate this plot, we first let the vanilla Alg. 3.1 run non-stop until it converged with extremely high precision. Then we took this solution as an optimal point $\mathbf{x}^\star$ and calculated the absolute difference between the values of the objective function $|f(\mathbf{x}) - f(\mathbf{x}^\star)|$ at each iteration. Each technique did help to accelerate Alg. 3.1 in comparison to "baseline", where we set $\rho = 1$. The number of iterations is given in Tab. 3.1 for this and five other cases. As can be observed, the combination of diagonal preconditioning and over-relaxation was the most competitive one. This will therefore be adopted for all the ADMM-based algorithms in the following.

Last but not least, we applied the accelerated sparse recovery algorithm to the Munich data set (see Sec. 2.1) in the full scene extent. The tomographic results are illustrated in Fig. 3.2, where there are a total of 2711820 single and 475182 double scatterers. By using 20 threads, the tomographic processing took circa 48.91 hours on a Linux server with an Intel processor at 3.30 GHz.

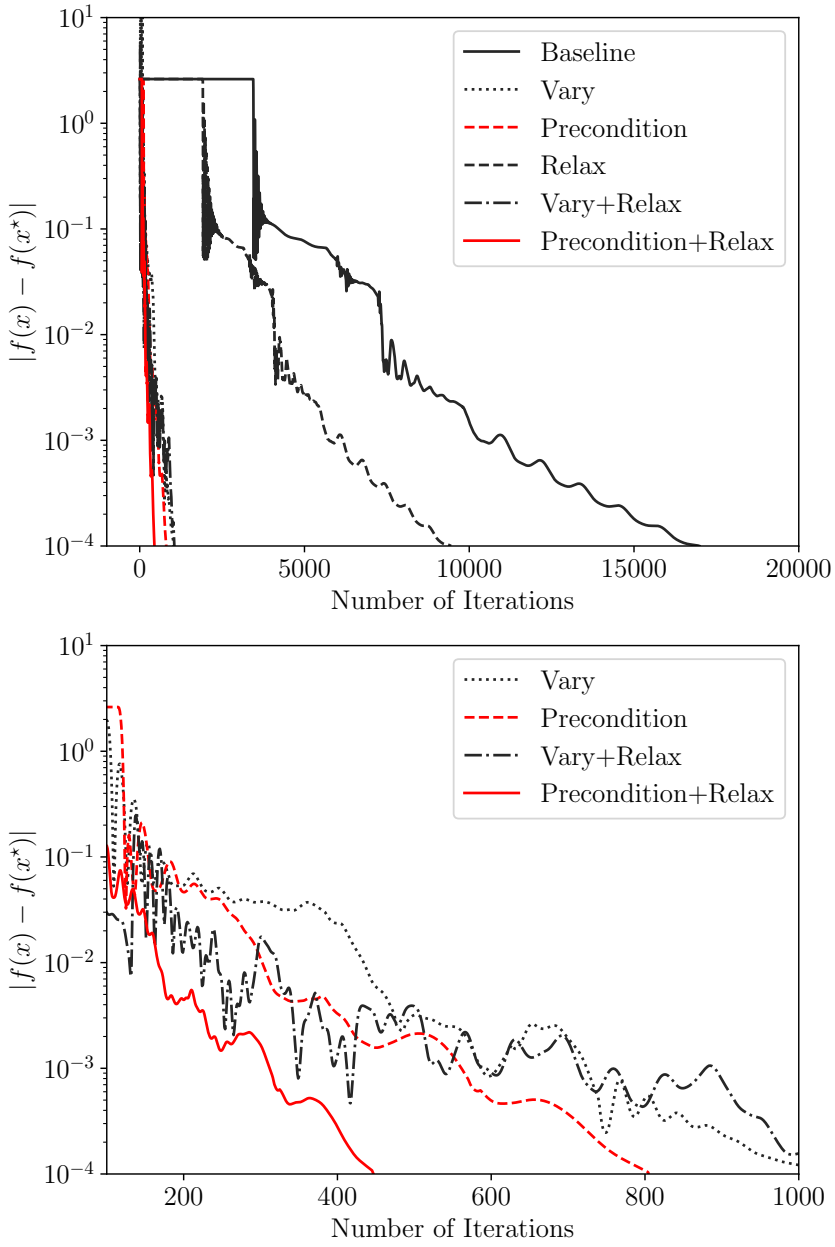

Figure 3.1: Convergence curves of Alg. 3.1 using different acceleration techniques. "Baseline": $\rho = 1$. "Vary": varying penalty parameter. "Precondition": diagonal preconditioning. "Relax": over-relaxation. Bottom: a close-up of the top figure.

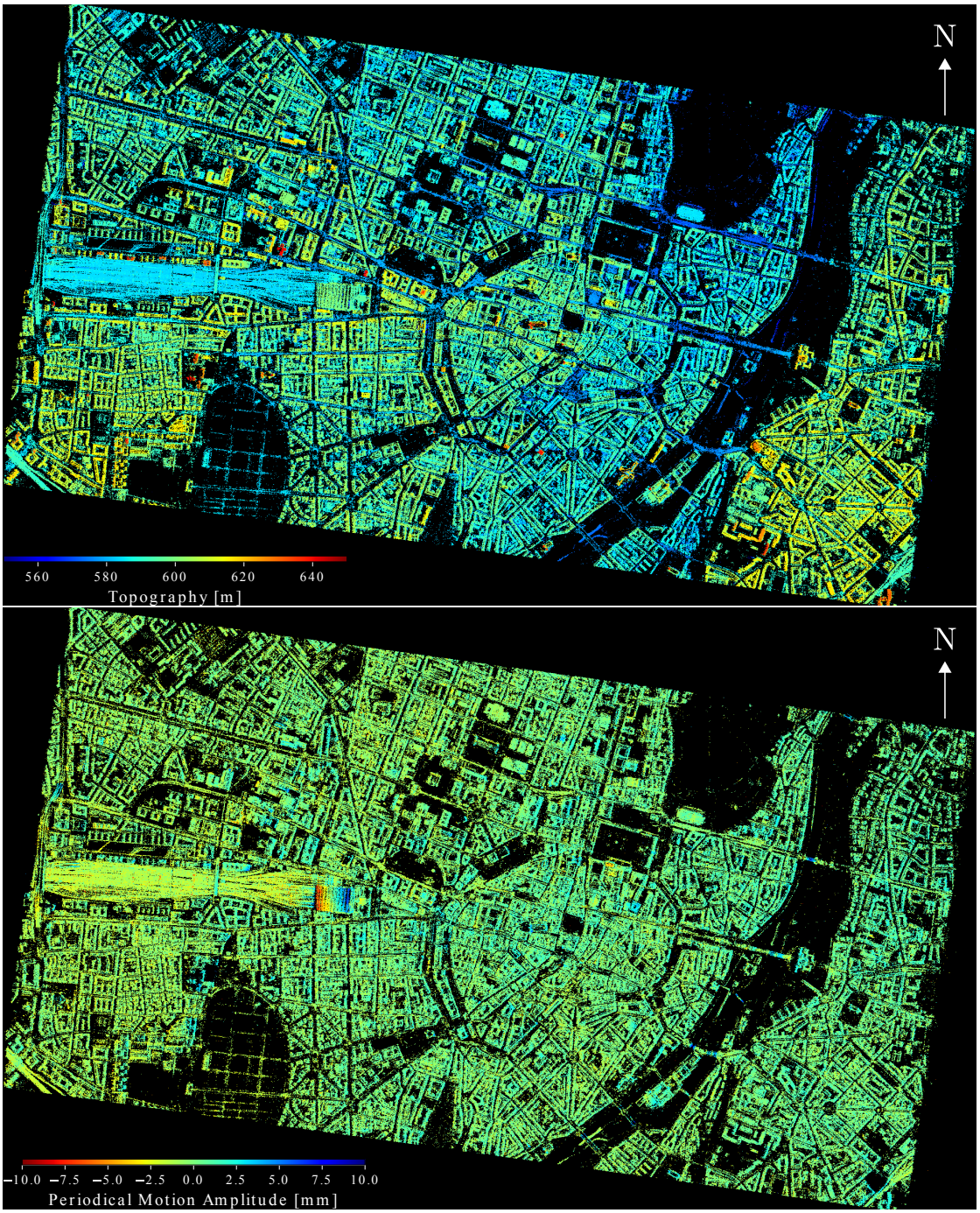

Figure 3.2: Single-look single-master tomographic estimates of the Munich data set with L1RLS. Top: topography. Bottom: periodical motion amplitude.

3.1.2 Automatic Regularization Parameter Tuning

In this subsection, we develop a scheme for automatic regularization parameter tuning based on the theory of vector optimization.

Let $f(\mathbf{x}) \coloneqq (1/2)\|\mathbf{A}\mathbf{x}-\mathbf{b}\|_2^2$ and $g(\mathbf{x}) \coloneqq \|\mathbf{x}\|_1$. Consider the unconstrained bi-criterion optimization problem

$$\underset{\mathbf{x}}{\text{minimize}}\ (\text{w.r.t. } \mathbb{R}_+^2)\,(f(\mathbf{x}), g(\mathbf{x}))\,, \tag{3.22}$$

which is a special case of the more general vector optimization problem [76, §4.7.1]. The rationale is to minimize $f(\mathbf{x})$ and $g(\mathbf{x})$ at the same time w.r.t. the nonnegative quadrant. However, it can be shown that, for this specific problem, there is no *minimum* element of the set of objective function values. That is, $\nexists \mathbf{x}^\star$ such that $(f(\mathbf{x}^\star), g(\mathbf{x}^\star)) \preceq_{\mathbb{R}_+^2} (f(\mathbf{x}), g(\mathbf{x}))$, i.e., $f(\mathbf{x}^\star) \leq f(\mathbf{x})$ and $g(\mathbf{x}^\star) \leq g(\mathbf{x})$, $\forall \mathbf{x} \in \mathbb{C}^L$. Instead, we are interested in its *minimal* elements, i.e., any $(f(\mathbf{x}^\star), g(\mathbf{x}^\star))$ such that $(f(\mathbf{x}), g(\mathbf{x})) \preceq_{\mathbb{R}_+^2} (f(\mathbf{x}^\star), g(\mathbf{x}^\star)) \implies (f(\mathbf{x}), g(\mathbf{x})) = (f(\mathbf{x}^\star), g(\mathbf{x}^\star))$. In other words,

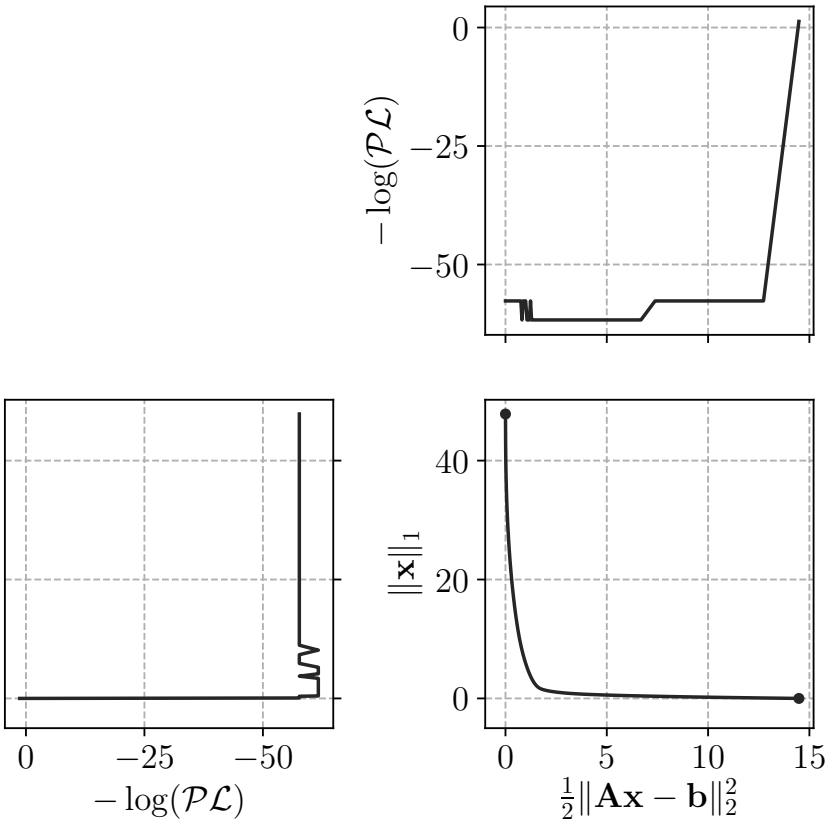

Figure 3.3: Optimal trade-off curve of an L1RLS problem. Top right: model goodness of fit vs. negative penalized log-likelihood. Bottom left: negative penalized log-likelihood vs. regularization term.

any $\mathbf{x}$ that is no worse than $\mathbf{x}^\star$ has the same objective value as $\mathbf{x}^\star$. In this case, $\mathbf{x}^\star$ is referred to as a Pareto optimal point [76, §4.7.3].

A standard technique for finding Pareto optimal points is to scalarize (3.22), i.e.,

$$\underset{\mathbf{x}}{\text{minimize}}\, \boldsymbol{\lambda}^T \left(f(\mathbf{x}), g(\mathbf{x})\right), \tag{3.23}$$

where $\boldsymbol{\lambda} \in \mathbb{R}^2_{++}$. A direct application of the results in [76, §4.7.4] leads to the following corollary.

Corollary 3.2. For any $\boldsymbol{\lambda} \in \mathbb{R}^2_{++}$, $\arg\min_{\mathbf{x}} \boldsymbol{\lambda}^T \left(f(\mathbf{x}), g(\mathbf{x})\right)$ is Pareto optimal for the bi-criterion optimization problem (3.22). Partially conversely, for any Pareto optimal $\mathbf{x}^\star$, $\exists \boldsymbol{\lambda} \in \mathbb{R}^2_{+}$, $\boldsymbol{\lambda} \neq \mathbf{0}$ such that $\mathbf{x}^\star$ is a solution of the scalarized problem (3.23).

Basically, we can find all Pareto optimal points by varying $\boldsymbol{\lambda}$ over the nonnegative quadrant. In other words, we trace the optimal trade-off curve, which is defined as the set of Pareto optimal values. An optimal trade-off curve is provided in Fig. 3.3 (bottom right) for the same example in Fig. 3.1. The top left dot is the Pareto optimal point where $\lambda_1/\lambda_2 \to \infty$. It can be proved that [73, Proposition 15.1]

$$\lim_{\lambda_1/\lambda_2 \to \infty} \arg\min_{\mathbf{x}} \left(\lambda_1 f(\mathbf{x}) + \lambda_2 g(\mathbf{x})\right) = \arg\min_{\mathbf{x}} \|\mathbf{x}\|_1 \text{ subject to } \mathbf{A}\mathbf{x} = \mathbf{b}, \tag{3.24}$$

i.e., this point corresponds to the solution of the equality-constrained ℓ_1 minimization problem. On the other hand, the bottom right dot denotes the point where the solution is zero. This is bound to happen since

$$\lambda_1/\lambda_2 < 1/\|\mathbf{A}^H\mathbf{b}\|_\infty \implies \arg\min_{\mathbf{x}} \left(\lambda_1 f(\mathbf{x}) + \lambda_2 g(\mathbf{x})\right) = \mathbf{0}. \tag{3.25}$$

A popular heuristic is to sample the optimal trade-off curve by utilizing (3.25), and to select the point having the highest penalized log-likelihood via model-order selection (3.6). We adopt this idea, and replace the likelihood by the one after off-grid correction (3.8), since any quantization error would also propagate to it. The top right and bottom left subfigures in Fig. 3.3 show the negative penalized log-likelihood along the optimal trade-off curve. As can be observed, it reaches its minimum when $f(\mathbf{x})$ is within the interval of approximately $[1, 7]$, where two scatterers are correctly detected.

The next section addresses a sparse recovery problem in the multi-look single-master setting.

3.2 Multi-Look Case: Joint Tensor Mode Recovery

In this section, we consider a specific problem in the multi-look case described as follows. Suppose there are a total of P looks of SLC measurements. Every look contains a certain number of scatterers, each of which is located at the same elevation position as another one in any other look. However, they are not necessarily subject to the same motion. Following the conventions in Sec. 3.1, suppose scatterers' motion can be decomposed into

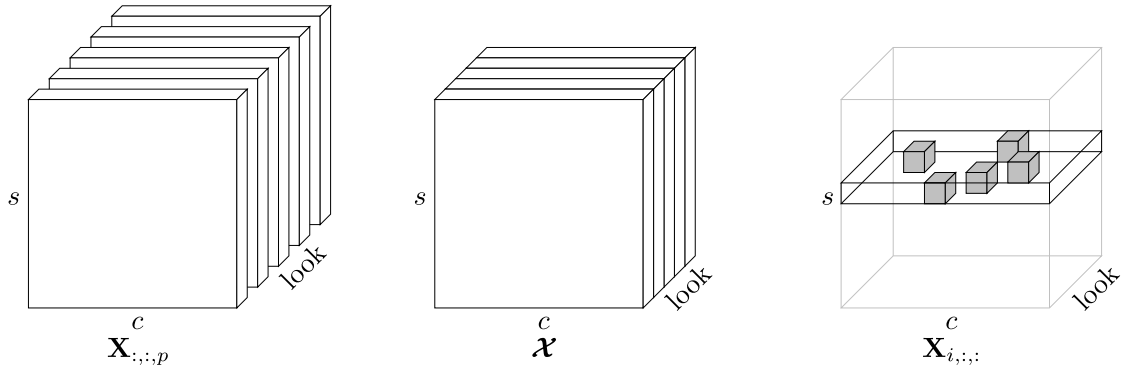

Figure 3.4: Discrete reflectivity tensor $\boldsymbol{\mathcal{X}}$. Left: frontal slices $\mathbf{X}_{:,:,p}$. Right: a horizontal slice $\mathbf{X}_{i,:,:}$ consisting of scatterers at the same elevation whose motion parameters are different.

M basis functions. Let $\mathbf{s}$ be the discretization of elevation, and $\mathbf{c}_m$ be the discretization of motion parameters, $\forall m \in [M]$. The discrete reflectivity can be represented by an $(M+2)$-way tensor $\boldsymbol{\mathcal{X}} \in \mathbb{C}^{|\mathbf{s}|\times|\mathbf{c}_1|\times\cdots\times|\mathbf{c}_M|\times P}$ [79]. Fig. 3.4 shows such a tensor with $M = 1$, i.e., the discrete reflectivity is a three-way tensor $\boldsymbol{\mathcal{X}} \in \mathbb{C}^{|\mathbf{s}|\times|\mathbf{c}|\times P}$. Each frontal slice $\mathbf{X}_{:,:,p} \in \mathbb{C}^{|\mathbf{s}|\times|\mathbf{c}|}$, $p \in [P]$, is the discrete reflectivity matrix of the pth look. An instance of the aforementioned prior knowledge is illustrated in Fig. 3.4 (right).

In principle, we want to promote scatterers among different looks to align exclusively in s, i.e., in the first mode. For any $p \in [P]$, let $\mathbf{R}^{(p)}$ and $\mathbf{g}^{(p)}$ denote the corresponding tomographic sensing matrix and SLC measurement vector, respectively. We propose the following Joint Tensor Mode-Regularized Least Squares (JTMRLS) problem:

$$\underset{\boldsymbol{\mathcal{X}}}{\text{minimize}}\, \frac{1}{2} \sum_{p\in[P]} \|\mathbf{R}^{(p)} \operatorname{Vec}(\boldsymbol{\mathcal{X}}_{:,\ldots,p}) - \mathbf{g}^{(p)}\|_2^2 + \lambda \sum_{i\in[|\mathbf{s}|]} \|\boldsymbol{\mathcal{X}}_{i,\ldots,:}\|_F, \tag{3.26}$$

where $\operatorname{Vec} : \mathbb{C}^{d_1\times\ldots d_m} \to \mathbb{C}^{\prod_{i=1}^m d_i}$ is the vectorization operator, and the tensor Frobenius norm is defined as [79]

$$\|\boldsymbol{\mathcal{Y}}\|_F \coloneqq \sqrt{\sum_{i_1\in[d_1]} \cdots \sum_{i_m\in[d_m]} |y_{i_1,\ldots,i_m}|^2}, \tag{3.27}$$

for any $\boldsymbol{\mathcal{Y}} \in \mathbb{C}^{d_1\times\ldots d_m}$.

Let $\mathbf{g} \coloneqq (\mathbf{g}^{(1)}, \ldots, \mathbf{g}^{(P)})$ be the concatenated SLC measurement vector. The JTMRLS problem is equivalent to a Group Sparsity-Regularized Least Squares (GSRLS) problem:

$$\underset{\boldsymbol{\gamma}}{\text{minimize}}\, \frac{1}{2}\|\mathbf{R}\boldsymbol{\gamma} - \mathbf{g}\|_2^2 + \lambda \sum_{\boldsymbol{\eta}\in\mathbf{H}} \|\boldsymbol{\gamma}_{\boldsymbol{\eta}}\|_2, \tag{3.28}$$

where $\mathbf{R}$ is the block diagonal matrix given by

$$\mathbf{R} \coloneqq \begin{pmatrix} \mathbf{R}^{(1)} & & \\ & \ddots & \\ & & \mathbf{R}^{(P)} \end{pmatrix}, \tag{3.29}$$

Algorithm 3.2 An ADMM-based algorithm for solving (3.30)

1: **Input:** $\mathbf{A}$, $\mathbf{b}$, $\mathbf{H}$, $\mathbf{z}^{(0)}$, λ, ρ
2: **Initialize** $\mathbf{z} \leftarrow \mathbf{z}^{(0)}$
3: **Until** stopping criterion is satisfied, **Do**
4: $\quad \mathbf{x} \leftarrow (\mathbf{A}^H\mathbf{A} + \rho\mathbf{I})^{-1}(\mathbf{A}^H\mathbf{b} + \rho\mathbf{z} - \mathbf{y})$
5: $\quad \mathbf{z} \leftarrow \mathrm{Prox}_{\mathbf{H},\lambda/\rho}\left(\mathbf{x} + (1/\rho)\mathbf{y}\right)$
6: $\quad \mathbf{y} \leftarrow \mathbf{y} + \rho\left(\mathbf{x} - \mathbf{z}\right)$
7: **Output:** $\mathbf{z}$

$\boldsymbol{\gamma} \coloneqq (\mathrm{Vec}(\boldsymbol{\mathcal{X}}_{:,\ldots,1}), \ldots, \mathrm{Vec}(\boldsymbol{\mathcal{X}}_{:,\ldots,P}))$ is the concatenated discrete reflectivity vector, and each $\boldsymbol{\eta} \in \mathbf{H}$ is an index set corresponding to a specific elevation position such that $\mathbf{H}$ forms a partition of $[L]$, $L \coloneqq |\mathbf{s}| \prod_{m\in[M]} |\mathbf{c}_m| P$. Note that this generalizes the Joint Sparsity-Regularized Least Squares (JSRLS) problem in which no motion is considered [42].

By a change of variables, the GSRLS problem (3.28) becomes

$$\underset{\mathbf{x}}{\text{minimize}}\, \frac{1}{2}\|\mathbf{A}\mathbf{x} - \mathbf{b}\|_2^2 + \lambda \sum_{\boldsymbol{\eta}\in\mathbf{H}} \|\mathbf{x}_{\boldsymbol{\eta}}\|_2, \tag{3.30}$$

or equivalently

$$\begin{aligned} \underset{\mathbf{x},\mathbf{z}}{\text{minimize}} \quad & \frac{1}{2}\|\mathbf{A}\mathbf{x} - \mathbf{b}\|_2^2 + \lambda \sum_{\boldsymbol{\eta}\in\mathbf{H}} \|\mathbf{z}_{\boldsymbol{\eta}}\|_2 \\ \text{subject to} \quad & \mathbf{x} - \mathbf{z} = \mathbf{0}. \end{aligned} \tag{3.31}$$

Applying the ADMM update rules leads to Alg. 3.2. The proximal operator $\mathrm{Prox}_{\mathbf{H},\lambda} : \mathbb{C}^L \to \mathbb{C}^L$ of the group sparsity norm scaled by λ is given by:

$$\mathrm{Prox}_{\mathbf{H},\lambda}(\mathbf{x}) \coloneqq \arg\min_{\mathbf{z}}\, \lambda \sum_{\boldsymbol{\eta}\in\mathbf{H}} \|\mathbf{z}_{\boldsymbol{\eta}}\|_2 + \frac{1}{2}\|\mathbf{x} - \mathbf{z}\|_2^2, \tag{3.32}$$

whose $\boldsymbol{\eta}$-group entries are given by [75, §6.5.4]

$$\mathrm{Prox}_{\mathbf{H},\lambda}(\mathbf{x})_{\boldsymbol{\eta}} = (1 - \lambda/\|\mathbf{x}_{\boldsymbol{\eta}}\|_2)_+ \, \mathbf{x}_{\boldsymbol{\eta}}, \tag{3.33}$$

which can be interpreted as a blockwise soft thresholding.

As a proof of concept, we applied this method to the Munich data set described in Sec. 2.1. In particular, we exploited the matched PSs in Fig. 2.3 (left) to extract five clusters, each of which comprises five looks that contain scatterers at the same elevation position. As already explained in Sec. 2.1, we used one sinusoidal basis function to account for the periodical motion induced by temperature change. The height estimates of L1RLS (3.5) and JTMRLS (3.26) are shown in Fig. 3.5, while the periodical motion amplitude estimates are shown in Fig. 3.6. These estimates seem very similar and it is really difficult to visually observe any difference. Fig. 3.7 (left) shows the height estimates along azimuth. Obviously, the L1RLS estimates jitter around the JTMRLS

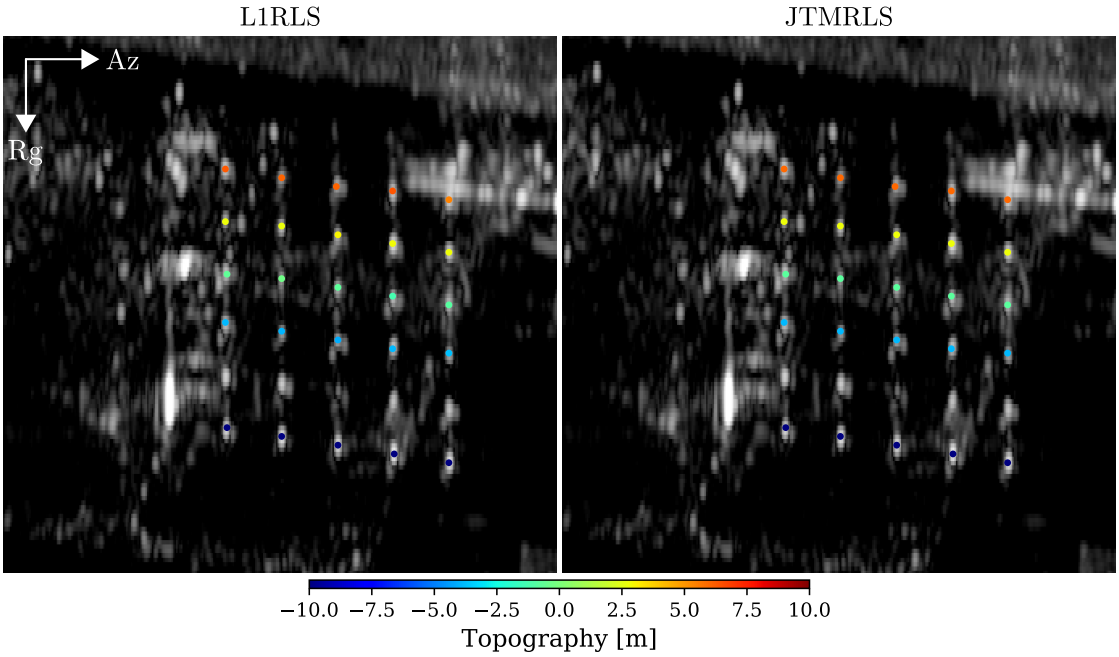

Figure 3.5: L1RLS vs. JTMRLS: height estimates.

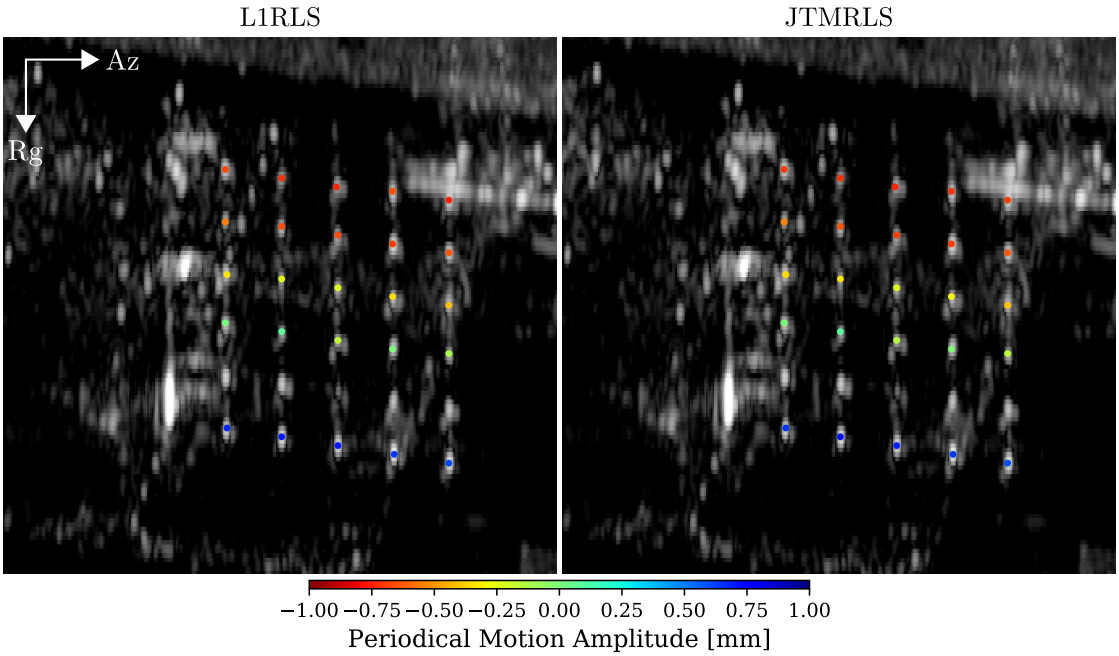

Figure 3.6: L1RLS vs. JTMRLS: periodical motion amplitude estimates.

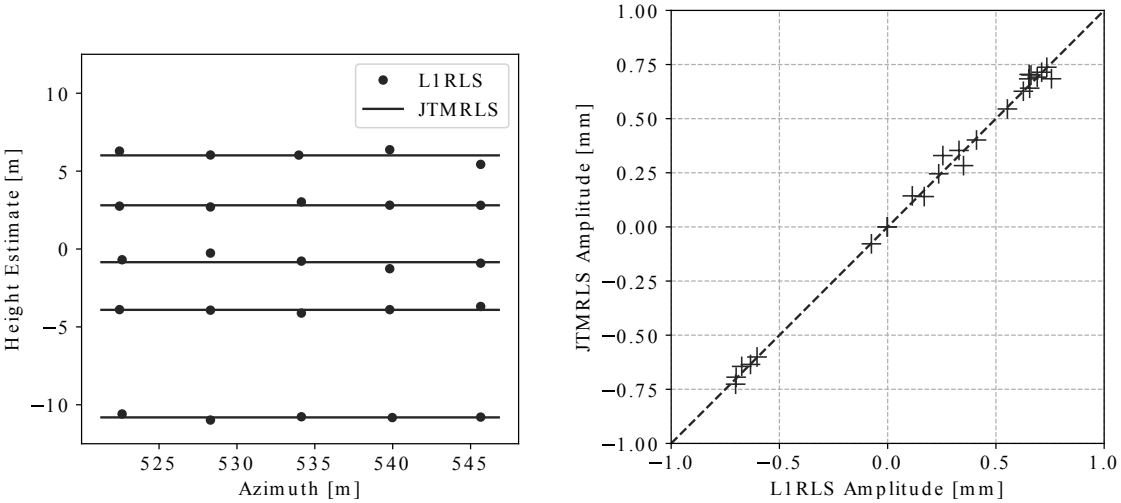

Figure 3.7: L1RLS vs. JTMRLS. Left: height estimates along azimuth. Right: scatter plot of estimated periodical motion amplitude.

ones, showing the superiority of the latter. On the other hand, their periodical motion parameter estimates are highly correlated, as can be observed in Fig. 3.7 (right). This implies that JTMRLS did not compromise on motion estimation by enforcing iso-height scatterers to also share the same motion parameter.

The next chapter addresses spaceborne SAR tomography in the single-look multi-master setting.

4 Single-Look Multi-Master SAR Tomography

In this chapter, we tackle the general problem of single-look multi-master SAR tomography. Sec. 4.1 establishes the single-look multi-master data model, analyzes its implications for single and double scatterers, and introduces a generic inversion framework consisting of nonconvex sparse recovery, model-order selection and off-grid correction. For the nonconvex sparse recovery problem, two algorithms, namely NLS and Bi-Convex Relaxation and Alternating Minimization (BiCRAM), are developed in Sec. 4.2 and 4.3, respectively. Sec. 4.4 reports an experiment with the Munich data set (see Sec. 2.1). The main theorems in this chapter are proved in Sec. 4.5.

4.1 From Data Model to Inversion Framework

Suppose we have a multi-master stack. By using the language of basic graph theory (e.g., [80, §1]), this stack can be described by an acyclic directed graph. Denote it as $\mathbf{G} \coloneqq (\mathbf{V}(\mathbf{G}), \mathbf{E}(\mathbf{G}))$ that is associated with an incidence function $\psi_{\mathbf{G}}$, where $\mathbf{V}(\mathbf{G}) \coloneqq [N]$ is a set of SLCs as vertices, and $\mathbf{E}(\mathbf{G})$ is a set of interferograms as edges. For each $e \in \mathbf{E}(\mathbf{G})$, $\exists m, n \in \mathbf{V}(\mathbf{G})$ such that $\psi_{\mathbf{G}}(e) = (m, n)$. The adjacency matrix $\mathbf{A}(\mathbf{G}) \coloneqq (a_{m,n}) \in \{0, 1\}^{N \times N}$ is defined as

$$a_{m,n} \coloneqq \begin{cases} 1 & : (m, n) \in \mathbf{E}(\mathbf{G}), \\ 0 & : (m, n) \notin \mathbf{E}(\mathbf{G}). \end{cases} \tag{4.1}$$

Since $\mathbf{G}$ is acyclic by definition, $a_{n,n} = 0$, $\forall n \in \mathbf{V}(\mathbf{G})$, i.e., the diagonal of $\mathbf{A}(\mathbf{G})$ contains only zero entries. We further assume that, without loss of generality, every vertex is connected to at least another one. That $\mathbf{G}$ represents a multi-master stack implies $\nexists i \in [N]$ such that $a_{i,n} = 1$, $\mathbf{a}^m = \mathbf{0}$, $\forall m, n \in [N] \setminus \{i\}$, since it would otherwise be a single-master stack. For each $(m, n) \in \mathbf{E}(\mathbf{G})$, an interferogram is formed:

$$g_n \overline{g_m} = \int \int \gamma(s) \overline{\gamma(s')} \exp\left(-j(k_n s - k_m s')\right) \mathrm{d}s \mathrm{d}s'. \tag{4.2}$$

An extension to the differential case, where scatterers' motion is modeled as a linear combination of basis functions, is straightforward (see also Sec. 3.1).

From now on, we assume that the sensor far field is compressible such that it can be well approximated by a small number of scatterers, i.e.,

$$g_n \approx \sum_l \gamma_l \exp(-j k_n s_l), \quad \forall n \in [N], \tag{4.3}$$

where $\gamma_l \in \mathbb{C}$ is the reflectivity of the lth scatterer located at the elevation position s_l. By means of this, the single-look multi-master data model (4.2) becomes

$$g_n\overline{g_m} \approx \sum_{l,l'} \gamma_l\overline{\gamma_{l'}} \exp\left(-j(k_n s_l - k_m s_{l'})\right), \quad \forall (m,n) \in \mathbf{E}(\mathbf{G}). \tag{4.4}$$

In the *single-scatterer* case, (4.4) can be simplified as

$$g_n\overline{g_m} \approx |\gamma|^2 \exp\left(-j(k_n - k_m)s\right), \tag{4.5}$$

i.e., the multi-master observation is in fact the Fourier transform of the scatterer's *power* at the wavenumber baseline $k_n - k_m$. Consequently, the nonnegativity of the scatterer's power should be taken into account in the tomographic inversion. Since both the real and imaginary parts of $g_n\overline{g_m}$ are parametrized by $|\gamma|^2$, i.e.,

$$\Re(g_n\overline{g_m}) \approx |\gamma|^2 \cos\left((k_n - k_m)s\right), \quad \Im(g_n\overline{g_m}) \approx |\gamma|^2 \sin\left(-(k_n - k_m)s\right), \tag{4.6}$$

the inversion problem can be reformulated in the real vector space.

In the case of *double scatterers*, the multi-master observation (4.4) becomes

$$\begin{aligned} g_n\overline{g_m} \approx\ & |\gamma_1|^2 \exp\left(-j(k_n - k_m)s_1\right) + \gamma_1\overline{\gamma_2} \exp\left(-j(k_n s_1 - k_m s_2)\right) + \\ & \overline{\gamma_1}\gamma_2 \exp\left(-j(k_n s_2 - k_m s_1)\right) + |\gamma_2|^2 \exp\left(-j(k_n - k_m)s_2\right). \end{aligned} \tag{4.7}$$

Besides the Fourier transform of the scatterers' power at the wavenumber baseline $k_n - k_m$, the right-hand side contains the second and third "cross-terms", in which not only the scatterers' reflectivity but also their wavenumber-elevation-products are coupled. This essentially rules out any linear model for single-look multi-master SAR tomography.

Remark. A *single-look* bistatic or pursuit monostatic (see Sec. 2.2) stack is in general not motion-free in the case of double or multiple scatterers.

In order to demonstrate this, consider for example a linear motion model $d(t_n) \coloneqq vt_n$, where v and t denote the linear motion rate and time, respectively. Observe

$$\begin{aligned} g_n\overline{g_m} \approx\ & \sum_{l,l'} \gamma_l\overline{\gamma_{l'}} \exp(-j(k_n s_l - k_m s_{l'} + 4\pi d_l(t_n)/\lambda - 4\pi d_{l'}(t_m)/\lambda)) \\ =\ & |\gamma_1|^2 \exp\left(-j\left((k_n - k_m)s_1 + 4\pi v_1(t_n - t_m)/\lambda\right)\right) + \\ & \gamma_1\overline{\gamma_2} \exp\left(-j\left((k_n s_1 - k_m s_2) + 4\pi(v_1 t_n - v_2 t_m)/\lambda\right)\right) + \\ & \overline{\gamma_1}\gamma_2 \exp\left(-j\left((k_n s_2 - k_m s_1) + 4\pi(v_2 t_n - v_1 t_m)/\lambda\right)\right) + \\ & |\gamma_2|^2 \exp\left(-j\left((k_n - k_m)s_2 + 4\pi v_2(t_n - t_m)/\lambda\right)\right). \end{aligned} \tag{4.8}$$

In the case of $t_m = t_n$, the motion-induced phase in the cross-terms vanishes if and only if $v_1 = v_2$.

The single-look multi-master data model (4.4) already suggests a nonlinear equation system. Suppose $\mathbf{G}$ comprises a total of $N' \coloneqq |\mathbf{E}(\mathbf{G})|$ multi-master interferograms, and $e_1, \ldots, e_{N'}$ is an ordered sequence of them. Let $\mathcal{M}, \mathcal{S} : [N'] \to [N]$ be the mappings

from the interferogram index to the master and slave indices, respectively, such that a multi-master interferogram $g_{\mathcal{S}(n)}\overline{g_{\mathcal{M}(n)}}$ is obtained for each e_n, $n \in [N']$. Let $\mathbf{g} \in \mathbb{C}^{N'}$ denote the vector of multi-master interferograms so that $g_n \coloneqq g_{\mathcal{S}(n)}\overline{g_{\mathcal{M}(n)}}$, $\forall n \in [N']$. Let $s_1, \ldots, s_L$ be a discretization of the elevation axis s. The single-look multi-master data model in matrix notations is

$$\mathbf{g} \approx (\mathbf{R}\boldsymbol{\gamma}) \circ (\overline{\mathbf{S}\boldsymbol{\gamma}}), \tag{4.9}$$

where $\mathbf{R}, \mathbf{S} \in \mathbb{C}^{N' \times L}$ represent the tomographic sensing matrices of the slaves and masters, respectively, $r_{n,l} \coloneqq \exp(-jk_{\mathcal{S}(n)}s_l)$, $s_{n,l} \coloneqq \exp(-jk_{\mathcal{M}(n)}s_l)$, $\forall n \in [N']$, $l \in [L]$, and $\boldsymbol{\gamma} \in \mathbb{C}^L$ is the unknown discrete reflectivity vector.

In light of (4.9), we propose the following generic framework for tomographic inversion.

(1) *Nonconvex sparse recovery:* Consider the minimization problem

$$\begin{aligned} \hat{\boldsymbol{\gamma}} \coloneqq \underset{\boldsymbol{\gamma}}{\arg\min} \quad & \frac{1}{2}\|(\mathbf{R}\boldsymbol{\gamma}) \circ (\overline{\mathbf{S}\boldsymbol{\gamma}}) - \mathbf{g}\|_2^2 \\ \text{subject to} \quad & |\operatorname{Supp}(\boldsymbol{\gamma})| \leq K, \end{aligned} \tag{4.10}$$

where $K \in \mathbb{Z}_{++}$. The objective function measures the model goodness of fit, and the inequality constraint enforces $\boldsymbol{\gamma}$ to be sparse (as is implicitly assumed in (4.4)). Provided that $\sum_{l=0}^{K} \binom{L}{l}$ is small, it is feasible to solve (4.10) heuristically by means of the algorithms to be developed in Sec. 4.2. Sec. 4.3 is devoted to another algorithm that solves a similar problem based on bi-convex relaxation.

(2) *Model-order selection:* Similar as in the single-master setting (see Sec. 3.1), we employ this procedure in order to remove outliers and thereby to reduce false positive rate. By means of BIC, model-order selection can be formulated as the following constrained minimization problem (cf. (3.6)):

$$\begin{aligned} \hat{\boldsymbol{\Omega}} \coloneqq \underset{\boldsymbol{\Omega}(,\boldsymbol{\delta})}{\arg\min} \quad & 2N' \ln\left(\|(\mathbf{R}_{\boldsymbol{\Omega}}\boldsymbol{\delta}_{\boldsymbol{\Omega}}) \circ (\overline{\mathbf{S}_{\boldsymbol{\Omega}}\boldsymbol{\delta}_{\boldsymbol{\Omega}}}) - \mathbf{g}\|_2^2/N'\right) + (5|\boldsymbol{\Omega}| + 1)\ln(N') \\ \text{subject to} \quad & \operatorname{Supp}(\boldsymbol{\delta}) = \boldsymbol{\Omega} \subset \operatorname{Supp}(\hat{\boldsymbol{\gamma}}), \end{aligned} \tag{4.11}$$

where $\boldsymbol{\Omega}$ is the support of the auxiliary variable $\boldsymbol{\delta} \in \mathbb{C}^L$. Since $|\operatorname{Supp}(\hat{\boldsymbol{\gamma}})|$ is typically small, (4.11) boils down to solving a sequence of subset least squares problems in the form of

$$\underset{\boldsymbol{\epsilon}}{\text{minimize}}\, \frac{1}{2}\|(\mathbf{R}_{\boldsymbol{\Omega}}\boldsymbol{\epsilon}) \circ (\overline{\mathbf{S}_{\boldsymbol{\Omega}}\boldsymbol{\epsilon}}) - \mathbf{g}\|_2^2, \tag{4.12}$$

for which two algorithms will be developed in Sec. 4.2.

(3) *Off-grid correction:* Likewise, the off-grid or quantization problem arises when scatterers are not located on the discrete elevation grid $s_1, \ldots, s_L$. Let $\hat{K} \coloneqq |\hat{\boldsymbol{\Omega}}|$ denote the number of scatterers after model-order selection. Denote the real and imaginary parts of the lth scatterer's reflectivity γ_l as γ_l^R and γ_l^I, respectively,

i.e., $\gamma_l = \gamma_l^R + j\gamma_l^I$, and its elevation position as s_l, $\forall l \in [\hat{K}]$. Based on the underlying single-look multi-master data model (4.4), we seek a solution of the following nonlinear and nonconvex minimization problem (cf. (3.8)):

$$\underset{\gamma_l^R,\gamma_l^I,s_l}{\text{minimize}} \sum_n \left| g_n - \sum_{l,l'} (\gamma_l^R + j\gamma_l^I)(\gamma_{l'}^R - j\gamma_{l'}^I) \exp\left(-j(k_{\mathcal{S}(n)} s_l - k_{\mathcal{M}(n)} s_{l'})\right) \right|^2, \quad (4.13)$$

whose objective function is differentiable w.r.t. γ_l^R, γ_l^I and s_l, $\forall l \in [\hat{K}]$. Naturally, the on-grid estimates from (4.11) can be used as an initialization for, e.g., the BFGS algorithm.

So far we have established a generic inversion framework for single-look multi-master SAR tomography. The next two sections will deal with the optimization problems (4.10)–(4.13) from an algorithmic point of view.

4.2 Nonlinear Least Squares (NLS)

As a parametric method, NLS divides a sparse recovery problem into a sequence of subset linear least squares subproblems [81, §6.4]. In this section, we extend the concept of NLS to the single-look multi-master data model (4.9), and tackle its subproblems (4.12). In order to simplify notation, we consider the following equivalent problem:

$$\underset{\mathbf{x}}{\text{minimize}} \frac{1}{2} \|(\mathbf{A}\mathbf{x}) \circ (\overline{\mathbf{B}\mathbf{x}}) - \mathbf{b}\|_2^2, \quad (4.14)$$

where $\mathbf{A}, \mathbf{B} \in \mathbb{C}^{m \times n}$, $\mathbf{x} \in \mathbb{C}^n$, and $\mathbf{b} \in \mathbb{C}^m$ with $m > n$. As already indicated in Sec. 4.1, (4.14) is clearly worth investigation, since it not only solves the nonconvex spare recovery problem (4.10), but also underlies model-order selection (4.11).

4.2.1 Algorithms

In this subsection, we develop two algorithms for solving (4.14).

The first algorithm is based on the ADMM [72] (cf. Alg. 3.1). Consider (4.14) in its equivalent form:

$$\begin{aligned} \underset{\mathbf{x},\mathbf{z}}{\text{minimize}} \quad & \frac{1}{2} \|(\mathbf{A}\mathbf{x}) \circ (\overline{\mathbf{B}\mathbf{z}}) - \mathbf{b}\|_2^2 \\ \text{subject to} \quad & \mathbf{x} - \mathbf{z} = \mathbf{0}, \end{aligned} \quad (4.15)$$

which is essentially a bi-convex problem with affine constraint [72, §9.2]. Applying the ADMM update rules gives Alg. 4.1. Note that both the $\mathbf{x}$- and $\mathbf{z}$-updates amount to solving linear least squares problems.

Algorithm 4.1 An ADMM-based algorithm for solving (4.14)

Input: $\mathbf{A}$, $\mathbf{B}$, $\mathbf{b}$, $\mathbf{z}^{(0)}$, ρ
Initialize $\mathbf{z} \leftarrow \mathbf{z}^{(0)}$
Until stopping criterion is satisfied, **Do**
  $\tilde{\mathbf{A}} \leftarrow \mathrm{Diag}(\overline{\mathbf{B}\mathbf{z}})\mathbf{A}$
  $\mathbf{x} \leftarrow (\tilde{\mathbf{A}}^H\tilde{\mathbf{A}} + \rho\mathbf{I})^{-1}(\tilde{\mathbf{A}}^H\mathbf{b} + \rho\mathbf{z} - \mathbf{y})$
  $\tilde{\mathbf{B}} \leftarrow \mathrm{Diag}(\overline{\mathbf{A}\mathbf{x}})\mathbf{B}$
  $\mathbf{z} \leftarrow (\tilde{\mathbf{B}}^H\tilde{\mathbf{B}} + \rho\mathbf{I})^{-1}(\tilde{\mathbf{B}}^H\overline{\mathbf{b}} + \rho\mathbf{x} + \mathbf{y})$
  $\mathbf{y} \leftarrow \mathbf{y} + \rho(\mathbf{x} - \mathbf{z})$
Output: $\mathbf{z}$

The second algorithm employs the trust-region Newton's method that solves general unconstrained nonlinear minimization problems by exploiting first- and second-order information [71, §4]. The rationale behind this choice is to avoid saddle points that cannot be identified by first-order information [82]. In each iteration, a norm ball, commonly referred to as the "trust region", centered at the current iterate is chosen adaptively. If the second-order Taylor polynomial of the objective function is a sufficiently good approximation, we find a descent direction by solving a quadratically constrained quadratic minimization problem. Let $f : \mathbb{R}^n \to \mathbb{R}$ denote the objective function, the subproblem at the iterate $\mathbf{x} \in \mathbb{R}^n$ is

$$\begin{aligned} \underset{\Delta\mathbf{x}}{\text{minimize}} \quad & f(\mathbf{x}) + \nabla f(\mathbf{x})^T\Delta\mathbf{x} + \frac{1}{2}\Delta\mathbf{x}^T\nabla^2 f(\mathbf{x})\Delta\mathbf{x} \\ \text{subject to} \quad & \|\Delta\mathbf{x}\|_2 \le r, \end{aligned} \tag{4.16}$$

where $\Delta\mathbf{x} \in \mathbb{R}^n$ is the unknown search direction, ∇f and $\nabla^2 f$ denote respectively the gradient and Hessian of f, and $r \in \mathbb{R}_{++}$ is the radius of the current trust region. By using the Karush-Kuhn-Tucker (KKT) conditions for nonconvex problems, Nocedal and Wright broke down (4.16) into several cases [71, §4.3]: in one case a 1-D root-finding problem w.r.t. the dual variable is solved by using, e.g., the Newton's method, while in the others there exist analytic solutions. Due to the overwhelming technical details, we do not provide an exposition here. Interested readers are suggested to refer to [71, §4.3]. It can be proved that the trust-region Newton's method converges to a critical point with high accuracy under very general conditions [71, p. 92].

Now we turn back to our complex-valued NLS problem (4.14). By verifying the Cauchy-Riemann equations (e.g., [83, p. 50]), it can be shown that the objective function of (4.14) is not complex-differentiable w.r.t. $\mathbf{x}$. Instead of using Wirtinger differentiation that lacks in parts of the second-order information, we exploit the isomorphic mapping $\mathbf{x} \mapsto (\mathbf{x}_R, \mathbf{x}_I)$ and define

$$f(\mathbf{x}_R, \mathbf{x}_I) \coloneqq \frac{1}{2}\|(\mathbf{A}\mathbf{x}) \circ (\overline{\mathbf{B}\mathbf{x}}) - \mathbf{b}\|_2^2, \tag{4.17}$$

where $f : \mathbb{R}^n \times \mathbb{R}^n \to \mathbb{R}$ is real-differentiable w.r.t. $\mathbf{x}_R$ and $\mathbf{x}_I$. Its gradient is given by

$$\nabla f(\mathbf{x}_R, \mathbf{x}_I) = \begin{pmatrix} \frac{\partial f}{\partial \mathbf{x}_R} \\ \frac{\partial f}{\partial \mathbf{x}_I} \end{pmatrix} = \begin{pmatrix} \Re\left(\mathbf{d}\right) \\ \Im\left(\mathbf{d}\right) \end{pmatrix}, \tag{4.18}$$

where

$$\mathbf{d} \coloneqq \mathbf{A}^H \left(((\mathbf{A}\mathbf{x}) \circ (\overline{\mathbf{B}\mathbf{x}}) - \mathbf{b}) \circ (\mathbf{B}\mathbf{x})\right) + \mathbf{B}^H \left(((\overline{\mathbf{A}\mathbf{x}}) \circ (\mathbf{B}\mathbf{x}) - \overline{\mathbf{b}}) \circ (\mathbf{A}\mathbf{x})\right). \tag{4.19}$$

In addition, its Hessian is given by

$$\nabla^2 f(\mathbf{x}_R, \mathbf{x}_I) = \begin{pmatrix} \frac{\partial^2 f}{\partial \mathbf{x}_R^2} & \frac{\partial^2 f}{\partial \mathbf{x}_R \partial \mathbf{x}_I} \\ \frac{\partial^2 f}{\partial \mathbf{x}_I \partial \mathbf{x}_R} & \frac{\partial^2 f}{\partial \mathbf{x}_I^2} \end{pmatrix} = \begin{pmatrix} \Re\left(\mathbf{C} + \mathbf{D} + \mathbf{E}\right) & -\Im\left(\mathbf{C} - \mathbf{D} + \mathbf{E}\right) \\ \Im\left(\mathbf{C} + \mathbf{D} + \mathbf{E}\right) & \Re\left(\mathbf{C} - \mathbf{D} + \mathbf{E}\right) \end{pmatrix}, \tag{4.20}$$

where

$$\begin{aligned} \mathbf{C} &\coloneqq \mathbf{A}^H \operatorname{Diag}\left((\mathbf{B}\mathbf{x}) \circ (\overline{\mathbf{B}\mathbf{x}})\right) \mathbf{A} + \mathbf{B}^H \operatorname{Diag}\left((\mathbf{A}\mathbf{x}) \circ (\overline{\mathbf{A}\mathbf{x}})\right) \mathbf{B}, \\ \mathbf{D} &\coloneqq \mathbf{A}^H \operatorname{Diag}\left((\mathbf{A}\mathbf{x}) \circ (\mathbf{B}\mathbf{x})\right) \overline{\mathbf{B}} + \mathbf{B}^H \operatorname{Diag}\left((\mathbf{A}\mathbf{x}) \circ (\mathbf{B}\mathbf{x})\right) \overline{\mathbf{A}}, \\ \mathbf{E} &\coloneqq \mathbf{A}^H \operatorname{Diag}\left((\mathbf{A}\mathbf{x}) \circ (\overline{\mathbf{B}\mathbf{x}}) - \mathbf{b}\right) \mathbf{B} + \mathbf{B}^H \operatorname{Diag}\left((\overline{\mathbf{A}\mathbf{x}}) \circ (\mathbf{B}\mathbf{x}) - \overline{\mathbf{b}}\right) \mathbf{A}. \end{aligned} \tag{4.21}$$

Note that $\mathbf{d} : \mathbb{C}^n \to \mathbb{C}^n$ and $\mathbf{C}, \mathbf{D}, \mathbf{E} : \mathbb{C}^n \to \mathbb{C}^{n \times n}$ are, as a matter of fact, functions of $\mathbf{x}$. In order to simplify notation, the parentheses have been dropped. For the same purpose, we define

$$f(\mathbf{x}) \coloneqq f\left(\Re(\mathbf{x}), \Im(\mathbf{x})\right) = f(\mathbf{x}_R, \mathbf{x}_I). \tag{4.22}$$

By means of the first- and second-order information of (4.17), the trust-region Newton's method can be directly invoked, which boils down to solving a sequence of subproblems in the form of (4.16). For any optimal point $\mathbf{x}^\star$, the KKT condition reads

$$\nabla f(\mathbf{x}^\star) = \mathbf{0} \iff \mathbf{d}(\mathbf{x}^\star) = \mathbf{0}. \tag{4.23}$$

However, none of these algorithms is guaranteed to always converge to a global minimum. In Sec. 4.4, we will demonstrate that the solutions are often sufficiently good. Fig. 4.1 illustrates typical convergence curves in the case of double scatterers (#6 in Sec. 4.4.2). Similar as in Sec. 3.1.1, we let one of the algorithms deliver a numerical solution with very high precision, took it as an optimal point $\mathbf{x}^\star$, and computed the absolute difference between the values of the objective function $|f(\mathbf{x}) - f(\mathbf{x}^\star)|$. Both the ADMM and the trust-region Newton's method converged to the same solution (up to a constant phase angle, see Sec. 4.2.2). Since the latter only used fewer than 10 iterations to converge, it will be employed in Sec. 4.4. In spite of this, the former can still be interesting due to its simple update rules (see Alg. 4.1).

4.2.2 Analysis of the Objective Function

In terms of the nonconvex objective function (4.17), we are first and foremost interested in the following two questions:

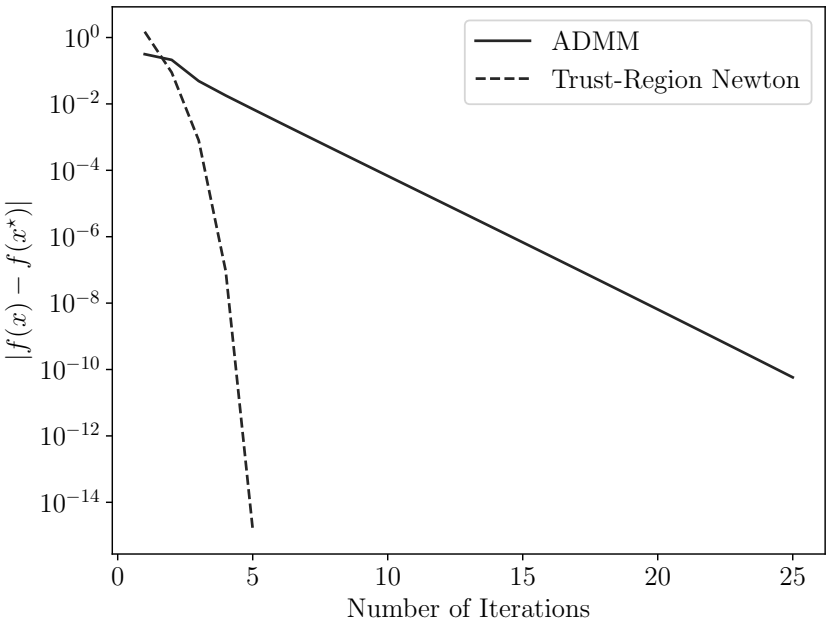

Figure 4.1: Convergence curves of NLS using ADMM (solid line) and the trust-region Newton's method (dashed line).

(1) Under which conditions do critical points or local extrema exist?

(2) Provided that they do exist, how many of them are there?

This subsection provides a partial answer to these questions.

First of all, we make the following general statement.

Proposition 4.1. For any $\mathbf{x} \in \mathbb{C}^n$ and $\phi \in \mathbb{R}$, any eigenvalue of $\nabla^2 f(\mathbf{x})$ is also an eigenvalue of $\nabla^2 f\left(\mathbf{x}\exp(j\phi)\right)$ and vice versa.

Proof. See Sec. 4.5.1. □

Informally, this proposition implies that the definiteness of the Hessian is invariant under any rotation with a constant phase angle.

Now we state the main theorem for the general case.

Theorem 4.2. Properties of the critical points of $f(\mathbf{x})$.

(1) $\mathbf{0}$ is a critical point: it is a local minimum if $\mathbf{A}^H \operatorname{Diag}(\mathbf{b})\mathbf{B} + \mathbf{B}^H \operatorname{Diag}(\overline{\mathbf{b}})\mathbf{A} \prec \mathbf{0}$, and a local maximum if $\mathbf{A}^H \operatorname{Diag}(\mathbf{b})\mathbf{B} + \mathbf{B}^H \operatorname{Diag}(\overline{\mathbf{b}})\mathbf{A} \succ \mathbf{0}$.

(2) If there exists a *nonzero* critical point, then $\mathbf{A}^H \operatorname{Diag}(\mathbf{b})\mathbf{B} + \mathbf{B}^H \operatorname{Diag}(\overline{\mathbf{b}})\mathbf{A} \not\succ \mathbf{0}$.

(3) Suppose there exists a *nonzero* critical point $\mathbf{z}$. Then

(3a) $\nabla^2 f(\mathbf{z})$ is rank deficient.

(3b) There exist an infinite number of critical points in the form of $\mathbf{z}\exp(j\phi)$, $\phi \in \mathbb{R} \setminus \{0\}$. Each has the same objective function value as $\mathbf{z}$, and its Hessian has the same definiteness.

Proof. See Sec. 4.5.2. □

This theorem implies that if there exists one critical point, then there are an infinite number of them up to a constant phase angle, and each is exactly as good in terms of objective function value. Informally, it also suggests that the NLS problem (4.14) may not be as difficult as it appears, since we only need to find one critical point out of infinitely many. In addition, we conjecture that $\mathbf{A}^H \operatorname{Diag}(\mathbf{b})\mathbf{B} + \mathbf{B}^H \operatorname{Diag}(\overline{\mathbf{b}})\mathbf{A} \succ \mathbf{0}$ is a necessary and sufficient condition (cf. Thm. 4.2(2)), and each *nonzero* critical point is also a local minimum under some mild conditions.

The main theorem for the special case $n = 1$, i.e., $\mathbf{A}, \mathbf{B} \in \mathbb{C}^m$, $\mathbf{x} \in \mathbb{C}$, is much stronger.

Theorem 4.3 ($n = 1$)**.** Properties of the critical points of $f(\mathbf{x})$.

(1) $\mathbf{0}$ is a critical point: it is a local minimum if $\Re\left((\mathbf{A} \circ \overline{\mathbf{B}})^H \mathbf{b}\right) < 0$, and a local maximum if $\Re\left((\mathbf{A} \circ \overline{\mathbf{B}})^H \mathbf{b}\right) > 0$.

(2) There exists a *nonzero* critical point if and only if $\Re\left((\mathbf{A} \circ \overline{\mathbf{B}})^H \mathbf{b}\right) > 0$.

(3) Suppose there exists a *nonzero* critical point $\mathbf{z}$. Then

(3a) $\nabla^2 f(\mathbf{z})$ is positive semi-definite and rank deficient[1].

(3b) There exist an infinite number of critical points in the form of $\mathbf{z}\exp(j\phi)$, $\phi \in \mathbb{R} \setminus \{0\}$. Each has the same objective function value as $\mathbf{z}$, and its Hessian has the same definiteness.

(3c) $\mathbf{z}$ is a local minimum.

Proof. See Sec. 4.5.3. □

Hence a *nonzero local minimum* exists if and only if $\Re\left((\mathbf{A} \circ \overline{\mathbf{B}})^H \mathbf{b}\right) > 0$. If this condition is fulfilled, then there exist infinitely many local minima that are exactly as good in terms of objective function value. As an example, Fig. 4.2 illustrates the negative logarithm of (4.17) with a circle of local maxima. This corresponds to a single scatterer in Fig. 2.3 (left).

Lastly, the following corollary follows directly from the proof of Thm. 4.3.

Corollary 4.4 ($n = 1$)**.** Each *nonzero local minimum* (provided it exists) is given by

$$\mathbf{z} = \frac{\Re\left((\mathbf{A} \circ \overline{\mathbf{B}})^H \mathbf{b}\right)^{1/2}}{\|\mathbf{A} \circ \overline{\mathbf{B}}\|_2} \exp(j\phi), \tag{4.24}$$

for some $\phi \in \mathbb{R}$.

[1] Note that $\nabla^2 f(\mathbf{z}) \in \mathbb{R}^{2\times 2}$ by definition.

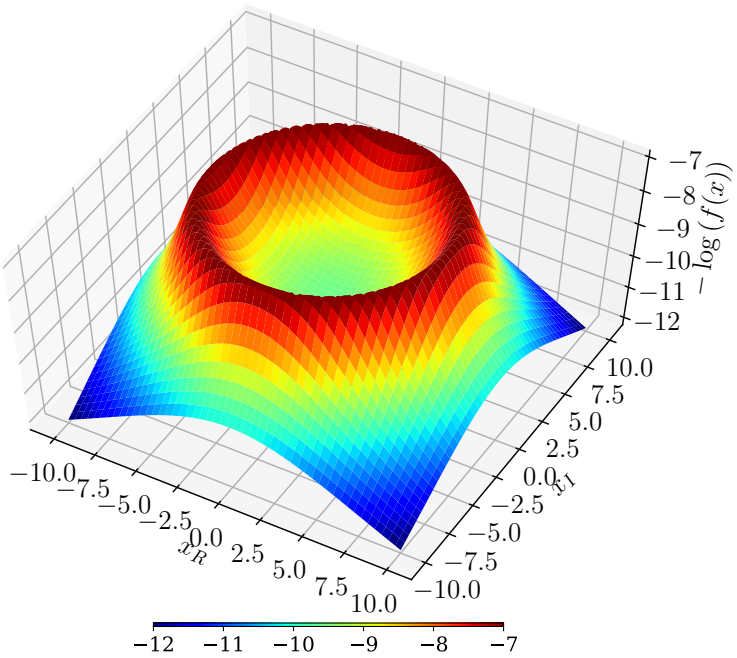

Figure 4.2: Negative logarithm of an NLS objective function ($n = 1$) with a circle of local maxima at the verge of the "crater".

Proof. See the proof of Thm. 4.3(2). □

Let us turn back to the problem in SAR tomography. For the single-look multi-master data model (4.9), this corollary motivates the following 1-D spectral estimator:

$$|\hat{\gamma}_l| := \begin{cases} \frac{\Re\left((\mathbf{r}_l \circ \overline{\mathbf{s}_l})^H \mathbf{g}\right)^{1/2}}{\|\mathbf{r}_l \circ \overline{\mathbf{s}_l}\|_2} & \text{if } \Re\left((\mathbf{r}_l \circ \overline{\mathbf{s}_l})^H \mathbf{g}\right) > 0 \\ 0 & \text{otherwise,} \end{cases} \tag{4.25}$$

$\forall l \in [L]$. Note that (4.25) also provides the solution of any 1-D NLS subproblem up to a constant phase angle. As can be expected, this estimator does not have any super-resolution power in the case of multiple scatterers.

4.3 Bi-Convex Relaxation and Alternating Minimization (BiCRAM)

In this section, we develop a second algorithm for solving the nonconvex sparse recovery problem (4.10).

We start by replacing the inequality constraint in (4.10) with a sparsity-inducing regularization term, e.g.,

$$\underset{\boldsymbol{\gamma}}{\text{minimize}}\ \frac{1}{2}\|(\mathbf{R}\boldsymbol{\gamma}) \circ (\overline{\mathbf{S}\boldsymbol{\gamma}}) - \mathbf{g}\|_2^2 + \lambda\|\boldsymbol{\gamma}\|_1, \tag{4.26}$$

where $\lambda \in \mathbb{R}_{++}$ is a regularization parameter that controls the balance between the model goodness of fit and the sparsity of $\boldsymbol{\gamma}$. In light of (4.23), the necessary condition for any $\boldsymbol{\gamma}^\star$ to be an optimal point is

$$\frac{1}{\lambda}\left(\mathbf{R}^H\left((\mathbf{g}-(\mathbf{R}\boldsymbol{\gamma}^\star)\circ(\overline{\mathbf{S}\boldsymbol{\gamma}^\star})\right)\circ(\mathbf{S}\boldsymbol{\gamma}^\star)\right)+\mathbf{S}^H\left((\overline{\mathbf{g}}-(\overline{\mathbf{R}\boldsymbol{\gamma}^\star})\circ(\mathbf{S}\boldsymbol{\gamma}^\star))\circ(\mathbf{R}\boldsymbol{\gamma}^\star)\right)\right)\in\partial\|\boldsymbol{\gamma}^\star\|_1, \tag{4.27}$$

i.e., the left-hand side is a subgradient of the ℓ_1 norm at $\boldsymbol{\gamma}^\star$. Obviously, $\mathbf{0}$ always fulfills this condition, which complicates solving (4.26).

In principle, an ADMM-based algorithm similar to Alg. 4.1 can be developed for solving (4.26). However, our experience with real tomographic SAR data shows that such an algorithm often diverges, presumably due to the high mutual coherence of the sensing matrices and the nonconvexity of (4.26). Therefore, we consider instead the following relaxed problem:

$$\underset{\boldsymbol{\gamma},\boldsymbol{\theta}}{\text{minimize}}\ \frac{1}{2}\|(\mathbf{R}\boldsymbol{\gamma})\circ(\overline{\mathbf{S}\boldsymbol{\theta}})-\mathbf{g}\|_2^2+\frac{\lambda_1}{2}\|\boldsymbol{\gamma}-\boldsymbol{\theta}\|_2^2+\lambda_2\|\begin{pmatrix}\boldsymbol{\gamma} & \boldsymbol{\theta}\end{pmatrix}\|_{1,2}, \tag{4.28}$$

where $\lambda_1, \lambda_2 \in \mathbb{R}_{++}$ are regularization parameters. Its objective function $\mathbb{C}^L \times \mathbb{C}^L \to \mathbb{R}$ is bi-convex, i.e., it is convex in $\boldsymbol{\gamma}$ with $\boldsymbol{\theta}$ fixed, and convex in $\boldsymbol{\theta}$ with $\boldsymbol{\gamma}$ fixed. The first regularization term enforces $\boldsymbol{\gamma}$ and $\boldsymbol{\theta}$ to have similar entries, while the second one promotes the same support. Since (4.28) is essentially an unconstrained bi-convex problem, it can be solved via alternating minimization by Alg. 4.2.

Algorithm 4.2 An alternating algorithm for solving (4.28)

1: **Input:** $\mathbf{R}$, $\mathbf{S}$, $\mathbf{g}$, $\boldsymbol{\gamma}^{(0)}$, λ_1, λ_2
2: **Initialize** $\boldsymbol{\gamma} \leftarrow \boldsymbol{\gamma}^{(0)}$
3: **Until** stopping criterion is satisfied, **Do**
4: $\quad\tilde{\mathbf{S}} \leftarrow \mathrm{Diag}(\overline{\mathbf{R}\boldsymbol{\gamma}})\mathbf{S}$
5: $\quad\boldsymbol{\theta} \leftarrow \arg\min_{\boldsymbol{\theta}} \frac{1}{2}\|\tilde{\mathbf{S}}\boldsymbol{\theta}-\overline{\mathbf{g}}\|_2^2+\frac{\lambda_1}{2}\|\boldsymbol{\theta}-\boldsymbol{\gamma}\|_2^2+\lambda_2\|\begin{pmatrix}\boldsymbol{\theta} & \boldsymbol{\gamma}\end{pmatrix}\|_{1,2}$
6: $\quad\tilde{\mathbf{R}} \leftarrow \mathrm{Diag}(\overline{\mathbf{S}\boldsymbol{\theta}})\mathbf{R}$
7: $\quad\boldsymbol{\gamma} \leftarrow \arg\min_{\boldsymbol{\gamma}} \frac{1}{2}\|\tilde{\mathbf{R}}\boldsymbol{\gamma}-\mathbf{g}\|_2^2+\frac{\lambda_1}{2}\|\boldsymbol{\gamma}-\boldsymbol{\theta}\|_2^2+\lambda_2\|\begin{pmatrix}\boldsymbol{\gamma} & \boldsymbol{\theta}\end{pmatrix}\|_{1,2}$
8: **Output:** $\boldsymbol{\gamma}$

At each iteration, when either $\boldsymbol{\gamma}$ or $\boldsymbol{\theta}$ is fixed, (4.28) becomes a convex problem in the form of

$$\underset{\mathbf{x}}{\text{minimize}}\ \frac{1}{2}\|\mathbf{A}\mathbf{x}-\mathbf{b}\|_2^2+\frac{\lambda_1}{2}\|\mathbf{x}-\mathbf{u}\|_2^2+\lambda_2\|\begin{pmatrix}\mathbf{x} & \mathbf{u}\end{pmatrix}\|_{1,2}, \tag{4.29}$$

or equivalently

$$\begin{aligned}\underset{\mathbf{x},\mathbf{Z}}{\text{minimize}}\quad & \frac{1}{2}\|\mathbf{A}\mathbf{x}-\mathbf{b}\|_2^2+\frac{\lambda_1}{2}\|\mathbf{x}-\mathbf{u}\|_2^2+\lambda_2\|\mathbf{Z}\|_{1,2}\\ \text{subject to}\quad & \begin{pmatrix}\mathbf{x} & \mathbf{u}\end{pmatrix}-\mathbf{Z}=\mathbf{0},\end{aligned} \tag{4.30}$$

where $\mathbf{Z} \in \mathbb{C}^{L\times 2}$ is an auxiliary variable. Applying the ADMM update rules leads to Alg. 4.3.

Algorithm 4.3 An ADMM-based algorithm for solving (4.29)

1: **Input:** $\mathbf{A}$, $\mathbf{b}$, $\mathbf{u}$, $\mathbf{Z}^{(0)}$, λ_1, λ_2, ρ
2: **Initialize** $\mathbf{Z} \leftarrow \mathbf{Z}^{(0)}$
3: **Until** stopping criterion is satisfied, **Do**
4: $\quad \mathbf{x} \leftarrow (\mathbf{A}^H\mathbf{A} + (\lambda_1 + \rho)\mathbf{I})^{-1}(\mathbf{A}^H\mathbf{b} + \lambda_1\mathbf{u} + \rho\mathbf{z}_1 - \mathbf{y}_1)$
5: $\quad \mathbf{Z} \leftarrow \mathrm{Prox}_{\ell_{1,2},\lambda_2/\rho}\left(\begin{pmatrix}\mathbf{x} & \mathbf{u}\end{pmatrix} + (1/\rho)\mathbf{Y}\right)$
6: $\quad \mathbf{Y} \leftarrow \mathbf{Y} + \rho\left(\begin{pmatrix}\mathbf{x} & \mathbf{u}\end{pmatrix} - \mathbf{Z}\right)$
7: **Output:** $\mathbf{z}_1$

$\mathrm{Prox}_{\ell_{1,2},\lambda} : \mathbb{C}^{L\times 2} \to \mathbb{C}^{L\times 2}$ is the proximal operator of the $\ell_{1,2}$ norm scaled by λ (e.g., [75]), i.e.,

$$\mathrm{Prox}_{\ell_{1,2},\lambda}(\mathbf{X}) \coloneqq \arg\min_{\mathbf{Z}} \lambda\|\mathbf{Z}\|_{1,2} + \frac{1}{2}\|\mathbf{X} - \mathbf{Z}\|_F^2, \tag{4.31}$$

whose i-th row is given by [75, §6.5.4]

$$\mathrm{Prox}_{\ell_{1,2},\lambda}(\mathbf{X})^i = (1 - \lambda/\|\mathbf{x}^i\|_2)_+ \mathbf{x}^i. \tag{4.32}$$

This proximal operator promotes the two columns of $\mathbf{Z}$ to be sparse in a joint manner and therefore $\mathbf{x}$ to share the same support with $\mathbf{u}$.

In general, it is very difficult to establish any convergence guarantee for Alg. 4.2 from a theoretical point of view, mainly due to the nonconvexity of (4.28). Nevertheless, our experiments with real tomographic SAR data (see Sec. 4.4) show that it converges empirically. Fig. 4.3 illustrates as an example a convergence curve in the case of two scatterers that are closely located (#6 in Sec. 4.4.2).

Regarding regularization parameter tuning, we adopt the same heuristic introduced in Sec. 3.1.2: we sample the solution path $(\lambda_1, \lambda_2) \mapsto \mathbf{x}$, and select the solution with the highest penalized likelihood (4.11), in which the likelihood is replaced with the one after off-grid correction (4.13). Last but not least, this procedure can be simplified by performing alternating 1-D searches, i.e., fixing one parameter and tuning the other at a time.

4.4 Experiment and Validation

This section reports our experimental results with the Munich data set (see Sec. 2.1).

4.4.1 Design of Experiment

A *single-master* stack was created with the acquisition from December 20, 2016 chosen as the one and only master. Its absolute vertical wavenumbers can be found in Fig. 2.1. A sinusoidal basis function was employed for modeling periodical motion induced by temperature change. As already mentioned in Sec. 2.1, the vertical Rayleigh resolution at scene center is approximately 12.66 m. Given the periodical motion model and a nominal SNR of 2 dB, the CRLB of height estimates is approximately 1.10 m (cf. 1.02 m without

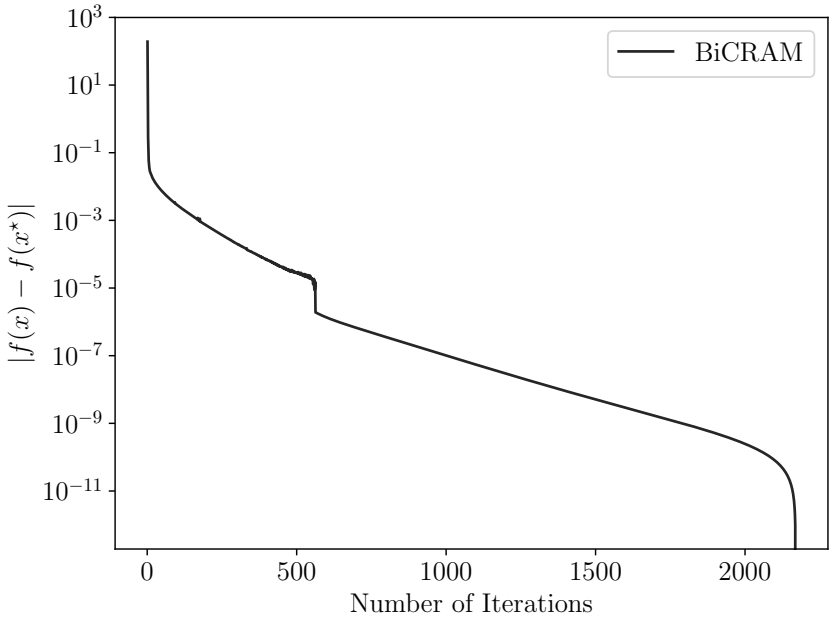

Figure 4.3: Convergence curve of BiCRAM. The horizontal axis refers to the number of outer iterations in Alg. 4.2.

motion model in Sec. 2.1). NLS and L1RLS were applied to this stack for tomographic reconstruction. For the latter, Alg. 3.1 was augmented with diagonal preconditioning and over-relaxation (see Sec. 3.1.1), where we set $\beta = 1.8$, and the choice of α is irrelevant, for $\mathbf{A}$ is in this case a Fourier matrix. The optimal trade-off curve of L1RLS was sampled 11 times with the regularization parameter varying logarithmically from $\lambda_{\min} \coloneqq 5 \cdot 10^{-2} \|\mathbf{R}^H \mathbf{g}\|_\infty$ to $\lambda_{\max} \coloneqq 5 \cdot 10^{-1} \|\mathbf{R}^H \mathbf{g}\|_\infty$.

We formed a *multi-master* stack comprising interferograms of small time intervals: let $1', 2', 3', 4', \ldots$ be a chronologically ordered sequence of SLCs, then the interferograms or edges are $(1', 2')$, $(3', 4')$, etc. Consequently, this stack contains 15 interferograms. Due to the small time intervals, we did not employ any motion model in order to avoid overfitting. NLS and BiCRAM were applied to this stack to estimate the elevation profile. Alg. 4.3, augmented by diagonal preconditioning and over-relaxation, was employed to solve the subproblems in Alg. 4.2 for the latter. Likewise, the solution path of BiCRAM was sampled 11 times as well, where λ_1 was fixed as one since, as far as our experience went, it was found to be relatively uninfluencial, and λ_2 was set to vary logarithmically from $\lambda_{\min} \coloneqq 5 \cdot 10^{-2} \max\left\{\|\mathbf{R}^H \mathbf{g}\|_\infty, \|\mathbf{S}^H \mathbf{g}\|_\infty\right\}$ to $\lambda_{\max} \coloneqq 5 \cdot 10^{-1} \max\left\{\|\mathbf{R}^H \mathbf{g}\|_\infty, \|\mathbf{S}^H \mathbf{g}\|_\infty\right\}$. The initial solution was set to be $\boldsymbol{\gamma}^{(0)} = (\mathbf{R} \circ \overline{\mathbf{S}})^H \mathbf{g}$ due to its simplicity. Alternatively, the 1-D estimator (4.25) could be employed. With regard to off-grid correction, forward-mode automatic differentiation [84] was used in order to avoid the necessity of analytically differentiating the objective function of (4.13) for any number of scatterers, and the optimization problem was solved by using a BFGS implementation [85].

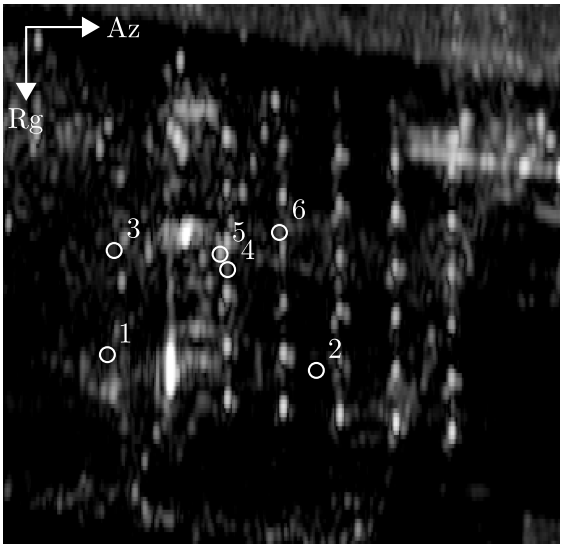

Figure 4.4: Six looks subject to roof-facade layover.

In the end, we created a second *multi-master* stack in the identical way as the previous one. Besides, we normalized each interferogram with the corresponding master amplitude. It will be referred to as the *fake single-master* stack, since it was treated as if it had been a *single-master* one. In order to apply the *single-master* approach, we computed for each interferogram the difference between slave and master wavenumbers, and used this difference as if it had been the wavenumber baseline in a single-master stack. Likewise, NLS and L1RLS were applied in the exactly same way as in the single-master case.

4.4.2 Experimental Results

The experiments can be divided into three settings: single-master, multi-master and fake single-master (see Sec. 4.4.1). In each setting, two algorithms were applied to reconstruct the elevation profile.

As a proof of concept, we picked six looks that are very likely subject to roof-facade layover. These six looks were selected in a systematic way: we applied Tikhonov regularization (i.e., the ℓ_1 norm in the regularization term of (3.9) is substituted by the ℓ_2 norm) to the *single-master* stack, chose all the seven looks consisting of double scatterers, and disposed of one look in which scatterers' elevation distance is almost identical to the one in another look. Fig. 4.4 illustrates these six looks, whose indices increase with decreasing estimated elevation distance from approximately 1.5 to 0.8 times the Rayleigh resolution. Under the assumption that the roof is entirely flat, this ordering agrees very well with intuition: the higher the scatterer is on the facade, the less is its elevation distance to the roof.

The estimated height profile is shown in Fig. 4.5 (#1–3) and 4.6 (#4–6), where we used the vertical Rayleigh resolution of the *single-master* stack (see Sec. 4.4.1) to normalize

Table 4.1: Single- and multi-master height estimates of looks subject to layover #1–3 [m]

		#1		#2		#3	
		h_1	h_2	h_1	h_2	h_1	h_2
RaySAR		−9.22	–	−8.91	–	−2.39	–
Single-Master	NLS	−10.27	9.10	−8.14	6.97	−4.27	10.72
	L1RLS	−10.27	9.10	−8.14	6.97	−4.27	10.72
Multi-Master	NLS	−10.15	9.47	−8.96	8.23	−3.50	9.98
	BiCRAM	−10.15	9.47	−8.96	8.23	−3.50	9.98
Fake Single-Master	NLS	9.35	–	−9.12	–	−1.64	–
	L1RLS	9.35	–	−9.12	–	−1.64	–

the x-axis. The height estimates are given in Tab. 4.1 and 4.2. In the *single-master* setting, NLS and L1RLS delivered very similar height profiles, in spite of the sporadic artifacts in the latter that are known to occur with ℓ_1-regularization [69]. Besides, the height estimates were identical after off-grid correction, as can be observed in Tab. 4.1 and 4.2. In each case, the height estimate of the lower scatterer agrees very well with the Level 2 height ground truth of facade (see Sec. 2.1). Overall, the *multi-master* height estimates are consistent with the *single-master* ones, with deviations typically of several decimeters. In the *fake single-master* setting, layover separation was however merely successful for #5, presumably due to its high SNR (see the brightness of #5 in Fig. 4.4). When the height distance is significantly larger than the vertical Rayleigh resolution (#1–2), both NLS and L1RLS could retrieve two scatterers, but only the one with the larger amplitude could pass model-order selection. When the height distance approaches the vertical Rayleigh resolution or becomes even smaller (#3, 4, 6), neither algorithm could retrieve a second scatterer, and the height estimate of the retrieved single scatterer after off-grid correction is also arguably wrong. Thus, we are convinced by this simple experiment that the conventional *single-master* approach, if applied to a *single-look multi-master* stack, can be insufficient for layover separation.

Naturally, we also applied tomographic reconstruction to all the 594 looks within the building footprint (see Fig. 2.3 (right)). Tab. 4.3 provides the overall runtime on a desktop with 16-GB RAM and a quad-core Intel processor at 3.40 GHz. Note that the periodical motion model was only employed in the *single-master* setting, and the solution paths of L1RLS and BiCRAM were sampled 11 times (see Sec. 4.4.1). The height estimates of single and double scatterers are illustrated in Fig. 4.7–4.9 for the three settings, respectively. In the case of double scatterers, the higher one was plotted. The apparently messy appearance (e.g., in the left column) is caused by the fact that single scatterers are located on both roof and facade. Despite this, the gradual color transition at the 30 PSs from far- to near-range agrees visually very well with the Level 1 ground truth (see Fig. 2.3 (left)). Tab. 4.4 gives the number of scatterers. In the *single-*

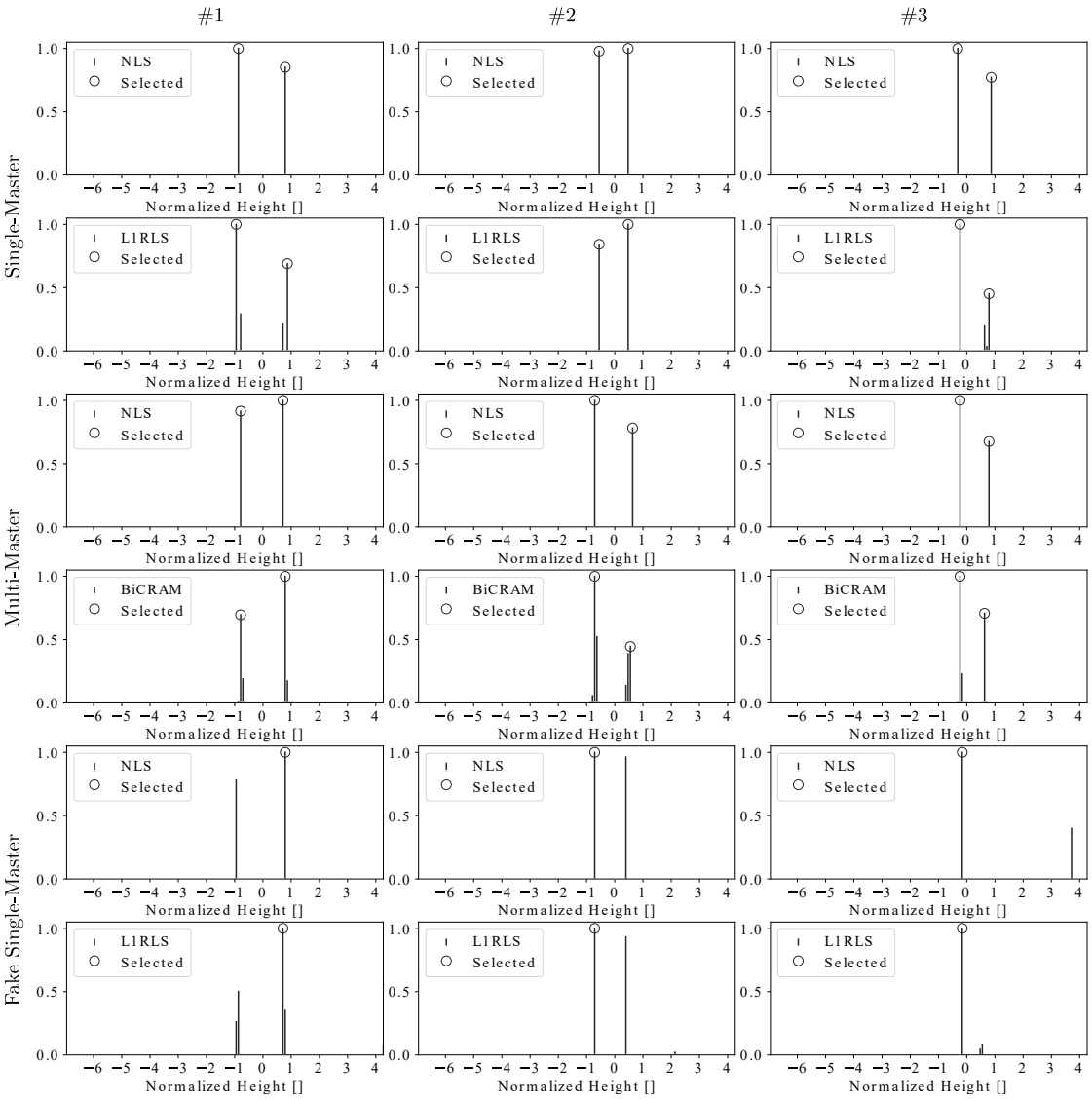

Figure 4.5: Estimated height profile of #1–3 in Fig. 4.4. Vertical line: before model-order selection. Circle: after model-order selection. The height values are given in Tab. 4.1.

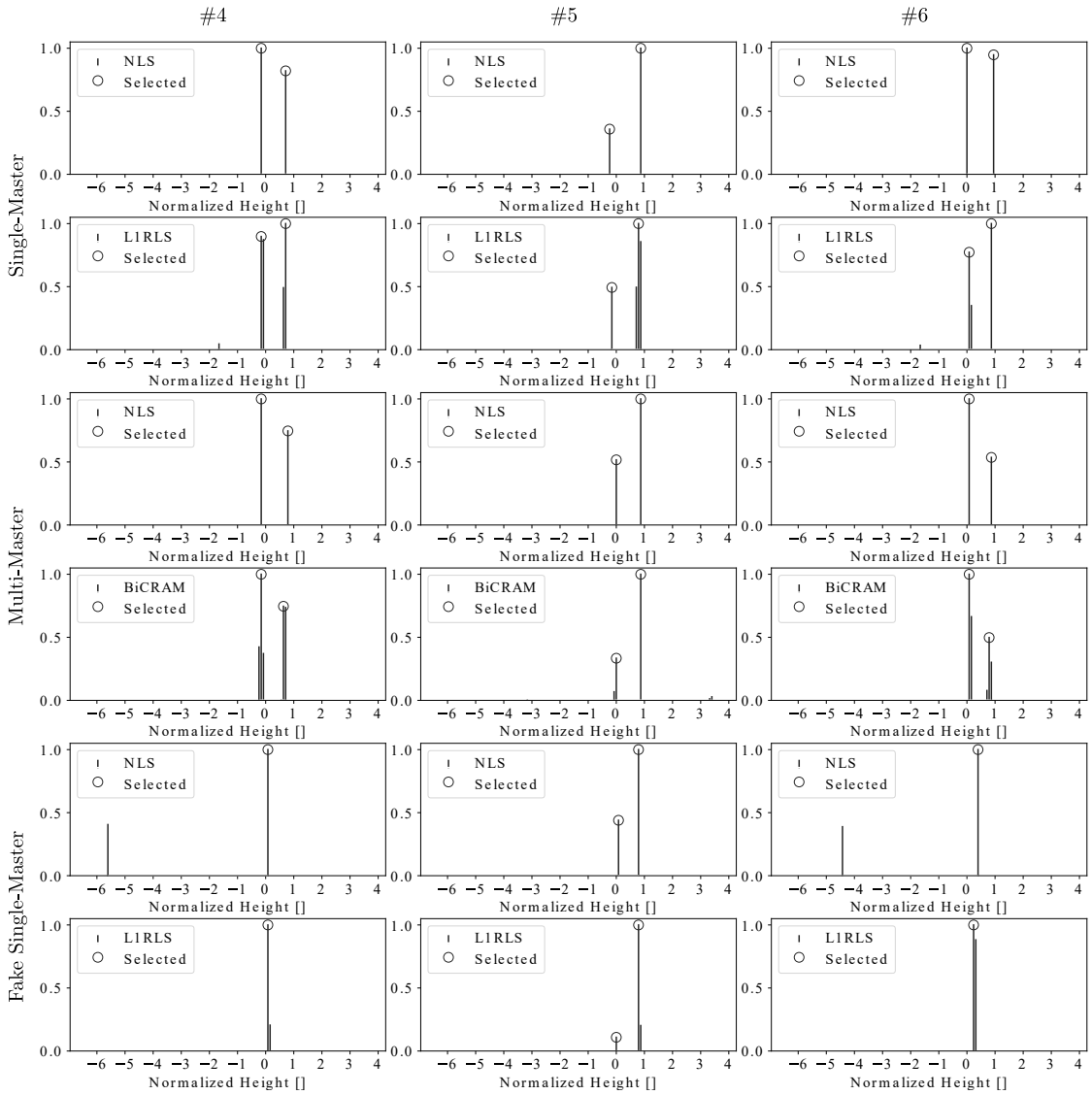

Figure 4.6: Estimated height profile of #4–6 in Fig. 4.4. Vertical line: before model-order selection. Circle: after model-order selection. The height values are given in Tab. 4.2.

Table 4.2: Single- and multi-master height estimates of looks subject to layover #4–6 [m]

		#4		#5		#6	
		h_1	h_2	h_1	h_2	h_1	h_2
RaySAR		−2.87	–	−1.59	–	0.55	–
Single-Master	NLS	−2.63	9.97	−1.95	10.03	0.98	11.34
	L1RLS	−2.63	9.97	−1.95	10.03	0.98	11.34
Multi-Master	NLS	−2.06	10.45	−0.37	10.90	0.66	10.85
	BiCRAM	−2.06	10.45	−0.37	10.90	0.66	10.85
Fake Single-Master	NLS	1.19	–	0.63	10.03	3.47	–
	L1RLS	1.19	–	0.63	10.03	3.47	–

Table 4.3: Single- and multi-master runtime

		Runtime [s]
Single-Master	NLS	6154
	L1RLS	736
Multi-Master	NLS	460
	BiCRAM	6853
Fake Single-Master	NLS	48
	L1RLS	65

scatterer setting, NLS retrieved almost twice as many double scatterers as L1RLS. This is presumably due to a higher false positive rate: at 2 out of 30 PSs (5th/2nd row from near range, and 5th/5th column from late azimuth on the 6×5 regular grid) double scatterers were estimated, although there should only be two single ones. In the *multi-master* setting, the number of double scatterers is of the same order as the one in the *single-master* L1RLS, and the ratio between the numbers of single and double scatterers is also comparable. We attribute the smaller number of single scatterers to the nonconvexity of the sparse recovery problem (4.10): as implied by Thm. 4.2(2), a certain condition needs to be satisfied for any nonzero height profile to exist at all, let alone whether any algorithm can provably recover it. In the *fake single-master* setting, a lot fewer double scatterers were retrieved. This is presumably a result of double scatterers being misdetected as single scatterers, which happened 5 out of 6 times in the previous proof-of-concept experiment (see Fig. 4.5 and 4.6).

In the next subsection, these height estimates will be systematically validated with Level 1 and 2 ground truth data.

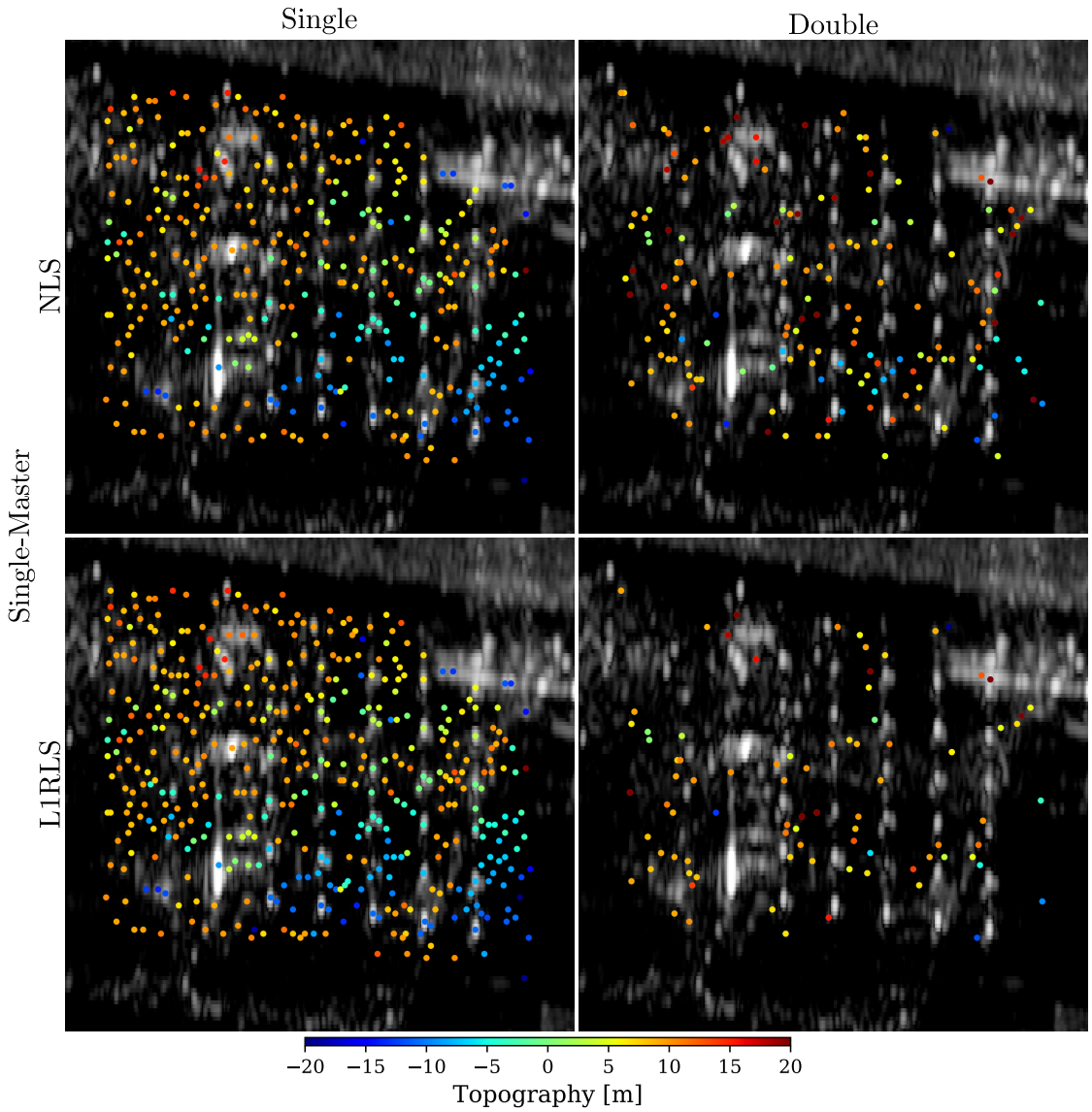

Figure 4.7: Single-master height estimates of single and double scatterers. Top: NLS. Bottom: L1RLS.

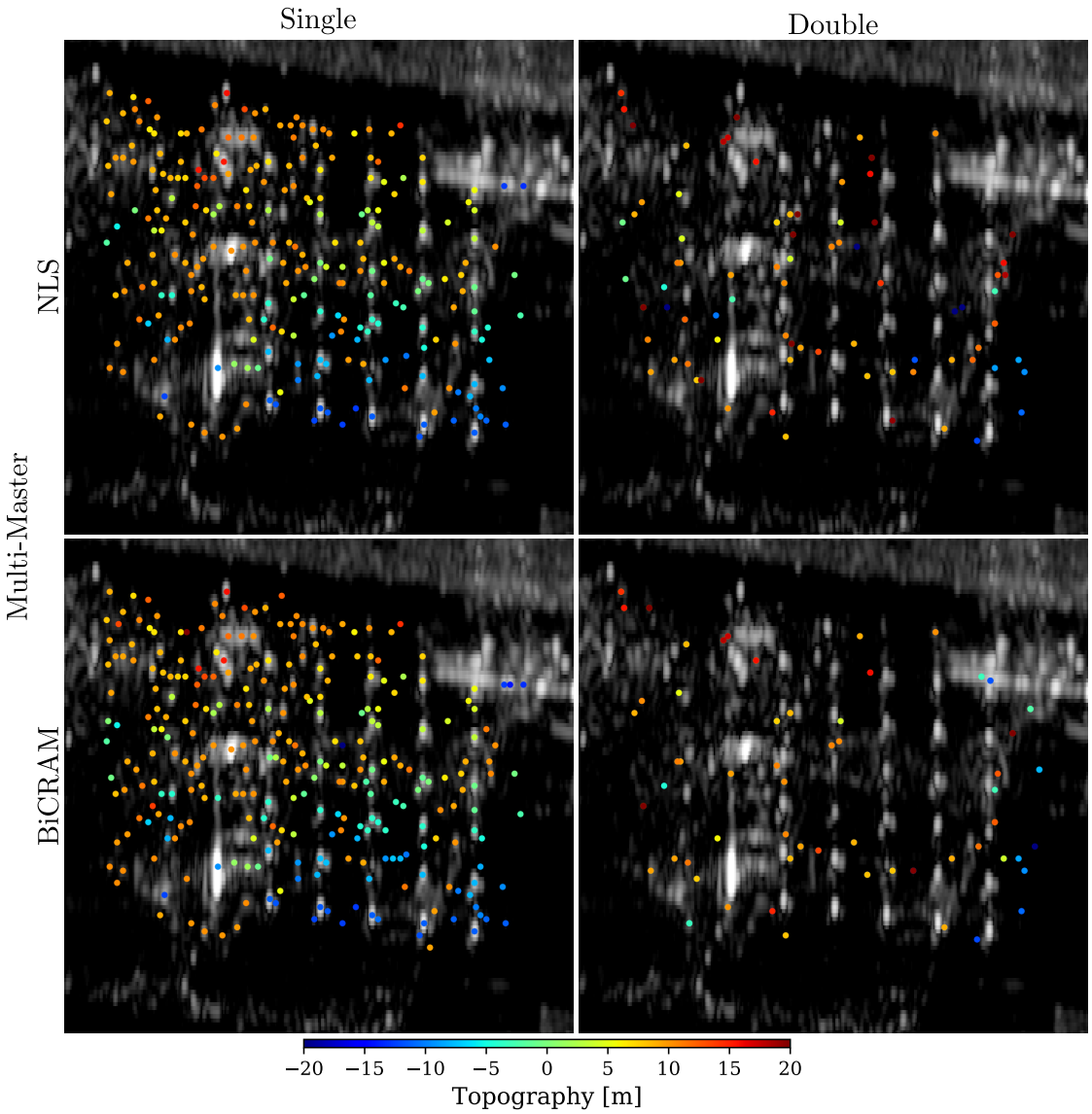

Figure 4.8: Multi-master height estimates of single and double scatterers. Top: NLS. Bottom: BiCRAM.

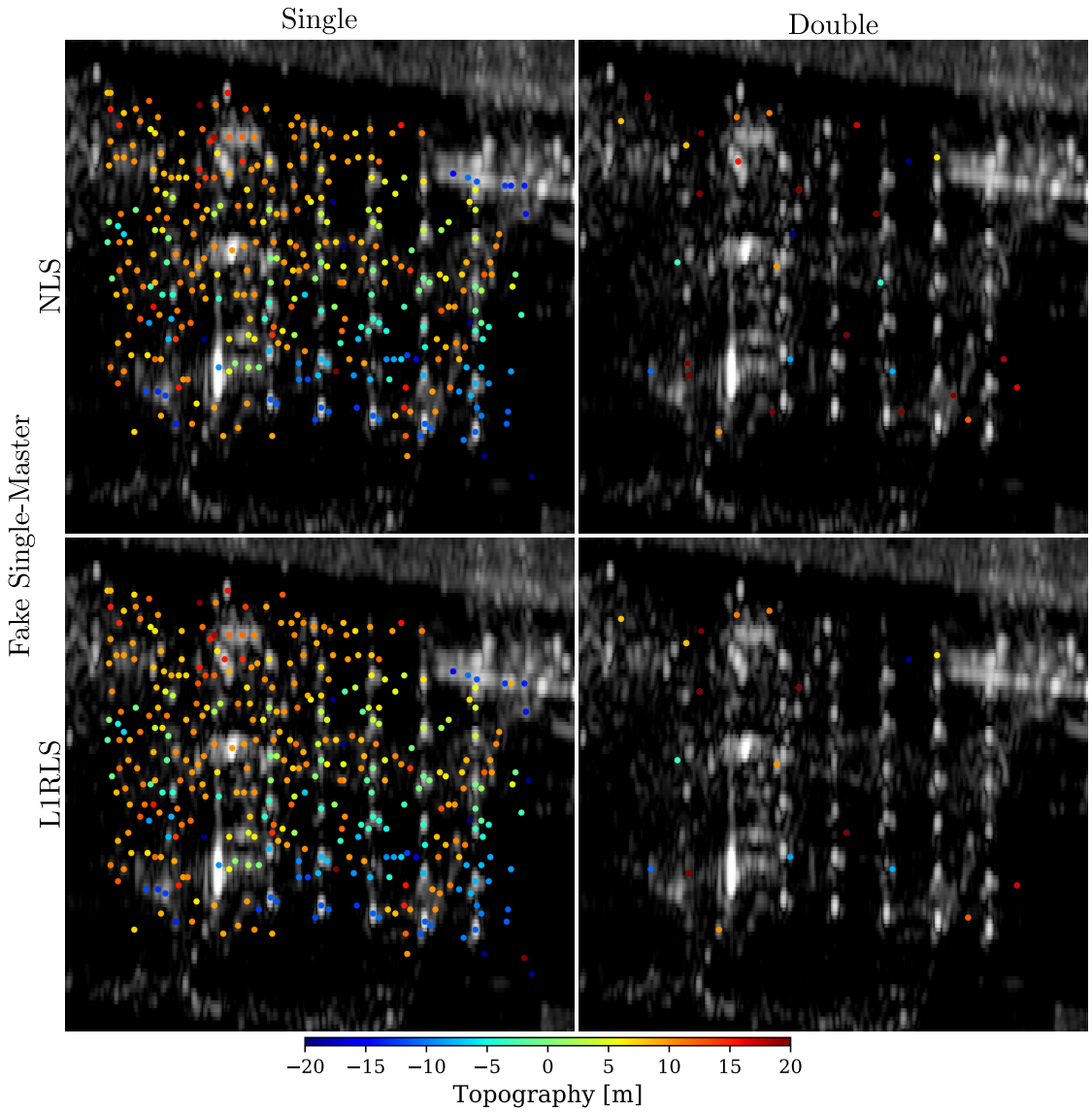

Figure 4.9: Fake single-master height estimates of single and double scatterers. Top: NLS. Bottom: L1RLS.

Table 4.4: Single- and multi-master number of scatterers

		Single	Double	Ratio	Facade
Single-Master	NLS	359	332	1.08	148
	L1RLS	446	168	2.65	189
Multi-Master	NLS	260	158	1.65	124
	BiCRAM	291	118	2.47	133
Fake Single-Master	NLS	360	60	6.00	134
	L1RLS	381	38	10.03	143

4.4.3 Validation

Since the height ground truth is restricted to the TUM-Nordbau building facade (see Sec. 2.1), we focused our validation on single scatterers by following two approaches: the first one is based on 30 PSs, and the second one uses extracted scatterers that correspond to the building facade.

As already explained in Sec. 4.4.1, the 30 PSs comprising the Level 1 ground truth (see Fig. 2.3 (left)) result from triple reflections on the building facade, and are located on a regular grid of salient points. Because of the nearly identical scattering geometry, these PSs should have very similar SNRs and are thus ideal for the validation of height estimates. In each of the six cases (3 settings $\times$ 2 algorithms), single scatterers were correctly detected at all the 30 PSs—with the exception that two were misdetected as double scatterers by NLS in the *single-master* setting (see Fig. 4.7 (top)). As a result, the height estimate error could be evaluated directly. Fig. 4.10 illustrates the normalized histogram of height estimate error, whose statistical parameters are provided in Tab. 4.5. As a reference, the SD and MAD of height estimate error in the PSI result were reported to be 0.28 and 0.22 m, respectively [1]. In each of the three settings, the corresponding two algorithms performed similarly and no significant difference can be visually observed. A comparison of the multi-master and fake single-master results revealed the superiority of the former: its histogram is more centered around zero with both slightly smaller SD and MAD. This is not unexpected, since we have already analyzed the implication of the single-look *multi-master* data model for single scatterers in Sec. 4.1. At this point, we could confidently claim that the minor difference in the modeling does make a difference in practice, albeit small, despite the longer (by approximately one order, taking into account that the solution path of BiCRAM was sampled 11 times) processing time. Somewhat surprisingly, the *multi-master* height estimate seems to be slightly better than the *single-master* one. This can be attributed to the complication of *single-master* tomographic processing by using an imperfect periodical motion model. On the other hand, the simplification in the *multi-master* setting is justified, since motion-induced phase was mitigated by generating interferograms of small time intervals.

The second approach employs all the facade looks contained in the Level 2 ground truth (see Fig. 2.3 (right)). Fig. 4.12 illustrates the scatter plots of simulated and

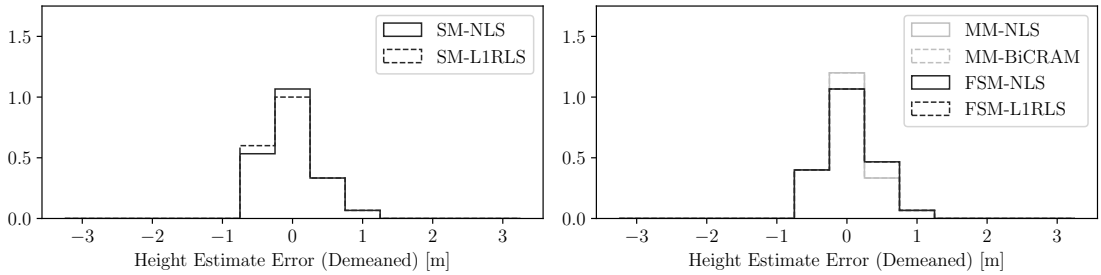

Figure 4.10: Normalized histogram of height estimate error of 30 PSs (Level 1). SM: single-master. MM: multi-master. FSM: fake single-master.

Table 4.5: Statistics of height estimate error [m]: 30 PSs (Level 1)

		Min	Max	Mean	Median	SD	MAD
Single-Master	NLS	−0.81	0.65	−0.30	−0.29	0.34	0.35
	L1RLS	−0.81	0.65	−0.31	−0.29	0.34	0.37
Multi-Master	NLS	−0.88	0.55	−0.33	−0.36	0.31	0.28
	BiCRAM	−0.88	0.55	−0.33	−0.36	0.31	0.28
Fake Single-Master	NLS	−1.02	0.68	−0.43	−0.48	0.34	0.30
	L1RLS	−1.02	0.68	−0.43	−0.48	0.34	0.30

estimated height of single scatterers. As can be observed, many single scatterers are located on the building roof (see the gray dots above the diagonal line). In order to extract facade scatterers, we used an interval of simulated height $\pm 3 \times$ CRLB. The number of extracted facade scatterers is given in the rightmost column of Tab. 4.4. These scatterers, depicted as black dots in Fig. 4.12, were used for the validation of height estimates. Fig. 4.11 illustrates the normalized histogram of height estimate error, whose statistical parameters are listed in Tab. 4.6. Likewise, the two corresponding algorithms performed similarly in each setting, and the *multi-master* height estimate error is characterized by slightly less deviation. Compared to the SD and MAD in Tab. 4.5, these parameters are worse due to the much larger range of SNRs.

4.5 Proofs of Theorems

The proofs of the main theorems are provided in this section.

4.5.1 Proof of Proposition 4.1

The proof uses the following minor result.

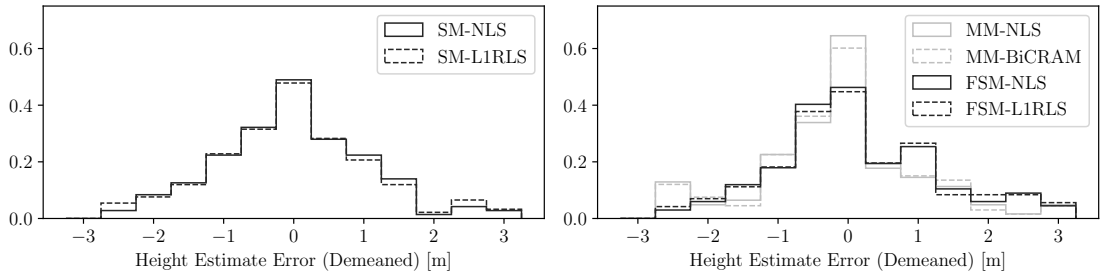

Figure 4.11: Normalized histogram of height estimate error of extracted facade scatterers (Level 2). SM: single-master. MM: multi-master. FSM: fake single-master.

Table 4.6: Statistics of height estimate error [m]: extracted facade scatterers (Level 2)

		Min	Max	Mean	Median	SD	MAD
Single-Master	NLS	−3.03	2.99	−0.40	−0.51	1.23	0.96
	L1RLS	−3.03	2.99	−0.42	−0.49	1.25	0.99
Multi-Master	NLS	−3.04	2.71	−0.49	−0.40	1.13	0.85
	BiCRAM	−3.04	2.71	−0.50	−0.40	1.12	0.86
Fake Single-Master	NLS	−2.93	2.70	−0.38	−0.50	1.15	0.91
	L1RLS	−2.93	2.70	−0.35	−0.48	1.21	1.05

Lemma 4.5. For any $\mathbf{F}, \mathbf{G} \in \mathbb{R}^{n\times n}$ and $c, d \in \mathbb{R}$ such that $c^2 + d^2 = 1$, the following equalities hold:

$$\begin{aligned}\begin{pmatrix} c\mathbf{I} & d\mathbf{I} \\ -d\mathbf{I} & c\mathbf{I} \end{pmatrix}^{-1} \begin{pmatrix} \mathbf{F} & -\mathbf{G} \\ \mathbf{G} & \mathbf{F} \end{pmatrix} \begin{pmatrix} c\mathbf{I} & d\mathbf{I} \\ -d\mathbf{I} & c\mathbf{I} \end{pmatrix} &= \begin{pmatrix} \mathbf{F} & -\mathbf{G} \\ \mathbf{G} & \mathbf{F} \end{pmatrix}, \\ \begin{pmatrix} c\mathbf{I} & d\mathbf{I} \\ -d\mathbf{I} & c\mathbf{I} \end{pmatrix}^{-1} \begin{pmatrix} \mathbf{F} & \mathbf{G} \\ \mathbf{G} & -\mathbf{F} \end{pmatrix} &= \begin{pmatrix} \mathbf{F} & \mathbf{G} \\ \mathbf{G} & -\mathbf{F} \end{pmatrix} \begin{pmatrix} c\mathbf{I} & d\mathbf{I} \\ -d\mathbf{I} & c\mathbf{I} \end{pmatrix}. \end{aligned} \tag{4.33}$$

Proof. Observe that for any $a, b \in \mathbb{R}$ such that $a^2 + b^2 \neq 0$,

$$\begin{pmatrix} a\mathbf{I} & b\mathbf{I} \\ -b\mathbf{I} & a\mathbf{I} \end{pmatrix}^{-1} = \frac{1}{a^2+b^2} \begin{pmatrix} a\mathbf{I} & -b\mathbf{I} \\ b\mathbf{I} & a\mathbf{I} \end{pmatrix}. \tag{4.34}$$

The rest of the proof follows via straightforward computations. □

Now we turn our attention to the proposition.

Proof of Proposition 4.1. First, we prove that $\nabla^2 f(\mathbf{x})$ and $\nabla^2 f\left(\mathbf{x}\exp(j\phi)\right)$ are similar, i.e., there exists an invertible $\mathbf{P}$ such that $\nabla^2 f(\mathbf{x}) = \mathbf{P}^{-1}\nabla^2 f\left(\mathbf{x}\exp(j\phi)\right)\mathbf{P}$.

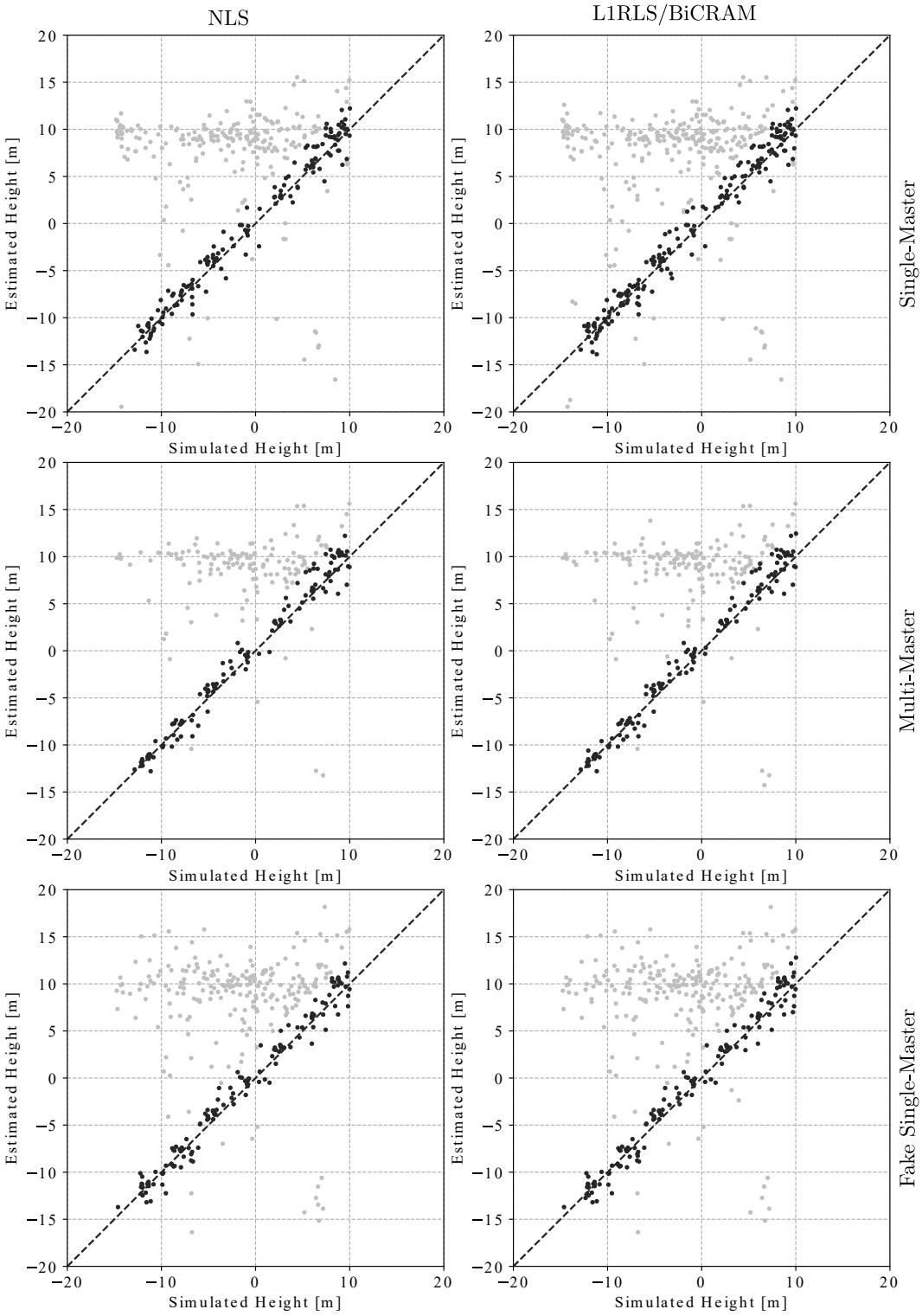

Figure 4.12: Scatter plot of simulated and estimated height of single scatterers using Level 2 height ground truth. Black: extracted facade scatterers. Gray: non-facade scatterers.

Observe that

$$\begin{aligned}
\mathbf{C}\left(\mathbf{x}\exp(j\phi)\right) &= \mathbf{A}^H \operatorname{Diag}\left(\left(\mathbf{B}\mathbf{x}\exp(j\phi)\right) \circ \left(\overline{\mathbf{B}\mathbf{x}\exp(j\phi)}\right)\right)\mathbf{A} + \\
&\quad \mathbf{B}^H \operatorname{Diag}\left(\left(\mathbf{A}\mathbf{x}\exp(j\phi)\right) \circ \left(\overline{\mathbf{A}\mathbf{x}\exp(j\phi)}\right)\right)\mathbf{B} \\
&= \mathbf{C}(\mathbf{x}), \\
\mathbf{D}\left(\mathbf{x}\exp(j\phi)\right) &= \mathbf{A}^H \operatorname{Diag}\left(\left(\mathbf{A}\mathbf{x}\exp(j\phi)\right) \circ \left(\mathbf{B}\mathbf{x}\exp(j\phi)\right)\right)\overline{\mathbf{B}} + \\
&\quad \mathbf{B}^H \operatorname{Diag}\left(\left(\mathbf{A}\mathbf{x}\exp(j\phi)\right) \circ \left(\mathbf{B}\mathbf{x}\exp(j\phi)\right)\right)\overline{\mathbf{A}} \\
&= \mathbf{D}(\mathbf{x})\exp(j2\phi), \\
\mathbf{E}\left(\mathbf{x}\exp(j\phi)\right) &= \mathbf{A}^H \operatorname{Diag}\left(\left(\mathbf{A}\mathbf{x}\exp(j\phi)\right) \circ \left(\overline{\mathbf{B}\mathbf{x}\exp(j\phi)}\right) - \mathbf{b}\right)\mathbf{B} + \\
&\quad \mathbf{B}^H \operatorname{Diag}\left(\left(\overline{\mathbf{A}\mathbf{x}\exp(j\phi)}\right) \circ \left(\mathbf{B}\mathbf{x}\exp(j\phi)\right) - \overline{\mathbf{b}}\right)\mathbf{A} \\
&= \mathbf{E}(\mathbf{x}).
\end{aligned} \tag{4.35}$$

Let $\mathbf{C} \coloneqq \mathbf{C}(\mathbf{x})$, $\mathbf{D} \coloneqq \mathbf{D}(\mathbf{x})$, $\mathbf{E} \coloneqq \mathbf{E}(\mathbf{x})$. The Hessian becomes

$$\begin{aligned}
\nabla^2 f\left(\mathbf{x}\exp(j\phi)\right) = &\begin{pmatrix} \Re(\mathbf{C}) & -\Im(\mathbf{C}) \\ \Im(\mathbf{C}) & \Re(\mathbf{C}) \end{pmatrix} + \begin{pmatrix} \Re\left(\mathbf{D}\exp(j2\phi)\right) & \Im\left(\mathbf{D}\exp(j2\phi)\right) \\ \Im\left(\mathbf{D}\exp(j2\phi)\right) & -\Re\left(\mathbf{D}\exp(j2\phi)\right) \end{pmatrix} + \\
&\begin{pmatrix} \Re(\mathbf{E}) & -\Im(\mathbf{E}) \\ \Im(\mathbf{E}) & \Re(\mathbf{E}) \end{pmatrix} \\
= &\begin{pmatrix} \Re(\mathbf{C}+\mathbf{E}) & -\Im(\mathbf{C}+\mathbf{E}) \\ \Im(\mathbf{C}+\mathbf{E}) & \Re(\mathbf{C}+\mathbf{E}) \end{pmatrix} + \\
&\begin{pmatrix} \Re(\mathbf{D}) & \Im(\mathbf{D}) \\ \Im(\mathbf{D}) & -\Re(\mathbf{D}) \end{pmatrix} \begin{pmatrix} \cos(2\phi)\mathbf{I} & \sin(2\phi)\mathbf{I} \\ -\sin(2\phi)\mathbf{I} & \cos(2\phi)\mathbf{I} \end{pmatrix}.
\end{aligned} \tag{4.36}$$

The choice of $\mathbf{P}$ can be divided into two cases depending on the value of ϕ.

(1) In the trivial case, $\phi = (2k+1)\pi/2$ for some $k \in \mathbb{Z}$. Let

$$\mathbf{P} \coloneqq \begin{pmatrix} \mathbf{0} & -\mathbf{I} \\ \mathbf{I} & \mathbf{0} \end{pmatrix}. \tag{4.37}$$

This leads to

$$\begin{aligned}\mathbf{P}^{-1}\nabla^2 f\left(\mathbf{x}\exp(j\phi)\right)\mathbf{P} = &\begin{pmatrix}\mathbf{0} & -\mathbf{I}\\ \mathbf{I} & \mathbf{0}\end{pmatrix}^{-1}\begin{pmatrix}\Re(\mathbf{C}+\mathbf{E}) & -\Im(\mathbf{C}+\mathbf{E})\\ \Im(\mathbf{C}+\mathbf{E}) & \Re(\mathbf{C}+\mathbf{E})\end{pmatrix}\begin{pmatrix}\mathbf{0} & -\mathbf{I}\\ \mathbf{I} & \mathbf{0}\end{pmatrix}+\\ &\begin{pmatrix}\mathbf{0} & -\mathbf{I}\\ \mathbf{I} & \mathbf{0}\end{pmatrix}^{-1}\begin{pmatrix}\Re(\mathbf{D}) & \Im(\mathbf{D})\\ \Im(\mathbf{D}) & -\Re(\mathbf{D})\end{pmatrix}\begin{pmatrix}-\mathbf{I} & \mathbf{0}\\ \mathbf{0} & -\mathbf{I}\end{pmatrix}\begin{pmatrix}\mathbf{0} & -\mathbf{I}\\ \mathbf{I} & \mathbf{0}\end{pmatrix}\\ = &\begin{pmatrix}\Re(\mathbf{C}+\mathbf{E}) & -\Im(\mathbf{C}+\mathbf{E})\\ \Im(\mathbf{C}+\mathbf{E}) & \Re(\mathbf{C}+\mathbf{E})\end{pmatrix}+\\ &\begin{pmatrix}\Re(\mathbf{D}) & \Im(\mathbf{D})\\ \Im(\mathbf{D}) & -\Re(\mathbf{D})\end{pmatrix}\begin{pmatrix}\mathbf{0} & -\mathbf{I}\\ \mathbf{I} & \mathbf{0}\end{pmatrix}\begin{pmatrix}-\mathbf{I} & \mathbf{0}\\ \mathbf{0} & -\mathbf{I}\end{pmatrix}\begin{pmatrix}\mathbf{0} & -\mathbf{I}\\ \mathbf{I} & \mathbf{0}\end{pmatrix}\\ = &\begin{pmatrix}\Re(\mathbf{C}+\mathbf{E}) & -\Im(\mathbf{C}+\mathbf{E})\\ \Im(\mathbf{C}+\mathbf{E}) & \Re(\mathbf{C}+\mathbf{E})\end{pmatrix}+\begin{pmatrix}\Re(\mathbf{D}) & \Im(\mathbf{D})\\ \Im(\mathbf{D}) & -\Re(\mathbf{D})\end{pmatrix}\\ = &\nabla^2 f(\mathbf{x}),\end{aligned} \tag{4.38}$$

where the second equality follows from Lemma 4.5.

(2) In the non-trivial case, $\phi \neq (2k+1)\pi/2$ for any $k \in \mathbb{Z}$. Let

$$\mathbf{P} \coloneqq \begin{pmatrix}\sqrt{\frac{1+\cos(2\phi)}{2}}\mathbf{I} & -\frac{\sin(2\phi)}{\sqrt{2(1+\cos(2\phi))}}\mathbf{I}\\ \frac{\sin(2\phi)}{\sqrt{2(1+\cos(2\phi))}}\mathbf{I} & \sqrt{\frac{1+\cos(2\phi)}{2}}\mathbf{I}\end{pmatrix}. \tag{4.39}$$

Likewise, the same equality holds.

Finally, we use the similarity property to show that an eigenvalue of $\nabla^2 f(\mathbf{x})$ is also an eigenvalue of $\nabla^2 f\left(\mathbf{x}\exp(j\phi)\right)$.

Let $(\lambda, \mathbf{v})$ be an eigenpair of $\nabla^2 f(\mathbf{x})$. The similarity property implies

$$\lambda\mathbf{v} = \nabla^2 f(\mathbf{x})\mathbf{v} = \mathbf{P}^{-1}\nabla^2 f\left(\mathbf{x}\exp(j\phi)\right)\mathbf{P}\mathbf{v} \implies \nabla^2 f\left(\mathbf{x}\exp(j\phi)\right)\mathbf{P}\mathbf{v} = \lambda\mathbf{P}\mathbf{v}, \tag{4.40}$$

i.e., $(\lambda, \mathbf{P}\mathbf{v})$ is an eigenpair of $\nabla^2 f\left(\mathbf{x}\exp(j\phi)\right)$. The proof in the other direction is straightforward. □

4.5.2 Proof of Theorem 4.2

Before we delve into the proof, it is useful to define a few auxiliary variables. Let

$$\tilde{\mathbf{C}} \coloneqq \begin{pmatrix}\Re(\mathbf{C}) & -\Im(\mathbf{C})\\ \Im(\mathbf{C}) & \Re(\mathbf{C})\end{pmatrix}, \quad \tilde{\mathbf{D}} \coloneqq \begin{pmatrix}\Re(\mathbf{D}) & \Im(\mathbf{D})\\ \Im(\mathbf{D}) & -\Re(\mathbf{D})\end{pmatrix}, \quad \tilde{\mathbf{E}} \coloneqq \begin{pmatrix}\Re(\mathbf{E}) & -\Im(\mathbf{E})\\ \Im(\mathbf{E}) & \Re(\mathbf{E})\end{pmatrix}, \tag{4.41}$$

so that $\nabla^2 f(\mathbf{x}) = \tilde{\mathbf{C}} + \tilde{\mathbf{D}} + \tilde{\mathbf{E}}$. Likewise, $\tilde{\mathbf{C}}, \tilde{\mathbf{D}}, \tilde{\mathbf{E}} : \mathbb{C}^n \to \mathbb{R}^{2n\times 2n}$ are de facto (composite) functions of $\mathbf{x}$. The proof of the main theorem is based on the following minor result.

Lemma 4.6. For any $\mathbf{x} \coloneqq \mathbf{x}_R + j\mathbf{x}_I$, the following equalities hold:

$$\begin{aligned}
\begin{pmatrix}\mathbf{x}_R^T & \mathbf{x}_I^T\end{pmatrix} \tilde{\mathbf{C}} \begin{pmatrix}\mathbf{x}_R \\ \mathbf{x}_I\end{pmatrix} &= \mathbf{x}^H \mathbf{C} \mathbf{x}, \\
\begin{pmatrix}\mathbf{x}_R^T & \mathbf{x}_I^T\end{pmatrix} \tilde{\mathbf{D}} \begin{pmatrix}\mathbf{x}_R \\ \mathbf{x}_I\end{pmatrix} &= \Re\left(\mathbf{x}^H \mathbf{D} \overline{\mathbf{x}}\right), \\
\begin{pmatrix}\mathbf{x}_R^T & \mathbf{x}_I^T\end{pmatrix} \tilde{\mathbf{E}} \begin{pmatrix}\mathbf{x}_R \\ \mathbf{x}_I\end{pmatrix} &= \mathbf{x}^H \mathbf{E} \mathbf{x}, \\
\tilde{\mathbf{C}} \begin{pmatrix}\mathbf{x}_R \\ \mathbf{x}_I\end{pmatrix} &= \begin{pmatrix}\Re(\mathbf{C}\mathbf{x}) \\ \Im(\mathbf{C}\mathbf{x})\end{pmatrix}, \\
\tilde{\mathbf{D}} \begin{pmatrix}\mathbf{x}_R \\ \mathbf{x}_I\end{pmatrix} &= \begin{pmatrix}\Re(\mathbf{D}\overline{\mathbf{x}}) \\ \Im(\mathbf{D}\overline{\mathbf{x}})\end{pmatrix}, \\
\tilde{\mathbf{E}} \begin{pmatrix}\mathbf{x}_R \\ \mathbf{x}_I\end{pmatrix} &= \begin{pmatrix}\Re(\mathbf{E}\mathbf{x}) \\ \Im(\mathbf{E}\mathbf{x})\end{pmatrix}.
\end{aligned} \tag{4.42}$$

Proof. The proof follows via straightforward computations. □

Proof of Theorem 4.2. (1) Since $\nabla f(\mathbf{0}) = \mathbf{0}$, $\mathbf{0}$ is a critical point. Observe that

$$\mathbf{C}(\mathbf{0}) = \mathbf{D}(\mathbf{0}) = \mathbf{0}, \quad \mathbf{E}(\mathbf{0}) = -\mathbf{A}^H \operatorname{Diag}(\mathbf{b})\mathbf{B} - \mathbf{B}^H \operatorname{Diag}(\overline{\mathbf{b}})\mathbf{A}. \tag{4.43}$$

For any $\mathbf{x} \coloneqq \mathbf{x}_R + j\mathbf{x}_I \neq \mathbf{0}$,

$$\begin{pmatrix}\mathbf{x}_R^T & \mathbf{x}_I^T\end{pmatrix} \nabla^2 f(\mathbf{0}) \begin{pmatrix}\mathbf{x}_R \\ \mathbf{x}_I\end{pmatrix} = \begin{pmatrix}\mathbf{x}_R^T & \mathbf{x}_I^T\end{pmatrix} \tilde{\mathbf{E}}(\mathbf{0}) \begin{pmatrix}\mathbf{x}_R \\ \mathbf{x}_I\end{pmatrix} = \mathbf{x}^H \mathbf{E}(\mathbf{0}) \mathbf{x}, \tag{4.44}$$

where the second equality is given by Lemma 4.6. Since $\mathbf{E}(\mathbf{0})$ is Hermitian, we have

$$\begin{cases} \mathbf{x}^H \mathbf{E}(\mathbf{0}) \mathbf{x} > 0 & \text{if } \mathbf{A}^H \operatorname{Diag}(\mathbf{b})\mathbf{B} + \mathbf{B}^H \operatorname{Diag}(\overline{\mathbf{b}})\mathbf{A} \prec \mathbf{0} \\ \mathbf{x}^H \mathbf{E}(\mathbf{0}) \mathbf{x} < 0 & \text{if } \mathbf{A}^H \operatorname{Diag}(\mathbf{b})\mathbf{B} + \mathbf{B}^H \operatorname{Diag}(\overline{\mathbf{b}})\mathbf{A} \succ \mathbf{0} \end{cases} \tag{4.45}$$

for any $\mathbf{x} \in \mathbb{C}^n \setminus \{\mathbf{0}\}$.

(2) Suppose $\exists \mathbf{z} \neq \mathbf{0}$ such that $\nabla f(\mathbf{z}) = \mathbf{0}$. (4.23) implies

$$\mathbf{d}(\mathbf{z}) = \mathbf{A}^H \left(((\mathbf{A}\mathbf{z}) \circ (\overline{\mathbf{B}\mathbf{z}}) - \mathbf{b}) \circ (\mathbf{B}\mathbf{z})\right) + \mathbf{B}^H \left(((\overline{\mathbf{A}\mathbf{z}}) \circ (\mathbf{B}\mathbf{z}) - \overline{\mathbf{b}}) \circ (\mathbf{A}\mathbf{z})\right) = \mathbf{0}. \tag{4.46}$$

A few manipulations lead to

$$\mathbf{A}^H \left((\mathbf{A}\mathbf{z}) \circ (\overline{\mathbf{B}\mathbf{z}}) \circ (\mathbf{B}\mathbf{z})\right) + \mathbf{B}^H \left((\overline{\mathbf{A}\mathbf{z}}) \circ (\mathbf{B}\mathbf{z}) \circ (\mathbf{A}\mathbf{z})\right) = \mathbf{A}^H \operatorname{Diag}(\mathbf{b})\mathbf{B}\mathbf{z} + \mathbf{B}^H \operatorname{Diag}(\overline{\mathbf{b}})\mathbf{A}\mathbf{z}. \tag{4.47}$$

Multiplying both sides with $\mathbf{z}^H$ on the left yields

$$\mathbf{z}^H \left(\mathbf{A}^H \operatorname{Diag}(\mathbf{b})\mathbf{B} + \mathbf{B}^H \operatorname{Diag}(\overline{\mathbf{b}})\mathbf{A}\right) \mathbf{z} = 2\|(\mathbf{A}\mathbf{z}) \circ (\overline{\mathbf{B}\mathbf{z}})\|_2^2 \geq 0, \tag{4.48}$$

which implies $\mathbf{A}^H \operatorname{Diag}(\mathbf{b})\mathbf{B} + \mathbf{B}^H \operatorname{Diag}(\overline{\mathbf{b}})\mathbf{A} \not\prec \mathbf{0}$.

(3a) We prove that $\nabla^2 f(\mathbf{z})$ is rank deficient by showing $\nabla^2 f(\mathbf{z}) \begin{pmatrix}\mathbf{x}_R \\ \mathbf{x}_I\end{pmatrix} = \mathbf{0}$, where $\mathbf{x} \coloneqq \mathbf{z}_I - j\mathbf{z}_R$. Observe

(1) $(\mathbf{Ax}) \circ (\overline{\mathbf{Bz}}) + (\mathbf{Az}) \circ (\overline{\mathbf{Bx}}) = \mathbf{0}$.

(2) For any $\mathbf{F}$, $\mathbf{Fz} = \mathbf{0} \implies \mathbf{Fx} = \mathbf{0}$, which together with (4.46) implies

$$\mathbf{A}^H \operatorname{Diag}\left((\mathbf{Az}) \circ (\overline{\mathbf{Bz}}) - \mathbf{b}\right) \mathbf{Bx} + \mathbf{B}^H \operatorname{Diag}\left((\overline{\mathbf{Az}}) \circ (\mathbf{Bz}) - \overline{\mathbf{b}}\right) \mathbf{Ax} = \mathbf{0}. \tag{4.49}$$

By Lemma 4.6, it suffices to check $\mathbf{Cx} + \mathbf{D}\overline{\mathbf{x}} + \mathbf{Ex}$:

$$\begin{aligned}
\mathbf{Cx} + \mathbf{D}\overline{\mathbf{x}} + \mathbf{Ex} = {} & \mathbf{A}^H \operatorname{Diag}\left((\mathbf{Bz}) \circ (\overline{\mathbf{Bz}})\right) \mathbf{Ax} + \mathbf{B}^H \operatorname{Diag}\left((\mathbf{Az}) \circ (\overline{\mathbf{Az}})\right) \mathbf{Bx} + \\
& \mathbf{A}^H \operatorname{Diag}\left((\mathbf{Az}) \circ (\mathbf{Bz})\right) \overline{\mathbf{B}}\overline{\mathbf{x}} + \mathbf{B}^H \operatorname{Diag}\left((\mathbf{Az}) \circ (\mathbf{Bz})\right) \overline{\mathbf{A}}\overline{\mathbf{x}} + \\
& \mathbf{A}^H \operatorname{Diag}\left((\mathbf{Az}) \circ (\overline{\mathbf{Bz}}) - \mathbf{b}\right) \mathbf{Bx} + \mathbf{B}^H \operatorname{Diag}\left((\overline{\mathbf{Az}}) \circ (\mathbf{Bz}) - \overline{\mathbf{b}}\right) \mathbf{Ax} \\
= {} & \mathbf{A}^H \operatorname{Diag}(\mathbf{Bz}) \left((\mathbf{Ax}) \circ (\overline{\mathbf{Bz}}) + (\mathbf{Az}) \circ (\overline{\mathbf{Bx}})\right) + \\
& \mathbf{B}^H \operatorname{Diag}(\mathbf{Az}) \left((\overline{\mathbf{Az}}) \circ (\mathbf{Bx}) + (\overline{\mathbf{Ax}}) \circ (\mathbf{Bz})\right) \\
= {} & \mathbf{0}.
\end{aligned} \tag{4.50}$$

(3b) For any $\phi \in \mathbb{R}$, it is obvious that

$$\mathbf{d}\left(\mathbf{z}\exp(j\phi)\right) = \mathbf{d}(\mathbf{z}) = \mathbf{0}, \quad f\left(\mathbf{z}\exp(j\phi)\right) = f(\mathbf{z}), \tag{4.51}$$

i.e., $\mathbf{z}\exp(j\phi)$ is also a nonzero critical point that is as good. By Proposition 4.1, $\nabla^2 f\left(\mathbf{x}\exp(j\phi)\right)$ has the same eigenvalues as $\nabla^2 f(\mathbf{x})$ and therefore the same definiteness. □

4.5.3 Proof of Theorem 4.3

Without loss of generality, assume that $\|\mathbf{A} \circ \overline{\mathbf{B}}\| \neq 0$.

Proof of Thm. 4.3. (1) When $n = 1$, observe that

$$\mathbf{A}^H \operatorname{Diag}(\mathbf{b})\mathbf{B} + \mathbf{B}^H \operatorname{Diag}(\overline{\mathbf{b}})\mathbf{A} = 2\,\Re\left((\mathbf{A} \circ \overline{\mathbf{B}})^H b\right). \tag{4.52}$$

The rest follows directly from Thm. 4.2(1).

(2) For any $\mathbf{z} \in \mathbb{C} \setminus \{0\}$, we have

$$\begin{aligned}
\mathbf{d}(\mathbf{z}) &= \mathbf{A}^H \left(((\mathbf{Az}) \circ (\overline{\mathbf{Bz}}) - \mathbf{b}) \circ (\mathbf{Bz})\right) + \mathbf{B}^H \left(((\overline{\mathbf{Az}}) \circ (\mathbf{Bz}) - \overline{\mathbf{b}}) \circ (\mathbf{Az})\right) \\
&= \mathbf{z}|\mathbf{z}|^2 \mathbf{A}^H (\mathbf{A} \circ \overline{\mathbf{B}} \circ \mathbf{B}) - \mathbf{z}\mathbf{A}^H (\mathbf{b} \circ \mathbf{B}) + \mathbf{z}|\mathbf{z}|^2 \mathbf{B}^H (\overline{\mathbf{A}} \circ \mathbf{B} \circ \mathbf{A}) - \mathbf{z}\mathbf{B}^H (\overline{\mathbf{b}} \circ \mathbf{A}) \\
&= \mathbf{z}|\mathbf{z}|^2 \|\mathbf{A} \circ \overline{\mathbf{B}}\|_2^2 - \mathbf{z}(\mathbf{A} \circ \overline{\mathbf{B}})^H \mathbf{b} + \mathbf{z}|\mathbf{z}|^2 \|\mathbf{A} \circ \overline{\mathbf{B}}\|_2^2 - \mathbf{z}(\overline{\mathbf{A}} \circ \mathbf{B})^H \overline{\mathbf{b}} \\
&= 2\mathbf{z}\left(\|\mathbf{A} \circ \overline{\mathbf{B}}\|_2^2 |\mathbf{z}|^2 - \Re\left((\mathbf{A} \circ \overline{\mathbf{B}})^H \mathbf{b}\right)\right),
\end{aligned} \tag{4.53}$$

which has a nonzero root if and only if $\Re\left((\mathbf{A} \circ \overline{\mathbf{B}})^H \mathbf{b}\right) > 0$. If this condition is satisfied, its power is given by

$$|\mathbf{z}|^2 = \Re\left((\mathbf{A} \circ \overline{\mathbf{B}})^H \mathbf{b}\right) / \|\mathbf{A} \circ \overline{\mathbf{B}}\|_2^2. \tag{4.54}$$

(3a) Suppose $\exists \mathbf{z} \neq \mathbf{0}$ such that $\nabla f(\mathbf{z}) = \mathbf{0}$. (4.23) and (2) imply

$$\|\mathbf{A} \circ \overline{\mathbf{B}}\|_2^2 |\mathbf{z}|^2 - \Re\left((\mathbf{A} \circ \overline{\mathbf{B}})^H \mathbf{b}\right) = \mathbf{0}. \tag{4.55}$$

By Lemma 4.6, we have for any $\mathbf{x} \coloneqq \mathbf{x}_R + j\mathbf{x}_I \neq 0$

$$\begin{aligned}
&\begin{pmatrix}\mathbf{x}_R^T & \mathbf{x}_I^T\end{pmatrix} \nabla^2 f(\mathbf{z}) \begin{pmatrix}\mathbf{x}_R \\ \mathbf{x}_I\end{pmatrix} \\
=\;& \mathbf{x}^H \mathbf{C}(\mathbf{z})\mathbf{x} + \Re\left(\mathbf{x}^H \mathbf{D}(\mathbf{z})\overline{\mathbf{x}}\right) + \mathbf{x}^H \mathbf{E}(\mathbf{z})\mathbf{x} \\
=\;& |\mathbf{x}|^2 \mathbf{A}^H \operatorname{Diag}\left((\mathbf{B}\mathbf{z}) \circ (\overline{\mathbf{B}\mathbf{z}})\right) \mathbf{A} + |\mathbf{x}|^2 \mathbf{B}^H \operatorname{Diag}\left((\mathbf{A}\mathbf{z}) \circ (\overline{\mathbf{A}\mathbf{z}})\right) \mathbf{B} + \\
& \Re\left(\overline{\mathbf{x}}^2 \mathbf{A}^H \operatorname{Diag}\left((\mathbf{A}\mathbf{z}) \circ (\mathbf{B}\mathbf{z})\right) \overline{\mathbf{B}}\right) + \Re\left(\overline{\mathbf{x}}^2 \mathbf{B}^H \operatorname{Diag}\left((\mathbf{A}\mathbf{z}) \circ (\mathbf{B}\mathbf{z})\right) \overline{\mathbf{A}}\right) + \\
& |\mathbf{x}|^2 \mathbf{A}^H \operatorname{Diag}\left((\mathbf{A}\mathbf{z}) \circ (\overline{\mathbf{B}\mathbf{z}}) - \mathbf{b}\right) \mathbf{B} + |\mathbf{x}|^2 \mathbf{B}^H \operatorname{Diag}\left((\overline{\mathbf{A}\mathbf{z}}) \circ (\mathbf{B}\mathbf{z}) - \overline{\mathbf{b}}\right) \mathbf{A} \\
=\;& 2\|\mathbf{A} \circ \overline{\mathbf{B}}\|_2^2 |\mathbf{x}|^2 |\mathbf{z}|^2 + 2\|\mathbf{A} \circ \overline{\mathbf{B}}\|_2^2 \Re(\overline{\mathbf{x}}^2 \mathbf{z}^2) + 2|\mathbf{x}|^2 \left(\|\mathbf{A} \circ \overline{\mathbf{B}}\|_2^2 |\mathbf{z}|^2 - \Re\left((\mathbf{A} \circ \overline{\mathbf{B}})^H \mathbf{b}\right)\right) \\
=\;& \|\mathbf{A} \circ \overline{\mathbf{B}}\|_2^2 \left(2|\mathbf{x}|^2 |\mathbf{z}|^2 + 2\,\Re(\overline{\mathbf{x}}^2 \mathbf{z}^2)\right) \\
=\;& \|\mathbf{A} \circ \overline{\mathbf{B}}\|_2^2 (\overline{\mathbf{x}}\mathbf{z} + \mathbf{x}\overline{\mathbf{z}})^2 \geq 0,
\end{aligned} \tag{4.56}$$

where the equality can be attained with $\mathbf{x} = \mathbf{z}_I - j\mathbf{z}_R$.

That $\nabla^2 f(\mathbf{z})$ is rank deficient is implied by Thm. 4.2(3a).

(3b) This follows directly from Thm. 4.2(3b).

(3c) Let us perturb $\mathbf{z}$ by $\epsilon \in \mathbb{C}$ with $|\epsilon|$ being arbitrarily small and observe

$$\begin{aligned}
f(\mathbf{z}+\epsilon) &= \frac{1}{2}\| \left(\mathbf{A}(\mathbf{z}+\epsilon)\right) \circ \left(\overline{(\mathbf{B}\mathbf{z} + \epsilon)}\right) - \mathbf{b}\|_2^2 \\
&= \frac{1}{2}\|(\mathbf{A}\mathbf{z}) \circ (\overline{\mathbf{B}\mathbf{z}}) + (\mathbf{A}\mathbf{z}) \circ (\overline{\mathbf{B}\epsilon}) + (\mathbf{A}\boldsymbol{\epsilon}) \circ (\overline{\mathbf{B}\mathbf{z}}) + (\mathbf{A}\boldsymbol{\epsilon}) \circ (\overline{\mathbf{B}\boldsymbol{\epsilon}}) - \mathbf{b}\|_2^2 \\
&= \frac{1}{2}\|(\mathbf{A}\mathbf{z}) \circ (\overline{\mathbf{B}\mathbf{z}}) - \mathbf{b} + \mathbf{A} \circ \overline{\mathbf{B}}(\overline{\epsilon}\mathbf{z} + \epsilon\overline{\mathbf{z}} + |\epsilon|^2)\|_2^2 \\
&= \frac{1}{2}\|(\mathbf{A}\mathbf{z}) \circ (\overline{\mathbf{B}\mathbf{z}}) - \mathbf{b}\|_2^2 + \frac{1}{2}\|\mathbf{A} \circ \overline{\mathbf{B}}(2\,\Re(\overline{\epsilon}\mathbf{z}) + |\epsilon|^2)\|_2^2 + \\
&\quad \Re\left(\left((\mathbf{A}\mathbf{z}) \circ (\overline{\mathbf{B}\mathbf{z}}) - \mathbf{b}\right)^H \left(\mathbf{A} \circ \overline{\mathbf{B}}(2\,\Re(\overline{\epsilon}\mathbf{z}) + |\epsilon|^2)\right)\right) \\
&= \frac{1}{2}\|(\mathbf{A}\mathbf{z}) \circ (\overline{\mathbf{B}\mathbf{z}}) - \mathbf{b}\|_2^2 + \frac{1}{2}\|\mathbf{A} \circ \overline{\mathbf{B}}\|_2^2 (2\,\Re(\overline{\epsilon}\mathbf{z}) + |\epsilon|^2)^2 + \\
&\quad \Re\left(\|\mathbf{A} \circ \overline{\mathbf{B}}\|_2^2 |\mathbf{z}|^2 - \mathbf{b}^H (\mathbf{A} \circ \overline{\mathbf{B}})\right) (2\,\Re(\overline{\epsilon}\mathbf{z}) + |\epsilon|^2) \\
&= f(\mathbf{z}) + \frac{1}{2}\|\mathbf{A} \circ \overline{\mathbf{B}}\|_2^2 (2\,\Re(\overline{\epsilon}\mathbf{z}) + |\epsilon|^2)^2 + \\
&\quad \left(\|\mathbf{A} \circ \overline{\mathbf{B}}\|_2^2 |\mathbf{z}|^2 - \Re\left((\mathbf{A} \circ \overline{\mathbf{B}})^H \mathbf{b}\right)\right) (2\,\Re(\overline{\epsilon}\mathbf{z}) + |\epsilon|^2) \\
&= f(\mathbf{z}) + \frac{1}{2}\|\mathbf{A} \circ \overline{\mathbf{B}}\|_2^2 (2\,\Re(\overline{\epsilon}\mathbf{z}) + |\epsilon|^2)^2,
\end{aligned} \tag{4.57}$$

where the last equality is given by (4.55). As a result,

$$f(\mathbf{z}+\epsilon) - f(\mathbf{z}) = \frac{1}{2}\|\mathbf{A} \circ \overline{\mathbf{B}}\|_2^2 (2\,\Re(\overline{\epsilon}\mathbf{z}) + |\epsilon|^2)^2 \geq 0, \tag{4.58}$$

i.e., $\mathbf{z}$ is a local minimum. □

5 A Hybrid Approach for Pursuit Monostatic Acquisitions

In this short chapter, we develop a framework for single-look differential SAR tomography using pursuit monostatic acquisitions. This framework consists of two consecutive steps: the first one reconstructs the elevation profile from pursuit monostatic interferograms, which is essentially a special case of single-look multi-master SAR tomography (see Sec. 4.1); the second one uses the previous elevation estimates as deterministic prior for estimating scatterers' motion parameters from all acquisitions, which is a variant of single-look single-master SAR tomography (see Sec. 3.1).

This framework has two advantages. First of all, forming pursuit monostatic interferograms contributes to curtailing APS, to reducing temporal decorrelation of non-PSs, and to diminishing motion-induced phase for single scatterers (see Sec. 4.1). As a result, this leads to better elevation reconstruction, and in turn to more accurate motion estimation. Second of all, the original problem of estimating elevation and motion parameters at the same time can be large-scale (see Sec. 3.1). By means of this divide-and-conquer strategy, its size is downscaled multiplicatively in each step, which improves on the whole the algorithmic efficiency.

In the next two sections, the technical details of the this two-step framework will be elucidated. Sec. 5.3 gives an account of an experiment with the Las Vegas data set (see Sec. 2.2).

5.1 Single-Look Pursuit Monostatic SAR Tomography

Suppose there are a total of $2N$ pursuit monostatic acquisitions. In the first step, we reconstruct the elevation profile from the N pursuit monostatic interferograms (depicted as solid lines in Fig. 5.1). This is in fact a special case of single-look multi-master SAR tomography (see Sec. 4.1). Without loss of generality, let us employ the acquisitions

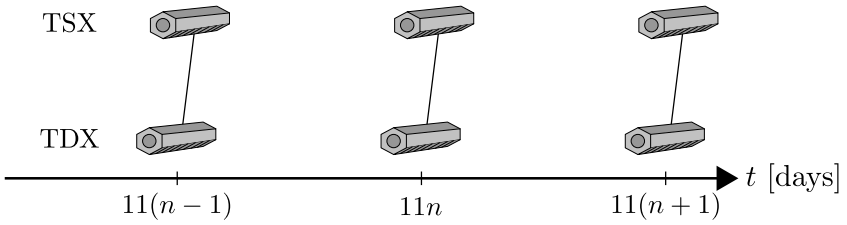

Figure 5.1: Pursuit monostatic interferometric combinations (solid lines) of TanDEM-X acquisitions by the two satellites TSX and TDX.

from one satellite (say TSX) as masters, and the ones from the other (TDX) as slaves. Denote their SLC measurement vectors as $\mathbf{g}$ and $\mathbf{h}$, respectively. The nonconvex sparse recovery problem reads:

$$\begin{aligned} \underset{\boldsymbol{\gamma}}{\text{minimize}} \quad & \frac{1}{2}\|(\mathbf{R}\boldsymbol{\gamma}) \circ (\overline{\mathbf{S}\boldsymbol{\gamma}}) - \mathbf{g} \circ \overline{\mathbf{h}}\|_2^2 \\ \text{subject to} \quad & |\operatorname{Supp}(\boldsymbol{\gamma})| \leq K, \end{aligned} \tag{4.10}$$

where $\mathbf{R}, \mathbf{S} \in \mathbb{C}^{N \times L}$ denote the tomographic sensing matrices of the TSX and TDX acquisitions, respectively. Two algorithms, namely NLS (see Sec. 4.2) and BiCRAM (see Sec. 4.3), have been developed for solving (4.10). Following the nonconvex sparse recovery, model-order selection (4.11) and off-grid correction (4.13) are performed.

5.2 Single-Look Single-Master SAR "Motiography"

In the second step, we estimate scatterers' motion parameters from all the $2N$ acquisitions. Let $\hat{K}$ be the number of scatterers after model-order selection. Let $\hat{s}_l$ denote the elevation estimate of the lth scatterer, $\forall l \in [\hat{K}]$. We utilize this information as deterministic prior for motion parameter estimation. Following the conventions in Sec. 3.1, let ψ_m be the mth motion basis function and $\mathbf{c}_m$ be its discrete motion parameter vector, $\forall m \in [M]$. Denote as a shorthand $\psi_n^m \coloneqq \psi_m(t_n)$. For each scatterer, we build two "motiographic" sensing matrices of the masters and slaves, respectively, i.e., $\mathbf{R}^{(l)}, \mathbf{S}^{(l)} \in \mathbb{C}^{N \times \prod_{m \in [M]} |\mathbf{c}_m|}$, $\forall l \in [\hat{K}]$, whose nth rows are given by (cf. the construction in Sec. 3.1)

$$\begin{aligned} \left(\mathbf{R}^{(l)}\right)^n &\coloneqq \exp(-j\psi^M_{\mathcal{M}(n)}\mathbf{c}_M) \otimes \cdots \otimes \exp(-j\psi^1_{\mathcal{M}(n)}\mathbf{c}_1) \otimes \exp(-jk_{\mathcal{M}(n)}\hat{s}_l), \\ \left(\mathbf{S}^{(l)}\right)^n &\coloneqq \exp(-j\psi^M_{\mathcal{S}(n)}\mathbf{c}_M) \otimes \cdots \otimes \exp(-j\psi^1_{\mathcal{S}(n)}\mathbf{c}_1) \otimes \exp(-jk_{\mathcal{S}(n)}\hat{s}_l), \end{aligned} \tag{5.1}$$

$\forall n \in [N]$, where $\mathcal{M}, \mathcal{S} : [N] \to [2N]$ are the mappings from the interferogram index to the master and slave indices, respectively (see Sec. 4.1). The "motiographic" inverse problem can be formulated as

$$\begin{aligned} \underset{\boldsymbol{\gamma}^{(l)}}{\text{minimize}} \quad & \frac{1}{2}\Big\|\sum_{l \in [\hat{K}]} \mathbf{R}^{(l)}\boldsymbol{\gamma}^{(l)} - \mathbf{g}\Big\|_2^2 + \frac{1}{2}\Big\|\sum_{l \in [\hat{K}]} \mathbf{S}^{(l)}\boldsymbol{\gamma}^{(l)} - \mathbf{h}\Big\|_2^2 \\ \text{subject to} \quad & |\operatorname{Supp}(\boldsymbol{\gamma}^{(l)})| = 1, \ \forall l \in [\hat{K}]. \end{aligned} \tag{5.2}$$

Let $\tilde{\mathbf{R}}^{(l)} \coloneqq (\mathbf{R}^{(l)}, \mathbf{S}^{(l)})$, $\tilde{\mathbf{g}} \coloneqq (\mathbf{g}, \mathbf{h})$. Thereby (5.2) can be written more compactly as

$$\begin{aligned} \underset{\boldsymbol{\gamma}^{(l)}}{\text{minimize}} \quad & \frac{1}{2}\Big\|\sum_{l \in [\hat{K}]} \tilde{\mathbf{R}}^{(l)}\boldsymbol{\gamma}^{(l)} - \tilde{\mathbf{g}}\Big\|_2^2 \\ \text{subject to} \quad & |\operatorname{Supp}(\boldsymbol{\gamma}^{(l)})| = 1, \ \forall l \in [\hat{K}], \end{aligned} \tag{5.3}$$

Table 5.1: Single-master vs. hybrid approach: NLS runtime

	Runtime [s]
Single-Master Tomography	82876
Pursuit Monostatic Tomography	3047
Single-Master "Motiography"	21

Table 5.2: Single-master vs. pursuit monostatic tomography: number of scatterers

	Single	Double	Ratio	Facade
Single-Master	2985	852	3.50	2450
Pursuit Monostatic	2873	1696	1.69	2410

which can be solved by a variant of NLS. Each NLS subproblem boils down to a subset least squares problem in the form of

$$\underset{\tilde{\boldsymbol{\gamma}}}{\text{minimize}}\, \frac{1}{2}\|\tilde{\mathbf{R}}\tilde{\boldsymbol{\gamma}} - \tilde{\mathbf{g}}\|_2^2, \tag{5.4}$$

where $\tilde{\gamma}_l$ and $\tilde{\mathbf{r}}_l$ correspond to the lth scatterer, $\forall l \in [\hat{K}]$.

5.3 Experiment and Assessment

As a demonstration, we applied the proposed hybrid approach to the Las Vegas data set (see Sec. 2.2). Due to the rather short time span of 132 days, we employed a sinusoidal basis function for modeling periodical motion induced by temperature change. For the single-look pursuit monostatic SAR tomography (see Sec. 5.1), the NLS algorithm from Sec. 4.2 was used.

As a comparison, Fig. 5.2 shows the height and periodical motion amplitude estimated with the single-master approach using conventional NLS. The estimates with the hybrid approach are shown in Fig. 5.3. These results seem quite similar, despite the fact that the uppermost part of the facade and roof of the building are missing in the former. We suspect that the high-rise building bent at different angles in the wind on different days of acquisition, which led to decorrelation in the single-master interferograms. In addition, the hybrid approach was computationally less expensive due to its inherent divide-and-conquer nature, as can be observed in Tab. 5.1. Tab. 5.2 provides the number of scatterers in both cases.

In order to access the quality of the reconstructed point cloud, we adopted the following strategy. First of all, we transformed each point cloud of single scatterers from SAR into Universal Transverse Mercator (UTM) coordinates. Subsequently, we extracted the facade segment by thresholding of the 2-D point density. Afterwards, we fitted a vertical plane into the extracted facade segment with an ℓ_1 loss function, and considered

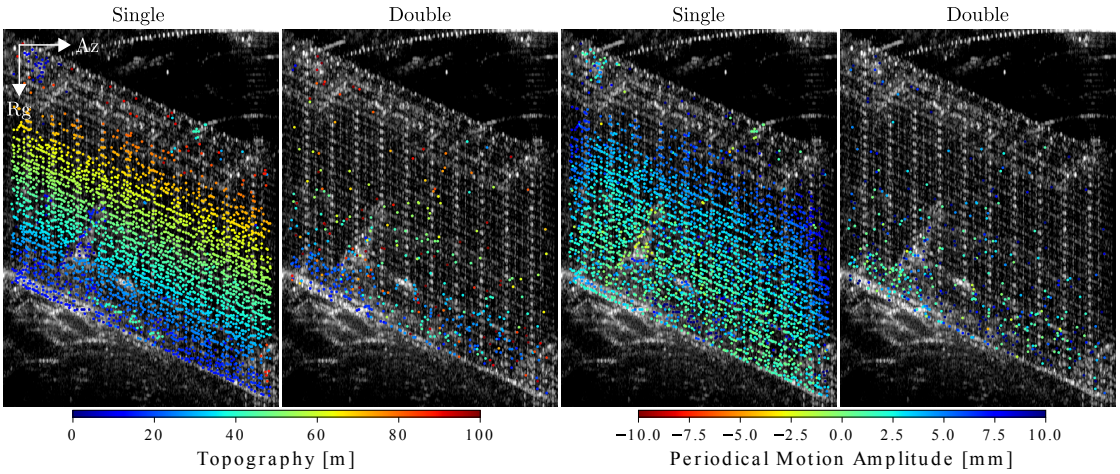

Figure 5.2: Single-master approach: estimated height and periodical motion amplitude. In the case of double scatterers, the higher one is shown.

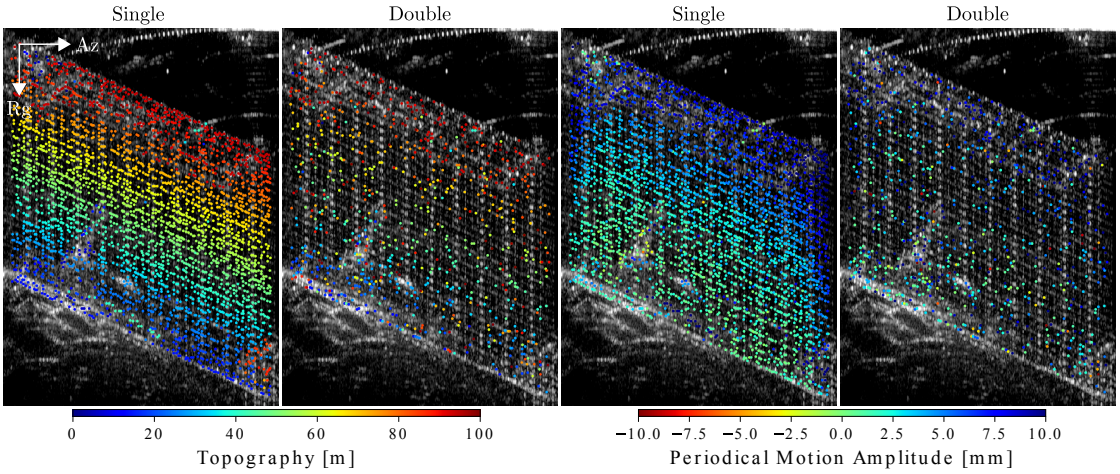

Figure 5.3: Hybrid approach: estimated height and periodical motion amplitude. In the case of double scatterers, the higher one is shown.

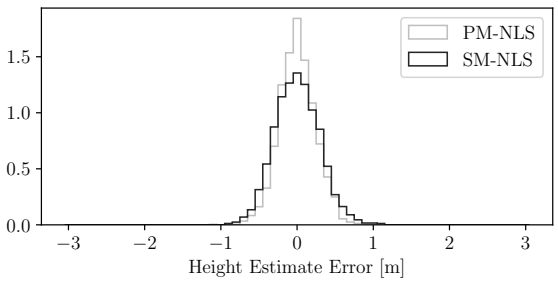

Figure 5.4: Normalized histogram of height estimate error relative to a fitted vertical plane. PM: pursuit monostatic. SM: single-master.

Table 5.3: Single-master vs. pursuit monostatic tomography: height estimate error [m]

	Min	Max	Mean	Median	SD	MAD
Single-Master	−0.87	1.11	0.00	0.00	0.29	0.29
Pursuit Monostatic	−1.09	0.97	0.00	0.00	0.24	0.23

it as a reference. For each point, we calculated its signed distance to the fitted plane, and projected it into the vertical direction. We refer to this projected distance as the height estimate error relative to the fitted vertical plane. The number of points in each facade segment is given in the rightmost column of Tab. 5.2. Fig. 5.4 illustrates the normalized histogram of the height estimate error, whose statistical parameters are listed in Tab. 5.3. Although the two histograms have very similar sample sizes and are both centered around zero, the pursuit monostatic one has slightly less deviation, which can also be visually observed.

The next chapter summarizes this dissertation, and suggests some follow-on research topics.

6 Summary and Outlook

The preceding chapters are centered around a few sparse recovery problems in spaceborne SAR tomography with a focus on urban scenarios.

In the *single-look single-master* setting, a common approach involves solving a large-scale L1RLS problem. Despite its popularity, first-order methods are often plagued by convergence issues due to the notoriously ill-conditioned tomographic sensing matrix. In order to resolve this problem, we developed an accelerated algorithm based on the ADMM. In particular, we applied the matrix inversion lemma so as to facilitate the primal variable update, which is the most computationally expensive step in this alternating algorithm. Besides, we experimented with three different acceleration techniques, namely varying penalty parameter, diagonal preconditioning, and over-relaxation, as well as their combinations. We showed empirically that these techniques did contribute to improving convergence as applied to real tomographic SAR data, and the combination of diagonal preconditioning and over-relaxation provided the most acceleration among all. The outcome of this experiment has very high practical importance, since it shows the feasibility of using sparse recovery in large-area processing. Another equally important issue of L1RLS or any other regularized sparse recovery problem is the tuning of regularization parameter. In order to gain more insight, we inspected it from the viewpoint of bi-criterion optimization. Based on a known theorem in the more general vector optimization, each solution associated with a fixed regularization parameter is essentially a Pareto optimal point of the bi-criterion optimization problem, and a partial converse exists as well. In light of this, we proposed to sample the optimal trade-off curve, and to choose the one with the largest penalized likelihood after off-grid correction. This heuristic is in general directly applicable to any regularized optimization problem. Last but not least, we showed that the CRLB of elevation estimates, given that scatterers' motion can be described by a single basis function, is in fact the motion-free version scaled by a simple function of the correlation coefficient between the wavenumber and motion basis function.

In the *multi-look single-master* configuration, we considered the problem of jointly reconstructing different looks containing scatterers located at the same elevation position, albeit possibly subject to different motion patterns. We formulated this as a joint tensor mode recovery problem, i.e., we enforced scatterers to align only in the first mode or elevation, which still allowed them to have different motion parameters. We showed that the resulted JTMRLS is equivalent to a GSRLS problem, for which we developed an algorithm based on the ADMM. We applied this algorithm to a real SAR tomographic data set that satisfies the aforementioned requirement. The experiment confirmed the validity of our approach: the jointly reconstructed elevation had less deviation, and the motion parameter estimation stayed unaffected.

Many pages were dedicated to the study of *single-look multi-master* SAR tomography. We established the single-look multi-master data model in the first place. For any single scatterer, this model implies that the single-look multi-master observation is, as a matter of fact, the Fourier transform of its power at the wavenumber baseline. As a result, the nonnegativity of the power needs to be taken into account during tomographic inversion, and the inverse problem can be recast as a real-valued one. For double scatterers, the single-look multi-master observation contains additional cross-terms of scatterers' reflectivity and their wavenumber-elevation-products, which indicates a nonlinear model for SAR tomography. We also showed that any single-look bistatic interferogram is in general not motion-free in the case of layover. Based on the single-look multi-master data model, we proposed a generic framework for tomographic inversion, which consists of nonconvex sparse recovery, model-order selection, and off-grid correction. For nonconvex sparse recovery, we developed two algorithms, namely, NLS and BiCRAM.

- In the former, the conventional NLS was extended to the single-look multi-master data model. For solving the NLS subproblems, we developed two algorithms based on the ADMM and the trust-region Newton's method, respectively. The development of the first one was straightforward, while that of the second one was less so, since the objective function of any NLS subproblem is not complex differentiable. In order to circumvent this issue, we exploited the fact that the mapping from a complex-valued vector to its real and imaginary parts is isomorphic and viewed the objective function as one of two real-valued vectors. By means of this trick, we derived analytically the gradient and Hessian of the objective function, so that any first- or second-order method can be employed. We showed empirically that the algorithm based on the trust-region Newton's method often converged with extremely high precision in a few iterations. We went on and proved two insightful theorems regarding the critical points of the objective function for the general and special (1-D) cases, respectively.
  - In the general case, zero is always a critical point. More specifically, whether it is a local minimum or maximum depends on whether a quantity is negative or positive definite. That the same quantity is not negative definite is in fact a sufficient condition for the existence of any nonzero critical point. If there exists a nonzero critical point, then its Hessian is always rank deficient (implying that the Hessian cannot be used to determine whether any nonzero critical point is a local minimum or maximum), and an infinite number of critical points along a circle exist as well.
  - The theorem for the special case turned out to be much stronger. In addition to the results already implied by the first theorem, that a quantity is positive is a necessary and sufficient condition for the existence of any nonzero critical point. If there exists one nonzero critical point, then its rank deficient Hessian is also positive semi-definite, and this point is certainly a local minimum.

  A corollary of the second theorem provides, given that the previously mentioned condition is satisfied, the expression of any nonzero local minimum, which is also

the analytical solution of the NLS subproblem in the special case. This motivates in turn a 1-D spectral estimator for single-look multi-master SAR tomography.

- The latter is closely related to a variant of the L1RLS problem, whose optimality condition is always satisfied by zero. Due to the nonconvexity of this problem and the very high mutual coherence of tomographic sensing matrices, an algorithm directly based on the ADMM was found to often diverge. For this reason, we applied bi-convex relaxation and introduced an auxiliary variable. We replaced the regularization term by two terms: one enforces the two variables to have similar entries, and the other promotes them to share the same support. We developed an alternating algorithm for solving this relaxed bi-convex problem, whose two subproblems share the same form of a convex problem that can be solved by an ADMM-based algorithm. We showed empirically that this alternating algorithm converged with real SAR tomographic data.

We designed a delicate experiment in order to demonstrate the feasibility of the proposed framework. This experiment consists of three single-look interferometric stacks: a single-master one, a multi-master one comprising interferograms of small time intervals, and a duplicate of the multi-master one that we treated as if it had been a single-master one (by purposely mistaking the multi-master wavenumber difference for the single-master wavenumber baseline). For the first and third stacks, we applied NLS and L1RLS to reconstruct the elevation profile. For the second stack, NLS and BiCRAM were employed. The ADMM-based sparse recovery algorithms were augmented with diagonal preconditioning and over-relaxation. In terms of solution path sampling, the range of regularization parameter and the number of samples were given. The experiment can be divided into two parts.

- In the first part of the experiment, we tried to reconstruct the elevation profiles of six looks subject to roof-facade layover and chosen in a systematic way. According to the results of the single-master stack, the elevation distance decreases from approximately 1.5 to 0.8 times the Rayleigh resolution in these six looks. This agrees very well with the locations of the looks, since their range distances are also in a predominantly increasing order. In each of the three settings, namely single-mater, multi-master and fake single-master, the corresponding two algorithms produced almost identical elevation estimates after off-grid correction. The results in the single- and multi-master settings are consistent with each other, and the elevation estimates of the lower scatterers agree very well with the facade predications made available via a SAR imaging geodesy and simulation framework. In the fake single-master setting, layover separation only succeeded in one of the six looks. When the elevation distance is significantly larger than the Rayleigh resolution, both algorithms could produce two scatterers, but only the one with the larger amplitude could pass model-order selection. As the elevation distance draws near to the Rayleigh resolution or becomes even smaller, neither algorithm could deliver a second scatterer, and the elevation estimates of the single scatterers are also arguably wrong in comparison to the facade predications. This simple experiment

shows that the single-master approach, if mistakenly applied to a multi-master stack, can be insufficient for layover separation.

- The second part of the experiment involves tomographic reconstruction of all the looks within a building footprint. The validation of the elevation estimates with facade predications were divided into two cases. In one case, we employed directly the height simulations of 30 PSs located on the building facade. In the other, we had to perform a segmentation of the single scatterers first in order to discard the ones located on the building roof. In both cases, the multi-master approach slightly outperformed the fake single-master one, despite being computationally more expensive by approximately one order. This shows empirically that the single-look multi-master data model does make a difference, albeit small, even for single scatterers in real data processing.

The aforementioned two single-look approaches were merged in a hybrid approach for pursuit monostatic acquisitions. We developed a generic framework that splits the original problem of estimating scatterers' elevation and motion into two consecutive steps: in the first step, we estimate scatterers' elevation from only pursuit monostatic interferograms, which is a special case of single-look multi-master SAR tomography; in the second step, we incorporate the previous elevation estimates as deterministic prior into the tomographic sensing matrix for motion parameter estimation, which is a variant of single-look single-master SAR tomography. The advantages of this divide-and-conquer strategy are two-fold: 1) In comparison to conventional repeat-pass interferograms, pursuit monostatic ones are much less affected by APS, temporal decorrelation and motion. They are therefore more suitable for elevation reconstruction. 2) In each step, the dimension of the original problem is downscaled by a multiplicative factor, which improves the algorithmic efficiency. We applied this framework to a real SAR data set. As a comparison, we also employed the conventional single-look single-master approach. Their results are quite similar, except that the latter could not reconstruct the uppermost part of the facade or the roof, which we attributed to decorrelation due to different wind speeds in repeat-pass acquisitions. In addition, we accessed the quality of each tomographic point cloud by fitting a vertical plane into it. The height estimate error relative to this fitted plane has slightly less deviation in the pursuit monostatic setting, which is consistent with our findings in the more general single-look multi-master SAR tomography. As a final note, this framework is directly applicable to bi- or multistatic acquisitions.

Lastly, we state three follow-on research topics that are motivated by this dissertation.

(1) *Single-Look Single-Master SAR Tomography: Sparse Low-Rank Tensor Recovery* Following the conventions in Sec. 3.1, suppose scatterers' motion can be decomposed into a linear combination of M basis functions. Denote the mth basis function as ψ_m, and $\psi_m(t_n) \coloneqq \psi_n^m$, $\forall m \in [M]$. Let

$$\mathbf{u}_n \coloneqq \exp(-jk_n\mathbf{s}), \quad \mathbf{v}_n^{(m)} \coloneqq \exp(-j\psi_n^m\mathbf{c}_m), \tag{6.1}$$

$\forall m \in [M]$, $n \in [N]$. Define $d_1 \coloneqq |\mathbf{s}|$, and $d_m \coloneqq |\mathbf{c}_{m-1}|$, $\forall m \in [M+1] \setminus \{1\}$. Motivated by the JTMRLS problem in Sec. 3.2, the discrete reflectivity vector

in (3.5) is essentially an $(M+1)$-way tensor $\boldsymbol{\mathcal{X}} \in \mathbb{C}^{d_1 \times d_2 \times \ldots \times d_{M+1}}$, and the linear model (1.2) can be expressed elementwise by using the tensor n-mode products [79]:

$$g_n \approx \boldsymbol{\mathcal{X}} \times_1 \mathbf{u}_n \times_2 \mathbf{v}_n^{(1)} \times_3 \cdots \times_{M+1} \mathbf{v}_n^{(M)}, \quad \forall n \in [N]. \tag{6.2}$$

Under the assumption that the discrete reflectivity vector is K-sparse, $\boldsymbol{\mathcal{X}}$ can be decomposed into a sum of sparse rank-one tensors [79], i.e.,

$$\boldsymbol{\mathcal{X}} = \sum_{l \in [K]} \gamma_l \boldsymbol{\chi}_l^{(1)} \otimes \boldsymbol{\chi}_l^{(2)} \otimes \cdots \otimes \boldsymbol{\chi}_l^{(M+1)}, \tag{6.3}$$

where γ_l denotes the reflectivity of the lth scatterer, $\boldsymbol{\chi}_l^{(m)}$ is a unit vector in the standard basis $\mathbb{S}^{d_m}$, $\forall l \in [K]$, $m \in [M+1]$, and $\otimes$ denotes the outer product (not to be confused with the Kronecker product in Sec. 3.1). Fig. 6.1 illustrates such a sparse low-rank tensor and its decomposition. Combining these two equations leads to

$$g_n \approx \sum_{l \in [K]} \gamma_l \langle \mathbf{u}_n, \boldsymbol{\chi}_l^{(1)} \rangle \langle \mathbf{v}_n^{(1)}, \boldsymbol{\chi}_l^{(2)} \rangle \cdots \langle \mathbf{v}_n^{(M)}, \boldsymbol{\chi}_l^{(M+1)} \rangle, \quad \forall n \in [N]. \tag{6.4}$$

Consider for example the following sparse low-rank tensor recovery problem:

$$\begin{aligned} \underset{\gamma_l, \boldsymbol{\chi}_l^{(m)}}{\text{minimize}} \quad & \frac{1}{2} \sum_{n \in [N]} |g_n - \sum_{l \in [K]} \gamma_l \langle \mathbf{u}_n, \boldsymbol{\chi}_l^{(1)} \rangle \langle \mathbf{v}_n^{(1)}, \boldsymbol{\chi}_l^{(2)} \rangle \cdots \langle \mathbf{v}_n^{(M)}, \boldsymbol{\chi}_l^{(M+1)} \rangle|^2 \\ \text{subject to} \quad & \boldsymbol{\chi}_l^{(m)} \in \mathbb{S}^{d_m}, \ \forall l \in [K], \ m \in [M+1]. \end{aligned} \tag{6.5}$$

In comparison to the original sparse (vector) recovery problem, this one has clearly a smaller scale: instead of the $\prod_{m \in [M+1]} d_m$ entries in the $(M+1)$-way tensor, one only needs to estimate $K + K \sum_{m \in [M+1]} d_m$ scalars.

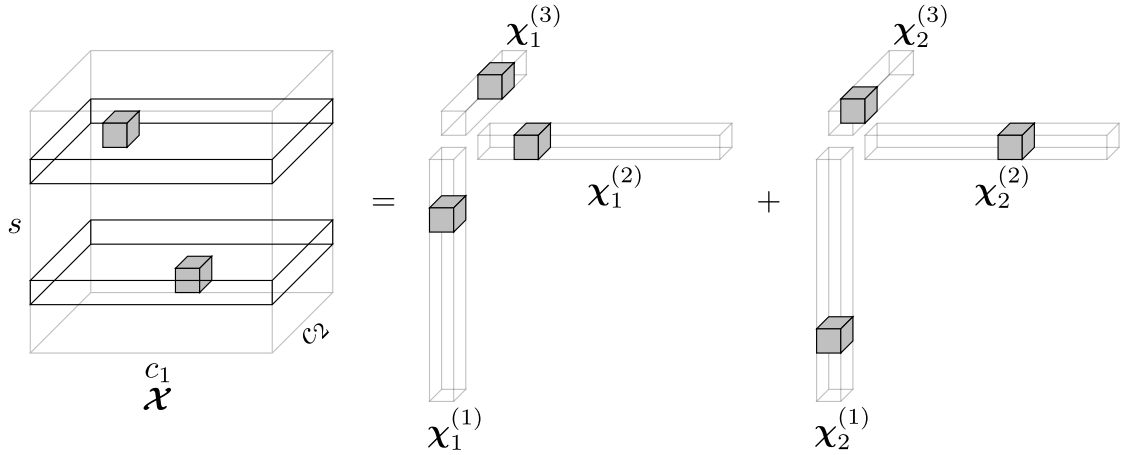

Figure 6.1: Discrete reflectivity tensor $\boldsymbol{\mathcal{X}}$ that can be decomposed into a sum of two rank-one sparse tensors with $\gamma_1 = \gamma_2 = 1$.

(2) *Single-Look Pursuit Monostatic SAR Tomography: An Alternative Problem*
Alternatively, we can parameterize the acquisition-specific phase artifacts including but not limited to APS without forming any interferogram (cf. (4.10)). Denote the SLC measurement vectors of the masters and slaves as $\mathbf{g}$ and $\mathbf{h}$, respectively. These can be treated as two correlated data sets, i.e.,

$$\mathbf{g} \approx (\mathbf{R}\boldsymbol{\gamma}) \circ \exp(j\boldsymbol{\phi}), \quad \mathbf{h} \approx (\mathbf{S}\boldsymbol{\gamma}) \circ \exp(j\boldsymbol{\phi}), \tag{6.6}$$

where $\boldsymbol{\phi} \in \mathbb{R}^{N'}$ is the phase artifact vector. Under the compressibility assumption of $\boldsymbol{\gamma}$, consider the following bi-convex sparse recovery problem:

$$\underset{\boldsymbol{\gamma},\boldsymbol{\phi}}{\text{minimize}} \frac{1}{2}\|(\mathbf{R}\boldsymbol{\gamma}) \circ \exp(j\boldsymbol{\phi}) - \mathbf{g}\|_2^2 + \frac{1}{2}\|(\mathbf{S}\boldsymbol{\gamma}) \circ \exp(j\boldsymbol{\phi}) - \mathbf{h}\|_2^2 + \lambda\|\boldsymbol{\gamma}\|_1, \tag{6.7}$$

or more compactly

$$\underset{\boldsymbol{\gamma},\boldsymbol{\phi}}{\text{minimize}} \frac{1}{2}\|(\tilde{\mathbf{R}}\boldsymbol{\gamma}) \circ (\tilde{\mathbf{I}}\exp(j\boldsymbol{\phi})) - \tilde{\mathbf{g}}\|_2^2 + \lambda\|\boldsymbol{\gamma}\|_1, \tag{6.8}$$

where $\tilde{\mathbf{R}} \coloneqq (\mathbf{R}, \mathbf{S})$, $\tilde{\mathbf{I}} \coloneqq (\mathbf{I}, \mathbf{I})$, and $\tilde{\mathbf{g}} \coloneqq (\mathbf{g}, \mathbf{h})$.

(3) *Multi-Look Single-Master SAR Tomography: A Graph-Based Approach*
A related problem is SAR tomography on edges, as inspired by PSI. Likewise, the rationale is to form interferometric combinations between neighboring looks in order to mitigate acquisition-specific phase artifacts such as APS. Suppose we have an acyclic directed graph consisting of different looks as vertices and edges connecting them. For any two neighboring looks that are connected via an edge, denote their tomographic sensing matrices as $\mathbf{R}$ and $\mathbf{S}$, their discrete reflectivity vectors as $\boldsymbol{\gamma}$ and $\boldsymbol{\theta}$, and their SLC measurement vectors as $\mathbf{g}$ and $\mathbf{h}$, respectively. Consider the following bi-convex sparse recovery problem:

$$\underset{\boldsymbol{\gamma},\boldsymbol{\theta}}{\text{minimize}} \frac{1}{2}\|(\mathbf{R}\boldsymbol{\gamma}) \circ (\overline{\mathbf{S}\boldsymbol{\theta}}) - \mathbf{g} \circ \overline{\mathbf{h}}\|_2^2 + \lambda_1\|\boldsymbol{\gamma}\|_1 + \lambda_2\|\boldsymbol{\theta}\|_1, \tag{6.9}$$

where $\lambda_1, \lambda_2 \in \mathbb{R}_{++}$ are regularization parameters.

This marks the end of this dissertation.

Bibliography

[1] S. Auer, C. Gisinger, N. Ge, F. R. Gonzalez, and X. X. Zhu. SIGS: A SAR imaging geodesy and simulation framework for generating 3-D ground truth. *In preparation.*

[2] A. Reigber and A. Moreira. First demonstration of airborne SAR tomography using multibaseline L-band data. *IEEE Transactions on Geoscience and Remote Sensing*, 38(5):2142–2152, 2000.

[3] F. Gini, F. Lombardini, and M. Montanari. Layover solution in multibaseline SAR interferometry. *IEEE Transactions on Aerospace and Electronic Systems*, 38(4):1344–1356, 2002.

[4] G. Fornaro, F. Serafino, and F. Soldovieri. Three-dimensional focusing with multipass SAR data. *IEEE Transactions on Geoscience and Remote Sensing*, 41(3):507–517, 2003.

[5] A. Ferretti, C. Prati, and F. Rocca. Permanent scatterers in SAR interferometry. *IEEE Transactions on Geoscience and Remote Sensing*, 39(1):8–20, 2001.

[6] C. Colesanti, A. Ferretti, F. Novali, C. Prati, and F. Rocca. SAR monitoring of progressive and seasonal ground deformation using the permanent scatterers technique. *IEEE Transactions on Geoscience and Remote Sensing*, 41(7):1685–1701, 2003.

[7] N. Adam, B. Kampes, and M. Eineder. Development of a scientific permanent scatterer system: Modifications for mixed ERS/ENVISAT time series. In *Envisat & ERS Symposium*, volume 572, 2005.

[8] G. Fornaro, F. Lombardini, and F. Serafino. Three-dimensional multipass SAR focusing: Experiments with long-term spaceborne data. *IEEE Transactions on Geoscience and Remote Sensing*, 43(4):702–714, 2005.

[9] R. Werninghaus and S. Buckreuss. The TerraSAR-X mission and system design. *IEEE Transactions on Geoscience and Remote Sensing*, 48(2):606–614, 2009.

[10] H. Breit, T. Fritz, U. Balss, M. Lachaise, A. Niedermeier, and M. Vonavka. TerraSAR-X SAR processing and products. *IEEE Transactions on Geoscience and Remote Sensing*, 48(2):727–740, 2009.

[11] W. Pitz and D. Miller. The TerraSAR-X satellite. *IEEE Transactions on Geoscience and Remote Sensing*, 48(2):615–622, 2010.

[12] Y. T. Yoon, M. Eineder, N. Yague-Martinez, and O. Montenbruck. TerraSAR-X precise trajectory estimation and quality assessment. *IEEE Transactions on Geoscience and Remote Sensing*, 47(6):1859–1868, 2009.

[13] R. Bamler, M. Eineder, N. Adam, X. Zhu, and S. Gernhardt. Interferometric potential of high resolution spaceborne SAR. *Photogrammetrie-Fernerkundung-Geoinformation*, 2009(5):407–419, 2009.

[14] E. Dilaveroglu. Nonmatrix Cramér-Rao bound expressions for high-resolution frequency estimators. *IEEE Transactions on Signal Processing*, 46(2):463–474, 1998.

[15] X. X. Zhu and R. Bamler. Super-resolution power and robustness of compressive sensing for spectral estimation with application to spaceborne tomographic SAR. *IEEE Transactions on Geoscience and Remote Sensing*, 50(1):247–258, 2011.

[16] G. Fornaro, D. Reale, and F. Serafino. Four-dimensional SAR imaging for height estimation and monitoring of single and double scatterers. *IEEE Transactions on Geoscience and Remote Sensing*, 47(1):224–237, 2008.

[17] X. X. Zhu and R. Bamler. Very high resolution spaceborne SAR tomography in urban environment. *IEEE Transactions on Geoscience and Remote Sensing*, 48(12):4296–4308, 2010.

[18] X. X. Zhu and R. Bamler. Sparse tomographic SAR reconstruction from mixed TerraSAR-X/TanDEM-X data stacks. In *2012 IEEE International Geoscience and Remote Sensing Symposium*, pages 7468–7471. IEEE, 2012.

[19] E. Aguilera, M. Nannini, and A. Reigber. Multisignal compressed sensing for polarimetric SAR tomography. *IEEE Geoscience and Remote Sensing Letters*, 9(5):871–875, 2012.

[20] M. Schmitt and U. Stilla. Compressive sensing based layover separation in airborne single-pass multi-baseline InSAR data. *IEEE Geoscience and Remote Sensing Letters*, 10(2):313–317, 2012.

[21] L. Liang, X. Li, L. Ferro-Famil, H. Guo, L. Zhang, and W. Wu. Urban area tomography using a sparse representation based two-dimensional spectral analysis technique. *Remote Sensing*, 10(1):109, 2018.

[22] Y. Shi, X. X. Zhu, and R. Bamler. Nonlocal compressive sensing-based SAR tomography. *IEEE Transactions on Geoscience and Remote Sensing*, 57(5):3015–3024, 2019.

[23] D. Perissin and T. Wang. Repeat-pass SAR interferometry with partially coherent targets. *IEEE Transactions on Geoscience and Remote Sensing*, 50(1):271–280, 2011.

[24] A. Ferretti, A. Fumagalli, F. Novali, C. Prati, F. Rocca, and A. Rucci. A new algorithm for processing interferometric data-stacks: SqueeSAR. *IEEE Transactions on Geoscience and Remote Sensing*, 49(9):3460–3470, 2011.

[25] A. Parizzi and R. Brcic. Adaptive InSAR stack multilooking exploiting amplitude statistics: A comparison between different techniques and practical results. *IEEE Geoscience and Remote Sensing Letters*, 8(3):441–445, 2010.

[26] H. Ansari, F. De Zan, and R. Bamler. Sequential estimator: Toward efficient InSAR time series analysis. *IEEE Transactions on Geoscience and Remote Sensing*, 55(10):5637–5652, 2017.

[27] H. Ansari, F. De Zan, and R. Bamler. Efficient phase estimation for interferogram stacks. *IEEE Transactions on Geoscience and Remote Sensing*, 56(7):4109–4125, 2018.

[28] F. Lombardini. Differential tomography: A new framework for SAR interferometry. *IEEE Transactions on Geoscience and Remote Sensing*, 43(1):37–44, 2005.

[29] S. Duque, P. López-Dekker, J. J. Mallorquí, A. Y. Nashashibi, and A. M. Patel. Experimental results with bistatic SAR tomography. In *2009 IEEE International Geoscience and Remote Sensing Symposium*, volume 2, pages II–37. IEEE, 2009.

[30] S. Duque, P. López-Dekker, J. C. Merlano, and J. J. Mallorquí. Bistatic SAR tomography: Processing and experimental results. In *2010 IEEE International Geoscience and Remote Sensing Symposium*, pages 154–157. IEEE, 2010.

[31] S. Duque, C. Rossi, and T. Fritz. Single-pass tomography with alternating bistatic TanDEM-X data. *IEEE Geoscience and Remote Sensing Letters*, 12(2):409–413, 2014.

[32] G. Fornaro, S. Verde, D. Reale, and A. Pauciullo. CAESAR: An approach based on covariance matrix decomposition to improve multibaseline–multitemporal interferometric SAR processing. *IEEE Transactions on Geoscience and Remote Sensing*, 53(4):2050–2065, 2014.

[33] S. R. Cloude. Polarization coherence tomography. *Radio Science*, 41(4), 2006.

[34] F. De Zan, K. Papathanassiou, and S. Lee. Tandem-L forest parameter performance analysis. In *Proceedings of International Workshop on Applications of Polarimetry and Polarimetric Interferometry, Frascati, Italy*, pages 1–6. Citeseer, 2009.

[35] S. Tebaldini. Algebraic synthesis of forest scenarios from multibaseline PolInSAR data. *IEEE Transactions on Geoscience and Remote Sensing*, 47(12):4132–4142, 2009.

[36] S. Tebaldini. Single and multipolarimetric SAR tomography of forested areas: A parametric approach. *IEEE Transactions on Geoscience and Remote Sensing*, 48(5):2375–2387, 2010.

[37] Y. Huang, L. Ferro-Famil, and A. Reigber. Under-foliage object imaging using SAR tomography and polarimetric spectral estimators. *IEEE Transactions on Geoscience and Remote Sensing*, 50(6):2213–2225, 2011.

[38] S.-K. Lee and T. E. Fatoyinbo. TanDEM-X Pol-InSAR inversion for mangrove canopy height estimation. *IEEE Journal of Selected Topics in Applied Earth Observations and Remote Sensing*, 8(7):3608–3618, 2015.

[39] M. Pardini and K. Papathanassiou. On the estimation of ground and volume polarimetric covariances in forest scenarios with SAR tomography. *IEEE Geoscience and Remote Sensing Letters*, 14(10):1860–1864, 2017.

[40] V. Cazcarra-Bes, M. Pardini, M. Tello, and K. P. Papathanassiou. Comparison of tomographic SAR reflectivity reconstruction algorithms for forest applications at L-band. *IEEE Transactions on Geoscience and Remote Sensing*, 2019.

[41] X. X. Zhu and R. Bamler. Demonstration of super-resolution for tomographic SAR imaging in urban environment. *IEEE Transactions on Geoscience and Remote Sensing*, 50(8):3150–3157, 2011.

[42] X. X. Zhu, N. Ge, and M. Shahzad. Joint sparsity in SAR tomography for urban mapping. *IEEE Journal of Selected Topics in Signal Processing*, 9(8):1498–1509, 2015.

[43] A. Moreira, G. Krieger, I. Hajnsek, K. Papathanassiou, M. Younis, P. Lopez-Dekker, S. Huber, M. Villano, M. Pardini, M. Eineder, et al. Tandem-L: A highly innovative bistatic SAR mission for global observation of dynamic processes on the Earth's surface. *IEEE Geoscience and Remote Sensing Magazine*, 3(2):8–23, 2015.

[44] G. Krieger, A. Moreira, H. Fiedler, I. Hajnsek, M. Werner, M. Younis, and M. Zink. TanDEM-X: A satellite formation for high-resolution SAR interferometry. *IEEE Transactions on Geoscience and Remote Sensing*, 45(11):3317–3341, 2007.

[45] P. Rizzoli, M. Martone, C. Gonzalez, C. Wecklich, D. B. Tridon, B. Bräutigam, M. Bachmann, D. Schulze, T. Fritz, M. Huber, et al. Generation and performance assessment of the global TanDEM-X digital elevation model. *ISPRS Journal of Photogrammetry and Remote Sensing*, 132:119–139, 2017.

[46] N. Gebert, B. C. Dominguez, M. W. Davidson, M. D. Martin, and P. Silvestrin. SAOCOM-CS-A passive companion to SAOCOM for single-pass L-band SAR interferometry. In *EUSAR 2014; 10th European Conference on Synthetic Aperture Radar*, pages 1–4. VDE, 2014.

[47] P. López-Dekker, H. Rot, S. Solberg, M. Zonno, M. Rodriguez-Cassola, P. Prats-Iraola, and A. Moreira. Companion SAR constellations for single-pass interferometric applications: The SESAME mission. In *2017 IEEE International Geoscience and Remote Sensing Symposium (IGARSS)*, pages 119–122. IEEE, 2017.

[48] D. Giudici, D. Mapelli, and F. Rocca. Exploring the potential of Sentinel-1 constellation in tandem and bi-static configurations. In *EUSAR 2018: 12th European Conference on Synthetic Aperture Radar*, pages 1–6. VDE, 2018.

[49] M. Bartusch. HRWS high resolution wide swath: The next national X-band SAR mission. In *Proc. TerraSAR-X/TanDEM-X Sci. Team Meeting*, pages 17–20, 2016.

[50] J. Janoth, M. Jochum, and A. Kaptein. The High Resolution Wide Swath mission and WorldSAR. In *Proc. 37th Int. Symp. Remote Sensors Environ.(ISRSE)*, 2017.

[51] G. Krieger, M. Zonno, M. Rodriguez-Cassola, P. Lopez-Dekker, J. Mittermayer, M. Younis, S. Huber, M. Villano, F. Q. de Almeida, P. Prats-Iraola, et al. MirrorSAR: A fractionated space radar for bistatic, multistatic and high-resolution wide-swath SAR imaging. In *2017 IEEE International Geoscience and Remote Sensing Symposium (IGARSS)*, pages 149–152. IEEE, 2017.

[52] G. Krieger, M. Zonno, J. Mittermayer, A. Moreira, S. Huber, and M. Rodriguez-Cassola. MirrorSAR: A fractionated space transponder concept for the implementation of low-cost multistatic SAR missions. In *EUSAR 2018: 12th European Conference on Synthetic Aperture Radar*, pages 1–6. VDE, 2018.

[53] M. Zonno, G. Krieger, M. Rodriguez-Cassola, J. Mittermayer, and A. Moreira. A MirrorSAR-based single-pass dual-baseline SAR interferometer for the generation of very high quality DEMs. In *EUSAR 2018: 12th European Conference on Synthetic Aperture Radar*, pages 1–6. VDE, 2018.

[54] H. Ansari, K. Goel, A. Parizzi, F. De Zan, N. Adam, and M. Eineder. Tandem-L performance analysis for three dimensional earth deformation monitoring. In *2015 IEEE International Geoscience and Remote Sensing Symposium (IGARSS)*, pages 4053–4056. IEEE, 2015.

[55] G. Krieger, A. Moreira, M. Zink, I. Hajnsek, S. Huber, M. Villano, K. Papathanassiou, M. Younis, P. L. Dekker, M. Pardini, et al. Tandem-L: Main results of the phase a feasibility study. In *2016 IEEE International Geoscience and Remote Sensing Symposium (IGARSS)*, pages 2116–2119. IEEE, 2016.

[56] P. Prats-Iraola, P. Lopez-Dekker, F. De Zan, N. Yagüe-Martínez, M. Zonno, and M. Rodriguez-Cassola. Performance of 3-D surface deformation estimation for simultaneous squinted SAR acquisitions. *IEEE Transactions on Geoscience and Remote Sensing*, 56(4):2147–2158, 2017.

[57] S. Suchandt, A. Pleskachevsky, and D. B. Tridon. Oceanographic data retrieval with Tandem-L. In *EUSAR 2018: 12th European Conference on Synthetic Aperture Radar*, pages 1–4. VDE, 2018.

[58] N. Adam, F. R. Gonzalez, A. Parizzi, and R. Brcic. Wide area persistent scatterer interferometry: current developments, algorithms and examples. In *2013 IEEE*

International Geoscience and Remote Sensing Symposium-IGARSS, pages 1857–1860. IEEE, 2013.

[59] F. R. Gonzalez, N. Adam, A. Parizzi, and R. Brcic. The integrated wide area processor (IWAP): A processor for wide area persistent scatterer interferometry. In *ESA Living Planet Symposium*, volume 722, page 353, 2013.

[60] S. J. Auer. *3D synthetic aperture radar simulation for interpreting complex urban reflection scenarios*. PhD thesis, Technische Universität München, 2011.

[61] M. Eineder, C. Minet, P. Steigenberger, X. Cong, and T. Fritz. Imaging geodesy—toward centimeter-level ranging accuracy with TerraSAR-X. *IEEE Transactions on Geoscience and Remote Sensing*, 49(2):661–671, 2010.

[62] C. Gisinger, U. Balss, R. Pail, X. X. Zhu, S. Montazeri, S. Gernhardt, and M. Eineder. Precise three-dimensional stereo localization of corner reflectors and persistent scatterers with TerraSAR-X. *IEEE Transactions on Geoscience and Remote Sensing*, 53(4):1782–1802, 2014.

[63] S. Hackel, C. Gisinger, U. Balss, M. Wermuth, and O. Montenbruck. Long-term validation of TerraSAR-X and TanDEM-X orbit solutions with laser and radar measurements. *Remote Sensing*, 10(5):762, 2018.

[64] S. Gernhardt, S. Auer, and K. Eder. Persistent scatterers at building facades–evaluation of appearance and localization accuracy. *ISPRS Journal of Photogrammetry and Remote Sensing*, 100:92–105, 2015.

[65] I. Hajnsek, T. Busche, G. Krieger, M. Zink, and A. Moreira. Announcement of opportunity: TanDEM-X science phase. *DLR Public Document TD-PD-PL-0032*, (1.0):1–27, 2014.

[66] X. X. Zhu and R. Bamler. Let's do the time warp: Multicomponent nonlinear motion estimation in differential SAR tomography. *IEEE Geoscience and Remote Sensing Letters*, 8(4):735–739, 2011.

[67] R. Tibshirani. Regression shrinkage and selection via the lasso. *Journal of the Royal Statistical Society: Series B (Methodological)*, 58(1):267–288, 1996.

[68] T. Hastie, R. Tibshirani, J. Friedman, and J. Franklin. *The elements of statistical learning: data mining, inference and prediction*. Springer Series in Statistics. Springer, 2001.

[69] P. Zhao and B. Yu. On model selection consistency of Lasso. *Journal of Machine Learning Research*, 7(Nov):2541–2563, 2006.

[70] P. Stoica and Y. Selen. Model-order selection: a review of information criterion rules. *IEEE Signal Processing Magazine*, 21(4):36–47, 2004.

[71] J. Nocedal and S. Wright. *Numerical optimization*. Springer Science & Business Media, 2006.

[72] S. Boyd, N. Parikh, E. Chu, B. Peleato, J. Eckstein, et al. Distributed optimization and statistical learning via the alternating direction method of multipliers. *Foundations and Trends® in Machine learning*, 3(1):1–122, 2011.

[73] S. Foucart and H. Rauhut. *A mathematical introduction to compressive sensing*. Springer Science & Business Media, 2017.

[74] D. L. Donoho. De-noising by soft-thresholding. *IEEE Transactions on Information Theory*, 41(3):613–627, 1995.

[75] N. Parikh, S. Boyd, et al. Proximal algorithms. *Foundations and Trends® in Optimization*, 1(3):127–239, 2014.

[76] S. Boyd and L. Vandenberghe. *Convex optimization*. Cambridge University Press, 2004.

[77] M. Fornasier, S. Peter, H. Rauhut, and S. Worm. Conjugate gradient acceleration of iteratively re-weighted least squares methods. *Computational Optimization and Applications*, 65(1):205–259, 2016.

[78] A. Chambolle and T. Pock. A first-order primal-dual algorithm for convex problems with applications to imaging. *Journal of Mathematical Imaging and Vision*, 40(1):120–145, 2011.

[79] T. G. Kolda and B. W. Bader. Tensor decompositions and applications. *SIAM Review*, 51(3):455–500, 2009.

[80] J. A. Bondy and U. S. R. Murty. *Graph Theory*. Springer, 2008.

[81] P. Stoica and R. Moses. *Spectral analysis of signals*. Pearson Prentice Hall Upper Saddle River, NJ, 2005.

[82] J. Sun, Q. Qu, and J. Wright. When are nonconvex problems not scary? *arXiv preprint arXiv:1510.06096*, 2015.

[83] E. Freitag and R. Busam. *Complex analysis*. Springer Science & Business Media, 2009.

[84] J. Revels, M. Lubin, and T. Papamarkou. Forward-mode automatic differentiation in Julia. *arXiv:1607.07892 [cs.MS]*, 2016. URL: `https://arxiv.org/abs/1607.07892`.

[85] P. K. Mogensen and A. N. Riseth. Optim: A mathematical optimization package for Julia. *Journal of Open Source Software*, 3(24):615, 2018. `doi:10.21105/joss.00615`.

[86] N. Ge, R. Bamler, D. Hong, and X. X. Zhu. Single-look multi-master SAR tomography: An introduction. *Submitted to IEEE Transactions on Geoscience and Remote Sensing*.

[87] N. Ge and X. X. Zhu. Bistatic-like differential SAR tomography. *IEEE Transactions on Geoscience and Remote Sensing*, 57(8):5883–5893, 2019.

[88] N. Ge, F. R. Gonzalez, Y. Wang, Y. Shi, and X. X. Zhu. Spaceborne staring spotlight SAR tomography—a first demonstration with TerraSAR-X. *IEEE Journal of Selected Topics in Applied Earth Observations and Remote Sensing*, 11(10):3743–3756, 2018.

A Appendix

A.1 Ge et al. (2019)

N. Ge, R. Bamler, D. Hong, and X. X. Zhu. Single-look multi-master SAR tomography: An introduction. *Submitted to IEEE Transactions on Geoscience and Remote Sensing*

Single-Look Multi-Master SAR Tomography: An Introduction

Nan Ge, Richard Bamler, *Fellow, IEEE,* Danfeng Hong, *Member, IEEE,*
and Xiao Xiang Zhu, *Senior Member, IEEE*

***Abstract*—This manuscript addresses the general problem of single-look multi-master SAR tomography. For this purpose, we establish the single-look multi-master data model, analyze its implications for single and double scatterers, and propose a generic inversion framework. The core of this framework is nonconvex sparse recovery, for which we develop two algorithms: one extends the conventional nonlinear least squares (NLS) to the single-look multi-master data model, and the other is based on bi-convex relaxation and alternating minimization (BiCRAM). We provide two theorems for the objective function of the NLS subproblem, which lead to its analytic solution up to a constant phase angle in the one-dimensional case. We also report our findings from the experiments on different acceleration techniques for BiCRAM. The proposed algorithms are applied to a real TerraSAR-X data set, and validated with height ground truth made available via a SAR imaging geodesy and simulation framework. This shows empirically that the *single-master* approach, if applied to a single-look *multi-master* stack, can be insufficient for layover separation, and the *multi-master* approach can indeed perform slightly better (despite being computationally more expensive) even in case of single scatterers. Besides, this manuscript also sheds light on the special case of single-look bistatic SAR tomography, which is relevant for current and future SAR missions such as TanDEM-X and Tandem-L.**

***Index Terms*—Synthetic aperture radar (SAR), bistatic SAR, TanDEM-X, Tandem-L, SAR tomography, sparse recovery, nonconvex optimization.**

I. Introduction

SYNTHETIC aperture radar (SAR) tomography is an interferometric SAR (InSAR) technique that reconstructs a three-dimensional far field from two-dimensional (2-D) azimuth-range measurements of radar echoes [1]–[3]. In the common case of spaceborne repeat-pass acquisitions, scatterers' motion can also be modeled and estimated [4]–[6]. SAR tomography is sometimes considered as an extension of persistent scatterer interferometry (PSI) [7]–[9] to the multi-scatterer case, although the inversion of the latter is performed on double-difference phase observations of persistent scatterers (PS) [10]. Extensive efforts were devoted to improving the super-resolution power, robustness and computational efficiency of tomographic inversion in urban scenarios (e.g., [11]–[20]).

The publications on SAR tomography can be roughly classified into the following four categories (see also Tab. I). Note that those listed below were only hand-picked, and we have no intention to provide a complete list.

- *Single-look single-master:*
  Reigber & Moreira (2000) did the pioneering work on airborne SAR tomography by densifying sampling via the integer interferogram combination technique and subsequently employing discrete Fourier transform on an interpolated linear array of baselines [1]. Fornaro et al. (2003, 2005, 2008) paved the way for spaceborne SAR tomography with long-term repeat-pass acquisitions and proposed to use more advanced inversion techniques such as truncated singular value decomposition [3], [5], [21]. Zhu & Bamler (2010a) provided the first demonstration of SAR tomography with very high resolution spaceborne SAR data by using Tikhonov regularization and nonlinear least squares (NLS) [22]. Budillon et al. (2010) and Zhu & Bamler (2010b) introduced compressive sensing techniques to tomographic inversion under the assumption of a compressible far-field profile. Zhu & Bamler (2011) proposed a generic algorithm (named SL1MMER) that is composed of spectral estimation, model-order selection and debiasing [23].
- *Single-look multi-master*[1]*:*
  To the best of our knowledge, the publications in this category are rather scarce. Zhu & Bamler (2012) extended the Tikhonov regularization, NLS and compressive sensing approaches to a mixed TerraSAR-X and TanDEM-X stack by using pre-estimated covariance matrix [24]. Ge & Zhu (2019) proposed a framework for SAR tomography using only bistatic or pursuit monostatic acquisitions: non-differential SAR tomography for height estimation by using bistatic or pursuit monostatic interferograms, and differential SAR tomography for deformation estimation by using conventional repeat-pass interferograms and the previous height estimates as deterministic prior

This work is jointly supported by the European Research Council (ERC) under the European Union's Horizon 2020 research and innovation programme (grant agreement No. [ERC-2016-StG-714087], acronym: *So2Sat*), the Helmholtz Association under the framework of the Young Investigator Group "SiPEO" (VH-NG-1018, www.sipeo.bgu.tum.de), and the Bavarian Academy of Sciences and Humanities in the framework of Junges Kolleg. *Corresponding author: Xiao Xiang Zhu.*

N. Ge and D. Hong are with the Remote Sensing Technology Institute (IMF), German Aerospace Center (DLR), 82234 Wessling, Germany (e-mail: Nan.Ge@dlr.de, Danfeng.Hong@dlr.de).

R. Bamler is with the Remote Sensing Technology Institute (IMF), German Aerospace Center (DLR), 82234 Wessling, Germany, and with the Chair of Remote Sensing Technology, Technical University of Munich (TUM), 80333 Munich, Germany (e-mail: richard.bamler@dlr.de).

X. X. Zhu is with the Remote Sensing Technology Institute (IMF), German Aerospace Center (DLR), 82234 Wessling, Germany, and with Signal Processing in Earth Observation (SiPEO), Technical University of Munich (TUM), 80333 Munich, Germany (e-mail: xiaoxiang.zhu@dlr.de).

[1]In this context, "multi-master" can be interpreted as "not single-master" (see also our definition in Sec. II-A).

TABLE I
A CLASSIFICATION OF TOMOGRAPHIC SAR ALGORITHMS

	Single-Master	Multi-Master
Single-Look	Reigber & Moreira (2000) Fornaro et al. (2003, 2005, 2008) Budillon et al. (2010) Zhu & Bamler (2010a, 2010b, 2011) Etc.	Zhu & Bamler (2012)† Ge & Zhu (2019)†
Multi-Look	Aguilera et al. (2012) Schmitt & Stilla (2012) Liang et al. (2018) Shi et al. (2019) Etc.	Gini et al. (2002) Lombardini (2005) Duque et al. (2009, 2010, 2014) Fornaro et al. (2014) Etc.

† Mistakenly uses the single-look single-master data model

[25]. However, the single-look single-master data model still underlies the algorithms in both publications.

- *Multi-look single-master:*
  Aguilera et al. (2012) exploited the common sparsity pattern among multiple polarimetric channels via distributed compressive sensing [13]. Schmitt & Stilla (2012) also employed distributed compressive sensing to jointly reconstruct an adaptively chosen neighborhood [14]. Liang et al. (2018) proposed an algorithm for 2-D range-elevation focusing on azimuth lines via compressive sensing [26]. Shi et al. (2019) performed nonlocal InSAR filtering before tomographic reconstruction [20].
- *Multi-look multi-master:*
  In general, any algorithm estimating the auto-correlation matrix belongs to this category. Note that this is closely related to modern adaptive multi-looking techniques that also exploit all possible interferometric combinations [27]–[31]. Gini et al. (2002) investigated the performance of different spectral estimators including Capon, multiple signal classification (MUSIC) and the multi-look relaxation (M-RELAX) algorithm [2]. Lombardini (2005) extended SAR tomography to the differential case by formulating it as a multi-dimensional spectral estimation problem and tackled it with higher-order Capon [4]. Duque et al. (2009, 2010) were the first to investigate bistatic SAR tomography by using ground-based receivers and spectral estimators such as Capon and MUSIC [32], [33]. Duque et al. (2014) demonstrated the feasibility of SAR tomography using a single pass of alternating bistatic acquisitions, in which the eigendecomposed empirical covariance matrix was exploited for the hypothesis test on the number of scatterers [34]. Fornaro et al. (2014) proposed an algorithm (named CAESAR) employing principal component analysis of the eigendecomposed empirical covariance matrix in an adaptively chosen neighborhood [15].

This list has a clear focus on urban scenarios. Needless to say, SAR tomography in forested scenarios involving random volume scattering in canopy and double-bounce scattering between ground and trunk (e.g., [35]–[42]) also falls in the *multi-look multi-master* category.

Let us follow the common conventions and denote the azimuth, range and elevation axes as x, r and s, respectively, where s is perpendicular to the x-r plane. For the sake of argument, suppose for any sample at the x and r positions, the N single-look complex (SLC) SAR measurements are noiseless. After deramping, each phase-calibrated SLC measurement can be modeled as the Fourier transform Γ of the elevation-dependent far-field reflectivity function $\gamma : \mathbb{R} \to \mathbb{C}$ at the corresponding wavenumber k [21]:

$$g_n = \Gamma(k_n) \coloneqq \int \gamma(s) \exp(-jk_n s) \mathrm{d}s, \quad n = 1, \ldots, N, \quad (1)$$

where $k_n \coloneqq -4\pi b_n/(\lambda r_0)$ is the nth wavenumber determined by the sensor position b_n along an axis $b \parallel s$ w.r.t. an arbitrary reference, the radar wavelength λ, and the slant-range distance r_0 w.r.t. a ground reference point. Here we consider the non-differential case. An extension to the differential case, in which scatterers' motion is modeled as linear combination of basis functions, is straightforward.

In the *single-look single-master* case, one SLC (say the ith, $i \in [N]$), typically near the center of joint orbital and temporal distribution, is selected as the unique master for generating interferograms, i.e., $g_n \overline{g_i}/|g_i|$, $\forall n \in [N] \setminus \{i\}$. This process, which can also be interpreted as a phase calibration step, converts k_n into the wavenumber baseline $\Delta k_n \coloneqq k_n - k_i$, $\forall n \in [N]$. As a result, the zero position of wavenumber baseline is fixed, i.e., $\Delta k_i = 0$. The rationale behind this is, e.g., to facilitate 2-D phase unwrapping for atmospheric phase screen (APS) compensation by smoothing out interferometric phase in x-r.

Likewise, the data model of random volume scattering is straightforward in the *multi-look multi-master* setting. Suppose $\gamma(s)$ is a white random signal. For any master and slave sampled at k and $k+\Delta k$, respectively, the Van Cittert–Zernike theorem implies that the expectation (due to multi-looking) of the interferogram, being the autocorrelation function $R_{\Gamma\Gamma}$ of Γ, is the Fourier transform of the elevation-dependent backscatter coefficient function $\sigma_0 : \mathbb{R} \to \mathbb{R}$ at Δk:

$$\mathrm{E}[\Gamma(k + \Delta k)\overline{\Gamma(k)}] = R_{\Gamma\Gamma}(\Delta k) = \int \sigma_0(s) \exp(-j\Delta k s) \mathrm{d}s, \quad (2)$$

where the property of $\gamma(s)$ being white, i.e., $\mathrm{E}[\gamma(s)\overline{\gamma(s')}] = \sigma_0(s)\delta(s-s')$, is utilized. This leads to an inverse problem similar to the one in the *single-look single-master* case.

This manuscript, on the other hand, addresses the general problem of SAR tomography using a *single-look multi-master* stack. Such a stack arises when, e.g.,

- a stack of bistatic interferograms is used in order to diminish APS, to minimize temporal decorrelation of non-PSs, and to eliminate motion-induced phase for single scatterers [33], [43], [44],
- repeat-pass interferograms of small (temporal) baselines are employed so as to limit the corresponding decorrelation effects of non-PSs [45]–[47].

While both previously mentioned categories have been intensively studied, it is not the case for *single-look multi-master* SAR tomography. To the best of our knowledge, all the existing work to date toward single-look *multi-master* SAR tomography is still incorrectly based on the single-look *single-master* data model [24], [25]. As will be demonstrated later with a real SAR data set, this approach can be insufficient for layover separation, even if the elevation distance between two scatterers is significantly larger than the Rayleigh resolution. This motivates us to fill the gap in the literature by revisiting the single-look data model in a multi-master multi-scatterer configuration, and by developing efficient methods for tomographic reconstruction. Naturally, this study is also inspired by prospective SAR missions such as Tandem-L that will deliver high-resolution wide-swath bistatic acquisitions in L-band as operational products [48].

Our main contributions can be summarized as follows.

- We establish the data model of single-look multi-master SAR tomography, by means of which both sparse recovery and model-order selection can be formulated as nonconvex minimization problems.
- We develop two algorithms for solving the aforementioned nonconvex sparse recovery problem, namely,
  1) NLS:
     we provide two theorems regarding the critical points of its subproblem's objective function that also underlies model-order selection;
  2) bi-convex relaxation and alternating minimization (BiCRAM):
     we propose to sample its solution path for the purpose of automatic regularization parameter tuning, and we show empirically that a simple diagonal preconditioning can effectively improve convergence.
- We propose to correct quantization errors by using (nonconvex) nonlinear optimization.
- We validate tomographic height estimates with ground truth generated by SAR simulations and geodetic corrections.

The rest of this manuscript is organized as follows. Sec. II introduces the data model and inversion framework for single-look multi-master SAR tomography. In Sec. III and IV, two algorithms for solving the nonconvex sparse recovery problem within the aforementioned framework, namely, NLS and BiCRAM, are elucidated and analyzed, respectively. Sec. V reports an experiment with TerraSAR-X data including a validation of tomographic height estimates. This manuscript is concluded by Sec. VI.

II. Single-look multi-master SAR tomography

In this section, we establish the data model for single-look multi-master SAR tomography, analyze its implications for two specific cases, and sketch out a generic inversion framework for it.

We start with the mathematical notations that are used throughout this manuscript.

Notation. We denote scalars as lower- or uppercase letters (e.g., m, N, λ), vectors as bold lowercase letters (e.g., $\mathbf{g}$, $\boldsymbol{\gamma}$), matrices, sets and ordered pairs as bold uppercase letters (e.g., $\mathbf{R}$, $\boldsymbol{\Omega}$), and number fields as blackboard bold uppercase letters (e.g., $\mathbb{Z}$, $\mathbb{R}$, $\mathbb{C}$) with the following conventions:

- g_n denotes the nth entry of $\mathbf{g}$.
- $\mathbf{a}^m$ and $\mathbf{a}_n$ denote the mth row and nth column of $\mathbf{A}$, respectively.
- $\mathrm{Diag}(\mathbf{a})$ denotes a square diagonal matrix whose entries on the main diagonal are equal to $\mathbf{a}$, and $\mathrm{Diag}(\mathbf{A})$ denotes a vector whose entries are equal to those on the main diagonal of $\mathbf{A}$.
- $\mathrm{Supp}(\mathbf{x})$ denotes the index set of nonzero entries or support of $\mathbf{x}$.
- $\overline{\mathbf{A}}$, $\mathbf{A}^T$ and $\mathbf{A}^H$ denote the (elementwise) complex conjugate, transpose and conjugate transpose of $\mathbf{A}$, respectively.
- $\mathbf{A}_R$ and $\Re(\mathbf{A})$ denote the real part of $\mathbf{A}$.
- $\mathbf{A}_I$ and $\Im(\mathbf{A})$ denote the imaginary part of $\mathbf{A}$.
- $\mathbf{A} \circ \mathbf{B}$ denotes the Hadamard product of $\mathbf{A}$ and $\mathbf{B}$.
- $\mathbf{A} \succ \mathbf{0}$, $\mathbf{B} \prec \mathbf{0}$ means that $\mathbf{A}$ is positive definite and $\mathbf{B}$ is negative definite.
- $\mathbf{A}_{\boldsymbol{\Omega}}$ denotes the matrix formed by extracting the columns of $\mathbf{A}$ indexed by $\boldsymbol{\Omega}$.
- $\|\mathbf{A}\|_{1,2}$ denotes the $\ell_{1,2}$ norm of $\mathbf{A}$, i.e., the sum of the ℓ_2 norms of its rows.
- $\mathbf{I}$ denotes the identity matrix.
- $[N]$ denotes the set $\{1, \ldots, N\}$.
- $|\boldsymbol{\Omega}|$ denotes the cardinality of the set $\boldsymbol{\Omega}$.
- The nonnegative and positive subsets of a number field $\mathbb{F}$ are denoted as $\mathbb{F}_+$ and $\mathbb{F}_{++}$, respectively.

A. Data Model

First of all, we give a definition of "single-master" and "multi-master" by using the language of basic graph theory (e.g., [49, §1]). Let $\mathbf{G} \coloneqq (\mathbf{V}(\mathbf{G}), \mathbf{E}(\mathbf{G}))$ be an acyclic directed graph that is associated with an incidence function $\psi_{\mathbf{G}}$, where $\mathbf{V}(\mathbf{G}) \coloneqq [N]$ is a set of vertices (SLCs), $\mathbf{E}(\mathbf{G})$ is a set of edges (interferograms), and for each $e \in \mathbf{E}(\mathbf{G})$, $\exists m, n \in \mathbf{V}(\mathbf{G})$ such that $\psi_{\mathbf{G}}(e) = (m, n)$. Its adjacency matrix $\mathbf{A}(\mathbf{G}) \coloneqq (a_{m,n}) \in \{0,1\}^{N \times N}$ is given by

$$a_{m,n} \coloneqq \begin{cases} 1 & : (m,n) \in \mathbf{E}(\mathbf{G}), \\ 0 & : (m,n) \notin \mathbf{E}(\mathbf{G}). \end{cases} \tag{3}$$

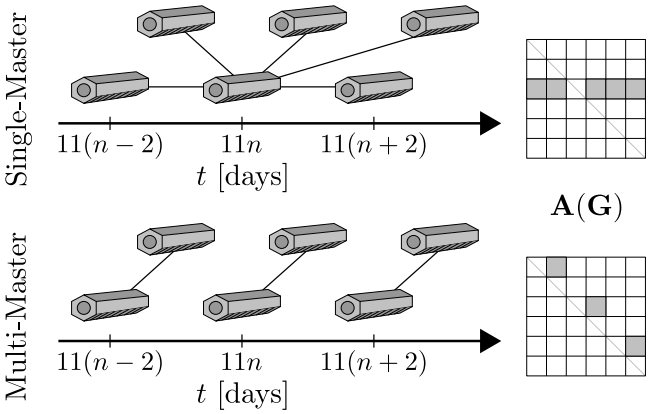

Fig. 1. Single-master vs. multi-master: two exemplary configurations and the corresponding adjacency matrices $\mathbf{A}(\mathbf{G})$.

Since $\mathbf{G}$ is acyclic, $a_{n,n} = 0, \forall n \in \mathbf{V}(\mathbf{G})$, i.e., the diagonal of $\mathbf{A}(\mathbf{G})$ contains only zero entries. Without loss of generality, assume that every vertex is connected to at least another one.

Definition 1. The *single-master* configuration means that there exists a unique $i \in [N]$ such that $a_{i,n} = 1$, $\mathbf{a}^m = \mathbf{0}$, $\forall m, n \in [N] \setminus \{i\}$. In this case, we refer to $\{g_n\overline{g_i}/|g_i|\}$ as the *single-master* stack with a master indexed by i.

Definition 2. The *multi-master* configuration means that $\nexists i \in [N]$ such that $a_{i,n} = 1$, $\mathbf{a}^m = \mathbf{0}$, $\forall m, n \in [N] \setminus \{i\}$. In this case, we refer to $\{g_n\overline{g_m}\}$ as the *multi-master* stack.

That is, "multi-master" is equivalent to "not single-master".

In the *multi-master* case, an interferogram is created for each $(m, n) \in \mathbf{E}(\mathbf{G})$:

$$g_n\overline{g_m} = \int\int \gamma(s)\overline{\gamma(s')} \exp\left(-j(k_n s - k_m s')\right) \mathrm{d}s\mathrm{d}s'. \quad (4)$$

Hereafter, we focus on the case in which the far field contains only a small number of scatterers such that

$$g_n \approx \sum_l \gamma_l \exp(-jk_n s_l), \quad n = 1, \ldots, N, \quad (5)$$

where $\gamma_l \in \mathbb{C}$ is the reflectivity of the lth scatterer located at the elevation position s_l. The single-look multi-master data model (4) becomes

$$g_n\overline{g_m} \approx \sum_{l,l'} \gamma_l\overline{\gamma_{l'}} \exp\left(-j(k_n s_l - k_m s_{l'})\right), \quad (6)$$

$\forall (m, n) \in \mathbf{E}(\mathbf{G})$.

In the next subsection, we analyze the implications of (6) for the single- and double-scatterer cases.

B. Implications

In the *single-scatterer* case, (6) becomes

$$g_n\overline{g_m} \approx |\gamma|^2 \exp\left(-j(k_n - k_m)s\right), \quad (7)$$

i.e., the multi-master observation is actually the Fourier transform of the reflectivity *power* at the wavenumber baseline $k_n - k_m$. As a result, the nonnegativity of $|\gamma|^2$ should be considered during inversion. Since both the real and imaginary parts of $g_n\overline{g_m}$ are parametrized by $|\gamma|^2$, i.e.,

$$\begin{aligned} \Re(g_n\overline{g_m}) &\approx |\gamma|^2 \cos\left((k_n - k_m)s\right), \\ \Im(g_n\overline{g_m}) &\approx |\gamma|^2 \sin\left(-(k_n - k_m)s\right), \end{aligned} \quad (8)$$

the inversion problem can be recast as a real-valued one.

For *double scatterers*, the multi-master observation is

$$\begin{aligned} g_n\overline{g_m} \approx\ & |\gamma_1|^2 \exp\left(-j(k_n - k_m)s_1\right) + \\ & \gamma_1\overline{\gamma_2} \exp\left(-j(k_n s_1 - k_m s_2)\right) + \\ & \overline{\gamma_1}\gamma_2 \exp\left(-j(k_n s_2 - k_m s_1)\right) + \\ & |\gamma_2|^2 \exp\left(-j(k_n - k_m)s_2\right). \end{aligned} \quad (9)$$

In addition to the Fourier transform of the reflectivity power at $k_n - k_m$, the right-hand side of (9) contains the second and third "cross-terms" in which the reflectivity values of the two scatterers (and their frequency-time-products) are coupled. This essentially rules out any linear model.

Remark. In the *multi-look* multi-master setting, the data model under random volume scattering is

$$\mathrm{E}[\Gamma(k_n)\overline{\Gamma(k_m)}] = \int \sigma_0(s) \exp(-j(k_n - k_m)s)\mathrm{d}s, \quad (10)$$

as already indicated in Eq. (2), i.e., no coupling is involved.

Remark. A *multi-master* bistatic or pursuit monostatic (i.e., 10-second temporal baseline [50]) stack is in general not motion-free for double (or multiple) scatterers.

To see this, consider for example the linear deformation model $d(t_n) \coloneqq vt_n$, where v and t denote linear deformation rate and temporal baseline, respectively. Observe that

$$\begin{aligned} & g_n\overline{g_m} \\ \approx & \sum_{l,l'} \gamma_l\overline{\gamma_{l'}} \cdot \\ & \exp(-j(k_n s_l - k_m s_{l'} + 4\pi d_l(t_n)/\lambda - 4\pi d_{l'}(t_m)/\lambda)) \\ = & |\gamma_1|^2 \exp\left(-j\left((k_n - k_m)s_1 + 4\pi v_1(t_n - t_m)/\lambda\right)\right) + \\ & \gamma_1\overline{\gamma_2} \exp\left(-j\left((k_n s_1 - k_m s_2) + 4\pi(v_1 t_n - v_2 t_m)/\lambda\right)\right) + \\ & \overline{\gamma_1}\gamma_2 \exp\left(-j\left((k_n s_2 - k_m s_1) + 4\pi(v_2 t_n - v_1 t_m)/\lambda\right)\right) + \\ & |\gamma_2|^2 \exp\left(-j\left((k_n - k_m)s_2 + 4\pi v_2(t_n - t_m)/\lambda\right)\right). \end{aligned} \quad (11)$$

In case of $t_m = t_n$, the motion-induced phase in the cross-terms vanishes if and only if $v_1 = v_2$.

The next subsection introduces a generic inversion framework for single-look multi-master SAR tomography.

C. Inversion Framework

The single-look multi-master data model (6) already indicates a nonlinear system of equations for a multi-master stack. Suppose $\mathbf{G}$ is the graph associated with this stack that contains a total of $N' \coloneqq |\mathbf{E}(\mathbf{G})|$ multi-master observations, and $e_1, \ldots, e_{N'}$ is an ordered sequence of all the edges in $\mathbf{E}(\mathbf{G})$. Let $\mathcal{M}, \mathcal{S} : [N'] \to [N]$ be the mappings to the master and slave image indices, respectively. For each e_n, $n \in [N']$, a multi-master observation $g_{\mathcal{S}(n)}\overline{g_{\mathcal{M}(n)}}$ is obtained. Let $\mathbf{g} \in \mathbb{C}^{N'}$ be the vector of multi-master observations such

that $g_n \coloneqq g_{\mathcal{S}(n)}\overline{g_{\mathcal{M}(n)}}$, $\forall n \in [N']$. Let $s_1, \ldots, s_L$ be a discretization of the elevation axis s. The data model in matrix notations is

$$\mathbf{g} \approx (\mathbf{R}\boldsymbol{\gamma}) \circ (\overline{\mathbf{S}\boldsymbol{\gamma}}), \tag{12}$$

where $\mathbf{R}, \mathbf{S} \in \mathbb{C}^{N' \times L}$ represent the tomographic observation matrices of the slave and master images, respectively, $r_{n,l} \coloneqq \exp(-jk_{\mathcal{S}(n)}s_l)$, $s_{n,l} \coloneqq \exp(-jk_{\mathcal{M}(n)}s_l)$, $\forall n \in [N']$, $l \in [L]$, and $\boldsymbol{\gamma} \in \mathbb{C}^L$ is the unknown reflectivity vector such that γ_l is associated with the scatterer (if any) at elevation position s_l.

In light of (12), we propose the following framework for tomographic inversion.

1) Nonconvex sparse recovery: We consider the problem

$$\begin{aligned} \hat{\boldsymbol{\gamma}} \coloneqq \underset{\boldsymbol{\gamma}}{\arg\min} \quad & \frac{1}{2}\|(\mathbf{R}\boldsymbol{\gamma}) \circ (\overline{\mathbf{S}\boldsymbol{\gamma}}) - \mathbf{g}\|_2^2 \\ \text{subject to} \quad & |\operatorname{Supp}(\boldsymbol{\gamma})| \leq K, \end{aligned} \tag{13}$$

where $K \in \mathbb{Z}_{++}$. The objective function measures the model goodness of fit and the constraint enforces $\boldsymbol{\gamma}$ to be sparse, as is implicitly assumed in (6). If $\sum_{l=0}^{K}\binom{L}{l}$ is small, (13) can be solved heuristically by using the algorithms that will be developed in Sec. III. Sec. IV is dedicated to another algorithm that solves a similar problem based on bi-convex relaxation.

2) Model-order selection: This procedure removes outliers and therefore reduces false positive rate. By using for example the Bayesian information criterion (e.g., [51]), model-order selection can be formulated as the following constrained minimization problem:

$$\begin{aligned} \hat{\boldsymbol{\Omega}} \coloneqq \underset{\boldsymbol{\Omega}(,\boldsymbol{\delta})}{\arg\min} \quad & 2\ln\left(\|(\mathbf{R}_{\boldsymbol{\Omega}}\boldsymbol{\delta}_{\boldsymbol{\Omega}}) \circ (\overline{\mathbf{S}_{\boldsymbol{\Omega}}\boldsymbol{\delta}_{\boldsymbol{\Omega}}}) - \mathbf{g}\|_2^2/N'\right) \\ & + (5|\boldsymbol{\Omega}| + 1)\ln(N')/N' \\ \text{subject to} \quad & \operatorname{Supp}(\boldsymbol{\delta}) = \boldsymbol{\Omega} \subset \operatorname{Supp}(\hat{\boldsymbol{\gamma}}), \end{aligned} \tag{14}$$

where $\boldsymbol{\delta} \in \mathbb{C}^L$ is an auxiliary variable, and $\boldsymbol{\Omega}$ is its support. Since $|\operatorname{Supp}(\hat{\boldsymbol{\gamma}})|$ is typically small, (14) can be tackled by solving a sequence of subset least squares problems in the form of

$$\underset{\boldsymbol{\epsilon}}{\text{minimize}}\ \frac{1}{2}\|(\mathbf{R}_{\boldsymbol{\Omega}}\boldsymbol{\epsilon}) \circ (\overline{\mathbf{S}_{\boldsymbol{\Omega}}\boldsymbol{\epsilon}}) - \mathbf{g}\|_2^2, \tag{15}$$

for which two solvers will be introduced in Sec. III.

3) Off-grid correction: The off-grid or quantization problem arises when scatterers are not located on the (regular) grid of $\boldsymbol{\gamma}$. Ge et al. [17] proposed to oversample $\hat{\boldsymbol{\gamma}}$ in the vicinity of selected scatterers in order to circumvent this problem. Here we propose a more elegant approach that is based on nonlinear optimization.

Denote $\hat{K} \coloneqq |\hat{\boldsymbol{\Omega}}|$ as the number of scatterers after model-order selection. Let γ_l^R and γ_l^I be the real and imaginary parts of the complex-valued reflectivity γ_l of the lth scatterer that is located at s_l, respectively, i.e., $\gamma_l = \gamma_l^R + j\gamma_l^I$, $\forall l \in [\hat{K}]$. On the basis of the single-look multi-master data model (6), we seek a solution of the following minimization problem:

$$\begin{aligned} \underset{\gamma_l^R, \gamma_l^I, s_l}{\text{minimize}} \sum_n \Big| g_n - \sum_{l,l'} (\gamma_l^R + j\gamma_l^I)(\gamma_{l'}^R - j\gamma_{l'}^I) \cdot \\ \exp\left(-j(k_{\mathcal{S}(n)}s_l - k_{\mathcal{M}(n)}s_{l'})\right) \Big|^2. \end{aligned} \tag{16}$$

Note that the objective function is differentiable w.r.t. γ_l^R, γ_l^I and s_l, $\forall l \in [\hat{K}]$. Needless to say, the on-grid estimates from (14) are used as the initial solution. We will revisit this problem in Sec. III-A.

Thus far the inversion framework has been established. In the next two sections, we will deal with the optimization problems (13)–(16) from the algorithmic point of view.

III. Nonlinear Least Squares (NLS)

NLS is a parametric method that breaks down a sparse recovery problem into a series of subset linear least squares subproblems [52, §6.4]. Here we extend the concept of NLS to the single-look multi-master data model (12) and address the subproblem (15), or equivalently,

$$\underset{\mathbf{x}}{\text{minimize}}\ \frac{1}{2}\|(\mathbf{A}\mathbf{x}) \circ (\overline{\mathbf{B}\mathbf{x}}) - \mathbf{b}\|_2^2, \tag{17}$$

where $\mathbf{A}, \mathbf{B} \in \mathbb{C}^{m \times n}$, $\mathbf{x} \in \mathbb{C}^n$, $\mathbf{b} \in \mathbb{C}^m$ with $m > n$. As can be concluded from Sec. II-C, (17) is clearly of interest, since it not only solves the nonconvex spare recovery problem (13), but also underlies model-order selection (14).

A. Algorithm

In this subsection, we develop two algorithms for solving (17).

The first algorithm is based on the alternating direction method of multipliers (ADMM) [53]. ADMM solves a minimization problem by alternatively minimizing its augmented Lagrangian [54, p. 509], in which the augmentation term is scaled by a penalty parameter $\rho \in \mathbb{R}_{++}$. A short recap can be found in Appendix A. It converges under very general conditions with medium accuracy [53, §3.2].

Now we consider (17) in its equivalent form:

$$\begin{aligned} \underset{\mathbf{x},\mathbf{z}}{\text{minimize}} \quad & \frac{1}{2}\|(\mathbf{A}\mathbf{x}) \circ (\overline{\mathbf{B}\mathbf{z}}) - \mathbf{b}\|_2^2 \\ \text{subject to} \quad & \mathbf{x} - \mathbf{z} = \mathbf{0}. \end{aligned} \tag{18}$$

This is essentially a bi-convex problem with affine constraint [53, §9.2]. Applying the ADMM update rules leads to Alg. 1. Note that both $\mathbf{x}$- and $\mathbf{z}$-updates boil down to solving linear least squares problems.

Algorithm 1 An ADMM-based algorithm for solving (17)

Input: $\mathbf{A}$, $\mathbf{B}$, $\mathbf{b}$, $\mathbf{z}^{(0)}$, ρ
Initialize $\mathbf{z} \leftarrow \mathbf{z}^{(0)}$
Until stopping criterion is satisfied, **Do**
  $\tilde{\mathbf{A}} \leftarrow \operatorname{Diag}(\overline{\mathbf{B}\mathbf{z}})\mathbf{A}$
  $\mathbf{x} \leftarrow (\tilde{\mathbf{A}}^H\tilde{\mathbf{A}} + \rho\mathbf{I})^{-1}(\tilde{\mathbf{A}}^H\mathbf{b} + \rho\mathbf{z} - \mathbf{y})$
  $\tilde{\mathbf{B}} \leftarrow \operatorname{Diag}(\overline{\mathbf{A}\mathbf{x}})\mathbf{B}$
  $\mathbf{z} \leftarrow (\tilde{\mathbf{B}}^H\tilde{\mathbf{B}} + \rho\mathbf{I})^{-1}(\tilde{\mathbf{B}}^H\overline{\mathbf{b}} + \rho\mathbf{x} + \mathbf{y})$
  $\mathbf{y} \leftarrow \mathbf{y} + \rho(\mathbf{x} - \mathbf{z})$
Output: $\mathbf{z}$

The second algorithm uses the trust-region Newton's method that exploits second-order information for solving general unconstrained nonlinear minimization problems [55, §4]. The rationale behind this choice is to circumvent saddle

points that cannot be identified by first-order information [56]. In each iteration, a norm ball or "trust region" centered at the current iterate is adaptively chosen. If the second-order Taylor polynomial of the objective function is sufficiently good for approximation, a descent direction is found via solving a quadratically constrained quadratic minimization problem. Suppose $f : \mathbb{R}^n \to \mathbb{R}$ is the objective function, the subproblem at the iterate $\mathbf{x} \in \mathbb{R}^n$ is

$$\begin{aligned} \underset{\Delta\mathbf{x}}{\text{minimize}} \quad & f(\mathbf{x}) + \nabla f(\mathbf{x})^T \Delta\mathbf{x} + \frac{1}{2}\Delta\mathbf{x}^T \nabla^2 f(\mathbf{x}) \Delta\mathbf{x} \\ \text{subject to} \quad & \|\Delta\mathbf{x}\|_2 \leq r, \end{aligned} \tag{19}$$

where $\Delta\mathbf{x} \in \mathbb{R}^n$ is the search direction, ∇f and $\nabla^2 f$ denote the gradient and Hessian of f, respectively, and $r \in \mathbb{R}_{++}$ is the current trust region radius. By means of the Karush-Kuhn-Tucker (KKT) conditions for nonconvex problems, Nocedal and Wright [55, §4.3] divided (19) into several cases: in one case a one-dimensional (1-D) root-finding problem w.r.t. the dual variable is solved by using for example the Newton's method, while in the others the solutions are analytic. Since the technical details are quite overwhelming, we do not intend to provide an exposition here. Interested readers are advised to refer to [55, §4.3]. It can be shown that the trust-region Newton's method converges to a critical point with high accuracy under general conditions [55, p. 92].

By verifying the Cauchy-Riemann equations (e.g., [57, p. 50]), it is easy to show that the objective function of (17) is not complex-differentiable w.r.t. $\mathbf{x}$. In lieu of using Wirtinger differentiation that does not contain all the second-order information, we exploit the fact that the mapping $\mathbf{x} \mapsto (\mathbf{x}_R, \mathbf{x}_I)$ is isomorphic and let

$$f(\mathbf{x}_R, \mathbf{x}_I) \coloneqq \frac{1}{2}\|(\mathbf{A}\mathbf{x}) \circ (\overline{\mathbf{B}\mathbf{x}}) - \mathbf{b}\|_2^2, \tag{20}$$

where $f : \mathbb{R}^n \times \mathbb{R}^n \to \mathbb{R}$ is real-differentiable w.r.t. $\mathbf{x}_R$ and $\mathbf{x}_I$. Straightforward computations reveal its gradient as

$$\nabla f(\mathbf{x}_R, \mathbf{x}_I) = \begin{pmatrix} \frac{\partial f}{\partial \mathbf{x}_R} \\ \frac{\partial f}{\partial \mathbf{x}_I} \end{pmatrix} = \begin{pmatrix} \Re(\mathbf{d}) \\ \Im(\mathbf{d}) \end{pmatrix}, \tag{21}$$

where

$$\begin{aligned} \mathbf{d} \coloneqq \mathbf{A}^H \left(((\mathbf{A}\mathbf{x}) \circ (\overline{\mathbf{B}\mathbf{x}}) - \mathbf{b}) \circ (\mathbf{B}\mathbf{x}) \right) + \\ \mathbf{B}^H \left(((\overline{\mathbf{A}\mathbf{x}}) \circ (\mathbf{B}\mathbf{x}) - \overline{\mathbf{b}}) \circ (\mathbf{A}\mathbf{x}) \right), \end{aligned} \tag{22}$$

and its Hessian as

$$\begin{aligned} \nabla^2 f(\mathbf{x}_R, \mathbf{x}_I) &= \begin{pmatrix} \frac{\partial^2 f}{\partial \mathbf{x}_R^2} & \frac{\partial^2 f}{\partial \mathbf{x}_R \partial \mathbf{x}_I} \\ \frac{\partial^2 f}{\partial \mathbf{x}_I \partial \mathbf{x}_R} & \frac{\partial^2 f}{\partial \mathbf{x}_I^2} \end{pmatrix} \\ &= \begin{pmatrix} \Re(\mathbf{C}+\mathbf{D}+\mathbf{E}) & -\Im(\mathbf{C}-\mathbf{D}+\mathbf{E}) \\ \Im(\mathbf{C}+\mathbf{D}+\mathbf{E}) & \Re(\mathbf{C}-\mathbf{D}+\mathbf{E}) \end{pmatrix}, \end{aligned} \tag{23}$$

where

$$\begin{aligned} \mathbf{C} \coloneqq \quad & \mathbf{A}^H \operatorname{Diag}\left((\mathbf{B}\mathbf{x}) \circ (\overline{\mathbf{B}\mathbf{x}})\right) \mathbf{A} + \\ & \mathbf{B}^H \operatorname{Diag}\left((\mathbf{A}\mathbf{x}) \circ (\overline{\mathbf{A}\mathbf{x}})\right) \mathbf{B}, \\ \mathbf{D} \coloneqq \quad & \mathbf{A}^H \operatorname{Diag}\left((\mathbf{A}\mathbf{x}) \circ (\mathbf{B}\mathbf{x})\right) \overline{\mathbf{B}} + \\ & \mathbf{B}^H \operatorname{Diag}\left((\mathbf{A}\mathbf{x}) \circ (\mathbf{B}\mathbf{x})\right) \overline{\mathbf{A}}, \\ \mathbf{E} \coloneqq \quad & \mathbf{A}^H \operatorname{Diag}\left((\mathbf{A}\mathbf{x}) \circ (\overline{\mathbf{B}\mathbf{x}}) - \mathbf{b}\right) \mathbf{B} + \\ & \mathbf{B}^H \operatorname{Diag}\left((\overline{\mathbf{A}\mathbf{x}}) \circ (\mathbf{B}\mathbf{x}) - \overline{\mathbf{b}}\right) \mathbf{A}. \end{aligned} \tag{24}$$

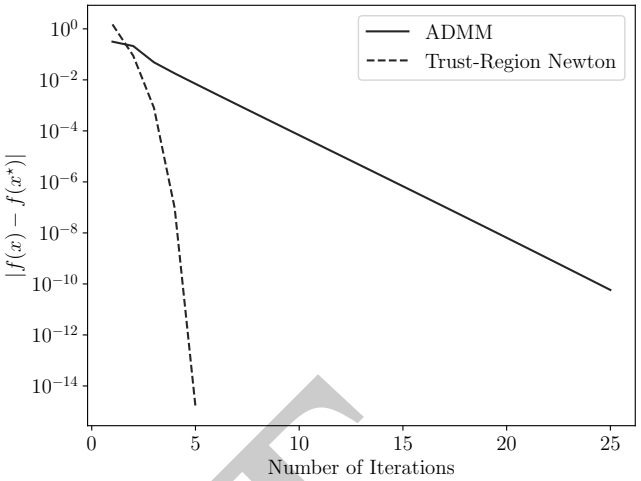

Fig. 2. Convergence curve of NLS using ADMM (solid line) and the trust-region Newton's method (dashed line).

Note that $\mathbf{d} : \mathbb{C}^n \to \mathbb{C}^n$ and $\mathbf{C}, \mathbf{D}, \mathbf{E} : \mathbb{C}^n \to \mathbb{C}^{n \times n}$ are essentially functions of $\mathbf{x}$. Here we drop the parentheses in order to simplify notation. For the same purpose, we adopt the following convention:

$$f(\mathbf{x}) \coloneqq f\left(\Re(\mathbf{x}), \Im(\mathbf{x})\right) = f(\mathbf{x}_R, \mathbf{x}_I). \tag{25}$$

By using the first- and second-order information of (20), (17) can be directly tackled by the trust-region Newton's method via solving a sequence of subproblems in the form of (19). For any optimal point $\mathbf{x}^\star$, the KKT condition is

$$\nabla f(\mathbf{x}^\star) = \mathbf{0} \iff \mathbf{d}(\mathbf{x}^\star) = \mathbf{0}. \tag{26}$$

Remark. Likewise, the objective function of (16) is real-differentiable w.r.t. γ_l^R, γ_l^I and s_l, $\forall l \in [\hat{K}]$. Therefore, the trust-region Newton's method is directly applicable. Alternatively, first-order methods such as Broyden-Fletcher-Goldfarb-Shanno (BFGS, see for example [55, §6.1] and the references therein) can also be used.

Needless to say, it is not guaranteed that these algorithms always converge to a global minimum. We will demonstrate later in Sec. V that the solutions are often good enough. Fig. 2 shows typical convergence curves in case of double scatterers (#6 in Sec. V-C). In order to generate this plot, we first let one algorithm run non-stop until it converged with very high precision. We then took this solution as an optimal point $\mathbf{x}^\star$ and compared the absolute difference of the objective value $|f(\mathbf{x}) - f(\mathbf{x}^\star)|$. Both ADMM and the trust-region Newton's method converged to the same solution (up to a constant phase angle, see Sec. III-B), although it only took the latter less than 10 iterations. Still, the former can be interesting due to the simplicity of its update rules (see Alg. 1). In Sec. V, the latter will be used for demonstration purposes.

B. Analysis of the Objective Function

Due to the nonconvexity of the objective function (20), its analysis is not straightforward. We are primarily concerned with the following two questions:

1) Under which circumstances do critical points or local extrema exist?
2) If they do exist, how many are they?

This subsection shall provide a partial answer to these questions.

First of all, we state the following general observation.

Proposition 1. For any $\mathbf{x} \in \mathbb{C}^n$ and $\phi \in \mathbb{R}$, any eigenvalue of $\nabla^2 f(\mathbf{x})$ is also an eigenvalue of $\nabla^2 f\left(\mathbf{x}\exp(j\phi)\right)$ and vice versa.

Proof. See Appendix B. □

Informally, this proposition implies that the definiteness of the Hessian is invariant under any rotation with a constant phase angle.

Now we state the main theorem for the general case.

Theorem 2. Properties of the critical points of $f(\mathbf{x})$.

(a) $\mathbf{0}$ is a critical point: it is a local minimum if $\mathbf{A}^H \operatorname{Diag}(\mathbf{b})\mathbf{B} + \mathbf{B}^H \operatorname{Diag}(\overline{\mathbf{b}})\mathbf{A} \prec \mathbf{0}$, and a local maximum if $\mathbf{A}^H \operatorname{Diag}(\mathbf{b})\mathbf{B} + \mathbf{B}^H \operatorname{Diag}(\overline{\mathbf{b}})\mathbf{A} \succ \mathbf{0}$.

(b) If there exists a *nonzero* critical point, then $\mathbf{A}^H \operatorname{Diag}(\mathbf{b})\mathbf{B} + \mathbf{B}^H \operatorname{Diag}(\overline{\mathbf{b}})\mathbf{A} \not\succ \mathbf{0}$.

(c) Suppose there exists a *nonzero* critical point $\mathbf{z}$. Then
   (1) $\nabla^2 f(\mathbf{z})$ is rank deficient.
   (2) There exist an infinite number of critical points in the form of $\mathbf{z}\exp(j\phi)$, $\phi \in \mathbb{R} \setminus \{0\}$. Each has the same objective function value as $\mathbf{z}$, and its Hessian has the same definiteness.

Proof. See Appendix C. □

This theorem implies that if there exists one critical point, then there are an infinite number of them up to a constant phase angle, and each is as good. Furthermore, we conjecture that $\mathbf{A}^H \operatorname{Diag}(\mathbf{b})\mathbf{B} + \mathbf{B}^H \operatorname{Diag}(\overline{\mathbf{b}})\mathbf{A} \succ \mathbf{0}$ is a necessary and sufficient condition (cf. Thm. 2(b)), and each *nonzero* critical point is also a local minimum under some mild conditions.

For the special case $n = 1$, i.e., $\mathbf{A}, \mathbf{B} \in \mathbb{C}^m$, $\mathbf{x} \in \mathbb{C}$, we have a much stronger result.

Theorem 3 ($n = 1$)**.** Properties of the critical points of $f(\mathbf{x})$.

(a) $\mathbf{0}$ is a critical point: it is a local minimum if $\Re\left((\mathbf{A} \circ \overline{\mathbf{B}})^H \mathbf{b}\right) < 0$, and a local maximum if $\Re\left((\mathbf{A} \circ \overline{\mathbf{B}})^H \mathbf{b}\right) > 0$.

(b) There exists a *nonzero* critical point if and only if $\Re\left((\mathbf{A} \circ \overline{\mathbf{B}})^H \mathbf{b}\right) > 0$.

(c) Suppose there exists a *nonzero* critical point $\mathbf{z}$. Then
   (1) $\nabla^2 f(\mathbf{z})$ is positive semi-definite and rank deficient[2].
   (2) There exist an infinite number of critical points in the form of $\mathbf{z}\exp(j\phi)$, $\phi \in \mathbb{R} \setminus \{0\}$. Each has the same objective function value as $\mathbf{z}$, and its Hessian has the same definiteness.
   (3) $\mathbf{z}$ is a local minimum.

Proof. See Appendix D. □

As a result, a *nonzero local minimum* exists if and only if $\Re\left((\mathbf{A} \circ \overline{\mathbf{B}})^H \mathbf{b}\right) > 0$. If this condition is satisfied, then there are infinitely many local minima that are exactly as good. Fig. 3 shows as an example the negative logarithm of (20) with a circle of local maxima.

[2]Note that $\nabla^2 f(\mathbf{z}) \in \mathbb{R}^{2\times 2}$ by definition.

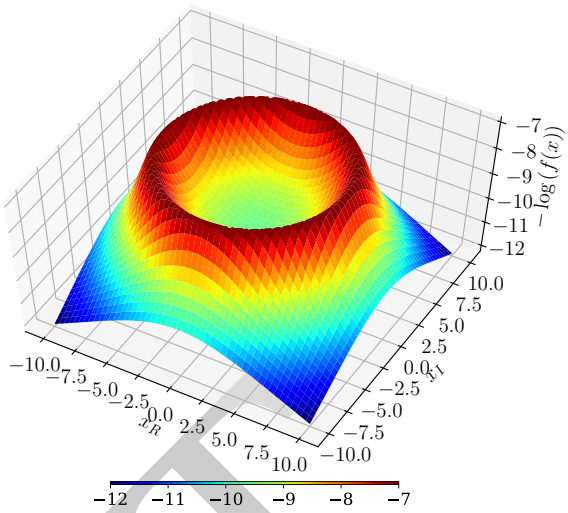

Fig. 3. Negative logarithm of the NLS objective function ($n = 1$) with a circle of local maxima at the verge of the "crater".

Lastly, Thm. 3 implies the following interesting result.

Corollary 4 ($n = 1$)**.** Each *nonzero local minimum* (if it exists) is given by

$$\mathbf{z} = \frac{\Re\left((\mathbf{A} \circ \overline{\mathbf{B}})^H \mathbf{b}\right)^{1/2}}{\|\mathbf{A} \circ \overline{\mathbf{B}}\|_2} \exp(j\phi), \tag{27}$$

for some $\phi \in \mathbb{R}$.

Proof. See the proof of Thm. 3(b). □

Now we return to our problem in SAR tomography. For the single-look multi-master data model (12), this corollary motivates the 1-D spectral estimator:

$$|\hat{\gamma}_l| := \begin{cases} \frac{\Re\left((\mathbf{r}_l \circ \overline{\mathbf{s}_l})^H \mathbf{g}\right)^{1/2}}{\|\mathbf{r}_l \circ \overline{\mathbf{s}_l}\|_2} & \text{if } \Re\left((\mathbf{r}_l \circ \overline{\mathbf{s}_l})^H \mathbf{g}\right) > 0 \\ 0 & \text{otherwise,} \end{cases} \tag{28}$$

$\forall l \in [L]$. Note that this also provides the solution for any 1-D NLS subproblem up to a constant phase angle. In case of multiple scatterers, this estimator does not have any super-resolution power.

IV. Bi-Convex Relaxation and Alternating Minimization (BiCRAM)

This section introduces a second algorithm for solving the nonconvex sparse recovery problem (13).

A. Algorithm

As a starting point, we replace the constraint in (13) with a sparsity-inducing regularization term, e.g.,

$$\underset{\boldsymbol{\gamma}}{\text{minimize}}\ \frac{1}{2}\|(\mathbf{R}\boldsymbol{\gamma}) \circ (\overline{\mathbf{S}\boldsymbol{\gamma}}) - \mathbf{g}\|_2^2 + \lambda\|\boldsymbol{\gamma}\|_1, \tag{29}$$

where $\lambda \in \mathbb{R}_{++}$ trades model goodness of fit for sparsity. In light of (26), the necessary condition for being an optimal point $\boldsymbol{\gamma}^\star$ is

$$\begin{aligned}\lambda\partial\|\boldsymbol{\gamma}^\star\|_1 \ni \mathbf{R}^H\left((\mathbf{g}-(\mathbf{R}\boldsymbol{\gamma}^\star)\circ(\overline{\mathbf{S}\boldsymbol{\gamma}^\star}))\circ(\mathbf{S}\boldsymbol{\gamma}^\star)\right)+\\ \mathbf{S}^H\left((\overline{\mathbf{g}}-(\overline{\mathbf{R}\boldsymbol{\gamma}^\star})\circ(\mathbf{S}\boldsymbol{\gamma}^\star))\circ(\mathbf{R}\boldsymbol{\gamma}^\star)\right),\end{aligned} \tag{30}$$

i.e., the right-hand side is a subgradient of the ℓ_1 norm at $\boldsymbol{\gamma}^\star$. Obviously, $\mathbf{0}$ always satisfies this condition.

In principle, an ADMM-based algorithm similar to Alg. 1 can be used to solve (29). However, our experience with real SAR tomographic data shows that it often diverges, presumably due to the high mutual coherence of $\mathbf{R}$ and $\mathbf{S}$ under nonconvexity. For this reason, we consider instead the following relaxed version of (29):

$$\begin{aligned}\underset{\boldsymbol{\gamma},\boldsymbol{\theta}}{\text{minimize}}\quad & \frac{1}{2}\|(\mathbf{R}\boldsymbol{\gamma})\circ(\overline{\mathbf{S}\boldsymbol{\theta}})-\mathbf{g}\|_2^2+\frac{\lambda_1}{2}\|\boldsymbol{\gamma}-\boldsymbol{\theta}\|_2^2+\\ & \lambda_2\|\begin{pmatrix}\boldsymbol{\gamma} & \boldsymbol{\theta}\end{pmatrix}\|_{1,2},\end{aligned} \tag{31}$$

where $\lambda_1, \lambda_2 \in \mathbb{R}_{++}$. The objective function $\mathbb{C}^L \times \mathbb{C}^L \to \mathbb{R}$ is bi-convex, i.e., it is convex in $\boldsymbol{\gamma}$ with $\boldsymbol{\theta}$ fixed, and convex in $\boldsymbol{\theta}$ with $\boldsymbol{\gamma}$ fixed. The first regularization term enforces $\boldsymbol{\gamma}$ and $\boldsymbol{\theta}$ to have similar entries, and the second one promotes the same support. Since (31) is essentially an unconstrained bi-convex problem, it can be solved by using alternating minimization via Alg. 2 (see also [58]–[60]).

Algorithm 2 An alternating algorithm for solving (31)

1: **Input:** $\mathbf{R}$, $\mathbf{S}$, $\mathbf{g}$, $\boldsymbol{\gamma}^{(0)}$, λ_1, λ_2
2: **Initialize** $\boldsymbol{\gamma} \leftarrow \boldsymbol{\gamma}^{(0)}$
3: **Until** stopping criterion is satisfied, **Do**
4: $\quad\tilde{\mathbf{S}} \leftarrow \mathrm{Diag}(\overline{\mathbf{R}\boldsymbol{\gamma}})\mathbf{S}$
5: $\quad\boldsymbol{\theta} \leftarrow \arg\min_{\boldsymbol{\theta}} \frac{1}{2}\|\tilde{\mathbf{S}}\boldsymbol{\theta}-\overline{\mathbf{g}}\|_2^2+\frac{\lambda_1}{2}\|\boldsymbol{\theta}-\boldsymbol{\gamma}\|_2^2+\lambda_2\|\begin{pmatrix}\boldsymbol{\theta} & \boldsymbol{\gamma}\end{pmatrix}\|_{1,2}$
6: $\quad\tilde{\mathbf{R}} \leftarrow \mathrm{Diag}(\overline{\mathbf{S}\boldsymbol{\theta}})\mathbf{R}$
7: $\quad\boldsymbol{\gamma} \leftarrow \arg\min_{\boldsymbol{\gamma}} \frac{1}{2}\|\tilde{\mathbf{R}}\boldsymbol{\gamma}-\mathbf{g}\|_2^2+\frac{\lambda_1}{2}\|\boldsymbol{\gamma}-\boldsymbol{\theta}\|_2^2+\lambda_2\|\begin{pmatrix}\boldsymbol{\gamma} & \boldsymbol{\theta}\end{pmatrix}\|_{1,2}$
8: **Output:** $\boldsymbol{\gamma}$

Each time when either $\boldsymbol{\gamma}$ or $\boldsymbol{\theta}$ is fixed, it becomes a convex problem in the generic form of:

$$\underset{\mathbf{x}}{\text{minimize}}\ \frac{1}{2}\|\mathbf{A}\mathbf{x}-\mathbf{b}\|_2^2+\frac{\lambda_1}{2}\|\mathbf{x}-\mathbf{u}\|_2^2+\lambda_2\|\begin{pmatrix}\mathbf{x} & \mathbf{u}\end{pmatrix}\|_{1,2}, \tag{32}$$

or equivalently

$$\begin{aligned}\underset{\mathbf{x},\mathbf{Z}}{\text{minimize}}\quad & \frac{1}{2}\|\mathbf{A}\mathbf{x}-\mathbf{b}\|_2^2+\frac{\lambda_1}{2}\|\mathbf{x}-\mathbf{u}\|_2^2+\lambda_2\|\mathbf{Z}\|_{1,2}\\ \text{subject to}\quad & \begin{pmatrix}\mathbf{x} & \mathbf{u}\end{pmatrix}-\mathbf{Z}=\mathbf{0},\end{aligned} \tag{33}$$

where $\mathbf{Z} \in \mathbb{C}^{L\times 2}$. Applying the ADMM update rules leads to Alg. 3.

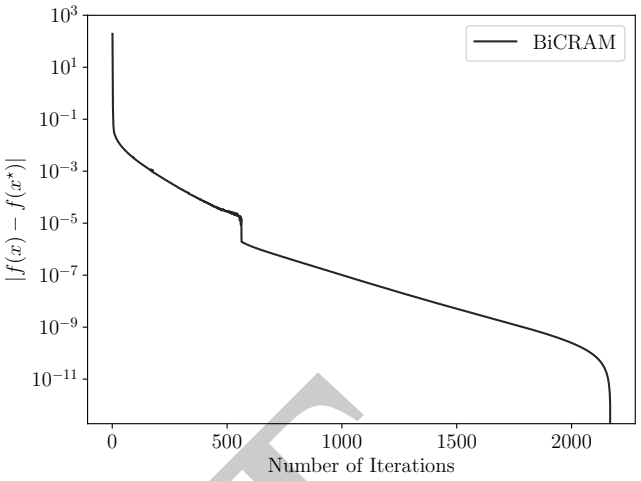

Fig. 4. Convergence curve of BiCRAM. The horizontal axis refers to the outer iterations in Alg. 2.

Algorithm 3 An ADMM-based algorithm for solving (32)

1: **Input:** $\mathbf{A}$, $\mathbf{b}$, $\mathbf{u}$, $\mathbf{Z}^{(0)}$, λ_1, λ_2, ρ
2: **Initialize** $\mathbf{Z} \leftarrow \mathbf{Z}^{(0)}$
3: **Until** stopping criterion is satisfied, **Do**
4: $\quad\mathbf{x} \leftarrow (\mathbf{A}^H\mathbf{A}+(\lambda_1+\rho)\mathbf{I})^{-1}(\mathbf{A}^H\mathbf{b}+\lambda_1\mathbf{u}+\rho\mathbf{z}_1-\mathbf{y}_1)$
5: $\quad\mathbf{Z} \leftarrow \mathrm{Prox}_{\ell_{1,2},\lambda_2/\rho}\left(\begin{pmatrix}\mathbf{x} & \mathbf{u}\end{pmatrix}+(1/\rho)\mathbf{Y}\right)$
6: $\quad\mathbf{Y} \leftarrow \mathbf{Y}+\rho\left(\begin{pmatrix}\mathbf{x} & \mathbf{u}\end{pmatrix}-\mathbf{Z}\right)$
7: **Output:** $\mathbf{z}_1$

$\mathrm{Prox}_{\ell_{1,2},\lambda} : \mathbb{C}^{L\times 2} \to \mathbb{C}^{L\times 2}$ is the proximal operator of the $\ell_{1,2}$ norm scaled by λ (e.g., [61]), i.e.,

$$\mathrm{Prox}_{\ell_{1,2},\lambda}(\mathbf{X}) \coloneqq \arg\min_{\mathbf{Z}}\ \lambda\|\mathbf{Z}\|_{1,2}+\frac{1}{2}\|\mathbf{X}-\mathbf{Z}\|_F^2, \tag{34}$$

whose i-th row is given by [61, §6.5.4]

$$\mathrm{Prox}_{\ell_{1,2},\lambda}(\mathbf{X})^i = (1-\lambda/\|\mathbf{x}^i\|_2)_+\,\mathbf{x}^i, \tag{35}$$

where $(x)_+ \coloneqq \max(x, 0)$. This proximal operator promotes (the columns of) $\mathbf{Z}$ to be jointly sparse and therefore $\mathbf{x}$ to share the same support with $\mathbf{u}$.

Due to the nonconvexity of (31), it is very difficult to establish a convergence guarantee for Alg. 2 from a theoretical point of view. However, our experiments with real SAR tomographic data (see Sec. V) show that it converges empirically. As an example, Fig. 4 depicts a convergence curve in case of two scatterers that are closely located (#6 in Sec. V-C).

In terms of regularization parameter tuning, we adopt the approach of sampling the solution path $(\lambda_1, \lambda_2) \mapsto \mathbf{x}$, and selecting the solution with the highest penalized likelihood (14). Last but not least, this procedure can be simplified by performing 1-D search, i.e., fixing one parameter and tuning the other at a time.

B. Implementation

This subsection addresses several implementation aspects that contribute to accelerating Alg. 3 (and therefore Alg. 2).

The exposition is based on an ADMM-based algorithm for solving the ℓ_1-regularized least squares (L1RLS) problem:

$$\underset{\mathbf{x}}{\text{minimize}}\, \frac{1}{2}\|\mathbf{A}\mathbf{x}-\mathbf{b}\|_2^2+\lambda\|\mathbf{x}\|_1. \tag{36}$$

This is more suitable for demonstrating the power of different acceleration techniques, since each of its subproblems has an analytical solution and does not involve iteratively solving another optimization problem (cf. Alg. 2). Besides, it will also be used as a reference in Sec. V.

Now consider (36) in its equivalent form:

$$\begin{aligned} \underset{\mathbf{x},\mathbf{z}}{\text{minimize}} \quad & \frac{1}{2}\|\mathbf{A}\mathbf{x}-\mathbf{b}\|_2^2+\lambda\|\mathbf{z}\|_1 \\ \text{subject to} \quad & \mathbf{x}-\mathbf{z}=\mathbf{0}. \end{aligned} \tag{37}$$

Applying the ADMM update rules leads to Alg. 4.

Algorithm 4 An ADMM-based algorithm for solving (36)

1: **Input:** $\mathbf{A}$, $\mathbf{b}$, $\mathbf{z}^{(0)}$, λ, ρ
2: **Initialize** $\mathbf{z}\leftarrow\mathbf{z}^{(0)}$
3: **Until** stopping criterion is satisfied, **Do**
4: $\quad\mathbf{x}\leftarrow(\mathbf{A}^H\mathbf{A}+\rho\mathbf{I})^{-1}(\mathbf{A}^H\mathbf{b}+\rho\mathbf{z}-\mathbf{y})$
5: $\quad\mathbf{z}\leftarrow\mathrm{Prox}_{\ell_1,\lambda/\rho}\left(\mathbf{x}+(1/\rho)\mathbf{y}\right)$
6: $\quad\mathbf{y}\leftarrow\mathbf{y}+\rho\left(\mathbf{x}-\mathbf{z}\right)$
7: **Output:** $\mathbf{z}$

Likewise, $\mathrm{Prox}_{\ell_1,\lambda}:\mathbb{C}^L\to\mathbb{C}^L$ is the proximal operator of the ℓ_1 norm scaled by λ (also known as the soft thresholding operator [62]):

$$\mathrm{Prox}_{\ell_1,\lambda}(\mathbf{x})\coloneqq\underset{\mathbf{z}}{\arg\min}\ \lambda\|\mathbf{z}\|_1+\frac{1}{2}\|\mathbf{x}-\mathbf{z}\|_2^2, \tag{38}$$

whose i-th entry is given by [61, §6.5.2]

$$\mathrm{Prox}_{\ell_1,\lambda}(\mathbf{x})_i=(1-\lambda/|x_i|)_+\,x_i. \tag{39}$$

The first technique provides an easier way for the $\mathbf{x}$-update.

1) Matrix inversion lemma: In Alg. 3 and 4, an L-by-L matrix needs to be inverted. For large L, a direct exact approach can be tedious. Instead, we exploit the following lemma.

Lemma 5 (Matrix inversion lemma [63])**.** For any $\mathbf{A}\in\mathbb{C}^{n\times m}$, $\mathbf{B}\in\mathbb{C}^{m\times n}$ and nonsingular $\mathbf{C}\in\mathbb{C}^{n\times n}$, we have

$$(\mathbf{A}\mathbf{B}+\mathbf{C})^{-1}=\mathbf{C}^{-1}-\mathbf{C}^{-1}\mathbf{A}(\mathbf{I}+\mathbf{B}\mathbf{C}^{-1}\mathbf{A})^{-1}\mathbf{B}\mathbf{C}^{-1}. \tag{40}$$

Lemma 5 suggests a more efficient method if inverting $\mathbf{C}$ is straightforward. This is the case for matrices in the form of $\mathbf{A}^H\mathbf{A}+\rho\mathbf{I}$ since

$$(\mathbf{A}^H\mathbf{A}+\rho\mathbf{I})^{-1}=\frac{1}{\rho}\mathbf{I}-\frac{1}{\rho^2}\mathbf{A}^H\left(\mathbf{I}+\frac{1}{\rho}\mathbf{A}\mathbf{A}^H\right)^{-1}\mathbf{A}, \tag{41}$$

i.e., instead of the original L-by-L matrix, only an N'-by-N' matrix needs to be inverted.

Alternatively, the least squares (sub)problems can be solved iteratively in order to deliver an approximate solution [64], which is known as inexact minimization [53, §3.4.4].

The following techniques can be employed to improve convergence.

2) Varying penalty parameter: The penalty parameter ρ can be updated at each iteration. Besides the convergence aspect, this also renders Alg. 4 less dependent on the initial choice of ρ. A common heuristic [53, §3.4.1] is to set

$$\rho^{(k+1)}\coloneqq\begin{cases}\tau\rho^{(k)} & \text{if } \|\mathbf{r}^{(k)}\|_2>\mu\|\mathbf{s}^{(k)}\|_2\\ \rho^{(k)}/\tau & \text{if } \|\mathbf{s}^{(k)}\|_2>\mu\|\mathbf{r}^{(k)}\|_2\\ \rho^{(k)} & \text{otherwise}\end{cases} \tag{42}$$

at the $(k+1)$th iteration, where $\tau,\mu>1$ are parameters, $\mathbf{r}^{(k)}\coloneqq\mathbf{x}^{(k)}-\mathbf{z}^{(k)}$ is the primal residual, and $\mathbf{s}^{(k)}\coloneqq\rho^{(k)}(\mathbf{z}^{(k)}-\mathbf{z}^{(k-1)})$ is the dual residual. As $k\to\infty$, $\mathbf{r}^{(k)}$ and $\mathbf{s}^{(k)}$ both converge to $\mathbf{0}$. Intuitively, increasing ρ tends to put a larger penalty on the augmenting term $(\rho/2)\|\mathbf{x}-\mathbf{z}\|_2^2$ in the augmented Lagrangian and consequently decrease $\|\mathbf{r}^{(k)}\|_2$ on the one hand, and to increase $\|\mathbf{s}^{(k)}\|_2$ by definition on the other and vice versa. The rationale is to balance $\mathbf{r}^{(k)}$ and $\mathbf{s}^{(k)}$ so that they are approximately of the same order. Naturally, one downside is that (41) needs to be recomputed whenever ρ changes.

3) Diagonal preconditioning: The augmenting term $(\rho/2)\|\mathbf{x}-\mathbf{z}\|_2^2$ in the augmented Lagrangian can be replaced by

$$(1/2)\langle\mathbf{P}(\mathbf{x}-\mathbf{z}),\mathbf{x}-\mathbf{z}\rangle, \tag{43}$$

where $\mathbf{P}\succ\mathbf{0}$ is a real diagonal matrix. Note that this falls under the category of more general augmenting terms [53, §3.4.2]. By means of this, Alg. 4 is deprived of the burden of choosing ρ and the ADMM updates become

$$\begin{aligned}\mathbf{x}&\leftarrow(\mathbf{A}^H\mathbf{A}+\mathbf{P})^{-1}(\mathbf{A}^H\mathbf{b}+\mathbf{P}\mathbf{z}-\mathbf{y})\\ \mathbf{z}&\leftarrow\mathrm{Prox}_{\ell_1,\lambda/\mathbf{p}}\left(\mathbf{x}+\mathbf{P}^{-1}\mathbf{y}\right)\\ \mathbf{y}&\leftarrow\mathbf{y}+\mathbf{P}\left(\mathbf{x}-\mathbf{z}\right),\end{aligned} \tag{44}$$

where $\mathbf{p}\coloneqq\mathrm{Diag}(\mathbf{P})$, and $\mathrm{Prox}_{\ell_1,\mathbf{w}}:\mathbb{C}^L\to\mathbb{C}^L$ is the proximal operator of the weighted ℓ_1 norm with weights $\mathbf{w}\in\mathbb{R}_{++}^L$:

$$\mathrm{Prox}_{\ell_1,\mathbf{w}}(\mathbf{x})\coloneqq\underset{\mathbf{z}}{\arg\min}\ \|\mathbf{z}\|_{\mathbf{w},1}+\frac{1}{2}\|\mathbf{x}-\mathbf{z}\|_2^2, \tag{45}$$

whose i-th entry is given by

$$\mathrm{Prox}_{\ell_1,\mathbf{w}}(\mathbf{x})_i=(1-w_i/|x_i|)_+\,x_i. \tag{46}$$

In case $\mathbf{A}^H\mathbf{A}$ is ill-conditioned (such as in SAR tomography), $\mathbf{P}$ can be interpreted as a preconditioner. Needless to say, Lemma 5 can be also applied to invert $\mathbf{A}^H\mathbf{A}+\mathbf{P}$.

Pock and Chambolle (2011) proposed a simple and elegant way to construct diagonal preconditioners for a primal-dual algorithm [65] [54, §15.2] with guaranteed convergence:

$$p_i\coloneqq1/\|\mathbf{a}_i\|_\alpha^\alpha,\quad\forall i\in[L], \tag{47}$$

where $\alpha\in[0,2]$ is a parameter.

4) Over-relaxation: This means inserting between the $\mathbf{x}$- and $\mathbf{z}$-updates of Alg. 4 the following additional update:

$$\mathbf{x}\leftarrow\beta\mathbf{x}+(1-\beta)\mathbf{z}, \tag{48}$$

where $\beta\in[1.5,1.8]$ (see for example [53, §3.4.3] and the references therein).

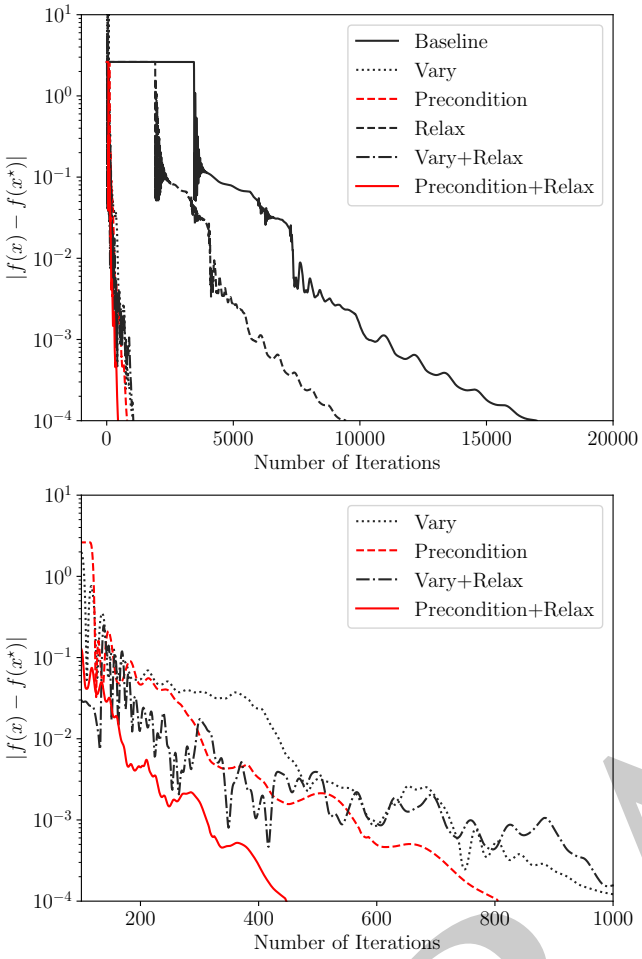

Fig. 5. Convergence curve of Alg. 4 using different acceleration techniques. "Baseline": $\rho = 1$. "Vary": varying penalty parameter. "Precondition": diagonal preconditioning. "Relax": over-relaxation. Bottom: a close-up of the top figure.

Fig. 5 shows the convergence curve of Alg. 4 using different acceleration techniques, as applied to real SAR tomographic data (#6 in Sec. V). Each technique did contribute to accelerating Alg. 4 in comparison to "baseline", where we set $\rho = 1$. The number of iterations of this and five other cases are listed in Tab. II. Obviously, the combination of diagonal preconditioning and over-relaxation was the most competitive one and will therefore be adopted for all the ADMM-based algorithms in the following.

V. Experiment with TerraSAR-X Data

In this section, we report our experimental results with a real SAR data set.

A. Design of Experiment

As a demonstration, we used 31 TerraSAR-X staring spotlight repeat-pass acquisitions of the central Munich area from March 31, 2016 to December 7, 2017. This data set was processed with DLR's Integrated Wide Area Processor [66], [67], as was elaborately described in [17]. In addition to side lobe detection (see [17] and the references therein), any non-peak point inside a main lobe was also removed, since it would otherwise lead to a "ghost" scatterer in the result, as any side lobe point would do too. Our region of interest contains a six-story building ("Nordbau") of the Technical University of Munich (TUM) shown in Fig. 6 (left). The building signature in the SAR intensity image can be observed in Fig. 9, where the regular grid of salient points within the building footprint is a result of triple reflections on three orthogonal surfaces: metal plate (behind window glass), window ledge and brick wall [68]. After main and side lobe detection, a total of 594 points were left, whose azimuth-range positions are shown in Fig. 8 (bottom).

A *single-master* stack was formed by choosing the acquisition from December 20, 2016 as the one and only master. Its vertical wavenumbers are shown in Fig. 7. A sinusoidal basis function was used for modeling periodical motion induced by temperature change. The vertical Rayleigh resolution at scene center is approximately 12.66 m. The Crámer-Rao lower bound (CRLB) of height estimates given the aforementioned periodical deformation model [25] and a nominal signal-to-noise ratio (SNR) of 2 dB is approximately 1.10 m. NLS and L1RLS were applied to this stack for tomographic reconstruction. The latter was solved by Alg. 4 augmented with diagonal preconditioning and over-relaxation (see Sec. IV-B), where we set $\beta = 1.8$ and the choice of α is irrelevant (since $\mathbf{A}$ is a Fourier matrix). The solution path of L1RLS was sampled 11 times with the regularization parameter varying logarithmically from $\lambda_{\min} := 5 \cdot 10^{-2} \|\mathbf{R}^H \mathbf{g}\|_\infty$ to $\lambda_{\max} := 5 \cdot 10^{-1} \|\mathbf{R}^H \mathbf{g}\|_\infty$.

We constructed a *multi-master* stack of small temporal baselines: suppose $1', 2', 3', 4', \ldots$ is a chronologically ordered sequence of SLCs, the interferograms (edges) are $(1', 2')$, $(3', 4')$, etc. (see Fig. 1). As a result, this stack consists of 15 interferograms. Due to the small-baseline feature of this stack, we did not employ any deformation model for the sake of simplicity. NLS and BiCRAM were applied to reconstruct the elevation profile, where the latter was solved by Alg. 3 employing diagonal preconditioning and over-relaxation. Likewise, the solution path of BiCRAM was also sampled 11 times, where λ_1 was fixed as one (since it was deemed relatively insignificant as far as our experience went), and λ_2 was set to vary logarithmically from $\lambda_{\min} := 5 \cdot 10^{-2} \max\left\{\|\mathbf{R}^H \mathbf{g}\|_\infty, \|\mathbf{S}^H \mathbf{g}\|_\infty\right\}$ to $\lambda_{\max} := 5 \cdot 10^{-1} \max\left\{\|\mathbf{R}^H \mathbf{g}\|_\infty, \|\mathbf{S}^H \mathbf{g}\|_\infty\right\}$. The initial solution was given by $\boldsymbol{\gamma}^{(0)} = (\mathbf{R} \circ \overline{\mathbf{S}})^H \mathbf{g}$ due to its simplicity. Alternatively, (28) could be used. In terms of off-grid correction, forward-mode automatic differentiation [69] was employed in order to circumvent analytically differentiating the objective function of (16) for any number of scatterers, and the optimization problem was solved by means of a BFGS implementation [70].

Finally, we built a second small-baseline *multi-master* stack in the identical way as the previous one. In addition, we normalized each interferogram with the corresponding master amplitude. We will refer to this as the *fake single-master* stack, since we treated it as if it had been a *single-master* one. In order to apply the *single-master* approach, we calculated for each interferogram the difference between slave and master

TABLE II
NUMBER OF ITERATIONS USING DIFFERENT ACCELERATION TECHNIQUES

	#1	#2	#3	#4	#5	#6
Baseline	20289	14250	15752	19571	23920	16983
Vary	1445	1101	1780	1958	2005	1033
Precondition	679	480	504	1074	840	805
Relax	11272	7916	8750	10866	13288	9446
Vary+Relax	767	625	871	821	834	1051
Precondition+Relax	377	260	288	595	467	447

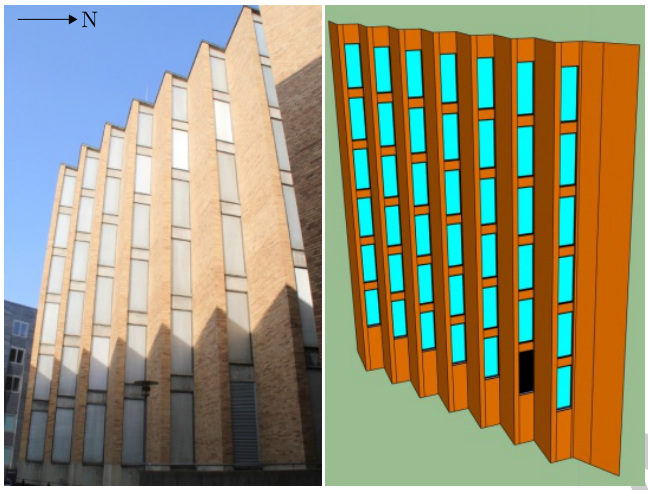

Fig. 6. Eastern facade of the six-story TUM-Nordbau building in our region of interest [68]. Left: in-situ photo. Right: 3-D facade model. The black shape corresponds to a metallic window.

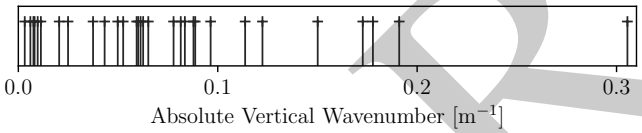

Fig. 7. Single-master absolute vertical wavenumbers. The largest one is approximately 0.31 m^{-1}.

wavenumbers, and used it as if it had been the wavenumber baseline, i.e., by inadequately assuming

$$g_n \overline{g_m} \approx \sum_l \gamma_l \exp\left(-j(k_n - k_m)s_l\right), \tag{49}$$

for each $(m,n) \in \mathbf{E}(\mathbf{G})$. Needless to say, NLS and L1RLS were employed exactly the same as in the single-master case.

The next subsection briefly explains how we generated ground truth data.

B. Generation of Height Ground Truth

Height ground truth data was made available via a SAR imaging geodesy and simulation framework [68]. The starting point was to create a three-dimensional (3-D) facade model from terrestrial measurements, via (drone-borne) camera, tachymeter, measuring rod and differential global positioning system (GPS), with an overall accuracy better than 2 cm and a very high level of details [68]. Ground control points were used for referencing this facade model to an international terrestrial reference frame. A visualization of the 3-D facade model is provided in Fig. 6 (right). The ray-tracing-based RaySAR simulator [71] was employed to simulate dominant scatterers that, as already mentioned in Sec. V-A, correspond to triple reflections on the building facade. With the help of atmospheric and geodynamic corrections from DLR's SAR Geodetic Processor [72], [73] and the newly enhanced TerraSAR-X orbit products [74], their absolute coordinates were converted into azimuth timing, range timing and height that we refer to as *Level 0* ground truth data.

Level 1 ground truth data consists of height at 30 simulated PSs that are matched with real ones. The matching was conducted in the azimuth-range geometry, so as not to be affected by any height estimate error [75]. Fig. 8 (top) shows the height simulations at the sub-pixel azimuth-range positions of the corresponding 30 PSs. This height is relative to a corner reflector that is located on top of a neighboring TUM building and next to a permanent GPS station [68].

In addition, we performed height interpolation for a total of 594 points (see Sec. V-A) in the following way. First of all, the height of each simulated PS was converted into interferometric phase. Next, the distance to the polyline representing the nearest-range cross-section of the building facade was used as the independent variable to construct a 1-D interpolator. In the end, the phase was interpolated at the previously mentioned 594 points and converted back into height. This interpolated height is referred to as the *Level* 2 ground truth and shown in Fig. 8 (bottom). Needless to say, one assumption is that each point, if it does exist, should lie on the building facade. A cross-validation of this 1-D interpolator was performed in [68], where the standard deviation (SD) and median absolute deviation (MAD) were shown to be 0.004 and 0.002 m, respectively.

In the next subsection, our preliminary results are reported.

C. Experimental Results

The experiments can be divided into three categories: single-master, multi-master and fake single-master (see Sec. V-A). In each category, two algorithms were applied for tomographic reconstruction.

As a proof of concept, we selected six points that are very likely subject to facade-roof layover. These six points were chosen in a systematic way: we performed tomographic reconstruction on the *single-master* stack by using Tikhonov regularization (i.e., the ℓ_1 norm in the regularization term

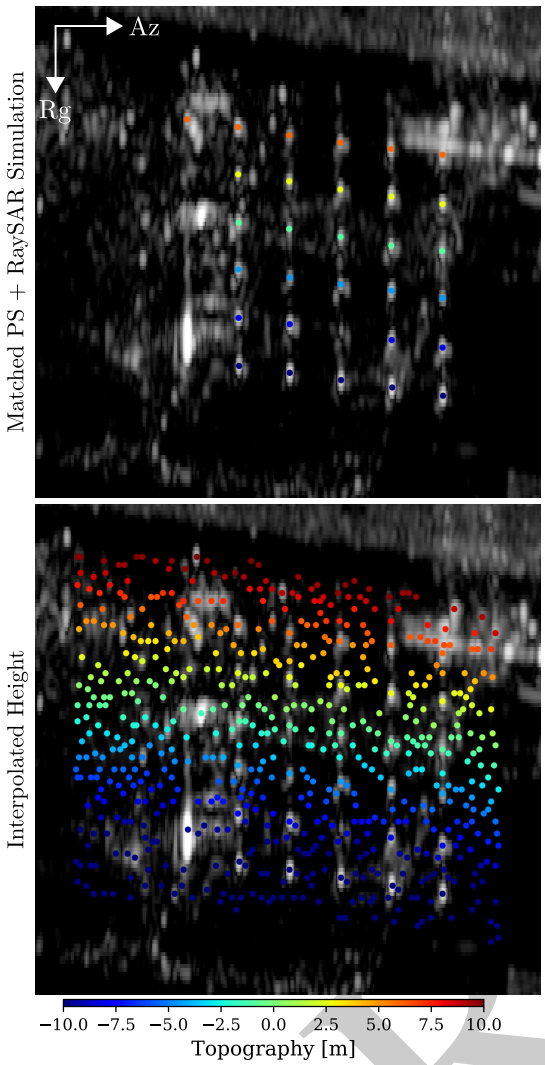

Fig. 8. SAR intensity image and height ground truth of our region of interest. Top: RaySAR height simulations at 30 matched PS coordinates (Level 1). Bottom: interpolated height at 594 facade points (Level 2).

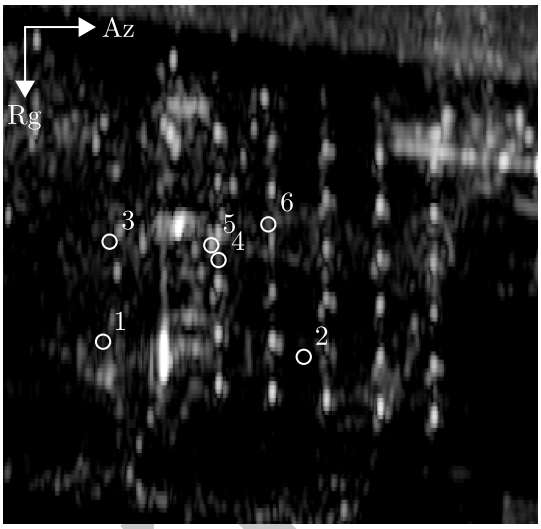

Fig. 9. Locations of six points subject to facade-roof layover.

of (36) is replaced by the ℓ_2 norm), extracted all the seven points containing double scatterers, and discarded one point whose height distance is almost identical to the one of another point. These six points are shown in Fig. 9, where the indices increase with decreasing estimated height distance from approximately 1.5 to 0.8 times the vertical Rayleigh resolution. This ordering agrees approximately with intuition under the assumption that the roof is entirely flat: the higher the scatterer is on the facade, the less is its height distance to the roof.

The estimated height profile is shown in Fig. 10 (#1–3) and 11 (#4–6), where we used the vertical Rayleigh resolution of the *single-master* stack (see Sec. V-A) for normalizing the x-axis. The height estimates are listed in Tab. III. In the *single-master* setting, NLS and L1RLS produced very similar height profiles, despite the occasional sporadic artifacts in the latter which are known to be an intrinsic problem of ℓ_1-regularization. Moreover, the height estimates were identical after off-grid correction. In each case, the height estimate of the lower scatterer fits very well the Level 2 RaySAR simulation of facade. Overall, the *multi-master* results are consistent with the *single-master* ones, with deviations of height estimates typically of several decimeters. In the *fake single-master* setting, however, layover separation was only successful in the fifth case, presumably due to the high SNR (see the brightness of the point in Fig. 9). When the height distance is significantly larger than the vertical Rayleigh resolution (#1–2), both NLS and L1RLS could reconstruct double scatterers, but only the one with larger amplitude could pass model-order selection. When the height distance approaches the vertical Rayleigh resolution or becomes even smaller (#3, 4, 6), neither algorithm could reconstruct a second scatterer, and the height estimate of the single scatterer after off-grid correction is also arguably wrong. We are therefore convinced by this simple experiment that the conventional *single-master* approach, if applied to a *multi-master* stack, can be insufficient for layover separation.

Naturally, we also performed tomographic reconstruction for all the 594 points within the building footprint in Fig. 8 (bottom). Tab. IV lists the overall runtime on a desktop with a quad-core Intel processor at 3.40 GHz and 16-GB RAM. Note that the periodical deformation model was only used in the *single-master* case, and the solution path of L1RLS or BiCRAM was sampled 11 times (see Sec. V-A). The height estimates of single and double scatterers are shown in Fig. 12–14 for the three categories, respectively. In case of double scatterers, the higher one was plotted. The seemingly messy appearance in the left column is due to the fact that single scatterers originate from both facade and roof. In spite of this, the gradual color transition at the 30 PSs from far- to near-range agrees visually very well with the Level 1 ground truth in Fig. 8 (top). Tab. V lists the number of scatterers in each case. In the *single-scatterer* setting, NLS detected almost twice as many double scatterers as L1RLS. This is presumably due to a higher false positive rate: at 2 out of 30 PSs (fifth/second row from near range, and fifth/fifth column

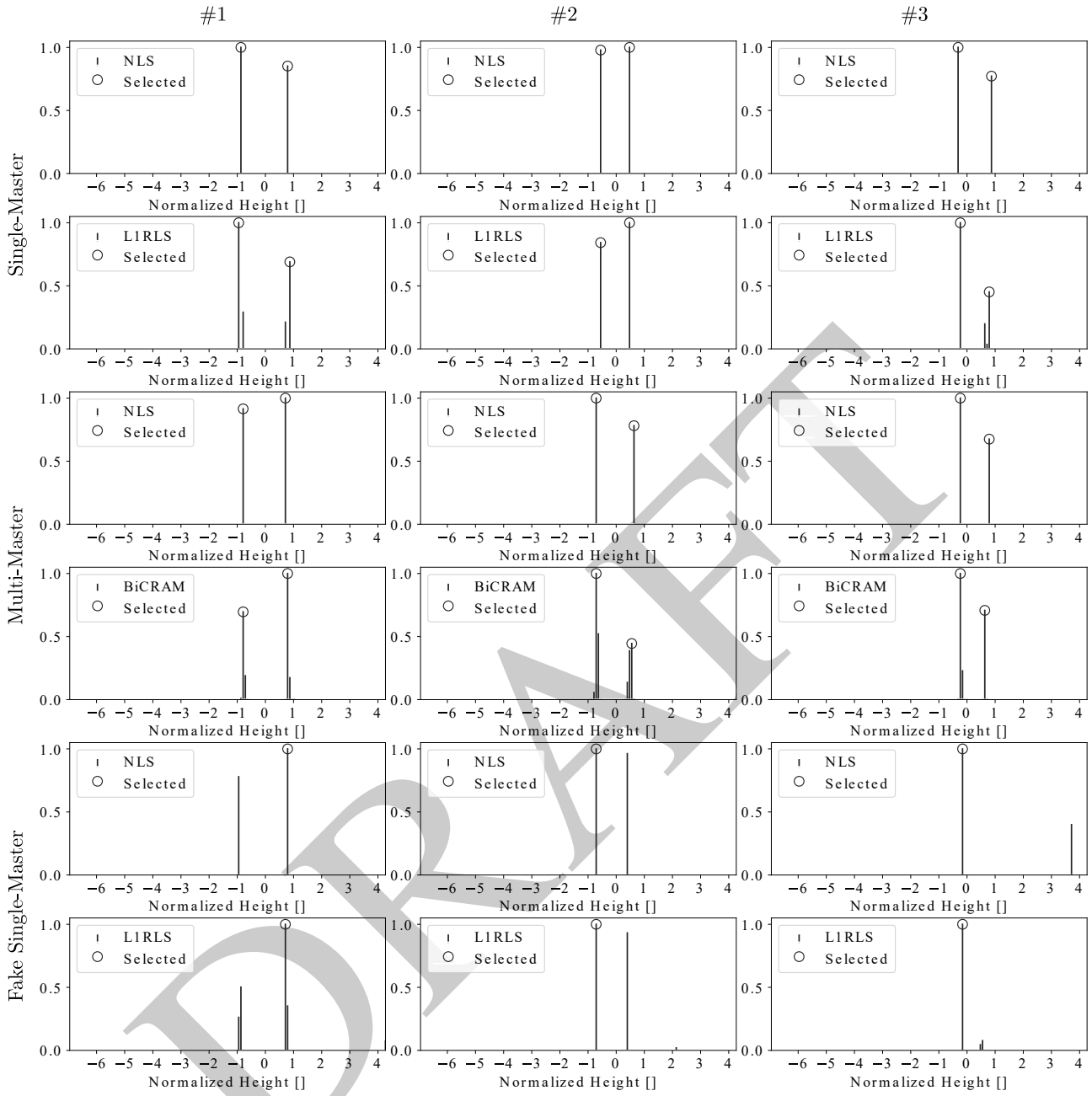

Fig. 10. Height profile estimate of #1–3 in Fig. 9. Vertical line: before model-order selection. Circle: after model-order selection.

TABLE III
SINGLE- AND MULTI-MASTER HEIGHT ESTIMATES OF SIX LAYOVER CASES [M]

		#1		#2		#3		#4		#5		#6	
		h_1	h_2	h_1	h_2	h_1	h_2	h_1	h_2	h_1	h_2	h_1	h_2
RaySAR		−9.22	–	−8.91	–	−2.39	–	−2.87	–	−1.59	–	0.55	–
Single-Master	NLS	−10.27	9.10	−8.14	6.97	−4.27	10.72	−2.63	9.97	−1.95	10.03	0.98	11.34
	L1RLS	−10.27	9.10	−8.14	6.97	−4.27	10.72	−2.63	9.97	−1.95	10.03	0.98	11.34
Multi-Master	NLS	−10.15	9.47	−8.96	8.23	−3.50	9.98	−2.06	10.45	−0.37	10.90	0.66	10.85
	BiCRAM	−10.15	9.47	−8.96	8.23	−3.50	9.98	−2.06	10.45	−0.37	10.90	0.66	10.85
Fake Single-Master	NLS	9.35	–	−9.12	–	−1.64	–	1.19	–	0.63	10.03	3.47	–
	L1RLS	9.35	–	−9.12	–	−1.64	–	1.19	–	0.63	10.03	3.47	–

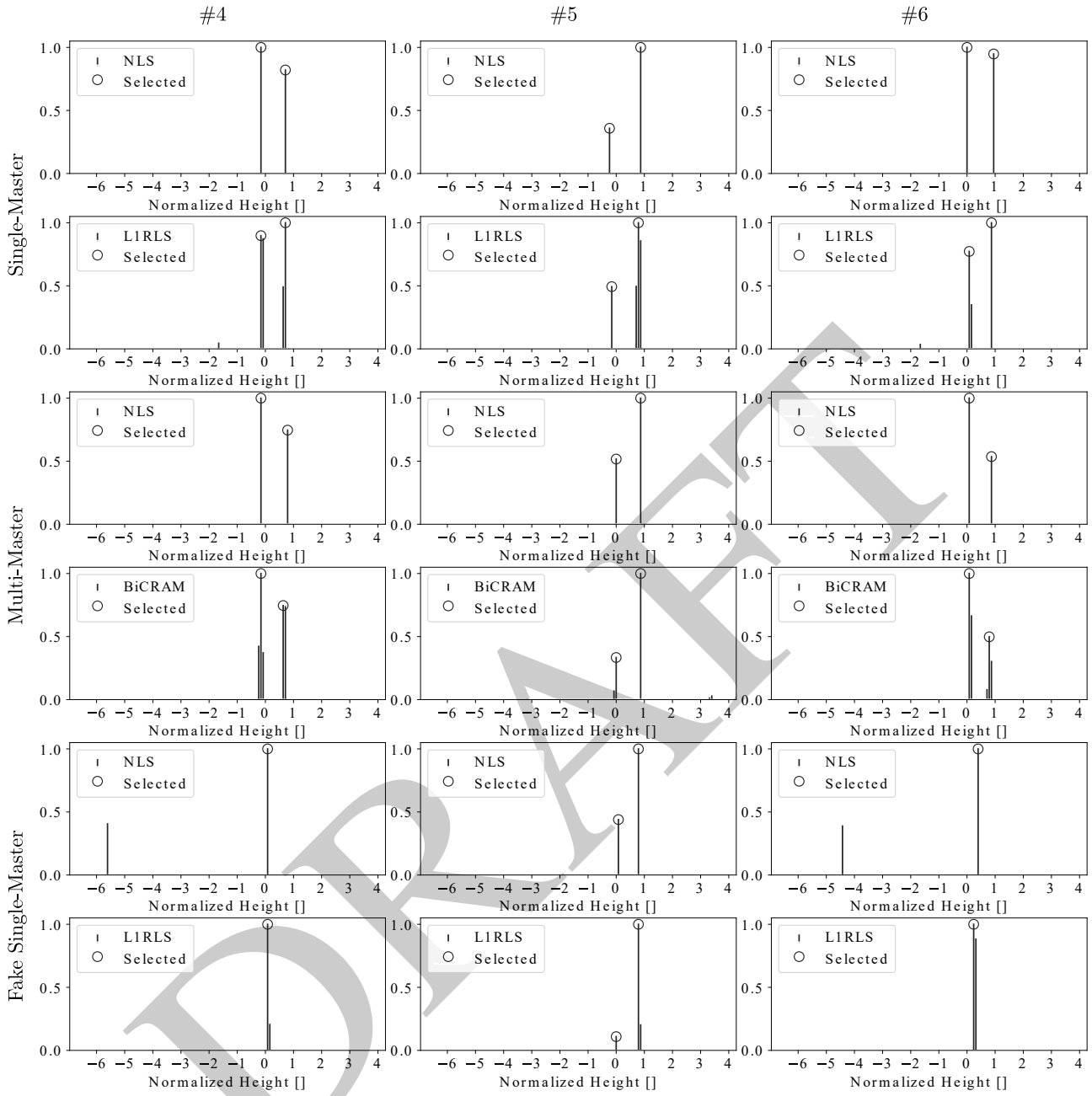

Fig. 11. Height profile estimate of #4–6 in Fig. 9. Vertical line: before model-order selection. Circle: after model-order selection.

from late azimuth on the 6×5 regular grid) double scatterers were detected, although there should only be single ones. The number of double scatterers in the *multi-master* case is in the same order as *single-master* L1RLS, and the ratio between the number of single and the one of double scatterers is also similar. We attribute the smaller number of single scatterers to the nonconvexity of the optimization problem. In particular, as Thm. 2(b) suggests, a certain condition needs to be fulfilled for any nonzero solution of height profile estimate to exist at all, let alone whether an algorithm can provably recover it. In the *fake single-master* category, many fewer double scatterers were produced. This is presumably due to double scatterers being misdetected as single scatterers, which occurred 5 out of 6 times in the previous experiment (see Fig. 10 and 11).

The next subsection elucidates how we validated the height estimates with Level 1 and 2 ground truth data.

D. Validation

Since the height ground truth is limited to facade only (see Sec. V-B), the validation was focused on single scatterers by following two approaches: the first one uses 30 PSs, and the second one is based on extracted facade points.

As already mentioned in Sec. V-A, the 30 PSs constituting the Level 1 ground truth in Fig. 8 (top) are caused by triple reflections on the building facade, and are located on

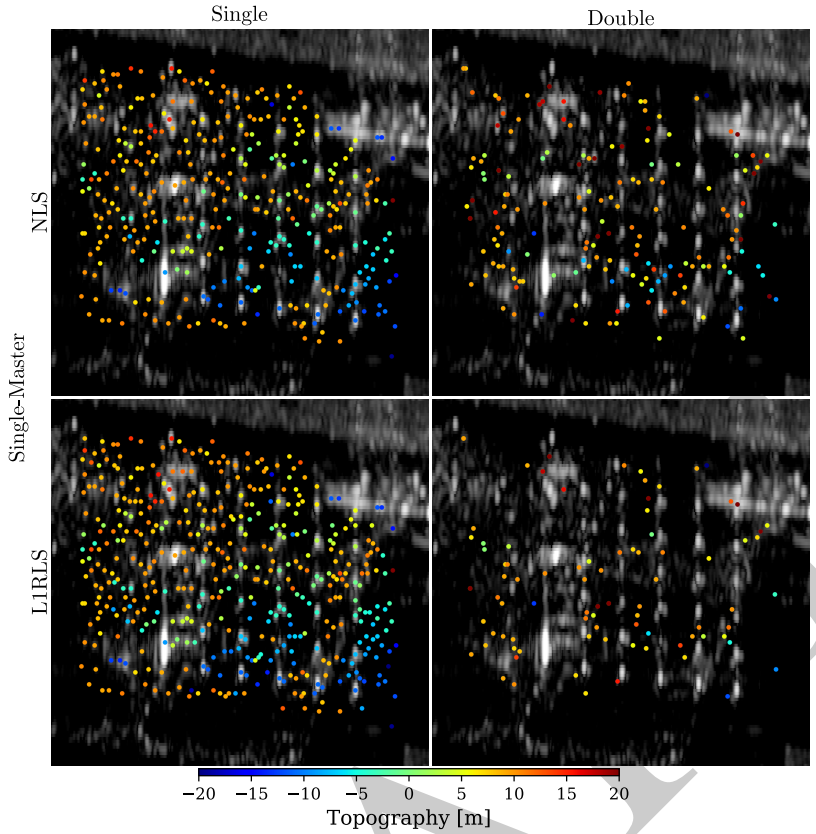

Fig. 12. Single-master height estimates of single and double scatterers. Top: NLS. Bottom: L1RLS.

TABLE IV
SINGLE- AND MULTI-MASTER RUNTIME

		Runtime [s]
Single-Master	NLS	6154
	L1RLS	736
Multi-Master	NLS	460
	BiCRAM	6853
Fake Single-Master	NLS	48
	L1RLS	65

TABLE V
SINGLE- AND MULTI-MASTER NUMBER OF SCATTERERS

		Single	Double	Ratio	Facade
Single-Master	NLS	359	332	1.08	148
	L1RLS	446	168	2.65	189
Multi-Master	NLS	260	158	1.65	124
	BiCRAM	291	118	2.47	133
Fake Single-Master	NLS	360	60	6.00	134
	L1RLS	381	38	10.03	143

a regular grid of salient points. Due to the (almost) identical scattering geometry, these PSs should have similar SNRs and are therefore ideal for height estimate validation. In each of the six cases, single scatterers were correctly detected at all the 30 PSs—with the exception that double scatterers were misdetected by NLS in the *single-master* setting (see Sec. V-C). For this reason, the height estimate error could be evaluated straightforwardly. Fig. 15 shows the normalized histogram and Tab. VI lists some of its statistical parameters. As a reference, the SD and MAD of height estimate error of the PSI result are about 0.28 and 0.22 m, respectively [68]. In each of the three settings (single-master, multi-master and fake single-master), the respective two algorithms performed similarly and no significant difference is visible. A cross-comparison between the multi-master and fake single-master cases revealed the superiority of the former: its histogram is more centered around zero, and both its SD and MAD are slightly smaller. This is unsurprising since we already analyzed the implications of the single-look *multi-master* data model for single scatterers in Sec. II-B. At this point, we could confidently assert that it does make a difference in practice, albeit small, despite the longer (approximately one order considering that the solution path of BiCRAM was sampled 11 times) processing time. Somewhat surprisingly, the *multi-master* result is also slightly better than the *single-master* one. We suspect that this is due to the complication of *single-master* tomographic processing by using the (imperfect) periodical deformation model, and the justified simplification in the *multi-master* case thanks to the small-baseline configuration (so that deformation-induced phase is mitigated via forming interferograms).

The second approach is based on all facade points (Level 2 ground truth) in Fig. 8 (bottom), given that they do exist.

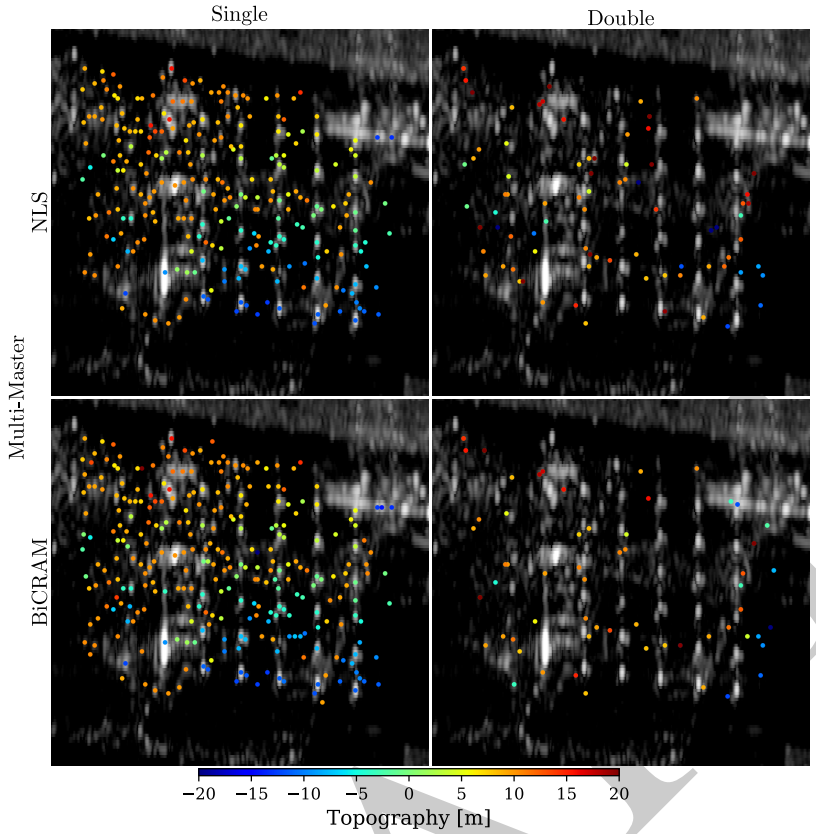

Fig. 13. Multi-master height estimates of single and double scatterers. Top: NLS. Bottom: BiCRAM.

Scatter plots of simulated and estimated height of single scatterers are shown in Fig. 17. It is obvious that many single scatterers are located on the building roof (see the gray dots above diagonal line). In order to extract facade points, we used a threshold of $\pm 3 \times$ CRLB added to the simulated value. The extracted facade points, whose number is given in Tab. V for each case, are shown as black dots and were used for height estimate validation. The normalized histogram is shown in Fig. 16 and some of its statistical parameters are provided in Tab. VII. Likewise, the two respective algorithms performed similarly in each setting, and the *multi-master* height estimate error has slightly less deviation. The SD and MAD are worse in comparison to those in Tab. VII due to the much larger range of SNRs.

The next section concludes this manuscript and suggests some prospective work.

VI. Conclusion and Discussion

The previous sections provided new insights into single-look multi-master SAR tomography. The single-look multi-master data model was established and two algorithms were developed within a common inversion framework. The first algorithm extends the conventional NLS to the single-look multi-master data model, and the second one uses bi-convex relaxation and alternating minimization. Extensive efforts were devoted to studying the nonconvex objective function of the NLS subproblem, and to experimenting with different acceleration techniques for ADMM-based algorithms. We demonstrated with the help of a real TerraSAR-X data set that the conventional *single-master* approach, if applied to a *multi-master* stack, can be insufficient for layover separation, even when the height distance between two scatterers is significantly larger than the vertical Rayleigh resolution. By means of a SAR imaging geodesy and simulation framework, we managed to generate two levels of height ground truth. The height estimates in each of the three settings were validated at either 30 PSs or hundreds of extracted facade points. Overall, the *multi-master* approach performed slightly better, although it was computationally more demanding.

A special case of the general problem analyzed so far is single-look bistatic SAR tomography using only bistatic (or pursuit monostatic) interferograms. On the one hand, the advantages are that bistatic interferograms are (almost) APS-free, and the data model is still linear for any single scatterer whose reflectivity can be estimated up to a constant phase angle (7). On the other, the disadvantages are that, for double or multiple scatterers, bistatic interferograms are not motion-free (see Sec. II-B), and the data model is nonlinear (9).

An alternative way to formulate the problem in the bistatic setting is to parameterize APS without forming any interferogram. Let $\mathbf{g}$ and $\mathbf{h}$ be the bistatic observations of the master and slave scenes, respectively. We have essentially two data sets:

$$\mathbf{g} \approx (\mathbf{R}\boldsymbol{\gamma}) \circ \exp(j\boldsymbol{\phi}), \quad \mathbf{h} \approx (\mathbf{S}\boldsymbol{\gamma}) \circ \exp(j\boldsymbol{\phi}), \tag{50}$$

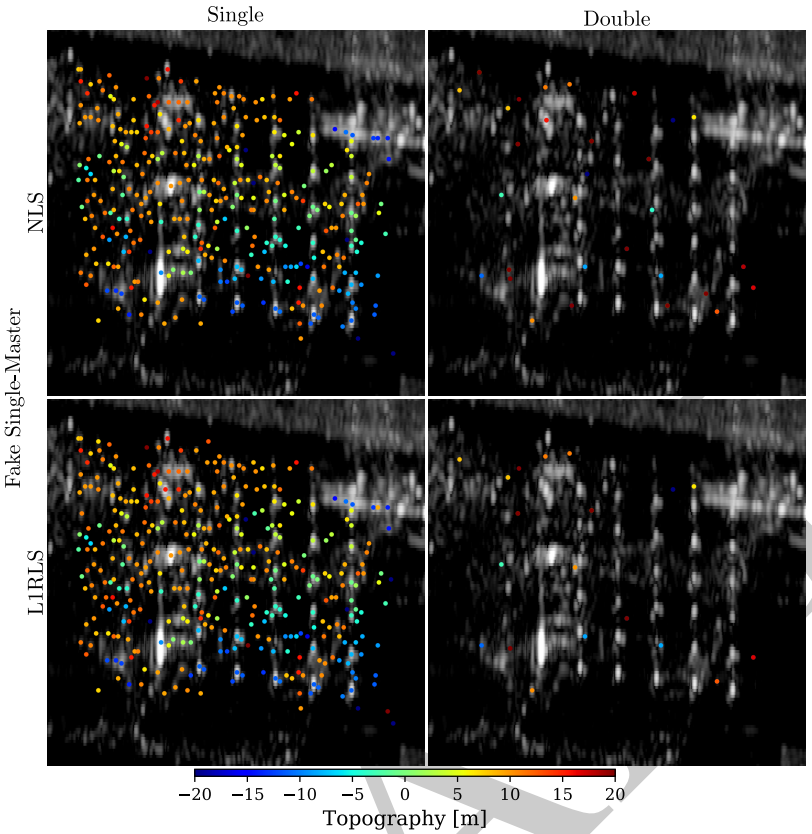

Fig. 14. Fake single-master height estimates of single and double scatterers. Top: NLS. Bottom: L1RLS.

TABLE VI
STATISTICS OF HEIGHT ESTIMATE ERROR [M]: 30 PSS (LEVEL 1)

		Min	Max	Mean	Median	SD	MAD
Single-Master	NLS	−0.81	0.65	−0.30	−0.29	0.34	0.35
	L1RLS	−0.81	0.65	−0.31	−0.29	0.34	0.37
Multi-Master	NLS	−0.88	0.55	−0.33	−0.36	0.31	0.28
	BiCRAM	−0.88	0.55	−0.33	−0.36	0.31	0.28
Fake Single-Master	NLS	−1.02	0.68	−0.43	−0.48	0.34	0.30
	L1RLS	−1.02	0.68	−0.43	−0.48	0.34	0.30

TABLE VII
STATISTICS OF HEIGHT ESTIMATE ERROR [M]: EXTRACTED FACADE POINTS (LEVEL 2)

		Min	Max	Mean	Median	SD	MAD
Single-Master	NLS	−3.03	2.99	−0.40	−0.51	1.23	0.96
	L1RLS	−3.03	2.99	−0.42	−0.49	1.25	0.99
Multi-Master	NLS	−3.04	2.71	−0.49	−0.40	1.13	0.85
	BiCRAM	−3.04	2.71	−0.50	−0.40	1.12	0.86
Fake Single-Master	NLS	−2.93	2.70	−0.38	−0.50	1.15	0.91
	L1RLS	−2.93	2.70	−0.35	−0.48	1.21	1.05

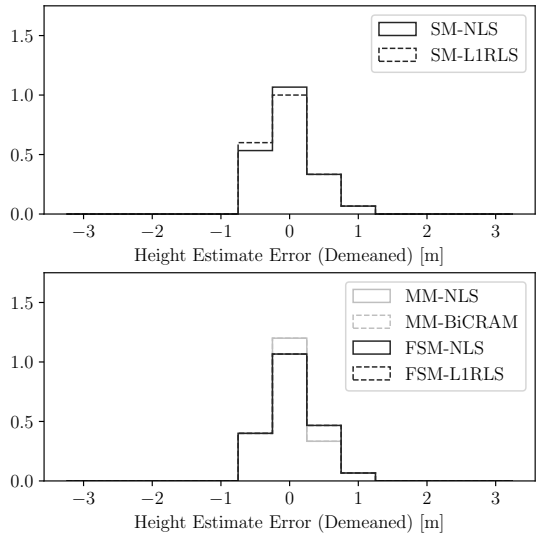

Fig. 15. Normalized histogram of height estimate error of 30 PSs (Level 1). SM: single-master. MM: multi-master. FSM: fake single-master.

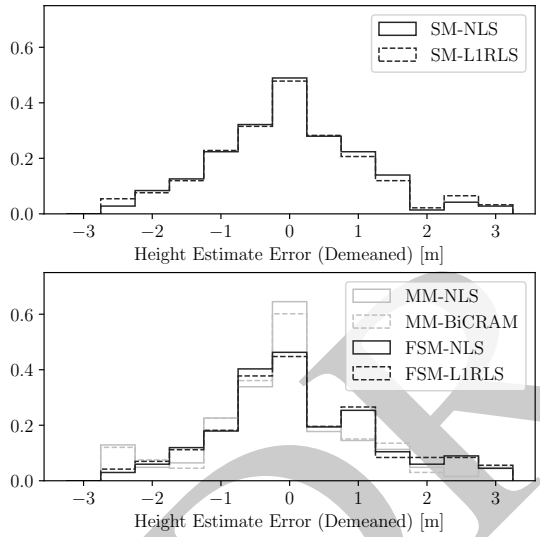

Fig. 16. Normalized histogram of height estimate error of extracted facade points (Level 2). SM: single-master. MM: multi-master. FSM: fake single-master.

where $\boldsymbol{\phi} \in \mathbb{R}^{N'}$ is the APS vector. Under the sparsity or compressibility assumption of $\boldsymbol{\gamma}$, one could consider the following problem:

$$\begin{aligned}\underset{\boldsymbol{\gamma},\boldsymbol{\phi}}{\text{minimize}} \quad & \frac{1}{2}\|(\mathbf{R}\boldsymbol{\gamma}) \circ \exp(j\boldsymbol{\phi}) - \mathbf{g}\|_2^2 + \\ & \frac{1}{2}\|(\mathbf{S}\boldsymbol{\gamma}) \circ \exp(j\boldsymbol{\phi}) - \mathbf{h}\|_2^2 + \lambda\|\boldsymbol{\gamma}\|_1,\end{aligned} \tag{51}$$

or more compactly

$$\underset{\boldsymbol{\gamma},\boldsymbol{\phi}}{\text{minimize}} \, \frac{1}{2}\|(\tilde{\mathbf{R}}\boldsymbol{\gamma}) \circ (\tilde{\mathbf{I}}\exp(j\boldsymbol{\phi})) - \tilde{\mathbf{g}}\|_2^2 + \lambda\|\boldsymbol{\gamma}\|_1, \tag{52}$$

where $\tilde{\mathbf{R}} \coloneqq \begin{pmatrix}\mathbf{R}\\ \mathbf{S}\end{pmatrix}$, $\tilde{\mathbf{I}} \coloneqq \begin{pmatrix}\mathbf{I}\\ \mathbf{I}\end{pmatrix}$, and $\tilde{\mathbf{g}} \coloneqq \begin{pmatrix}\mathbf{g}\\ \mathbf{h}\end{pmatrix}$. Note that this problem is bi-convex in $\boldsymbol{\gamma}$ and $\boldsymbol{\phi}$.

Inspired by PSI, another related problem is SAR tomography on edges. Let $\boldsymbol{\gamma}$ and $\boldsymbol{\theta}$ represent the reflectivity profiles of two neighboring points, and their interferometric observations be denoted as $\mathbf{g}$ and $\mathbf{h}$, respectively. Consider the following problem:

$$\underset{\boldsymbol{\gamma},\boldsymbol{\theta}}{\text{minimize}} \, \frac{1}{2}\|(\mathbf{R}\boldsymbol{\gamma}) \circ (\overline{\mathbf{S}\boldsymbol{\theta}}) - \mathbf{g} \circ \overline{\mathbf{h}}\|_2^2 + \lambda_1\|\boldsymbol{\gamma}\|_1 + \lambda_2\|\boldsymbol{\theta}\|_1, \tag{53}$$

which is bi-convex in $\boldsymbol{\gamma}$ and $\boldsymbol{\theta}$. Likewise, the rationale of $\mathbf{g} \circ \overline{\mathbf{h}}$ is to mitigate APS for neighboring points. Alternatively, a parametric approach similar to (51) could also be considered.

Appendix A
Recap of ADMM

ADMM [53] solves a minimization problem in the form of

$$\begin{aligned}\underset{\mathbf{x},\mathbf{z}}{\text{minimize}} \quad & f(\mathbf{x}) + g(\mathbf{z}) \\ \text{subject to} \quad & \mathbf{C}\mathbf{x} + \mathbf{D}\mathbf{z} = \mathbf{e}\end{aligned} \tag{54}$$

by alternatively minimizing its augmented Lagrangian [54, p. 509]

$$\begin{aligned}L_\rho(\mathbf{x},\mathbf{y},\mathbf{z}) \coloneqq & f(\mathbf{x}) + g(\mathbf{z}) + \Re\langle \mathbf{y}, \mathbf{C}\mathbf{x} + \mathbf{D}\mathbf{z} - \mathbf{e}\rangle + \\ & (\rho/2)\|\mathbf{C}\mathbf{x} + \mathbf{D}\mathbf{z} - \mathbf{e}\|_2^2,\end{aligned} \tag{55}$$

i.e.,

$$\begin{aligned}\mathbf{x}^{(k+1)} &\coloneqq \underset{\mathbf{x}}{\arg\min}\, L_\rho(\mathbf{x}, \mathbf{y}^{(k)}, \mathbf{z}^{(k)}) \\ \mathbf{z}^{(k+1)} &\coloneqq \underset{\mathbf{z}}{\arg\min}\, L_\rho(\mathbf{x}^{(k+1)}, \mathbf{y}^{(k)}, \mathbf{z}) \\ \mathbf{y}^{(k+1)} &\coloneqq \mathbf{y}^{(k)} + \rho(\mathbf{C}\mathbf{x}^{(k+1)} + \mathbf{D}\mathbf{z}^{(k+1)} - \mathbf{e})\end{aligned} \tag{56}$$

in the kth iteration, where $\rho \in \mathbb{R}_{++}$ is a penalty parameter.

Appendix B
Proof of Proposition 1

The proof uses the following minor result.

Lemma 6. For any $\mathbf{F}, \mathbf{G} \in \mathbb{R}^{n\times n}$ and $c, d \in \mathbb{R}$ such that $c^2 + d^2 = 1$, the following equalities hold:

$$\begin{aligned}\begin{pmatrix}c\mathbf{I} & d\mathbf{I}\\ -d\mathbf{I} & c\mathbf{I}\end{pmatrix}^{-1}\begin{pmatrix}\mathbf{F} & -\mathbf{G}\\ \mathbf{G} & \mathbf{F}\end{pmatrix}\begin{pmatrix}c\mathbf{I} & d\mathbf{I}\\ -d\mathbf{I} & c\mathbf{I}\end{pmatrix} &= \begin{pmatrix}\mathbf{F} & -\mathbf{G}\\ \mathbf{G} & \mathbf{F}\end{pmatrix}, \\ \begin{pmatrix}c\mathbf{I} & d\mathbf{I}\\ -d\mathbf{I} & c\mathbf{I}\end{pmatrix}^{-1}\begin{pmatrix}\mathbf{F} & \mathbf{G}\\ \mathbf{G} & -\mathbf{F}\end{pmatrix} &= \begin{pmatrix}\mathbf{F} & \mathbf{G}\\ \mathbf{G} & -\mathbf{F}\end{pmatrix}\begin{pmatrix}c\mathbf{I} & d\mathbf{I}\\ -d\mathbf{I} & c\mathbf{I}\end{pmatrix}.\end{aligned} \tag{57}$$

Proof. Observe that for any $a, b \in \mathbb{R}$ such that $a^2 + b^2 \neq 0$,

$$\begin{pmatrix}a\mathbf{I} & b\mathbf{I}\\ -b\mathbf{I} & a\mathbf{I}\end{pmatrix}^{-1} = \frac{1}{a^2+b^2}\begin{pmatrix}a\mathbf{I} & -b\mathbf{I}\\ b\mathbf{I} & a\mathbf{I}\end{pmatrix}. \tag{58}$$

The rest of the proof follows via straightforward computations. □

Now we turn our attention to the proposition.

Proof of Proposition 1. First, we prove that $\nabla^2 f(\mathbf{x})$ and $\nabla^2 f\left(\mathbf{x}\exp(j\phi)\right)$ are similar, i.e., there exists an invertible $\mathbf{P}$ such that $\nabla^2 f(\mathbf{x}) = \mathbf{P}^{-1}\nabla^2 f\left(\mathbf{x}\exp(j\phi)\right)\mathbf{P}$.

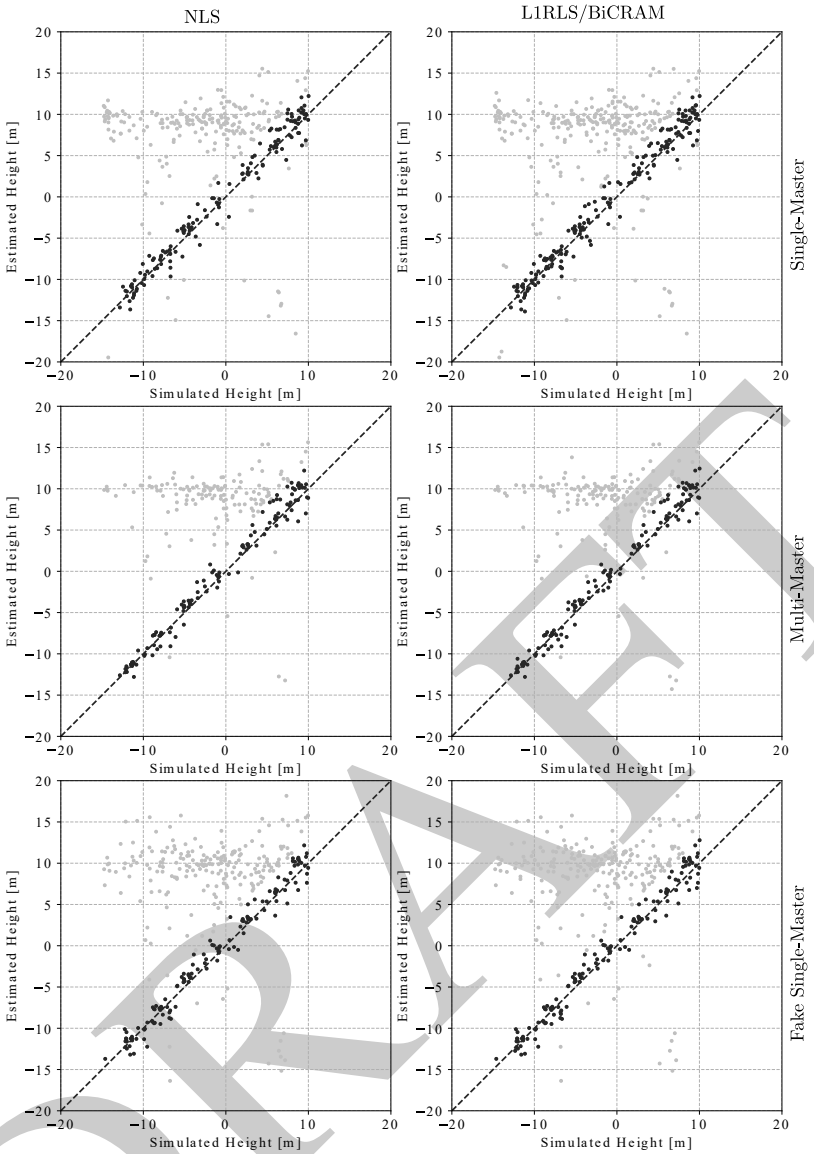

Fig. 17. Scatter plot of simulated and estimated height of single scatterers using Level 2 height ground truth. Black: extracted facade points. Gray: extracted non-facade points.

Observe that

$$\begin{aligned}
&\mathbf{C}\left(\mathbf{x}\exp(j\phi)\right)\\
=\;&\mathbf{A}^H\,\mathrm{Diag}\left((\mathbf{B}\mathbf{x}\exp(j\phi))\circ(\overline{\mathbf{B}\mathbf{x}\exp(j\phi)})\right)\mathbf{A}+\\
&\mathbf{B}^H\,\mathrm{Diag}\left((\mathbf{A}\mathbf{x}\exp(j\phi))\circ(\overline{\mathbf{A}\mathbf{x}\exp(j\phi)})\right)\mathbf{B}\\
=\;&\mathbf{C}(\mathbf{x}),\\
&\mathbf{D}\left(\mathbf{x}\exp(j\phi)\right)\\
=\;&\mathbf{A}^H\,\mathrm{Diag}\left((\mathbf{A}\mathbf{x}\exp(j\phi))\circ(\mathbf{B}\mathbf{x}\exp(j\phi))\right)\overline{\mathbf{B}}+\\
&\mathbf{B}^H\,\mathrm{Diag}\left((\mathbf{A}\mathbf{x}\exp(j\phi))\circ(\mathbf{B}\mathbf{x}\exp(j\phi))\right)\overline{\mathbf{A}}\\
=\;&\mathbf{D}(\mathbf{x})\exp(j2\phi),\\
&\mathbf{E}\left(\mathbf{x}\exp(j\phi)\right)\\
=\;&\mathbf{A}^H\,\mathrm{Diag}\left((\mathbf{A}\mathbf{x}\exp(j\phi))\circ(\overline{\mathbf{B}\mathbf{x}\exp(j\phi)})-\mathbf{b}\right)\mathbf{B}+\\
&\mathbf{B}^H\,\mathrm{Diag}\left((\overline{\mathbf{A}\mathbf{x}\exp(j\phi)})\circ(\mathbf{B}\mathbf{x}\exp(j\phi))-\overline{\mathbf{b}}\right)\mathbf{A}\\
=\;&\mathbf{E}(\mathbf{x}).
\end{aligned}\tag{59}$$

Let $\mathbf{C}\coloneqq\mathbf{C}(\mathbf{x})$, $\mathbf{D}\coloneqq\mathbf{D}(\mathbf{x})$, $\mathbf{E}\coloneqq\mathbf{E}(\mathbf{x})$. The Hessian becomes

$$\begin{aligned}
&\nabla^2 f\left(\mathbf{x}\exp(j\phi)\right)\\
=\;&\begin{pmatrix}\Re(\mathbf{C}) & -\Im(\mathbf{C})\\ \Im(\mathbf{C}) & \Re(\mathbf{C})\end{pmatrix}+\\
&\begin{pmatrix}\Re\left(\mathbf{D}\exp(j2\phi)\right) & \Im\left(\mathbf{D}\exp(j2\phi)\right)\\ \Im\left(\mathbf{D}\exp(j2\phi)\right) & -\Re\left(\mathbf{D}\exp(j2\phi)\right)\end{pmatrix}+\\
&\begin{pmatrix}\Re(\mathbf{E}) & -\Im(\mathbf{E})\\ \Im(\mathbf{E}) & \Re(\mathbf{E})\end{pmatrix}\\
=\;&\begin{pmatrix}\Re(\mathbf{C}+\mathbf{E}) & -\Im(\mathbf{C}+\mathbf{E})\\ \Im(\mathbf{C}+\mathbf{E}) & \Re(\mathbf{C}+\mathbf{E})\end{pmatrix}+\\
&\begin{pmatrix}\Re(\mathbf{D}) & \Im(\mathbf{D})\\ \Im(\mathbf{D}) & -\Re(\mathbf{D})\end{pmatrix}\begin{pmatrix}\cos(2\phi)\mathbf{I} & \sin(2\phi)\mathbf{I}\\ -\sin(2\phi)\mathbf{I} & \cos(2\phi)\mathbf{I}\end{pmatrix}.
\end{aligned}\tag{60}$$

The choice of $\mathbf{P}$ can be divided into two cases depending on the value of ϕ.

In the trivial case, $\phi = (2k+1)\pi/2$ for some $k \in \mathbb{Z}$. Let

$$\mathbf{P} \coloneqq \begin{pmatrix} \mathbf{0} & -\mathbf{I} \\ \mathbf{I} & \mathbf{0} \end{pmatrix}. \tag{61}$$

This leads to

$$\begin{aligned} & \mathbf{P}^{-1}\nabla^2 f\left(\mathbf{x}\exp(j\phi)\right)\mathbf{P} \\ = \; & \begin{pmatrix} \mathbf{0} & -\mathbf{I} \\ \mathbf{I} & \mathbf{0} \end{pmatrix}^{-1} \begin{pmatrix} \Re(\mathbf{C}+\mathbf{E}) & -\Im(\mathbf{C}+\mathbf{E}) \\ \Im(\mathbf{C}+\mathbf{E}) & \Re(\mathbf{C}+\mathbf{E}) \end{pmatrix} \begin{pmatrix} \mathbf{0} & -\mathbf{I} \\ \mathbf{I} & \mathbf{0} \end{pmatrix} + \\ & \begin{pmatrix} \mathbf{0} & -\mathbf{I} \\ \mathbf{I} & \mathbf{0} \end{pmatrix}^{-1} \begin{pmatrix} \Re(\mathbf{D}) & \Im(\mathbf{D}) \\ \Im(\mathbf{D}) & -\Re(\mathbf{D}) \end{pmatrix} \begin{pmatrix} -\mathbf{I} & \mathbf{0} \\ \mathbf{0} & -\mathbf{I} \end{pmatrix} \begin{pmatrix} \mathbf{0} & -\mathbf{I} \\ \mathbf{I} & \mathbf{0} \end{pmatrix} \\ = \; & \begin{pmatrix} \Re(\mathbf{C}+\mathbf{E}) & -\Im(\mathbf{C}+\mathbf{E}) \\ \Im(\mathbf{C}+\mathbf{E}) & \Re(\mathbf{C}+\mathbf{E}) \end{pmatrix} + \\ & \begin{pmatrix} \Re(\mathbf{D}) & \Im(\mathbf{D}) \\ \Im(\mathbf{D}) & -\Re(\mathbf{D}) \end{pmatrix} \begin{pmatrix} \mathbf{0} & -\mathbf{I} \\ \mathbf{I} & \mathbf{0} \end{pmatrix} \begin{pmatrix} -\mathbf{I} & \mathbf{0} \\ \mathbf{0} & -\mathbf{I} \end{pmatrix} \begin{pmatrix} \mathbf{0} & -\mathbf{I} \\ \mathbf{I} & \mathbf{0} \end{pmatrix} \\ = \; & \begin{pmatrix} \Re(\mathbf{C}+\mathbf{E}) & -\Im(\mathbf{C}+\mathbf{E}) \\ \Im(\mathbf{C}+\mathbf{E}) & \Re(\mathbf{C}+\mathbf{E}) \end{pmatrix} + \begin{pmatrix} \Re(\mathbf{D}) & \Im(\mathbf{D}) \\ \Im(\mathbf{D}) & -\Re(\mathbf{D}) \end{pmatrix} \\ = \; & \nabla^2 f(\mathbf{x}), \end{aligned} \tag{62}$$

where the second equality follows from Lemma 6.

In the non-trivial case, $\phi \neq (2k+1)\pi/2$ for any $k \in \mathbb{Z}$. Let

$$\mathbf{P} \coloneqq \begin{pmatrix} \sqrt{\frac{1+\cos(2\phi)}{2}}\mathbf{I} & -\frac{\sin(2\phi)}{\sqrt{2(1+\cos(2\phi))}}\mathbf{I} \\ \frac{\sin(2\phi)}{\sqrt{2(1+\cos(2\phi))}}\mathbf{I} & \sqrt{\frac{1+\cos(2\phi)}{2}}\mathbf{I} \end{pmatrix}. \tag{63}$$

Likewise, the same equality holds.

Finally, we use the similarity property to show that an eigenvalue of $\nabla^2 f(\mathbf{x})$ is also an eigenvalue of $\nabla^2 f\left(\mathbf{x}\exp(j\phi)\right)$.

Let $(\lambda, \mathbf{v})$ be an eigenpair of $\nabla^2 f(\mathbf{x})$. The similarity property implies

$$\begin{aligned} & \lambda\mathbf{v} = \nabla^2 f(\mathbf{x})\mathbf{v} = \mathbf{P}^{-1}\nabla^2 f\left(\mathbf{x}\exp(j\phi)\right)\mathbf{P}\mathbf{v} \\ \implies \quad & \nabla^2 f\left(\mathbf{x}\exp(j\phi)\right)\mathbf{P}\mathbf{v} = \lambda\mathbf{P}\mathbf{v}, \end{aligned} \tag{64}$$

i.e., $(\lambda, \mathbf{P}\mathbf{v})$ is an eigenpair of $\nabla^2 f\left(\mathbf{x}\exp(j\phi)\right)$. The proof in the other direction is straightforward. □

Appendix C
Proof of Theorem 2

Before we delve into the proof, it is useful to define a few auxiliary variables. Let

$$\begin{aligned} \tilde{\mathbf{C}} &\coloneqq \begin{pmatrix} \Re(\mathbf{C}) & -\Im(\mathbf{C}) \\ \Im(\mathbf{C}) & \Re(\mathbf{C}) \end{pmatrix}, \\ \tilde{\mathbf{D}} &\coloneqq \begin{pmatrix} \Re(\mathbf{D}) & \Im(\mathbf{D}) \\ \Im(\mathbf{D}) & -\Re(\mathbf{D}) \end{pmatrix}, \\ \tilde{\mathbf{E}} &\coloneqq \begin{pmatrix} \Re(\mathbf{E}) & -\Im(\mathbf{E}) \\ \Im(\mathbf{E}) & \Re(\mathbf{E}) \end{pmatrix}, \end{aligned} \tag{65}$$

so that $\nabla^2 f(\mathbf{x}) = \tilde{\mathbf{C}} + \tilde{\mathbf{D}} + \tilde{\mathbf{E}}$. Likewise, $\tilde{\mathbf{C}}, \tilde{\mathbf{D}}, \tilde{\mathbf{E}} : \mathbb{C}^n \to \mathbb{R}^{2n\times 2n}$ are de facto (composite) functions of $\mathbf{x}$. The proof of the main theorem is based on the following minor result.

Lemma 7. For any $\mathbf{x} \coloneqq \mathbf{x}_R + j\mathbf{x}_I$, the following equalities hold:

$$\begin{aligned} \begin{pmatrix} \mathbf{x}_R^T & \mathbf{x}_I^T \end{pmatrix} \tilde{\mathbf{C}} \begin{pmatrix} \mathbf{x}_R \\ \mathbf{x}_I \end{pmatrix} &= \mathbf{x}^H \mathbf{C} \mathbf{x}, \\ \begin{pmatrix} \mathbf{x}_R^T & \mathbf{x}_I^T \end{pmatrix} \tilde{\mathbf{D}} \begin{pmatrix} \mathbf{x}_R \\ \mathbf{x}_I \end{pmatrix} &= \Re\left(\mathbf{x}^H \mathbf{D} \overline{\mathbf{x}}\right), \\ \begin{pmatrix} \mathbf{x}_R^T & \mathbf{x}_I^T \end{pmatrix} \tilde{\mathbf{E}} \begin{pmatrix} \mathbf{x}_R \\ \mathbf{x}_I \end{pmatrix} &= \mathbf{x}^H \mathbf{E} \mathbf{x}, \\ \tilde{\mathbf{C}} \begin{pmatrix} \mathbf{x}_R \\ \mathbf{x}_I \end{pmatrix} &= \begin{pmatrix} \Re(\mathbf{C}\mathbf{x}) \\ \Im(\mathbf{C}\mathbf{x}) \end{pmatrix}, \\ \tilde{\mathbf{D}} \begin{pmatrix} \mathbf{x}_R \\ \mathbf{x}_I \end{pmatrix} &= \begin{pmatrix} \Re(\mathbf{D}\overline{\mathbf{x}}) \\ \Im(\mathbf{D}\overline{\mathbf{x}}) \end{pmatrix}, \\ \tilde{\mathbf{E}} \begin{pmatrix} \mathbf{x}_R \\ \mathbf{x}_I \end{pmatrix} &= \begin{pmatrix} \Re(\mathbf{E}\mathbf{x}) \\ \Im(\mathbf{E}\mathbf{x}) \end{pmatrix}. \end{aligned} \tag{66}$$

Proof. The proof follows via straightforward computations. □

Proof of Theorem 2. (a) Since $\nabla f(\mathbf{0}) = \mathbf{0}$, $\mathbf{0}$ is a critical point. Observe that

$$\begin{aligned} \mathbf{C}(\mathbf{0}) &= \mathbf{D}(\mathbf{0}) = \mathbf{0}, \\ \mathbf{E}(\mathbf{0}) &= -\mathbf{A}^H \operatorname{Diag}(\mathbf{b})\mathbf{B} - \mathbf{B}^H \operatorname{Diag}(\overline{\mathbf{b}})\mathbf{A}. \end{aligned} \tag{67}$$

For any $\mathbf{x} \coloneqq \mathbf{x}_R + j\mathbf{x}_I \neq \mathbf{0}$,

$$\begin{aligned} & \begin{pmatrix} \mathbf{x}_R^T & \mathbf{x}_I^T \end{pmatrix} \nabla^2 f(\mathbf{0}) \begin{pmatrix} \mathbf{x}_R \\ \mathbf{x}_I \end{pmatrix} \\ = \; & \begin{pmatrix} \mathbf{x}_R^T & \mathbf{x}_I^T \end{pmatrix} \tilde{\mathbf{E}}(\mathbf{0}) \begin{pmatrix} \mathbf{x}_R \\ \mathbf{x}_I \end{pmatrix} \\ = \; & \mathbf{x}^H \mathbf{E}(\mathbf{0}) \mathbf{x}, \end{aligned} \tag{68}$$

where the second equality is given by Lemma 7. Since $\mathbf{E}(\mathbf{0})$ is Hermitian, we have

$$\begin{cases} \mathbf{x}^H \mathbf{E}(\mathbf{0})\mathbf{x} > 0 & \text{if } \mathbf{A}^H \operatorname{Diag}(\mathbf{b})\mathbf{B} + \mathbf{B}^H \operatorname{Diag}(\overline{\mathbf{b}})\mathbf{A} \prec \mathbf{0} \\ \mathbf{x}^H \mathbf{E}(\mathbf{0})\mathbf{x} < 0 & \text{if } \mathbf{A}^H \operatorname{Diag}(\mathbf{b})\mathbf{B} + \mathbf{B}^H \operatorname{Diag}(\overline{\mathbf{b}})\mathbf{A} \succ \mathbf{0} \end{cases} \tag{69}$$

for any $\mathbf{x} \in \mathbb{C}^n \setminus \{\mathbf{0}\}$.

(b) Suppose $\exists \mathbf{z} \neq \mathbf{0}$ such that $\nabla f(\mathbf{z}) = \mathbf{0}$. (26) implies

$$\begin{aligned} \mathbf{d}(\mathbf{z}) = \; & \mathbf{A}^H \left(((\mathbf{A}\mathbf{z}) \circ (\overline{\mathbf{B}\mathbf{z}}) - \mathbf{b}) \circ (\mathbf{B}\mathbf{z})\right) + \\ & \mathbf{B}^H \left(((\overline{\mathbf{A}\mathbf{z}}) \circ (\mathbf{B}\mathbf{z}) - \overline{\mathbf{b}}) \circ (\mathbf{A}\mathbf{z})\right) \\ = \; & \mathbf{0}. \end{aligned} \tag{70}$$

A few manipulations lead to

$$\begin{aligned} & \mathbf{A}^H \left((\mathbf{A}\mathbf{z}) \circ (\overline{\mathbf{B}\mathbf{z}}) \circ (\mathbf{B}\mathbf{z})\right) + \mathbf{B}^H \left((\overline{\mathbf{A}\mathbf{z}}) \circ (\mathbf{B}\mathbf{z}) \circ (\mathbf{A}\mathbf{z})\right) \\ = \; & \mathbf{A}^H \operatorname{Diag}(\mathbf{b})\mathbf{B}\mathbf{z} + \mathbf{B}^H \operatorname{Diag}(\overline{\mathbf{b}})\mathbf{A}\mathbf{z}. \end{aligned} \tag{71}$$

Multiplying both sides with $\mathbf{z}^H$ on the left yields

$$\begin{aligned} & \mathbf{z}^H \left(\mathbf{A}^H \operatorname{Diag}(\mathbf{b})\mathbf{B} + \mathbf{B}^H \operatorname{Diag}(\overline{\mathbf{b}})\mathbf{A}\right)\mathbf{z} \\ = \; & 2\|(\mathbf{A}\mathbf{z}) \circ (\overline{\mathbf{B}\mathbf{z}})\|_2^2 \geq 0, \end{aligned} \tag{72}$$

which implies $\mathbf{A}^H \operatorname{Diag}(\mathbf{b})\mathbf{B} + \mathbf{B}^H \operatorname{Diag}(\overline{\mathbf{b}})\mathbf{A} \not\prec \mathbf{0}$.

(c1) We prove that $\nabla^2 f(\mathbf{z})$ is rank deficient by showing $\nabla^2 f(\mathbf{z}) \begin{pmatrix} \mathbf{x}_R \\ \mathbf{x}_I \end{pmatrix} = \mathbf{0}$, where $\mathbf{x} \coloneqq \mathbf{z}_I - j\mathbf{z}_R$. Observe

1) $(\mathbf{A}\mathbf{x}) \circ (\overline{\mathbf{B}\mathbf{z}}) + (\mathbf{A}\mathbf{z}) \circ (\overline{\mathbf{B}\mathbf{x}}) = \mathbf{0}$.

2) For any $\mathbf{F}$, $\mathbf{Fz}=\mathbf{0} \implies \mathbf{Fx}=\mathbf{0}$, which together with (70) implies

$$\begin{aligned}\mathbf{0} = \mathbf{A}^H \operatorname{Diag}\left((\mathbf{Az})\circ(\overline{\mathbf{Bz}})-\mathbf{b}\right)\mathbf{Bx}+\\ \mathbf{B}^H \operatorname{Diag}\left((\overline{\mathbf{Az}})\circ(\mathbf{Bz})-\overline{\mathbf{b}}\right)\mathbf{Ax}.\end{aligned} \tag{73}$$

By Lemma 7, it suffices to check $\mathbf{Cx}+\mathbf{D}\overline{\mathbf{x}}+\mathbf{Ex}$:

$$\begin{aligned}&\mathbf{Cx}+\mathbf{D}\overline{\mathbf{x}}+\mathbf{Ex}\\ =\;& \mathbf{A}^H \operatorname{Diag}\left((\mathbf{Bz})\circ(\overline{\mathbf{Bz}})\right)\mathbf{Ax}+\\ &\mathbf{B}^H \operatorname{Diag}\left((\mathbf{Az})\circ(\overline{\mathbf{Az}})\right)\mathbf{Bx}+\\ &\mathbf{A}^H \operatorname{Diag}\left((\mathbf{Az})\circ(\mathbf{Bz})\right)\overline{\mathbf{B}}\overline{\mathbf{x}}+\\ &\mathbf{B}^H \operatorname{Diag}\left((\mathbf{Az})\circ(\mathbf{Bz})\right)\overline{\mathbf{A}}\overline{\mathbf{x}}+\\ &\mathbf{A}^H \operatorname{Diag}\left((\mathbf{Az})\circ(\overline{\mathbf{Bz}})-\mathbf{b}\right)\mathbf{Bx}+\\ &\mathbf{B}^H \operatorname{Diag}\left((\overline{\mathbf{Az}})\circ(\mathbf{Bz})-\overline{\mathbf{b}}\right)\mathbf{Ax}\\ =\;& \mathbf{A}^H \operatorname{Diag}(\mathbf{Bz})\left((\mathbf{Ax})\circ(\overline{\mathbf{Bz}})+(\mathbf{Az})\circ(\overline{\mathbf{Bx}})\right)+\\ &\mathbf{B}^H \operatorname{Diag}(\mathbf{Az})\left((\overline{\mathbf{Az}})\circ(\mathbf{Bx})+(\overline{\mathbf{Ax}})\circ(\mathbf{Bz})\right)\\ =\;& \mathbf{0}.\end{aligned} \tag{74}$$

(c2) For any $\phi\in\mathbb{R}$, it is obvious that

$$\begin{aligned}\mathbf{d}\left(\mathbf{z}\exp(j\phi)\right)=\mathbf{d}(\mathbf{z})=\mathbf{0},\\ f\left(\mathbf{z}\exp(j\phi)\right)=f(\mathbf{z}),\end{aligned} \tag{75}$$

i.e., $\mathbf{z}\exp(j\phi)$ is also a nonzero critical point that is as good. By Proposition 1, $\nabla^2 f\left(\mathbf{x}\exp(j\phi)\right)$ has the same eigenvalues as $\nabla^2 f(\mathbf{x})$ and therefore the same definiteness. □

Appendix D
Proof of Theorem 3

Without loss of generality, assume that $\|\mathbf{A}\circ\overline{\mathbf{B}}\|\neq 0$.

Proof of Thm. 3. (a) When $n=1$, observe that

$$\mathbf{A}^H \operatorname{Diag}(\mathbf{b})\mathbf{B}+\mathbf{B}^H \operatorname{Diag}(\overline{\mathbf{b}})\mathbf{A}=2\,\Re\left((\mathbf{A}\circ\overline{\mathbf{B}})^H b\right). \tag{76}$$

The rest follows directly from Thm. 2(a).

(b) For any $\mathbf{z}\in\mathbb{C}\setminus\{0\}$, we have

$$\begin{aligned}\mathbf{d}(\mathbf{z}) =\;& \mathbf{A}^H\left(((\mathbf{Az})\circ(\overline{\mathbf{Bz}})-\mathbf{b})\circ(\mathbf{Bz})\right)+\\ &\mathbf{B}^H\left(((\overline{\mathbf{Az}})\circ(\mathbf{Bz})-\overline{\mathbf{b}})\circ(\mathbf{Az})\right)\\ =\;& \mathbf{z}|\mathbf{z}|^2\mathbf{A}^H(\mathbf{A}\circ\overline{\mathbf{B}}\circ\mathbf{B})-\mathbf{z}\mathbf{A}^H(\mathbf{b}\circ\mathbf{B})+\\ &\mathbf{z}|\mathbf{z}|^2\mathbf{B}^H(\overline{\mathbf{A}}\circ\mathbf{B}\circ\mathbf{A})-\mathbf{z}\mathbf{B}^H(\overline{\mathbf{b}}\circ\mathbf{A})\\ =\;& \mathbf{z}|\mathbf{z}|^2\|\mathbf{A}\circ\overline{\mathbf{B}}\|_2^2-\mathbf{z}(\mathbf{A}\circ\overline{\mathbf{B}})^H\mathbf{b}+\\ &\mathbf{z}|\mathbf{z}|^2\|\mathbf{A}\circ\overline{\mathbf{B}}\|_2^2-\mathbf{z}(\overline{\mathbf{A}}\circ\mathbf{B})^H\overline{\mathbf{b}}\\ =\;& 2\mathbf{z}\left(\|\mathbf{A}\circ\overline{\mathbf{B}}\|_2^2|\mathbf{z}|^2-\Re\left((\mathbf{A}\circ\overline{\mathbf{B}})^H\mathbf{b}\right)\right),\end{aligned} \tag{77}$$

which has a nonzero root if and only if $\Re\left((\mathbf{A}\circ\overline{\mathbf{B}})^H\mathbf{b}\right)>0$. If this condition is satisfied, its power is given by

$$|\mathbf{z}|^2=\Re\left((\mathbf{A}\circ\overline{\mathbf{B}})^H\mathbf{b}\right)/\|\mathbf{A}\circ\overline{\mathbf{B}}\|_2^2. \tag{78}$$

(c1) Suppose $\exists\mathbf{z}\neq\mathbf{0}$ such that $\nabla f(\mathbf{z})=\mathbf{0}$. (26) and (b) imply

$$\|\mathbf{A}\circ\overline{\mathbf{B}}\|_2^2|\mathbf{z}|^2-\Re\left((\mathbf{A}\circ\overline{\mathbf{B}})^H\mathbf{b}\right)=\mathbf{0}. \tag{79}$$

By Lemma 7, we have for any $\mathbf{x}:=\mathbf{x}_R+j\mathbf{x}_I\neq 0$

$$\begin{aligned}&\begin{pmatrix}\mathbf{x}_R^T & \mathbf{x}_I^T\end{pmatrix}\nabla^2 f(\mathbf{z})\begin{pmatrix}\mathbf{x}_R\\ \mathbf{x}_I\end{pmatrix}\\ =\;& \mathbf{x}^H\mathbf{C}(\mathbf{z})\mathbf{x}+\Re\left(\mathbf{x}^H\mathbf{D}(\mathbf{z})\overline{\mathbf{x}}\right)+\mathbf{x}^H\mathbf{E}(\mathbf{z})\mathbf{x}\\ =\;& |\mathbf{x}|^2\mathbf{A}^H\operatorname{Diag}\left((\mathbf{Bz})\circ(\overline{\mathbf{Bz}})\right)\mathbf{A}+\\ &|\mathbf{x}|^2\mathbf{B}^H\operatorname{Diag}\left((\mathbf{Az})\circ(\overline{\mathbf{Az}})\right)\mathbf{B}+\\ &\Re\left(\overline{\mathbf{x}}^2\mathbf{A}^H\operatorname{Diag}\left((\mathbf{Az})\circ(\mathbf{Bz})\right)\overline{\mathbf{B}}\right)+\\ &\Re\left(\overline{\mathbf{x}}^2\mathbf{B}^H\operatorname{Diag}\left((\mathbf{Az})\circ(\mathbf{Bz})\right)\overline{\mathbf{A}}\right)+\\ &|\mathbf{x}|^2\mathbf{A}^H\operatorname{Diag}\left((\mathbf{Az})\circ(\overline{\mathbf{Bz}})-\mathbf{b}\right)\mathbf{B}+\\ &|\mathbf{x}|^2\mathbf{B}^H\operatorname{Diag}\left((\overline{\mathbf{Az}})\circ(\mathbf{Bz})-\overline{\mathbf{b}}\right)\mathbf{A}\\ =\;& 2\|\mathbf{A}\circ\overline{\mathbf{B}}\|_2^2|\mathbf{x}|^2|\mathbf{z}|^2+2\|\mathbf{A}\circ\overline{\mathbf{B}}\|_2^2\,\Re(\overline{\mathbf{x}}^2\mathbf{z}^2)+\\ &2|\mathbf{x}|^2\left(\|\mathbf{A}\circ\overline{\mathbf{B}}\|_2^2|\mathbf{z}|^2-\Re\left((\mathbf{A}\circ\overline{\mathbf{B}})^H\mathbf{b}\right)\right)\\ =\;& \|\mathbf{A}\circ\overline{\mathbf{B}}\|_2^2\left(2|\mathbf{x}|^2|\mathbf{z}|^2+2\,\Re(\overline{\mathbf{x}}^2\mathbf{z}^2)\right)\\ =\;& \|\mathbf{A}\circ\overline{\mathbf{B}}\|_2^2(\overline{\mathbf{x}}\mathbf{z}+\mathbf{x}\overline{\mathbf{z}})^2\geq 0,\end{aligned} \tag{80}$$

where the equality can be attained with $\mathbf{x}=\mathbf{z}_I-j\mathbf{z}_R$.

That $\nabla^2 f(\mathbf{z})$ is rank deficient is implied by Thm. 2(c1).

(c2) This follows directly from Thm. 2(c2).

(c3) Let us perturb $\mathbf{z}$ by $\epsilon\in\mathbb{C}$ with $|\epsilon|$ being arbitrarily small and observe

$$\begin{aligned}f(\mathbf{z}+\epsilon) =\;& \frac{1}{2}\|\left(\mathbf{A}(\mathbf{z}+\epsilon)\right)\circ\left(\overline{(\mathbf{Bz}+\epsilon)}\right)-\mathbf{b}\|_2^2\\ =\;& \frac{1}{2}\|(\mathbf{Az})\circ(\overline{\mathbf{Bz}})+(\mathbf{Az})\circ(\overline{\mathbf{B}\epsilon})+\\ &(\mathbf{A}\epsilon)\circ(\overline{\mathbf{Bz}})+(\mathbf{A}\epsilon)\circ(\overline{\mathbf{B}\epsilon})-\mathbf{b}\|_2^2\\ =\;& \frac{1}{2}\|(\mathbf{Az})\circ(\overline{\mathbf{Bz}})-\mathbf{b}+\mathbf{A}\circ\overline{\mathbf{B}}(\overline{\epsilon}\mathbf{z}+\epsilon\overline{\mathbf{z}}+|\epsilon|^2)\|_2^2\\ =\;& \frac{1}{2}\|(\mathbf{Az})\circ(\overline{\mathbf{Bz}})-\mathbf{b}\|_2^2+\\ &\frac{1}{2}\|\mathbf{A}\circ\overline{\mathbf{B}}(2\,\Re(\overline{\epsilon}\mathbf{z})+|\epsilon|^2)\|_2^2+\\ &\Re\Big(\left((\mathbf{Az})\circ(\overline{\mathbf{Bz}})-\mathbf{b}\right)^H\cdot\\ &\quad\left(\mathbf{A}\circ\overline{\mathbf{B}}(2\,\Re(\overline{\epsilon}\mathbf{z})+|\epsilon|^2)\right)\Big)\\ =\;& \frac{1}{2}\|(\mathbf{Az})\circ(\overline{\mathbf{Bz}})-\mathbf{b}\|_2^2+\\ &\frac{1}{2}\|\mathbf{A}\circ\overline{\mathbf{B}}\|_2^2(2\,\Re(\overline{\epsilon}\mathbf{z})+|\epsilon|^2)^2+\\ &\Re\left(\|\mathbf{A}\circ\overline{\mathbf{B}}\|_2^2|\mathbf{z}|^2-\mathbf{b}^H(\mathbf{A}\circ\overline{\mathbf{B}})\right)\cdot\\ &(2\,\Re(\overline{\epsilon}\mathbf{z})+|\epsilon|^2)\\ =\;& f(\mathbf{z})+\frac{1}{2}\|\mathbf{A}\circ\overline{\mathbf{B}}\|_2^2(2\,\Re(\overline{\epsilon}\mathbf{z})+|\epsilon|^2)^2+\\ &\left(\|\mathbf{A}\circ\overline{\mathbf{B}}\|_2^2|\mathbf{z}|^2-\Re\left((\mathbf{A}\circ\overline{\mathbf{B}})^H\mathbf{b}\right)\right)\cdot\\ &(2\,\Re(\overline{\epsilon}\mathbf{z})+|\epsilon|^2)\\ =\;& f(\mathbf{z})+\frac{1}{2}\|\mathbf{A}\circ\overline{\mathbf{B}}\|_2^2(2\,\Re(\overline{\epsilon}\mathbf{z})+|\epsilon|^2)^2,\end{aligned} \tag{81}$$

where the last equality is given by (79). As a result,

$$f(\mathbf{z}+\epsilon)-f(\mathbf{z})=\frac{1}{2}\|\mathbf{A}\circ\overline{\mathbf{B}}\|_2^2(2\,\Re(\overline{\epsilon}\mathbf{z})+|\epsilon|^2)^2\geq 0, \tag{82}$$

i.e., $\mathbf{z}$ is a local minimum. □

ACKNOWLEDGMENT

TerraSAR-X data was provided by the German Aerospace Center (DLR) under the TerraSAR-X New Modes AO Project LAN2188.

N. Ge would like to thank Dr. S. Auer and Dr. C. Gisinger for preparing Level 0 ground truth data, Dr. S. Li for the insight from an algebraic geometric point of view, F. Rodriguez Gonzalez and A. Parizzi for valuable discussions, Dr. H. Ansari and Dr. S. Montazeri for explaining the sequential estimator and EMI, Dr. F. De Zan for providing an overview of multi-look multi-master SAR tomography in forested scenarios, Dr. Y. Huang and Prof. Dr. L. Ferro-Famil for discussing a preliminary version of this manuscript, and the reviewers for their constructive and insightful comments.

REFERENCES

[1] A. Reigber and A. Moreira, "First demonstration of airborne SAR tomography using multibaseline L-band data," *IEEE Transactions on Geoscience and Remote Sensing*, vol. 38, no. 5, pp. 2142–2152, 2000.

[2] F. Gini, F. Lombardini, and M. Montanari, "Layover solution in multibaseline SAR interferometry," *IEEE Transactions on Aerospace and Electronic Systems*, vol. 38, no. 4, pp. 1344–1356, 2002.

[3] G. Fornaro, F. Serafino, and F. Soldovieri, "Three-dimensional focusing with multipass SAR data," *IEEE Transactions on Geoscience and Remote Sensing*, vol. 41, no. 3, pp. 507–517, 2003.

[4] F. Lombardini, "Differential tomography: A new framework for SAR interferometry," *IEEE Transactions on Geoscience and Remote Sensing*, vol. 43, no. 1, pp. 37–44, 2005.

[5] G. Fornaro, D. Reale, and F. Serafino, "Four-dimensional SAR imaging for height estimation and monitoring of single and double scatterers," *IEEE Transactions on Geoscience and Remote Sensing*, vol. 47, no. 1, pp. 224–237, 2008.

[6] X. X. Zhu and R. Bamler, "Let's do the time warp: Multicomponent nonlinear motion estimation in differential SAR tomography," *IEEE Geoscience and Remote Sensing Letters*, vol. 8, no. 4, pp. 735–739, 2011.

[7] A. Ferretti, C. Prati, and F. Rocca, "Permanent scatterers in SAR interferometry," *IEEE Transactions on geoscience and remote sensing*, vol. 39, no. 1, pp. 8–20, 2001.

[8] C. Colesanti, A. Ferretti, F. Novali, C. Prati, and F. Rocca, "SAR monitoring of progressive and seasonal ground deformation using the permanent scatterers technique," *IEEE Transactions on Geoscience and Remote Sensing*, vol. 41, no. 7, pp. 1685–1701, 2003.

[9] N. Adam, B. Kampes, and M. Eineder, "Development of a scientific permanent scatterer system: Modifications for mixed ERS/ENVISAT time series," in *Envisat & ERS Symposium*, vol. 572, 2005.

[10] B. M. Kampes, *Radar Interferometry: Persistent Scatterer Technique*. Springer Science & Business Media, 2006, vol. 12.

[11] A. Budillon, A. Evangelista, and G. Schirinzi, "Three-dimensional SAR focusing from multipass signals using compressive sampling," *IEEE Transactions on Geoscience and Remote Sensing*, vol. 49, no. 1, pp. 488–499, 2010.

[12] X. X. Zhu and R. Bamler, "Tomographic SAR inversion by L_1-norm regularization–the compressive sensing approach," *IEEE Transactions on Geoscience and Remote Sensing*, vol. 48, no. 10, pp. 3839–3846, 2010.

[13] E. Aguilera, M. Nannini, and A. Reigber, "Multisignal compressed sensing for polarimetric SAR tomography," *IEEE Geoscience and Remote Sensing Letters*, vol. 9, no. 5, pp. 871–875, 2012.

[14] M. Schmitt and U. Stilla, "Compressive sensing based layover separation in airborne single-pass multi-baseline InSAR data," *IEEE Geoscience and Remote Sensing Letters*, vol. 10, no. 2, pp. 313–317, 2012.

[15] G. Fornaro, S. Verde, D. Reale, and A. Pauciullo, "CAESAR: An approach based on covariance matrix decomposition to improve multibaseline–multitemporal interferometric SAR processing," *IEEE Transactions on Geoscience and Remote Sensing*, vol. 53, no. 4, pp. 2050–2065, 2014.

[16] X. X. Zhu, N. Ge, and M. Shahzad, "Joint sparsity in SAR tomography for urban mapping," *IEEE Journal of Selected Topics in Signal Processing*, vol. 9, no. 8, pp. 1498–1509, 2015.

[17] N. Ge, F. R. Gonzalez, Y. Wang, Y. Shi, and X. X. Zhu, "Spaceborne staring spotlight SAR tomography—a first demonstration with TerraSAR-X," *IEEE Journal of Selected Topics in Applied Earth Observations and Remote Sensing*, vol. 11, no. 10, pp. 3743–3756, 2018.

[18] Y. Shi, X. X. Zhu, W. Yin, and R. Bamler, "A fast and accurate basis pursuit denoising algorithm with application to super-resolving tomographic SAR," *IEEE Transactions on Geoscience and Remote Sensing*, vol. 56, no. 10, pp. 6148–6158, 2018.

[19] Y. Shi, Y. Wang, J. Kang, M. Lachaise, X. X. Zhu, and R. Bamler, "3D reconstruction from very small TanDEM-X stacks," in *EUSAR 2018; 12th European Conference on Synthetic Aperture Radar*. VDE, 2018, pp. 1–4.

[20] Y. Shi, X. X. Zhu, and R. Bamler, "Nonlocal compressive sensing-based SAR tomography," *IEEE Transactions on Geoscience and Remote Sensing*, vol. 57, no. 5, pp. 3015–3024, 2019.

[21] G. Fornaro, F. Lombardini, and F. Serafino, "Three-dimensional multipass SAR focusing: Experiments with long-term spaceborne data," *IEEE Transactions on Geoscience and Remote Sensing*, vol. 43, no. 4, pp. 702–714, 2005.

[22] X. X. Zhu and R. Bamler, "Very high resolution spaceborne SAR tomography in urban environment," *IEEE Transactions on Geoscience and Remote Sensing*, vol. 48, no. 12, pp. 4296–4308, 2010.

[23] ——, "Super-resolution power and robustness of compressive sensing for spectral estimation with application to spaceborne tomographic SAR," *IEEE Transactions on Geoscience and Remote Sensing*, vol. 50, no. 1, pp. 247–258, 2011.

[24] ——, "Sparse tomographic SAR reconstruction from mixed TerraSAR-X/TanDEM-X data stacks," in *2012 IEEE International Geoscience and Remote Sensing Symposium*. IEEE, 2012, pp. 7468–7471.

[25] N. Ge and X. X. Zhu, "Bistatic-like differential SAR tomography," *IEEE Transactions on Geoscience and Remote Sensing*, vol. 57, no. 8, pp. 5883–5893, 2019.

[26] L. Liang, X. Li, L. Ferro-Famil, H. Guo, L. Zhang, and W. Wu, "Urban area tomography using a sparse representation based two-dimensional spectral analysis technique," *Remote Sensing*, vol. 10, no. 1, p. 109, 2018.

[27] D. Perissin and T. Wang, "Repeat-pass SAR interferometry with partially coherent targets," *IEEE Transactions on Geoscience and Remote Sensing*, vol. 50, no. 1, pp. 271–280, 2011.

[28] A. Ferretti, A. Fumagalli, F. Novali, C. Prati, F. Rocca, and A. Rucci, "A new algorithm for processing interferometric data-stacks: SqueeSAR," *IEEE Transactions on Geoscience and Remote Sensing*, vol. 49, no. 9, pp. 3460–3470, 2011.

[29] A. Parizzi and R. Brcic, "Adaptive InSAR stack multilooking exploiting amplitude statistics: A comparison between different techniques and practical results," *IEEE Geoscience and Remote Sensing Letters*, vol. 8, no. 3, pp. 441–445, 2010.

[30] H. Ansari, F. De Zan, and R. Bamler, "Sequential estimator: Toward efficient InSAR time series analysis," *IEEE Transactions on Geoscience and Remote Sensing*, vol. 55, no. 10, pp. 5637–5652, 2017.

[31] ——, "Efficient phase estimation for interferogram stacks," *IEEE Transactions on Geoscience and Remote Sensing*, vol. 56, no. 7, pp. 4109–4125, 2018.

[32] S. Duque, P. López-Dekker, J. J. Mallorquí, A. Y. Nashashibi, and A. M. Patel, "Experimental results with bistatic SAR tomography," in *2009 IEEE International Geoscience and Remote Sensing Symposium*, vol. 2. IEEE, 2009, pp. II–37.

[33] S. Duque, P. López-Dekker, J. C. Merlano, and J. J. Mallorquí, "Bistatic SAR tomography: Processing and experimental results," in *2010 IEEE International Geoscience and Remote Sensing Symposium*. IEEE, 2010, pp. 154–157.

[34] S. Duque, C. Rossi, and T. Fritz, "Single-pass tomography with alternating bistatic TanDEM-X data," *IEEE Geoscience and Remote Sensing Letters*, vol. 12, no. 2, pp. 409–413, 2014.

[35] S. R. Cloude, "Polarization coherence tomography," *Radio Science*, vol. 41, no. 4, 2006.

[36] F. De Zan, K. Papathanassiou, and S. Lee, "Tandem-L forest parameter performance analysis," in *Proceedings of international workshop on applications of polarimetry and polarimetric interferometry, Frascati, Italy*. Citeseer, 2009, pp. 1–6.

[37] S. Tebaldini, "Algebraic synthesis of forest scenarios from multibaseline PolInSAR data," *IEEE Transactions on Geoscience and Remote Sensing*, vol. 47, no. 12, pp. 4132–4142, 2009.

[38] ——, "Single and multipolarimetric SAR tomography of forested areas: A parametric approach," *IEEE Transactions on Geoscience and Remote Sensing*, vol. 48, no. 5, pp. 2375–2387, 2010.

[39] Y. Huang, L. Ferro-Famil, and A. Reigber, "Under-foliage object imaging using SAR tomography and polarimetric spectral estimators," *IEEE transactions on geoscience and remote sensing*, vol. 50, no. 6, pp. 2213–2225, 2011.

[40] S.-K. Lee and T. E. Fatoyinbo, "TanDEM-X Pol-InSAR inversion for mangrove canopy height estimation," *IEEE Journal of Selected Topics in Applied Earth Observations and Remote Sensing*, vol. 8, no. 7, pp. 3608–3618, 2015.

[41] M. Pardini and K. Papathanassiou, "On the estimation of ground and volume polarimetric covariances in forest scenarios with SAR tomography," *IEEE Geoscience and Remote Sensing Letters*, vol. 14, no. 10, pp. 1860–1864, 2017.

[42] V. Cazcarra-Bes, M. Pardini, M. Tello, and K. P. Papathanassiou, "Comparison of tomographic SAR reflectivity reconstruction algorithms for forest applications at L-band," *IEEE Transactions on Geoscience and Remote Sensing*, 2019.

[43] G. Krieger, A. Moreira, H. Fiedler, I. Hajnsek, M. Werner, M. Younis, and M. Zink, "TanDEM-X: A satellite formation for high-resolution SAR interferometry," *IEEE Transactions on Geoscience and Remote Sensing*, vol. 45, no. 11, pp. 3317–3341, 2007.

[44] K. Goel and N. Adam, "Fusion of monostatic/bistatic InSAR stacks for urban area analysis via distributed scatterers," *IEEE Geoscience and Remote Sensing Letters*, vol. 11, no. 4, pp. 733–737, 2013.

[45] P. Berardino, G. Fornaro, R. Lanari, and E. Sansosti, "A new algorithm for surface deformation monitoring based on small baseline differential SAR interferograms," *IEEE Transactions on geoscience and remote sensing*, vol. 40, no. 11, pp. 2375–2383, 2002.

[46] R. Lanari, O. Mora, M. Manunta, J. J. Mallorquí, P. Berardino, and E. Sansosti, "A small-baseline approach for investigating deformations on full-resolution differential SAR interferograms," *IEEE Transactions on Geoscience and Remote Sensing*, vol. 42, no. 7, pp. 1377–1386, 2004.

[47] A. Hooper, "A multi-temporal InSAR method incorporating both persistent scatterer and small baseline approaches," *Geophysical Research Letters*, vol. 35, no. 16, 2008.

[48] A. Moreira, G. Krieger, I. Hajnsek, K. Papathanassiou, M. Younis, P. Lopez-Dekker, S. Huber, M. Villano, M. Pardini, M. Eineder *et al.*, "Tandem-L: A highly innovative bistatic SAR mission for global observation of dynamic processes on the Earth's surface," *IEEE Geoscience and Remote Sensing Magazine*, vol. 3, no. 2, pp. 8–23, 2015.

[49] J. A. Bondy and U. S. R. Murty, *Graph Theory*. Springer, 2008.

[50] I. Hajnsek, T. Busche, G. Krieger, M. Zink, and A. Moreira, "Announcement of opportunity: TanDEM-X science phase," *DLR Public Document TD-PD-PL-0032*, no. 1.0, pp. 1–27, 2014.

[51] P. Stoica and Y. Selen, "Model-order selection: a review of information criterion rules," *IEEE Signal Processing Magazine*, vol. 21, no. 4, pp. 36–47, 2004.

[52] P. Stoica and R. Moses, *Spectral analysis of signals*. Pearson Prentice Hall Upper Saddle River, NJ, 2005.

[53] S. Boyd, N. Parikh, E. Chu, B. Peleato, J. Eckstein *et al.*, "Distributed optimization and statistical learning via the alternating direction method of multipliers," *Foundations and Trends® in Machine learning*, vol. 3, no. 1, pp. 1–122, 2011.

[54] S. Foucart and H. Rauhut, *A mathematical introduction to compressive sensing*. Springer Science & Business Media, 2017.

[55] J. Nocedal and S. Wright, *Numerical optimization*. Springer Science & Business Media, 2006.

[56] J. Sun, Q. Qu, and J. Wright, "When are nonconvex problems not scary?" *arXiv preprint arXiv:1510.06096*, 2015.

[57] E. Freitag and R. Busam, *Complex analysis*. Springer Science & Business Media, 2009.

[58] D. Hong, N. Yokoya, J. Chanussot, and X. X. Zhu, "An augmented linear mixing model to address spectral variability for hyperspectral unmixing," *IEEE Transactions on Image Processing*, vol. 28, no. 4, pp. 1923–1938, 2018.

[59] ——, "CoSpace: Common subspace learning from hyperspectral-multispectral correspondences," *IEEE Transactions on Geoscience and Remote Sensing*, vol. 57, no. 7, pp. 4349–4359, 2019.

[60] D. Hong, N. Yokoya, N. Ge, J. Chanussot, and X. X. Zhu, "Learnable manifold alignment (LeMA): A semi-supervised cross-modality learning framework for land cover and land use classification," *ISPRS journal of photogrammetry and remote sensing*, vol. 147, pp. 193–205, 2019.

[61] N. Parikh, S. Boyd *et al.*, "Proximal algorithms," *Foundations and Trends® in Optimization*, vol. 1, no. 3, pp. 127–239, 2014.

[62] D. L. Donoho, "De-noising by soft-thresholding," *IEEE transactions on information theory*, vol. 41, no. 3, pp. 613–627, 1995.

[63] S. Boyd and L. Vandenberghe, *Convex optimization*. Cambridge university press, 2004.

[64] M. Fornasier, S. Peter, H. Rauhut, and S. Worm, "Conjugate gradient acceleration of iteratively re-weighted least squares methods," *Computational Optimization and Applications*, vol. 65, no. 1, pp. 205–259, 2016.

[65] A. Chambolle and T. Pock, "A first-order primal-dual algorithm for convex problems with applications to imaging," *Journal of mathematical imaging and vision*, vol. 40, no. 1, pp. 120–145, 2011.

[66] N. Adam, F. R. Gonzalez, A. Parizzi, and R. Brcic, "Wide area persistent scatterer interferometry: current developments, algorithms and examples," in *2013 IEEE International Geoscience and Remote Sensing Symposium-IGARSS*. IEEE, 2013, pp. 1857–1860.

[67] F. R. Gonzalez, N. Adam, A. Parizzi, and R. Brcic, "The integrated wide area processor (IWAP): A processor for wide area persistent scatterer interferometry," in *ESA Living Planet Symposium*, vol. 722, 2013, p. 353.

[68] S. Auer, C. Gisinger, N. Ge, F. R. Gonzalez, and X. X. Zhu, "SIGS: A SAR imaging geodesy and simulation framework for generating 3-D ground truth," *in preparation*.

[69] J. Revels, M. Lubin, and T. Papamarkou, "Forward-mode automatic differentiation in Julia," *arXiv:1607.07892 [cs.MS]*, 2016. [Online]. Available: https://arxiv.org/abs/1607.07892

[70] P. K. Mogensen and A. N. Riseth, "Optim: A mathematical optimization package for Julia," *Journal of Open Source Software*, vol. 3, no. 24, p. 615, 2018.

[71] S. J. Auer, "3D synthetic aperture radar simulation for interpreting complex urban reflection scenarios," Ph.D. dissertation, Technische Universität München, 2011.

[72] M. Eineder, C. Minet, P. Steigenberger, X. Cong, and T. Fritz, "Imaging geodesytoward centimeter-level ranging accuracy with TerraSAR-X," *IEEE Transactions on Geoscience and Remote Sensing*, vol. 49, no. 2, pp. 661–671, 2010.

[73] C. Gisinger, U. Balss, R. Pail, X. X. Zhu, S. Montazeri, S. Gernhardt, and M. Eineder, "Precise three-dimensional stereo localization of corner reflectors and persistent scatterers with TerraSAR-X," *IEEE Transactions on Geoscience and Remote Sensing*, vol. 53, no. 4, pp. 1782–1802, 2014.

[74] S. Hackel, C. Gisinger, U. Balss, M. Wermuth, and O. Montenbruck, "Long-term validation of TerraSAR-X and TanDEM-X orbit solutions with laser and radar measurements," *Remote Sensing*, vol. 10, no. 5, p. 762, 2018.

[75] S. Gernhardt, S. Auer, and K. Eder, "Persistent scatterers at building facades–evaluation of appearance and localization accuracy," *ISPRS journal of photogrammetry and remote sensing*, vol. 100, pp. 92–105, 2015.

A.2 Ge & Zhu (2019)

N. Ge and X. X. Zhu. Bistatic-like differential SAR tomography. *IEEE Transactions on Geoscience and Remote Sensing*, 57(8):5883–5893, 2019

Bistatic-like Differential SAR Tomography

Nan Ge, Xiao Xiang Zhu, *Senior Member, IEEE*

***Abstract*—Motivated by prospective synthetic aperture radar (SAR) satellite missions, this paper addresses the problem of differential SAR tomography (D-TomoSAR) in urban areas using spaceborne bistatic or pursuit monostatic acquisitions. A bistatic or pursuit monostatic interferogram is not subject to significant temporal decorrelation or atmospheric phase screen and therefore ideal for elevation reconstruction. We propose a framework that incorporates this reconstructed elevation as deterministic prior into deformation estimation, which uses conventional repeat-pass interferograms generated from bistatic or pursuit monostatic pairs. By means of theoretical and empirical analyses, we show that this framework is, in the pursuit monostatic case, both statistically and computationally more efficient than standard D-TomoSAR. In the bistatic case, its theoretical bound is no worse by a factor of 2. We also show that reasonable results can be obtained by using merely 6 TanDEM-X pursuit monostatic pairs, if additional spatial prior is introduced. The proposed framework can be easily extended for multistatic configurations or external sources of scatterer's elevation.**

***Index Terms*—SAR tomography, Tandem-L, TanDEM-X, synthetic aperture radar (SAR).**

I. Introduction

A. Motivation

BISTATIC or multistatic configuration is a prominent feature of various future synthetic aperture radar (SAR) satellite missions. Some of these missions can be summarized as follows.

- Tandem-L, a German satellite mission concept whose primary goal is to observe the dynamic processes on earth's surface in high resolution with an unprecedented accuracy [1]. It comprises two satellites (e.g., TL-1 and TL-2). Each of them will have on board a high-resolution wide-swath L-band SAR. Basically, these two satellites will fly in close formation and operate in bistatic mode. This mode utilizes either TL-1 or TL-2 as a transmitter to illuminate a common radar footprint, while both receive radar echoes from earth's surface. In addition, a bidirectional radio frequency (RF) link is necessary for a highly accurate mutual time and phase referencing. This requirement will be easily fulfilled by means of the heritage of the TanDEM-X (TerraSAR-X add-on for Digital Elevation Measurements) mission [2]. Due to limited temporal decorrelation and atmospheric phase screen (APS), single-pass bistatic interferograms are characterized by better phase quality as compared to conventional repeat-pass ones and thus are more suitable for generating a global, consistent and high-resolution digital elevation model [3].
- SAOCOM-CS, a bistatic mission concept attaching to SAOCOM a passive companion SAR satellite operating in L-band [4].
- SEntinel-1 SAR Companion Multistatic Explorer (SESAME), a bistatic mission concept adding to Sentinel-1 two passive companion SAR satellites operating in C-band [5].
- Sentinel-1 "tandem" (i.e., one-day separation) or bistatic mission concept involving the prospective Sentinel-1C and another satellite from the series [6].
- High Resolution Wide Swath (HRWS), the successor of TerraSAR-X comprising one or two SAR satellites operating in X-band [7], [8], and possibly several additional passive companion transponder satellites without bidirectional phase synchronization link (MirrorSAR) [9]–[11].

Above all, Tandem-L is the most intriguing mission to us, not only because it is the one and only concept that has already undergone very comprehensive and intensive studies (see for example [12]–[16] and the references therein), but it is also extremely promising for a huge variety of geophysical applications.

In this paper, we address the problem of spaceborne differential SAR tomography (D-TomoSAR, see for instance [17]–[23]) in urban areas using bistatic or pursuit monostatic data. The latter, on the contrary, requires two satellites in close formation to operate *independently* from each other [2]. It can be employed as a backup solution in case pulse or phase synchronization fails. Given a temporal baseline of a few seconds and a moderate wind speed, the temporal decorrelation is still small for most terrain types including vegetation and atmospheric path delays can be assumed to cancel each other out during interferometric processing [24]. Hereafter we refer to bistatic and pursuit monostatic collectively as "bistatic-like".

We propose an austere framework which 1) reconstructs the elevation dimension with only bistatic-like interferograms, and subsequently 2) uses this as deterministic prior to estimate deformation parameters with conventional repeat-pass interferograms generated from bistatic-like pairs. Note that 1) is essentially a non-differential TomoSAR subproblem. We will refer to 2) as the DefoSAR subproblem. For point-like scatterers, the advantages of this framework are at least two-

This work is jointly supported by Helmholtz Association under the framework of the Young Investigators Group "SiPEO" (VH-NG-1018, www.sipeo.bgu.tum.de), DLR Space Administration under the project "J Lo—The Joy of Long Baselines" in the frame of "Entwicklung von innovativen wissenschaftlichen Methoden und Produkten im Rahmen der TanDEM-X Science Phase", the European Research Council (ERC) under the European Unions Horizon 2020 research and innovation programme (grant agreement No. [ERC-2016-StG-714087], acronym: *So2Sat*), and the Bavarian Academy of Sciences and Humanities in the framework of Junges Kolleg. *Corresponding author: Xiao Xiang Zhu.*

N. Ge is with the Remote Sensing Technology Institute (IMF), German Aerospace Center (DLR), 82234 Wessling, Germany (e-mail: Nan.Ge@dlr.de).

X. X. Zhu is with the Remote Sensing Technology Institute (IMF), German Aerospace Center (DLR), 82234 Wessling, Germany, and with Signal Processing in Earth Observation (SiPEO), Technical University of Munich (TUM), 80333 Munich, Germany (e-mail: xiaoxiang.zhu@dlr.de).

fold: a) the (almost) APS-free nature of bistatic-like interferograms leads to better elevation reconstruction, and in turn to more accurate deformation estimation; b) the dimension of the original problem is downscaled multiplicatively in each subproblem, which increases on the whole the algorithmic efficiency. For distributed scatterers, adaptive multilooking can be employed to increase their signal-to-noise ratio (SNR) to the level of point-like ones [25]–[27]. Therefore, the same arguments also apply. Besides, the elevation reconstruction of distributed scatterers relies less on the performance of adaptive multilooking, since their decorrelation is much less severe in bistatic-like interferograms than in conventional repeat-pass ones.

For the purpose of a practical demonstration, we use TanDEM-X—to date the sole civil spaceborne bistatic or multistatic mission—data in pursuit monostatic mode.

The proposed framework is envisioned to be incorporated into our Tandem-L processing chain. As one would expect, it is, with up to some minor adaptation, directly applicable to other prospective bi- or multistatic missions.

B. Notations and structure

We adopt the following mathematical notations throughout the whole paper. Scalars are denoted as lower- or uppercase letters, e.g., r, N, λ. Vectors are denoted as bold lowercase letters, e.g., $\mathbf{b}$, $\boldsymbol{\gamma}$. Their elements are denoted as lowercase letters with subscript, e.g., the n-th entry of $\mathbf{g}$ is denoted as g_n. For vectors, $\|\cdot\|_2$ and $\|\cdot\|_1$ denote the ℓ_2 and ℓ_1 norm, respectively. The supports of any vector $\boldsymbol{\beta}$, i.e., the index set of all nonzero entries of $\boldsymbol{\beta}$, are denoted as $\mathrm{supp}(\boldsymbol{\beta})$. Matrices and sets are denoted as bold uppercase letters, e.g., $\mathbf{R}$, $\boldsymbol{\Omega}$. Single rows of matrices are denoted as bold lowercase letters with superscript, e.g., the n-th row of $\mathbf{R}$ is denoted as $\mathbf{r}^n$. For matrices, $\|\cdot\|_{\mathrm{F}}$ and $\|\cdot\|_{1,2}$ denote the Frobenius and $\ell_{1,2}$ norm, respectively. For any set $\boldsymbol{\Omega}$, $|\boldsymbol{\Omega}|$ denotes its cardinality and $2^{\boldsymbol{\Omega}}$ its power set, i.e., the set of all subsets of $\boldsymbol{\Omega}$, including $\boldsymbol{\Omega}$ itself and the empty set $\varnothing$. The sets of integers, real and complex numbers are denoted as $\mathbb{Z}$, $\mathbb{R}$, $\mathbb{C}$, respectively. Their nonnegative subsets are denoted with the subscript $+$, e.g., $\mathbb{Z}_+$ denotes the set of nonnegative integers.

The remainder of this paper is organized as follows. Sec. II introduces the aforementioned framework together with a theoretical analysis of its performance and complexity. This is followed by Sec. III where an empirical experiment with TanDEM-X pursuit monostatic data can be found. Sec. IV concludes this paper.

II. The Tomo- and DefoSAR framework

As briefly mentioned in Sec. I, we divide the original differential TomoSAR problem using bistatic-like data sets into two ordered subproblems, namely (non-differential) Tomo- and DefoSAR. In the TomoSAR subproblem, the elevation dimension is reconstructed with only bistatic-like interferograms. Subsequently, the reconstructed elevation position of each scatterer is used as deterministic prior in the DefoSAR subproblem, where its deformation parameters are estimated with conventional repeat-pass interferograms. These two categories of interferometric combinations are illustrated in Fig. 1.

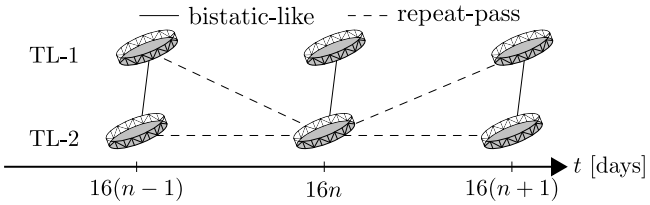

Fig. 1. A sketch of bistatic-like (solid lines) and conventional repeat-pass (dashed lines) interferometric combinations of future Tandem-L acquisitions. Bistatic-like pairs will be acquired repeatedly by TL-1 and TL-2 every 16 days.

A. TomoSAR

Given N coregistered bistatic-like complex interferograms, we aim to reconstruct the reflectivity profile along elevation.

For small N, however, the distribution of cross-track perpendicular baselines could be one-sided (see for example Fig. 2a). In this case, we propose to flip the sign of some of the baselines in order to maximize the standard deviation of their distribution. The rationale is to achieve a more uniform sampling of elevation frequencies [28], as well as a better Cramér-Rao lower bound on the error of elevation estimates [29]. Let $\mathbf{b} \in \mathbb{R}^N$ denote the vector of cross-track perpendicular baselines, the aforementioned problem can be formulated as

$$\underset{\mathbf{z}\in\{-1,+1\}^N}{\text{maximize}}\ \sigma(\mathbf{b}\odot\mathbf{z}), \tag{1}$$

where $\sigma : \mathbb{R}^N \to \mathbb{R}_+$ maps a vector to the sample standard deviation of its entries, and $\odot$ denotes the Hadamard product. Problem (1) is equivalent to

$$\underset{\mathbf{z}\in\{-1,+1\}^N}{\text{minimize}} -\left\|\mathbf{b}\odot\mathbf{z}-\mathbf{b}^{\mathrm{T}}\mathbf{z}/N\right\|_2^2, \tag{2}$$

which has two optimum points given unique entries of $\mathbf{b}$: suppose $\mathbf{z}^*$ is one of them, then $-\mathbf{z}^*$ is the other. Since N is small, we solve (2) by exhaustive search. In the unlikely case of one-sided baseline distribution with large N, the following heuristic can be adopted: sort baselines by their magnitude, choose a sign for the largest one in magnitude, set the second largest one to have the opposite sign, and so forth till all N baselines are exhausted. Accordingly, the signs of elevation frequency and interferometric phase are also flipped.

The optional sign flipping procedure is followed by layover separation. By the first-order Born approximation, far-field diffraction is often modeled as the integration of a phase-modulated elevation-dependent reflectivity profile (see for example [19]). After discretizing the elevation dimension and replacing integration with finite sum, bistatic-like InSAR observations $\mathbf{g} \in \mathbb{C}^N$ of a resolution cell can be approximated with the linear model $\mathbf{g} \approx \mathbf{R}\boldsymbol{\gamma}$, where $\mathbf{R} \in \mathbb{C}^{N\times L}$ is the TomoSAR design matrix, and $\boldsymbol{\gamma} \in \mathbb{C}^L$ denotes the discrete reflectivity profile along elevation. The n-th entry g_n of $\mathbf{g}$ is sampled at the elevation frequency $\xi_n := 2b_n/(\lambda r)$, where b_n is the corresponding cross-track perpendicular baseline (after sign flipping), λ denotes the radar carrier wavelength, and r is the slant-range distance in the master acquisition. Let $\mathbf{s} \in \mathbb{R}^L$ denote the discretization of the elevation dimension, the n-th row of $\mathbf{R}$ is defined as $\mathbf{r}^n := \exp(-j2\pi\xi_n\mathbf{s})$, where exp

operates elementwise. There exist numerous methods which estimate $\boldsymbol{\gamma}$ with given $\mathbf{R}$ and $\mathbf{g}$. Under the assumption that $\boldsymbol{\gamma}$ is sparse (i.e., its cardinality is small), a common approach is to solve the following ℓ_1-regularized least squares problem [30]

$$\hat{\boldsymbol{\gamma}} \coloneqq \arg\min_{\boldsymbol{\gamma}} \frac{1}{2}\|\mathbf{R}\boldsymbol{\gamma} - \mathbf{g}\|_2^2 + \lambda\|\boldsymbol{\gamma}\|_1, \tag{3}$$

where $\lambda > 0$ controls the trade-off between model goodness-of-fit and the sparsity of $\boldsymbol{\gamma}$. A similar formulation of (3) can be found in [31]. Despite its super-resolution power and robustness in terms of layover separation, ℓ_1 regularization is prone to spurious spikes. For this reason, it is often concatenated with model order selection which we state as follows [28]

$$\begin{aligned}\hat{\boldsymbol{\Omega}} \coloneqq &\arg\min_{\boldsymbol{\Omega}(,\boldsymbol{\beta})} \frac{1}{2}\|\mathbf{R}\boldsymbol{\beta} - \mathbf{g}\|_2^2 + \mathrm{C}(|\boldsymbol{\Omega}|) \\ &\text{subject to } \operatorname{supp}(\boldsymbol{\beta}) = \boldsymbol{\Omega} \subseteq \operatorname{supp}(\hat{\boldsymbol{\gamma}}),\end{aligned} \tag{4}$$

where $|\boldsymbol{\Omega}|$ denotes the cardinality of the index set $\boldsymbol{\Omega}$, $\mathrm{C} : \mathbb{Z}_+ \to \mathbb{R}_+$ evaluates the model complexity according to, e.g., Bayesian or Akaike information criterion (see [28] and the references therein), and $\operatorname{supp}(\boldsymbol{\beta}) = \{i \mid \beta_i \neq 0, i = 1, \ldots, L\}$, i.e., it is the set of the indices of nonzero entries or supports in $\boldsymbol{\beta}$. The constraint in (4) renders the supports of the final reflectivity profile estimate a subset of those of $\hat{\boldsymbol{\gamma}}$, and therefore allows outlier mitigation. Note that the underestimated amplitude is hereby debiased as a by-product.

In the next subsection, we introduce the DefoSAR subproblem which uses as deterministic prior the elevation estimates of single or multiple scatterers from TomoSAR reconstruction.

B. DefoSAR

Given $2N-2$ coregistered conventional repeat-pass complex interferograms generated from N bistatic-like pairs (see Fig. 1), and the elevation estimates $\hat{\mathbf{s}} \coloneqq \mathbf{s}_{\hat{\boldsymbol{\Omega}}}$ of a total number of $K \coloneqq |\hat{\boldsymbol{\Omega}}|$ scatterers, our objective is to reconstruct their deformation by means of a composite model.

For single point-like scatterers (i.e., no layover effect), the elevation estimates can be straightforwardly converted into topographic phase and compensated in the conventional repeat-pass interferograms. A similar approach for distributed scatterers can be found in [32].

In a more general sense, $\hat{\mathbf{s}}$ can be considered as deterministic prior. Let $\boldsymbol{\Psi} \coloneqq \{\boldsymbol{\psi}_m\}$ denote a set of M basis functions which are parametrized by the temporal baseline t_n and employed to model scatterer's deformation, and $\mathbf{c}_m \in \mathbb{R}^{|\mathbf{c}_m|}$ be the discretization of the unknown coefficient of $\boldsymbol{\psi}_m$, we can construct the DefoSAR design matrix $\tilde{\mathbf{R}}(\hat{\mathbf{s}}, \boldsymbol{\Psi}) \in \mathbb{C}^{(2N-2)\times\tilde{L}}$, where $\tilde{L} \coloneqq K\prod_{m=1}^{M}|\mathbf{c}_m|$. Its n-th row can be expressed as $\tilde{\mathbf{r}}^n \coloneqq \exp(-j2\pi\tilde{\xi}_n\hat{\mathbf{s}}) \otimes \exp(-j(4\pi/\lambda)\boldsymbol{\psi}_1(t_n)\mathbf{c}_1) \otimes \cdots \otimes \exp(-j(4\pi/\lambda)\boldsymbol{\psi}_M(t_n)\mathbf{c}_M)$, where $\tilde{\xi}_n$ is the elevation frequency of the n-th conventional repeat-pass interferogram with cross-track perpendicular baseline $\tilde{b}_n$, and $\otimes$ denotes the Kronecker product. Likewise, the repeat-pass InSAR observations $\tilde{\mathbf{g}} \in \mathbb{C}^{2N-2}$ of the same resolution cell can be approximated by $\tilde{\mathbf{g}} \approx \tilde{\mathbf{R}}(\hat{\mathbf{s}}, \boldsymbol{\Psi})\tilde{\boldsymbol{\gamma}}$, where $\tilde{\boldsymbol{\gamma}} \in \mathbb{C}^{\tilde{L}}$ denotes the discrete reflectivity profile along elevation and deformation. The coefficients of deformation basis functions can be estimated with a variant of non-linear least squares [22] which additionally constrains $\tilde{\boldsymbol{\gamma}}$ to have exactly one nonzero entry at each elevation position in $\hat{\mathbf{s}}$. In order to avoid overfitting, we propose furthermore to perform deformation model order selection. Let $2^{\boldsymbol{\Psi}}$ be the power set of $\boldsymbol{\Psi}$, i.e., all possible combinations of deformation basis functions including the non-differential case represented by the null set $\varnothing$, the deformation model order selection problem can be cast as

$$\begin{aligned}\hat{\boldsymbol{\Theta}} \coloneqq &\arg\min_{\boldsymbol{\Theta}\subseteq 2^{\boldsymbol{\Psi}}(,\tilde{\boldsymbol{\beta}})} \frac{1}{2}\|\tilde{\mathbf{R}}(\hat{\mathbf{s}}, \boldsymbol{\Theta})\tilde{\boldsymbol{\beta}} - \tilde{\mathbf{g}}\|_2^2 + \mathrm{C}(|\boldsymbol{\Theta}|) \\ &\text{subject to } |\operatorname{supp}(\tilde{\boldsymbol{\beta}})| = |\operatorname{supp}(\mathfrak{I}(\tilde{\boldsymbol{\beta}}))| = |\hat{\boldsymbol{\Omega}}|,\end{aligned} \tag{5}$$

where $\mathfrak{I} : \mathbb{C}^{\tilde{L}} \to \mathbb{C}^{K}$ integrates over each deformation coefficient. The constraint in (5) enforces that the discrete reflectivity profile in the elevation-deformation domain, and the one in the (integrated) elevation domain share the same number of supports, which leads to the previously mentioned desired effect. Again, we solve this subproblem by exhaustive search. In the case of a highly complex composite model, we can proceed in a greedy manner: choose from the remaining scatterers the one with the strongest power, rebuild the DefoSAR design matrix, find the best fit in terms of penalized likelihood (5), and subtract it from the residues of $\tilde{\mathbf{g}}$, etc.

Assuming that the elevation estimate of a single scatterer is perfect, the Cramér-Rao lower bound (CRLB) on the error of the coefficient estimate $\hat{c}$ of a single basis function ψ is

$$\sigma_{\hat{c}} \coloneqq \frac{\lambda}{4\pi\sqrt{2N-2}\sqrt{2SNR}\,\sigma_{\psi}}, \tag{6}$$

where σ_ψ is the standard deviation of ψ evaluated at different t_n, i.e., $\psi(t_1), \ldots, \psi(t_{2N-2})$. A proof of (6) is given in the appendix.

In a nutshell, our proposed framework can be summarized as follows. A simple theoretical analysis is provided in the next subsection.

Algorithm 1 Tomo- and DefoSAR

TomoSAR Input: cross-track perpendicular baselines $\mathbf{b}$, elevation frequencies $\{\xi_n\}$, bistatic-like InSAR observations $\mathbf{g}$

1: (optional) sign flipping (2)
2: sparse reconstruction (3)
3: model order selection for elevation estimation (4)

TomoSAR Output: elevation estimates $\hat{\mathbf{s}}$

DefoSAR Input: $\hat{\mathbf{s}}$, temporal baselines $\{t_n\}$, deformation basis functions $\boldsymbol{\Psi}$, repeat-pass InSAR observations $\tilde{\mathbf{g}}$

4: if $|\hat{\mathbf{s}}| \neq \varnothing$, deformation model order selection (5)

DefoSAR Output: selected deformation basis functions $\hat{\boldsymbol{\Theta}}$ and their estimated coefficients

C. Tomo- and DefoSAR vs. D-TomoSAR: a theoretical analysis

Now we analyze the performance and complexity of the proposed framework from a theoretical point of view.

We start with a proof that

Case 1 (pursuit monostatic): the proposed framework has a tighter theoretical bound, and

Case 2 (bistatic): its CRLB is no worse by a factor of 2.

In order to simplify the argument, suppose without loss of generality that N bistatic-like pairs are coregistered with a redundant master scene that is not used in tomographic processing. Thereby $2N$ (instead of $2N-1$ if we count the interferogram in the middle of Fig. 1 as a repeat-pass one with zero temporal baseline) conventional repeat-pass interferograms are generated from these pairs. Note that this assumption certainly favors the D-TomoSAR approach.

For TomoSAR using N bistatic-like pairs, the CRLB on the elevation estimate $\hat{s}$ of a single scatterer is [29]

$$\sigma_{\hat{s}} \coloneqq \frac{\lambda r}{4\pi\sqrt{N}\sqrt{2SNR}\,\sigma_b}, \tag{7}$$

where σ_b is the standard deviation of the perpendicular baselines $\{b_n\}$ of the N bistatic-like pairs. On the other hand, D-TomoSAR uses as inputs $2N$ conventional repeat-pass interferograms that are generated from the N bistatic-like pairs. For a single scatterer, suppose that its deformation time series is described by a basis function ψ. It can be shown that the CRLB on its elevation estimate is

$$\tilde{\sigma}_{\hat{s}} \coloneqq \frac{\lambda r}{4\pi\sqrt{2N}\sqrt{2SNR}\,\sqrt{1-\rho^2}\sigma_{\tilde{b}}}, \tag{8}$$

where $\sigma_{\tilde{b}}$ is the standard deviation of the perpendicular baselines $\{\tilde{b}_n\}$ of the $2N$ conventional repeat-pass interferograms, and ρ denotes the correlation coefficient between $\tilde{b}_n$ and $\psi_n \coloneqq \psi(t_n)$. The proof of (8) is similar to that of (6) with one minor difference: s is considered here as an unknown and therefore the corresponding Fisher information matrix is in $\mathbb{R}^{4\times 4}$.

We assume that $\{\tilde{b}_n\}$ are independent and identically distributed random variables.

Case 1 (pursuit monostatic):

For each b_n, there exist unique $k, l \in \mathbb{Z}_+$, $1 \le k \ne l \le 2N$, such that $b_n = \tilde{b}_k - \tilde{b}_l$. It follows that $\sigma_b^2 = 2\sigma_{\tilde{b}}^2$. For example, suppose that each $\tilde{b}_n$ is uniformly distributed in $[-b_{\max}, +b_{\max}]$, $b_{\max} > 0$. This implies that $\sigma_{\tilde{b}}^2 = (b_{\max})^2/3$. As a result, each b_n follows a symmetric triangular distribution with $\sigma_b^2 = 2(b_{\max})^2/3$. Dividing $\sigma_{\hat{s}}$ by $\tilde{\sigma}_{\hat{s}}$ yields

$$\frac{\sigma_{\hat{s}}}{\tilde{\sigma}_{\hat{s}}} = \sqrt{1-\rho^2} < 1. \tag{9}$$

Case 2 (bistatic):

From $b_n = (\tilde{b}_k - \tilde{b}_l)/2$ it follows that $\sigma_b^2 = \sigma_{\tilde{b}}^2/2$ and consequently $\sigma_{\hat{s}}/\tilde{\sigma}_{\hat{s}} < 2$, which completes the proof.

Note that similar results can be obtained for deformation parameter estimate.

Furthermore, we analyze the complexity of the proposed framework via flop count. In the case of a one-sided distribution of cross-track perpendicular baselines, the optional sign flipping problem (2) can be solved using exhaustive search in $\mathcal{O}(N2^{N-1})$ flops. For large N, the heuristic approach, which is based on a simple sorting, can be performed in $\mathcal{O}(N\log N)$ flops.

The sparse reconstruction problem (3) can be solved using the alternating direction method of multipliers [33] in $\mathcal{O}(LNT)$ flops[1], assuming that $N \ll L$ and $N \ll T$, where T is the number of iterations. The model order selection problem for elevation estimates (4) is essentially a series of subset least squares problems that can be solved in $\mathcal{O}(N)$ flops. The deformation model order selection problem (5) can be solved in $\mathcal{O}(N\tilde{L}^K)$ flops, or $\mathcal{O}(N\tilde{L})$ flops using the greedy approach. Therefore, the total cost of the proposed framework is at most $\mathcal{O}(LNT + N\tilde{L}^K)$ flops.

As a comparison, the total cost of applying the sparse reconstruction and model order selection directly to $2N$ repeat-pass interferograms is $\mathcal{O}(L\tilde{L}NT)$ flops. By assuming that $L \approx \tilde{L} \ll T$, the proposed framework is approximately $\tilde{L}$ times as simple (as opposed to complex) for single and double scatterers, which are considered as the most common cases in urban areas [34].

In Sec. III, we demonstrate the applicability of the proposed framework with a stack of TanDEM-X pursuit monostatic acquisitions.

III. Experiments with TanDEM-X Pursuit Monostatic Data

Due to the unavailability of suitable Tandem-L bistatic test data, we applied the proposed framework to a small TanDEM-X pursuit monostatic stack. The pursuit monostatic mode was temporarily put into practice from October 2014 to February 2015 during the TanDEM-X Science Phase [24]. In order to avoid RF interference between radar signals, the along-track distance was set to approximately 76 km, which corresponds to a temporal baseline of circa 10 seconds. During this five-month period, 12 staring spotlight scenes of the City of Las Vegas were acquired. Out of these, 6 pursuit monostatic interferograms were generated and their baselines are plotted in Fig. 2a. As can be observed, relatively large values in magnitude are available, whereas in the usual cases of TSX and TDX[2] the baselines are bounded between ± 250 m. As a matter of fact, in order to favor TomoSAR and other applications in polar regions, cross-track perpendicular baselines were programmed to slowly drift (in magnitude) from 0 to 750 m [24]. Since all baselines but one are negative, we applied the sign flipping procedure that was introduced in Sec. II-A. The baselines after sign flipping are plotted in Fig. 2b. The sign was indeed flipped for two baselines and the standard deviation increased from approximately 286.7 to 308.3 m. As a consequence, the CRLB was improved by 7.5%.

As a practical demonstration of the proposed framework, we focus on a small area which contains a high-rise building and is therefore subject to layover. The APS was compensated by subtracting the phase of a nearby ground reference point in each interferogram. This step is also known as phase calibration [35], [36]. Given a sufficiently large number of bistatic-like pairs (for example $N \ge 11$), a stack of $2N-1$ repeat-pass interferograms can be generated. Subsequently, a standard persistent scatterer interferometry (PSI) approach

[1]For the sake of simplicity, we count each complex addition or multiplication as one flop.

[2]In this context we refer to the two satellites in the TanDEM-X mission as TSX and TDX.

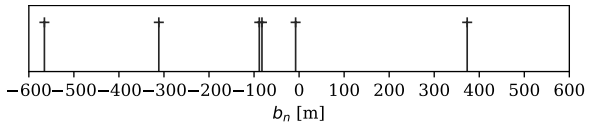

(a) Before sign flipping

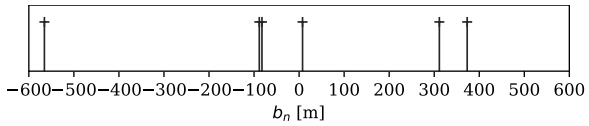

(b) After sign flipping

Fig. 2. Cross-track perpendicular baselines of 6 pursuit monostatic interferograms before (2a) and after sign flipping (2b). The height of ambiguity is approximately, in ascending order, 10, 15, 18, 64, 69 and 738 m.

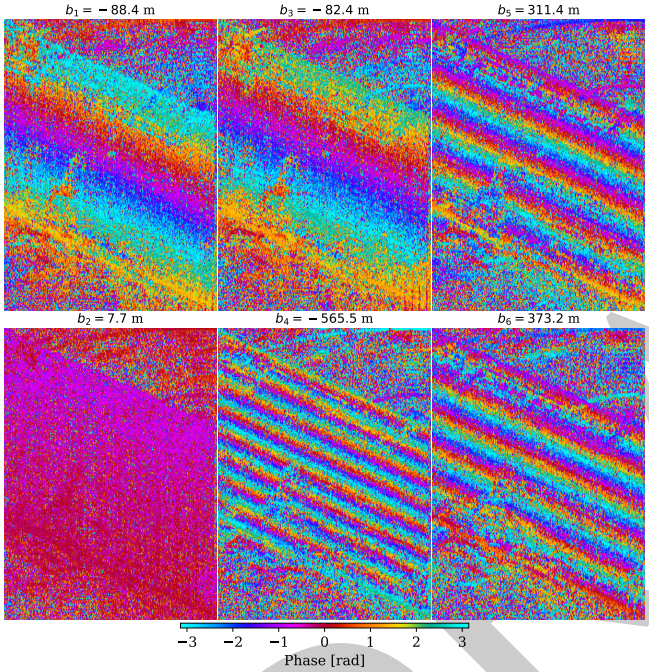

Fig. 3. Pursuit monostatic interferograms of a high-rise building, generated from 12 TSX and TDX acquisitions and annotated with their cross-track perpendicular baselines.

[37]–[39] can be applied to estimate the APS of single point-like scatterers. This can be resampled and compensated for the whole scene (see for example [40] and the references therein). Alternatively, topographic updates of single point-like scatterers can be first estimated using only bistatic-like interferograms and then compensated in conventional repeat-pass interferograms for APS estimation [32]. Fig. 3 shows the 6 pursuit monostatic interferograms of a high-rise building and its surroundings. Note that the fringes on the building facade appear to be highly coherent. For Tandem-L, we would expect even higher coherence, especially for distributed scatterers. This is due to minimized temporal decorrelation in the bistatic mode, as well as the outstanding penetration depth in L-band.

In the next subsection, the sparse reconstruction is enhanced by exploiting joint sparsity among different resolution cells, in order to circumvent the issue of the extremely small number of pursuit monostatic pairs.

A. Joint sparsity reconstruction for extremely small N

Although the pursuit monostatic interferograms in Fig. 3 are mostly unaffected by APS or temporal decorrelation, the number of elevation frequencies (i.e., 6) is extremely small. Zhu et al. reported that, for $N = 6$, not exploiting special signal structure can lead to results that are subject to outliers [41]. With the objective of achieving high-quality elevation reconstruction, we introduced spatial prior in the form of iso-height line segments along range on the building facade. The iso-height line segments were derived from freely available geospatial data containing building footprints. All resolution cells in a given line segment form an iso-height cluster, which was jointly reconstructed. In other words, we solve instead the $\ell_{1,2}$-regularized least squares problem

$$\hat{\mathbf{\Gamma}} := \arg\min_{\mathbf{\Gamma}} \frac{1}{2}\|\mathbf{R}\mathbf{\Gamma} - \mathbf{G}\|_{\mathrm{F}}^2 + \lambda\|\mathbf{\Gamma}\|_{1,2}, \tag{10}$$

where the p-th column of $\mathbf{\Gamma} \in \mathbb{C}^{L\times P}$ represents the discrete reflectivity profile in the p-th resolution cell (also known as snapshot) along the iso-height line segment, the p-th column of $\mathbf{G} \in \mathbb{C}^{N\times P}$ contains the InSAR observations of the p-th resolution cell, $\|\cdot\|_{\mathrm{F}}$ denotes the Frobenius norm, and $\|\cdot\|_{1,2}$ denotes $\ell_{1,2}$ norm, i.e., $\|\mathbf{\Gamma}\|_{1,2} := \sum_{i=1}^{L}\|\boldsymbol{\gamma}^i\|_2$. A treatise on this algorithm can be found in [41], where it was shown empirically that solving the $\ell_{1,2}$-regularized least squares problem (10) with N interferograms and P snapshots achieves almost the same performance, in terms of elevation estimate error, as solving the ℓ_1-regularized least squares problem (3) with NP interferograms. Similar approaches using multiple snapshots can be found in, e.g., [42], [43]. Subsequently, the model order selections (4) and (5) were performed individually for each resolution cell.

Fig. 4 shows the mean intensity map of the building of interest and several exemplary iso-height line segments. The height estimates of single and layover scatterers are plotted in Fig. 5. Roof interacts with facade and ground in the near range, while facade and ground are subject to layover in the far range. The smooth color transition from near to far range indicates a good quality of height estimates. Nevertheless, there are indeed a few outliers in the far range. These outliers, which we managed to reproduce with simulated data sets, are presumably due to the yet nonuniform distribution of the extremely small number of baselines. The height profile, generated via averaging within each iso-height cluster, can be found in Fig. 6, where roof and facade are clearly identifiable. In order to assess the relative accuracy of height estimates, we extracted the point cloud segment corresponding to facade by thresholding of point density [44] and fitted a vertical plane with ℓ_1-loss (see Fig. 7). From the bird's-eye view, all scatterers appear to be evenly distributed w.r.t. the fitted facade plane. We calculated the elevation distance of each scatterer's estimated position to the facade plane, and projected it into the vertical direction. We refer to this vertical component as the height estimate error relative to the fitted vertical plane. Its histogram resembles a zero-mean normal distribution (see Fig. 8). The relative vertical accuracy, which is defined in this context as the median absolute deviation (MAD) of height estimate error, was estimated to be approximately 0.29 m.

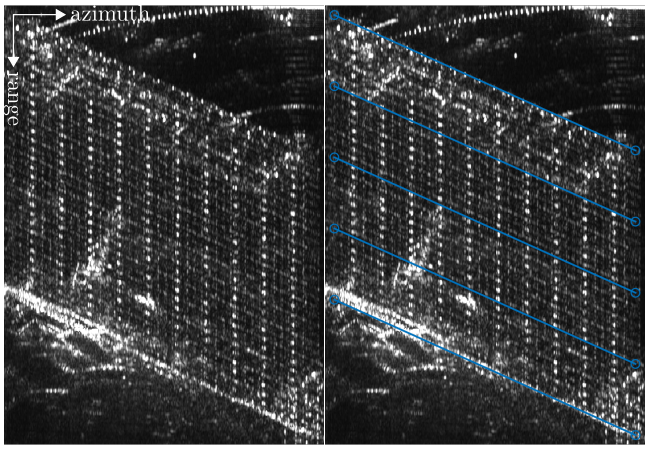

Fig. 4. Mean intensity map (left) and overlaying exemplary iso-height line segments (right).

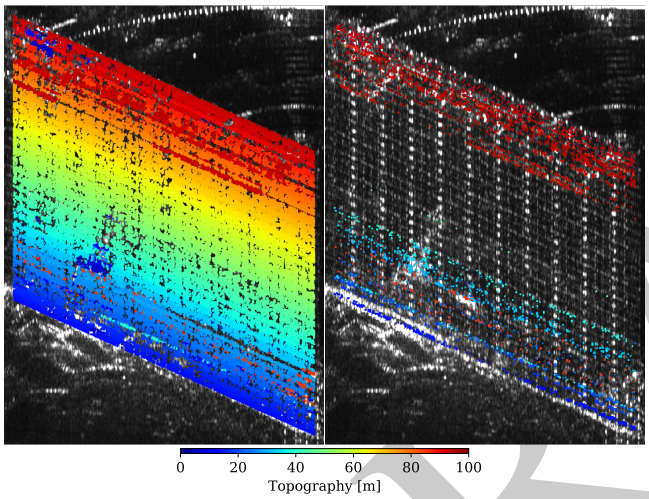

Fig. 5. Height estimates of single (left) and layover scatterers (right). In the case of layover, the height estimate of the highest scatterer is shown.

Note that this can be interpreted as an upper bound on the true relative vertical accuracy, since the building facade is not entirely flat.

As explained in Sec. II-B, these height estimates can be used as deterministic prior for repeat-pass interferometry. For single scatterers, the topographic phase was compensated by using the height-to-phase conversion factor (see Fig. 9). The residual phase is presumably mainly due to scatterer's motion and already reveals a pattern of it. Note that every pair of repeat-pass interferograms sharing the same temporal baseline (in days) appear almost identical after topographic phase compensation. This provides a compelling argument for limited temporal decorrelation and APS wihtin a pursuit monostatic pair. Needless to say, an increase in the coherence of prospective Tandem-L repeat-pass interferograms can be expected. Even for distributed scatterers, L-band signal is known to maintain a certain degree of coherence after more than two years of time [45], [46]. This would undoubtedly lead to a greater coverage of retrievable information. Given the span of temporal baselines of 132 days, the motion was assumed

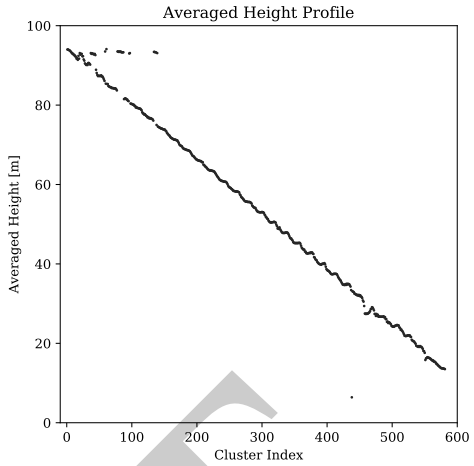

Fig. 6. Cluster-wise averaged height profile.

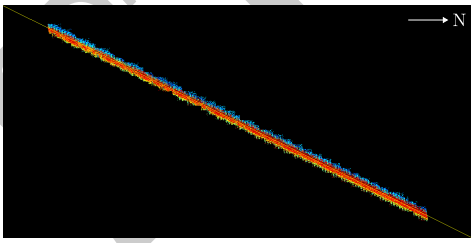

Fig. 7. Bird's-eye view of the point cloud segment corresponding to facade.

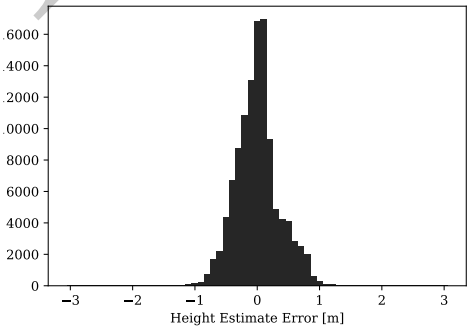

Fig. 8. Histogram of height estimate error relative to a fitted vertical plane. The median and MAD are approximately 0.00 and 0.29 m, respectively.

to consist primarily of thermal contraction and expansion due to temperature change (see for example [47]). To this end, a sinusoidal model was employed. By solving the DefoSAR subproblem (5), we obtained the amplitude estimates of periodical deformation for single and layover scatterers, which are shown in Fig. 10. In general, the amplitude of periodical deformation is positively correlated with height (see the scatter plot in Fig. 11) and relatively large in magnitude at the top of the building as well as at the side. This pattern accords with that of repeat-pass interferograms of single scatterers after topographic phase compensation in Fig. 9b, which partially validates our results.

A preliminary comparison with D-TomoSAR is provided in the next subsection.

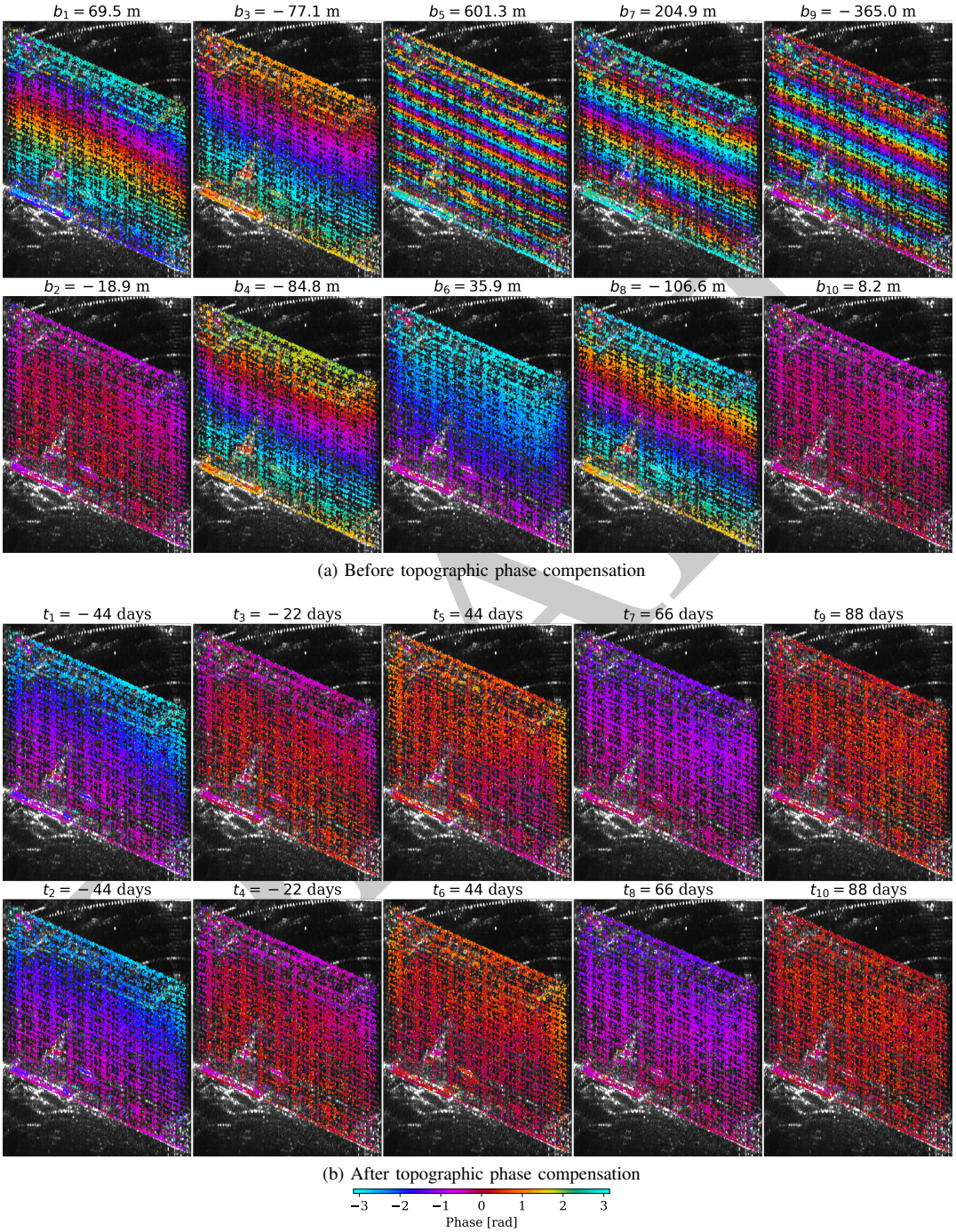

(a) Before topographic phase compensation

(b) After topographic phase compensation

Fig. 9. Repeat-pass interferometric phase of single scatterers before (9a) and after topographic phase compensation (9b), annotated with their cross-track perpendicular or temporal baselines.

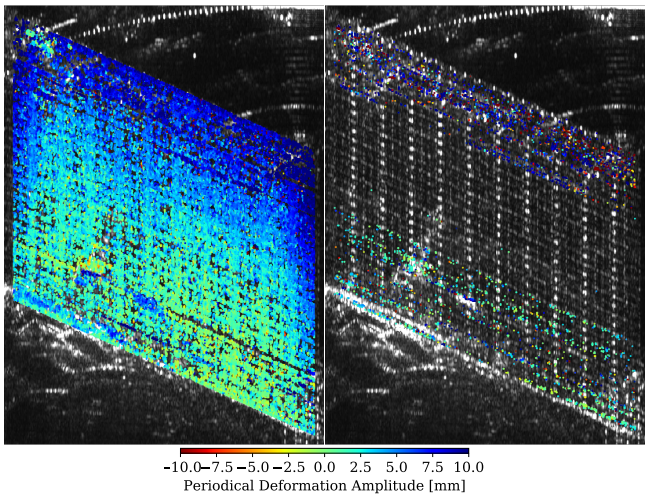

Fig. 10. Periodical deformation amplitude estimates of single (left) and layover scatterers (right). In the case of layover, the amplitude estimate of the highest scatterer is shown.

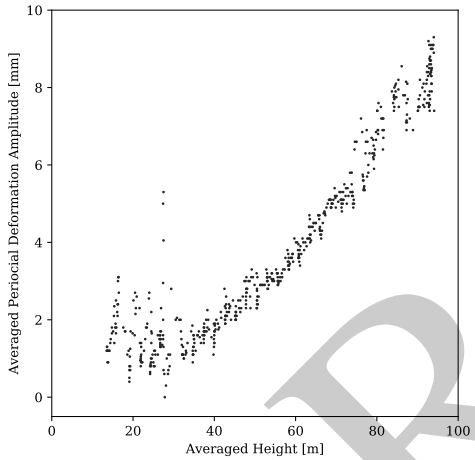

Fig. 11. Scatter plot of averaged height and periodical deformation amplitude.

B. Tomo- and DefoSAR vs. D-TomoSAR: an empirical analysis

In Sec. III-A, we introduced additional spatial prior in order to boost the sparse reconstruction for extremely small N. The joint sparsity reconstruction method (10) is, however, only applicable to bistatic-like data sets. Therefore, a direct comparison with the results generated by the same method using conventional repeat-pass interferograms is ruled out. For the sake of fairness, we employed the pixel-wise sparse reconstruction method (3) with identical parameter quantization for both TomoSAR and D-TomoSAR processing using 6 pursuit monostatic and 11 repeat-pass interferograms, respectively. As might be expected, the former was followed by DefoSAR processing for deformation parameter estimation. Tab. I summarizes the overall runtime on a desktop with a quad-core Intel processor at 3.40 GHz and 16 GB RAM. The Tomo- and DefoSAR framework was computationally approximately 6.4 times as efficient.

As listed in Tab. II, the standard deviation σ_b of the cross-track perpendicular baselines $\{b_n\}$ of the 6 pursuit monostatic

TABLE I
TOMO- AND DEFOSAR VS. D-TOMOSAR: RUNTIME

	Tomo- and DefoSAR	D-TomoSAR	Ratio
Runtime [h]	0.61	3.94	6.44

TABLE II
TOMOSAR VS. D-TOMOSAR: BASELINE STANDARD DEVIATION, $\sqrt{1-\rho^2}$ AND CRLB OF HEIGHT ESTIMATES ($SNR = 5$ DB)

	TomoSAR	D-TomoSAR	Ratio
Baseline σ [m]	308.31	226.33	1.36
$\sqrt{1-\rho^2}$	n.a.	0.92	n.a.
CRLB of height [m]	0.48	0.52	1.10

TABLE III
STATISTICS OF THE HEIGHT ESTIMATE ERROR IN FIG. 13

	TomoSAR	D-TomoSAR	Ratio
No. of scatterers	87595	91063	1.04
Median [m]	0.00	0.00	n.a.
Mean [m]	0.00	0.00	n.a.
MAD [m]	0.52	0.61	1.16
Standard Deviation [m]	0.50	0.58	1.16

interferograms is approximately 1.4 times as high as the one $\sigma_{\tilde{b}}$ of $\{\tilde{b}_n\}$ of the 11 repeat-pass interferograms. Note that our assumption in Sec. II-C implies that $\sigma_b = \sqrt{2}\sigma_{\tilde{b}}$. The correlation between $\tilde{b}_n$ and the deformation basis function ψ_n leads to $\sqrt{1-\rho^2} \approx 0.92$. This can be interpreted as a degradation of $\sigma_{\tilde{b}}$ by 8% at the expense of taking deformation into account. Given a single scatterer with an SNR of 5 dB, the CRLB of height estimates for the proposed framework is approximately 0.48 m, which is 1.1 times as low.

Same as in Sec. III-A, we extracted the point cloud segment corresponding to building facade by thresholding of the 2-D point density. This process also eliminated false alarms due to the extremely small number of interferograms. As shown in Fig. 12, both facade segments appear quite similar, except that the uppermost part of the facade is incomplete in the D-TomoSAR result. A possible explanation could be that the already complex short-distance roof-facade layover of point-like scatterers is furthermore complicated by their deformation behavior. The facade segment produced by D-TomoSAR has slightly more scatterers (see Tab. III), but we consider this difference to be insignificant. In order to access the quality of the point cloud, we followed the same approach that was introduced in the last subsection, namely to fit a vertical plane into each facade segment, project the distance of each point to the fitted plane into the vertical axis, and interpret it as the height estimate error relative to the fitted plane. The normalized histograms are shown in Fig. 13. While both histograms are centered around zero, the one of TomoSAR has less deviation. The MAD is in fact approximately 1.16 as low for TomoSAR (cf. 1.10 as predicted in Tab. II for an average SNR of 5 dB).

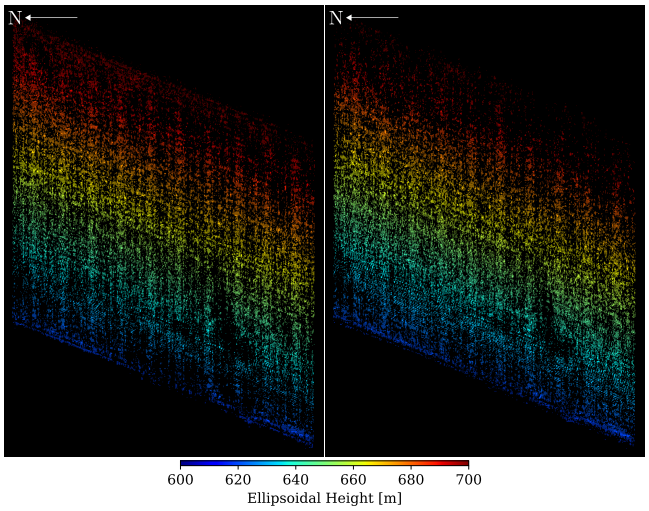

Fig. 12. Reconstructed facade segments (color-coded by ellipsoidal height). Left: TomoSAR using 6 pursuit monostatic interferograms. Right: D-TomoSAR using 11 repeat-pass interferograms.

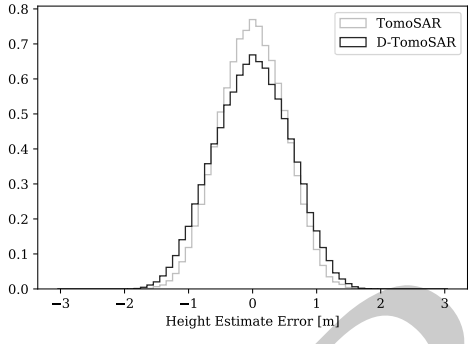

Fig. 13. Normalized histogram of height estimate error relative to a fitted vertical plane. Gray: TomoSAR using 6 pursuit monostatic interferograms. Black: D-TomoSAR using 11 repeat-pass interferograms. See Tab. III for more statistics.

IV. Conclusion

In the preceding sections, we tackled the problem of differential TomoSAR in urban areas using bistatic-like data sets, which will be delivered by the prospective Tandem-L mission as operational products. We proposed a framework which divides the original problem into two subsequent subproblems. The first subproblem is essentially non-differential TomoSAR with bistatic-like interferograms and can be dealt with using already existing methods. In the second subproblem, elevation estimates are incorporated as deterministic prior into the DefoSAR design matrix in order to estimate the coefficients of deformation basis functions with conventional repeat-pass interferograms. We showed via theoretical and empirical analyses that this framework, when applied to pursuit monostatic data, not only outperforms standard D-TomoSAR but is also less expensive. In an extreme case, we applied our framework to merely 6 TanDEM-X pursuit monostatic pairs and achieved reasonable results for both elevation and deformation estimates. The relative vertical accuracy of the resulted point cloud was estimated to be approximately 0.29 m.

Although we proposed to estimate each scatterer's elevation position using bistatic-like interferograms, it could indeed stem from other sources such as ray-tracing simulation with an external 3-D building model [48] or with one reconstructed from a single SAR intensity image [49]. The corresponding minor adaptation would extend the applicability of the proposed framework to interferometric stacks composed of nothing but conventional repeat-pass acquisitions and thereby allow precise object-based infrastructure monitoring.

Appendix
Proof of (6)

First we state the following result from [50].

Suppose that $\mathbf{x} \in \mathbb{R}^L$ and $\mathbf{y} \in \mathbb{C}^N$ are the parameter and data vectors, respectively, and $\mathbf{y}$ is the random Gaussian observation of the deterministic signal vector $\mathbf{u}(\mathbf{x}) \in \mathbb{C}^N$ with covariance matrix $\mathbf{C}_\mathbf{y}(\mathbf{x})$. The likelihood function is

$$f(\mathbf{y} \mid \mathbf{x}) \coloneqq \frac{1}{\pi^N \det\left(\mathbf{C}_\mathbf{y}(\mathbf{x})\right)} \cdot \exp\Big(-\big(\mathbf{y}-\mathbf{u}(\mathbf{x})\big)^{\mathrm{H}} \mathbf{C}_\mathbf{y}^{-1}(\mathbf{x}) \big(\mathbf{y}-\mathbf{u}(\mathbf{x})\big)\Big).$$

It can be shown that the Fisher information matrix $\mathbf{I}(\mathbf{x})$ is given by

$$[\mathbf{I}(\mathbf{x})]_{kl} \coloneqq \operatorname{tr}\left(\mathbf{C}_\mathbf{y}^{-1}(\mathbf{x}) \frac{\partial \mathbf{C}_\mathbf{y}(\mathbf{x})}{\partial x_k} \mathbf{C}_\mathbf{y}^{-1}(\mathbf{x}) \frac{\partial \mathbf{C}_\mathbf{y}(\mathbf{x})}{\partial x_l}\right) + 2\operatorname{Re}\left(\frac{\partial \mathbf{u}^{\mathrm{H}}(\mathbf{x})}{\partial x_k} \mathbf{C}_\mathbf{y}^{-1}(\mathbf{x}) \frac{\partial \mathbf{u}^{\mathrm{H}}(\mathbf{x})}{\partial x_l}\right), \tag{11}$$

$k, l = 1, \ldots, L$.

Now let us consider the DefoSAR data model

$$\tilde{g}_n = \tilde{\gamma} \exp(-j2\pi\tilde{\xi}_n s) \exp(-j(4\pi/\lambda)\psi_n c) + \tilde{\epsilon}_n,$$

$n = 1, \ldots, 2N-2$, where $\tilde{\epsilon}_n$ is complex white Gaussian noise with variance $\sigma_{\tilde{\epsilon}}^2$, and $\psi_n \coloneqq \psi(t_n)$. Here we assume that the elevation estimate is perfect, i.e., $\hat{s} = s$. By replacing $\tilde{\gamma}$ by $a\exp(j\phi)$ where $a, \phi \in \mathbb{R}$, we define the new real parameter vector as $\mathbf{x} \coloneqq \begin{pmatrix} a & c & \phi \end{pmatrix}^{\mathrm{T}}$. The signal vector is given by $u_n(\mathbf{x}) \coloneqq a\exp\big(j(\phi - 2\pi\tilde{\xi}_n s - (4\pi/\lambda)\psi_n c)\big)$, $n = 1, \ldots, 2N-2$. Straightforward computations using (11) yield the Fisher information matrix

$$\mathbf{I}(\mathbf{x}) = \frac{2}{\sigma_{\tilde{\epsilon}}^2} \begin{pmatrix} 2N-2 & 0 & 0 \\ 0 & \frac{(4\pi)^2 a^2}{\lambda^2} \sum_n \psi_n^2 & -\frac{4\pi a^2}{\lambda} \sum_n \psi_n \\ 0 & -\frac{4\pi a^2}{\lambda} \sum_n \psi_n & (2N-2)\gamma^2 \end{pmatrix}.$$

The CRLB for $\hat{c}$ is found to be

$$\sigma_{\hat{c}}^2 \coloneqq [\mathbf{I}^{-1}(\mathbf{x})]_{22} = \frac{\lambda^2 \sigma_{\tilde{\epsilon}}^2}{(4\pi)^2 (2N-2) 2a^2 \sigma_\psi^2}.$$

By defining $SNR \coloneqq a^2/\sigma_{\tilde{\epsilon}}^2$, this reduces to

$$\sigma_{\hat{c}} = \frac{\lambda}{4\pi\sqrt{2N-2}\sqrt{2SNR}\,\sigma_\psi},$$

which completes the proof.

ACKNOWLEDGMENT

TerraSAR-X data was provided by the German Aerospace Center (DLR) under the TanDEM-X Science Phase AO Project NTI_INSA6729. F. Rodriguez Gonzalez assisted on InSAR processing at different stages of the project and discussed with the first author about the pros and cons of the proposed framework. A. Parizzi lectured the first author about Tandem-L and L-band SAR interferometry. H. Breit offered fresh insights into future SAR missions. The original idea of deformation model order selection came out of a discussion with Dr. Y. Wang. The authors would also like to thank Prof. R. Bamler for valuable discussions and the reviewers for their constructive comments.

REFERENCES

[1] A. Moreira, G. Krieger, I. Hajnsek, K. Papathanassiou, M. Younis, P. Lopez-Dekker, S. Huber, M. Villano, M. Pardini, M. Eineder *et al.*, "Tandem-L: A highly innovative bistatic SAR mission for global observation of dynamic processes on the earth's surface," *IEEE Geoscience and Remote Sensing Magazine*, vol. 3, no. 2, pp. 8–23, 2015.

[2] G. Krieger, A. Moreira, H. Fiedler, I. Hajnsek, M. Werner, M. Younis, and M. Zink, "TanDEM-X: A satellite formation for high-resolution SAR interferometry," *IEEE Transactions on Geoscience and Remote Sensing*, vol. 45, no. 11, pp. 3317–3341, 2007.

[3] P. Rizzoli, M. Martone, C. Gonzalez, C. Wecklich, D. B. Tridon, B. Bräutigam, M. Bachmann, D. Schulze, T. Fritz, M. Huber *et al.*, "Generation and performance assessment of the global TanDEM-X digital elevation model," *ISPRS Journal of Photogrammetry and Remote Sensing*, vol. 132, pp. 119–139, 2017.

[4] N. Gebert, B. C. Dominguez, M. W. Davidson, M. D. Martin, and P. Silvestrin, "SAOCOM-CS – a passive companion to SAOCOM for single-pass L-band SAR interferometry," in *EUSAR 2014; 10th European Conference on Synthetic Aperture Radar; Proceedings of*. VDE, 2014, pp. 1–4.

[5] P. López-Dekker, H. Rot, S. Solberg, M. Zonno, M. Rodriguez-Cassola, P. Prats-Iraola, and A. Moreira, "Companion SAR constellations for single-pass interferometric applications: The SESAME mission," in *Geoscience and Remote Sensing Symposium (IGARSS), 2017 IEEE International*. IEEE, 2017, pp. 119–122.

[6] D. Giudici, D. Mapelli, and F. Rocca, "Exploring the potential of Sentinel-1 constellation in tandem and bi-static configurations," in *EUSAR 2018; 12th European Conference on Synthetic Aperture Radar*. VDE, 2018, pp. 1–6.

[7] M. Bartusch, "HRWS high resolution wide swath: the next national X-band SAR mission," in *TerraSAR-X/TanDEM-X Science Team Meeting*, 2016.

[8] J. Janoth, M. Jochum, and A. Kaptein, "The high resolution wide swath mission and WorldSAR," in *37th International Symposium on Remote Sensing of Environment (ISRSE-37)*, 2017.

[9] G. Krieger, M. Zonno, M. Rodriguez Cassola, P. Lopez Dekker, J. Mittermayer, M. Younis, S. Huber, M. Villano, F. Queiroz de Almeida, P. Prats *et al.*, "MirrorSAR: A fractionated space radar for bistatic, multistatic and high-resolution wide-swath SAR imaging," in *International Geoscience and Remote Sensing Symposium (IGARSS)*. IEEE, 2017.

[10] G. Krieger, M. Zonno, J. Mittermayer, A. Moreira, S. Huber, and M. Rodriguez-Cassola, "MirrorSAR: A fractionated space transponder concept for the implementation of low-cost multistatic SAR missions," in *EUSAR 2018; 12th European Conference on Synthetic Aperture Radar*. VDE, 2018, pp. 1–6.

[11] M. Zonno, G. Krieger, M. Rodriguez-Cassola, J. Mittermayer, and A. Moreira, "A MirrorSAR-based single-pass dual-baseline SAR interferometer for the generation of very high quality DEMs," in *EUSAR 2018; 12th European Conference on Synthetic Aperture Radar*. VDE, 2018, pp. 1–6.

[12] H. Ansari, K. Goel, A. Parizzi, F. De Zan, N. Adam, and M. Eineder, "Tandem-L performance analysis for three dimensional earth deformation monitoring," in *Geoscience and Remote Sensing Symposium (IGARSS), 2015 IEEE International*. IEEE, 2015, pp. 4053–4056.

[13] G. Krieger, A. Moreira, M. Zink, I. Hajnsek, S. Huber, M. Villano, K. Papathanassiou, M. Younis, P. L. Dekker, M. Pardini *et al.*, "Tandem-L: Main results of the Phase A feasibility study," in *Geoscience and Remote Sensing Symposium (IGARSS), 2016 IEEE International*. IEEE, 2016, pp. 2116–2119.

[14] P. Prats-Iraola, P. Lopez-Dekker, F. De Zan, N. Yagüe-Martínez, M. Zonno, and M. Rodriguez-Cassola, "Performance of 3-d surface deformation estimation for simultaneous squinted SAR acquisitions," *IEEE Transactions on Geoscience and Remote Sensing*, vol. 56, no. 4, pp. 2147–2158, 2018.

[15] S. Suchandt, A. Pleskachevsky, and D. B. Tridon, "Oceanographic data retrieval with Tandem-L," in *EUSAR 2018; 12th European Conference on Synthetic Aperture Radar*. VDE, 2018, pp. 1–4.

[16] M. Zonno, M. J. Sanjuan-Ferrer, M. Rodriguez-Cassola, G. Krieger, and A. Moreira, "The Tandem-L mission for monitoring of earth's dynamics: Main performance results during Phase-B1," in *EUSAR 2018; 12th European Conference on Synthetic Aperture Radar*. VDE, 2018, pp. 1–6.

[17] A. Reigber and A. Moreira, "First demonstration of airborne SAR tomography using multibaseline L-band data," *IEEE Transactions on Geoscience and Remote Sensing*, vol. 38, no. 5, pp. 2142–2152, 2000.

[18] F. Gini, F. Lombardini, and M. Montanari, "Layover solution in multibaseline SAR interferometry," *IEEE Transactions on Aerospace and Electronic Systems*, vol. 38, no. 4, pp. 1344–1356, 2002.

[19] G. Fornaro, F. Lombardini, and F. Serafino, "Three-dimensional multipass SAR focusing: Experiments with long-term spaceborne data," *IEEE Transactions on Geoscience and Remote Sensing*, vol. 43, no. 4, pp. 702–714, 2005.

[20] F. Lombardini, "Differential tomography: A new framework for SAR interferometry," *IEEE Transactions on Geoscience and Remote Sensing*, vol. 43, no. 1, pp. 37–44, 2005.

[21] G. Fornaro, D. Reale, and F. Serafino, "Four-dimensional SAR imaging for height estimation and monitoring of single and double scatterers," *IEEE Transactions on Geoscience and Remote Sensing*, vol. 47, no. 1, pp. 224–237, 2009.

[22] X. X. Zhu and R. Bamler, "Very high resolution spaceborne SAR tomography in urban environment," *IEEE Transactions on Geoscience and Remote Sensing*, vol. 48, no. 12, pp. 4296–4308, 2010.

[23] ——, "Superresolving SAR tomography for multidimensional imaging of urban areas: Compressive sensing-based TomoSAR inversion," *IEEE Signal Processing Magazine*, vol. 31, no. 4, pp. 51–58, 2014.

[24] I. Hajnsek, T. Busche, G. Krieger, M. Zink, and A. Moreira, "Announcement of opportunity: TanDEM-X science phase," *DLR Public Document TD-PD-PL-0032*, no. 10, 2014.

[25] A. Ferretti, A. Fumagalli, F. Novali, C. Prati, F. Rocca, and A. Rucci, "A new algorithm for processing interferometric data-stacks: SqueeSAR," *IEEE Transactions on Geoscience and Remote Sensing*, vol. 49, no. 9, pp. 3460–3470, 2011.

[26] A. Parizzi and R. Brcic, "Adaptive InSAR stack multilooking exploiting amplitude statistics: A comparison between different techniques and practical results," *IEEE Geoscience and Remote Sensing Letters*, vol. 8, no. 3, pp. 441–445, 2011.

[27] M. Schmitt and U. Stilla, "Adaptive multilooking of airborne single-pass multi-baseline InSAR stacks," *IEEE Transactions on Geoscience and Remote Sensing*, vol. 52, no. 1, pp. 305–312, 2014.

[28] X. X. Zhu and R. Bamler, "Super-resolution power and robustness of compressive sensing for spectral estimation with application to spaceborne tomographic SAR," *IEEE Transactions on Geoscience and Remote Sensing*, vol. 50, no. 1, pp. 247–258, 2012.

[29] R. Bamler, M. Eineder, N. Adam, X. Zhu, and S. Gernhardt, "Interferometric potential of high resolution spaceborne SAR," *Photogrammetrie-Fernerkundung-Geoinformation*, vol. 2009, no. 5, pp. 407–419, 2009.

[30] X. X. Zhu and R. Bamler, "Tomographic SAR inversion by L_1-norm regularization–the compressive sensing approach," *IEEE Transactions on Geoscience and Remote Sensing*, vol. 48, no. 10, pp. 3839–3846, 2010.

[31] A. Budillon, A. Evangelista, and G. Schirinzi, "Three-dimensional SAR focusing from multipass signals using compressive sampling," *IEEE Transactions on Geoscience and Remote Sensing*, vol. 49, no. 1, pp. 488–499, 2011.

[32] K. Goel and N. Adam, "Fusion of monostatic/bistatic InSAR stacks for urban area analysis via distributed scatterers," *IEEE Geoscience and Remote Sensing Letters*, vol. 11, no. 4, pp. 733–737, 2014.

[33] S. Boyd, N. Parikh, E. Chu, B. Peleato, J. Eckstein *et al.*, "Distributed optimization and statistical learning via the alternating direction method of multipliers," *Foundations and Trends® in Machine learning*, vol. 3, no. 1, pp. 1–122, 2011.

[34] X. Zhu and R. Bamler, "Demonstration of super-resolution for tomographic SAR imaging in urban environment." *IEEE Trans. Geoscience and Remote Sensing*, vol. 50, no. 8, pp. 3150–3157, 2012.

[35] M. Nannini, M. Martone, P. Rizzoli, P. Prats-Iraola, M. Rodriguez-Cassola, and A. Moreira, "Spaceborne demonstration of coherent SAR

tomography for future companion satellite SAR missions," in *Geoscience and Remote Sensing Symposium (IGARSS), 2017 IEEE International*. IEEE, 2017, pp. 129–132.

[36] F. Kugler, D. Schulze, I. Hajnsek, H. Pretzsch, and K. P. Papathanassiou, "TanDEM-X Pol-InSAR performance for forest height estimation," *IEEE Transactions on Geoscience and Remote Sensing*, vol. 52, no. 10, pp. 6404–6422, 2014.

[37] A. Ferretti, C. Prati, and F. Rocca, "Permanent scatterers in SAR interferometry," *IEEE Transactions on geoscience and remote sensing*, vol. 39, no. 1, pp. 8–20, 2001.

[38] C. Colesanti, A. Ferretti, F. Novali, C. Prati, and F. Rocca, "SAR monitoring of progressive and seasonal ground deformation using the permanent scatterers technique," *IEEE Transactions on Geoscience and Remote Sensing*, vol. 41, no. 7, pp. 1685–1701, 2003.

[39] N. Adam, B. Kampes, and M. Eineder, "Development of a scientific permanent scatterer system: Modifications for mixed ERS/ENVISAT time series," in *Envisat & ERS Symposium*, vol. 572, 2005.

[40] N. Ge, F. R. Gonzalez, Y. Wang, Y. Shi, and X. X. Zhu, "Spaceborne staring spotlight SAR tomographya first demonstration with TerraSAR-X," *IEEE Journal of Selected Topics in Applied Earth Observations and Remote Sensing*, no. 99, pp. 1–14, 2018.

[41] X. X. Zhu, N. Ge, and M. Shahzad, "Joint sparsity in SAR tomography for urban mapping," *IEEE Journal of Selected Topics in Signal Processing*, vol. 9, no. 8, pp. 1498–1509, 2015.

[42] G. Fornaro, S. Verde, D. Reale, and A. Pauciullo, "CAESAR: An approach based on covariance matrix decomposition to improve multibaseline–multitemporal interferometric sar processing," *IEEE Transactions on Geoscience and Remote Sensing*, vol. 53, no. 4, pp. 2050–2065, 2015.

[43] M. Schmitt and U. Stilla, "Compressive sensing based layover separation in airborne single-pass multi-baseline InSAR data," *IEEE Geoscience and Remote Sensing Letters*, vol. 10, no. 2, pp. 313–317, 2013.

[44] X. X. Zhu and M. Shahzad, "Facade reconstruction using multiview spaceborne TomoSAR point clouds," *IEEE Transactions on Geoscience and Remote Sensing*, vol. 52, no. 6, pp. 3541–3552, 2014.

[45] A. Parizzi, X. Cong, and M. Eineder, "First results from multifrequency interferometry. a comparison of different decorrelation time constants at L, C, and X band," *ESA Scientific Publications*, no. SP-677, pp. 1–5, 2009.

[46] Y. Morishita and R. F. Hanssen, "Temporal decorrelation in L-, C-, and X-band satellite radar interferometry for pasture on drained peat soils," *IEEE Transactions on Geoscience and Remote Sensing*, vol. 53, no. 2, pp. 1096–1104, 2015.

[47] S. Gernhardt and R. Bamler, "Deformation monitoring of single buildings using meter-resolution SAR data in PSI," *ISPRS journal of photogrammetry and remote sensing*, vol. 73, pp. 68–79, 2012.

[48] S. Auer, I. Hornig, M. Schmitt, and P. Reinartz, "Simulation-based interpretation and alignment of high-resolution optical and SAR images," *IEEE Journal of Selected Topics in Applied Earth Observations and Remote Sensing*, vol. 10, no. 11, pp. 4779–4793, 2017.

[49] Y. Sun, M. Shahzad, and X. X. Zhu, "Building height estimation in single SAR image using OSM building footprints," in *Urban Remote Sensing Event (JURSE), 2017 Joint*. IEEE, 2017, pp. 1–4.

[50] S. M. Kay, *Fundamentals of statistical signal processing: estimation theory*. Prentice Hall, 1993, vol. 1.

A.3 Ge et al. (2018)

N. Ge, F. R. Gonzalez, Y. Wang, Y. Shi, and X. X. Zhu. Spaceborne staring spotlight SAR tomography—a first demonstration with TerraSAR-X. *IEEE Journal of Selected Topics in Applied Earth Observations and Remote Sensing*, 11(10):3743–3756, 2018

Spaceborne Staring Spotlight SAR Tomography—A First Demonstration with TerraSAR-X

Nan Ge, Fernando Rodriguez Gonzalez, Yuanyuan Wang, *Member, IEEE,* Yilei Shi, Xiao Xiang Zhu, *Senior Member, IEEE*

***Abstract*—With the objective of exploiting hardware capabilities and preparing the ground for the next-generation X-band synthetic aperture radar (SAR) missions, TerraSAR-X and TanDEM-X are now able to operate in staring spotlight mode, which is characterized by an increased azimuth resolution of approximately 0.24 m compared to 1.1 m of the conventional sliding spotlight mode. In this paper, we demonstrate for the first time its potential for SAR tomography. To this end, we tailored our interferometric and tomographic processors for the distinctive features of the staring spotlight mode, which will be analyzed accordingly. By means of its higher spatial resolution, the staring spotlight mode will not only lead to a denser point cloud, but also to more accurate height estimates due to the higher signal-to-clutter ratio. As a result of a first comparison between sliding and staring spotlight TomoSAR, the following were observed: 1) the density of the *staring* spotlight point cloud is approximately 5.1–5.5 times as high; 2) the relative height accuracy of the *staring* spotlight point cloud is approximately 1.7 times as high.**

***Index Terms*—SAR tomography, staring spotlight, synthetic aperture radar (SAR), TerraSAR-X.**

I. Introduction

TERRASAR-X and TanDEM-X, the twin German satellites of almost identical build, have been delivering high-resolution X-band synthetic aperture radar (SAR) images since their launch in 2007 and 2010, respectively. Among civil SAR satellites, their unprecedented high spatial resolution in meter range and relatively short revisit time of 11 days opened up new applications of spaceborne SAR interferometry (InSAR). As a benchmark of medium-resolution spaceborne SAR sensors, a resolution cell in an ENVISAT ASAR stripmap product of the size 6-by-9 m^2 (azimuth-by-range) is resolved by approximately 5-by-15 pixels in a high-resolution sliding spotlight image of TerraSAR-X with 300 MHz range bandwidth [1]. Particularly in urban areas, this meter-level resolution provides the possibility of revealing detailed information in terms of geolocation and motion of single man-made objects. Adaptations of advanced time series analysis methods, such as persistent scatterer interferometry (PSI) and SAR tomography (TomoSAR), to sliding spotlight datasets showed promising results, see, for example, [2]–[5].

In order to fully exploit the capabilities of TerraSAR-X[1] and to prepare for the next-generation X-band SAR satellite missions, e.g., HRWS [6], the TerraSAR-X staring spotlight mode was conceptualized and consequently operationalized [7], [8]. Compared to the high-resolution sliding spotlight mode, the SAR sensor in staring spotlight mode employs a larger squint angle range to achieve a better azimuth resolution of approximately 0.24 m. As a result, the same ENVISAT ASAR stripmap pixel, as mentioned in the previous paragraph, is represented by 25-by-15 pixels in a staring spotlight image. The advantages of increased (azimuth) resolution for urban areas are at least two-fold: 1) it is more likely for point-like targets with similar azimuth-range coordinates to appear in different resolution cells, thus densifying the 4-D point cloud; 2) point-like targets stand out more prominently from clutter, which leads to higher signal-to-clutter ratio (SCR). These factors favor PSI and TomoSAR in different ways. While the former increases the amount of information of particularly single man-made objects, the latter provides a better lower bound on the variance of height estimates [9].

Although it seems encouraging to adapt and apply TomoSAR to staring spotlight datasets, yet to the best of our knowledge there has not been any published result. A lack of datasets could be one reason. On the other hand, several considerations regarding staring spotlight mode need to be taken into account during InSAR processing, which might also hinder such an application. By means of this paper, we intend to show that staring spotlight datasets are indeed suitable for TomoSAR. Based on a sufficient number of acquisitions, our first results on the scales of a city and of individual infrastructures are demonstrated to provide an argument in favor of this statement. We also perform a preliminary comparison between sliding and staring spotlight TomoSAR by using a limited number of datasets in both modes.

The remainder of this paper is organized as follows. Section II explains the TerraSAR-X staring spotlight mode and its related InSAR processing aspects. The principles of TomoSAR are briefly revisited in section III, where several technical

This work is jointly supported by Helmholtz Association under the framework of the Young Investigators Group "SiPEO" (VH-NG-1018, www.sipeo.bgu.tum.de), and the European Research Council (ERC) under the European Union's Horizon 2020 research and innovation program (ERC-2016-StG-714087, So2Sat). *Corresponding author: Xiao Xiang Zhu.*

Nan Ge and Fernando Rodriguez Gonzalez are with the Remote Sensing Technology Institute, German Aerospace Center (DLR), 82234 Wessling, Germany (e-mail: Nan.Ge@dlr.de; Fernando.RodriguezGonzalez@dlr.de).

Yuanyuan Wang is with Signal Processing in Earth Observation, Technical University of Munich, 80333 Munich, Germany (e-mail: wang@bv.tum.de).

Yilei Shi is with Remote Sensing Technology, Technical University of Munich, 80333 Munich, Germany (e-mail: yilei.shi@tum.de).

Xiao Xiang Zhu is with the Remote Sensing Technology Institute, German Aerospace Center (DLR), 82234 Wessling, Germany, and also with Signal Processing in Earth Observation, Technical University of Munich, 80333 Munich, Germany (e-mail: xiao.zhu@dlr.de).

[1]In the following TerraSAR-X is referred to as the monostatic constellation of TerraSAR-X and TanDEM-X, i.e., SAR instrument is activated on either TerraSAR-X or TanDEM-X but not both.

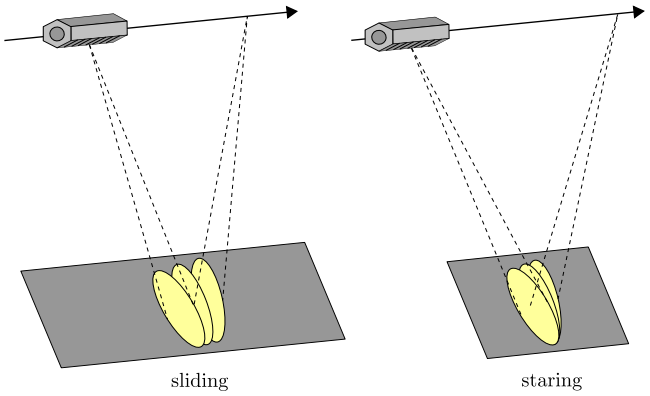

Fig. 1. TerraSAR-X sliding (left) and staring (right) spotlight imaging geometry. Modified from [1].

adaptations are elucidated as well. Section IV comprises our first results with an interferometric stack of Washington, D.C. and some interpretations thereof. In section V, a preliminary comparison of sliding and staring spotlight TomoSAR is made based on a small number of images. Conclusions are drawn and future work is proposed in section VI. The appendix clarifies the structure of the TerraSAR-X annotation component containing a 3-by-3 grid of Doppler centroid in focused image time, which could be used to avoid complex time conversion.

II. TerraSAR-X Staring Spotlight Interferometry

In spotlight mode, the SAR sensor steers the azimuth beam forth and back in order to increase the illumination (or aperture) time t_{AP} of a target, as illustrated in Fig. 1. As a side effect, the Doppler centroid frequency undergoes a negative drift in azimuth time t_{az} of the raw data (see Fig. 2). The beam sweep rate is a trade-off between azimuth resolution and spatial extent. In the TerraSAR-X sliding spotlight mode, the azimuth beam is swept at a moderate rate with a squint angle range up to $\pm 0.75°$ [10], while in the staring spotlight mode the azimuth beam is steered exactly towards a reference ground target as satellite proceeds. In other words, the beam sweep rate is configured to match the frequency modulation (FM) rate of the reference target, which enables longer azimuth illumination time. To be more specific, the acquisition squint angle range is restricted to approximately $\pm 2.2°$ due to antenna azimuth grating lobe [7]. As a consequence, t_{AP} is, in the ideal case, equal to the azimuth time span of the raw data Δt_{raw}. This leads to a maximized azimuth resolution, which is limited by the product of t_{AP} and the FM rate [1]. This improved azimuth resolution comes, however, at the expense of a reduced azimuth scene extent, i.e., the azimuth time span of a focused image $\Delta t_{\mathrm{image}}$ in staring spotlight mode is significantly shorter. Naturally, the intrinsic range bandwidth imposes a ceiling on the slant range resolution, which is normally solely enhanced by a hardware upgrade. Tab. I lists as an example the parameters of a TerraSAR-X staring spotlight acquisition of Washington, D.C.

Due to the longer integration time of approximately 7 s in the TerraSAR-X staring spotlight mode, several challenges

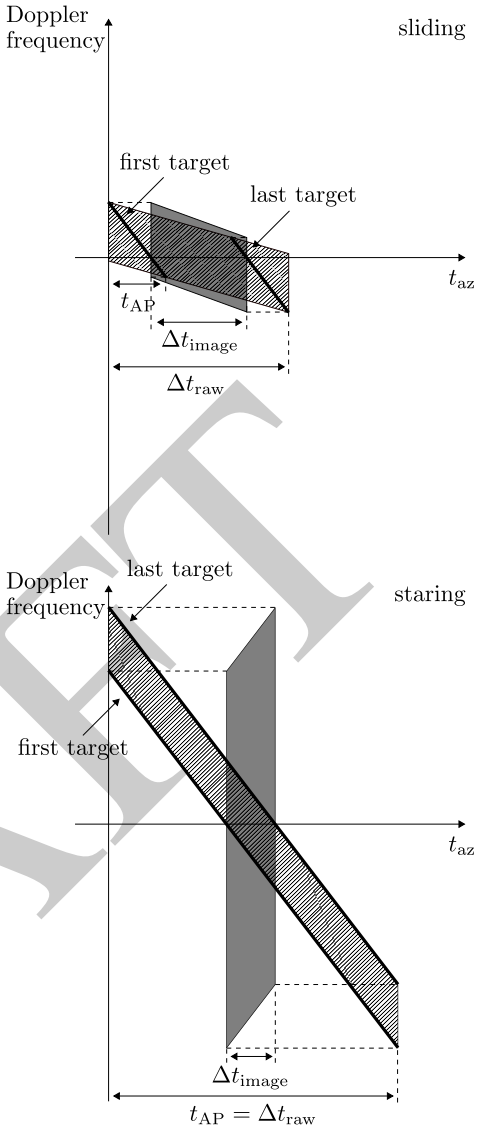

Fig. 2. Time-variant Doppler spectra of SAR raw data (//) with time span Δt_{raw}, and of focused image (shaded) with time span $\Delta t_{\mathrm{image}}$ in the sliding (top, modified from [1]) and staring (bottom) spotlight modes. Bold line segments denote the targets at the start and stop azimuth time (t_{az}) in the focused image, respectively. Both targets are illuminated with time t_{AP} and their zero-crossings define $\Delta t_{\mathrm{image}}$. In the staring spotlight mode, t_{AP} is set to equal Δt_{raw} in order to increase the azimuth resolution, which comes at the expense of significantly shorter $\Delta t_{\mathrm{image}}$.

arise in SAR processing [8], e.g., 1) the stop-and-go approximation becomes invalid, i.e., satellite movement between transmitting and receiving the chirp signal can no longer be neglected; 2) satellite trajectory deviates too much from a linear track, i.e., orbit curvature needs to be taken into account; 3) tropospheric delay could vary significantly within the large squint angle span and therefore needs to be corrected. All of these effects are considerately accounted for in a revised version of the TerraSAR-X multimode SAR processor [11], [12].

InSAR processing, on the other hand, requires merely few adaptations. As in the sliding spotlight mode, the master and slave images are coregistered (resampled) on the basis of

TABLE I
EXEMPLARY PARAMETERS OF A TERRASAR-X STARING SPOTLIGHT ACQUISITION OF WASHINGTON, D.C. (VALUES ARE ROUNDED)

Incidence angle at scene center	41°
Azimuth resolution	0.23 m
Slant range resolution	0.59 m
Azimuth scene extent	3.1 km
Ground Range scene extent	5.5 km
Range bandwidth	300 MHz
Antenna bandwidth	2589 Hz
Focused azimuth bandwidth	38275 Hz
Acquisition pulse repetition frequency (PRF)	4448 Hz
Focused PRF	42300 Hz
Number of azimuth beams	113
Squint angle range	±2.2°
Aperture time t_{AP}	7.24 s
Raw data scene duration Δt_{raw}	7.24 s
Focused scene duration $\Delta t_{\mathrm{image}}$	0.43 s
FM rate at scene center	−5301 Hz/s
Beam sweep rate at scene center	−5301 Hz/s

point-like scatterers in order to generate a coherent interferogram [1]. A requirement is the knowledge of the Doppler centroid frequency f_{DC} as a function of the focused image time t_{image}. Since f_{DC} is annotated as a (first-order) polynomial of the raw data time t_{raw} in the TerraSAR-X products, it is suggested in [1], [13] to perform time conversion for the sliding spotlight datasets via

$$t_{\mathrm{image}} = t_{\mathrm{raw}} - \frac{f_{\mathrm{DC}}(t_{\mathrm{raw}})}{\mathrm{FM}}. \tag{1}$$

This relation, however, does not hold for the staring spotlight mode, in which the FM rate equals the beam sweep rate, i.e., a target is visible throughout the whole raw data duration. In order to circumvent this problem, a 3-by-3 grid containing f_{DC} in t_{image} is provided as a TerraSAR-X annotation component [13]. Its structure is described in the appendix of this paper. This grid could be interpolated in order to derive the f_{DC} at every point of the focused image, which allows considering second-order variations of f_{DC} along range.

As an example, Fig. 3 shows a differential interferogram of Washington, D.C. with an effective baseline of approximately −71 m. The master and slave scenes were acquired respectively on October 31, 2015 and October 9, 2015 and processed with the integrated wide area processor (IWAP) [14], [15]. A low-pass filtered digital elevation model (DEM) with a spatial resolution of 1 arcsecond from the Shuttle Radar Topography Mission was used. The differential phase consists primarily of topographic phase which is related to residual height. As can be observed in Fig. 4, the Theodore Roosevelt Bridge in the lower left corner of Fig. 3 is subject to spatially correlated motion, presumably due to thermal dilation and contraction between piers caused by periodical temperature change.

The next section briefly revisits the principles of TomoSAR and elucidates the processing chain which was employed to produce the results in section IV and V.

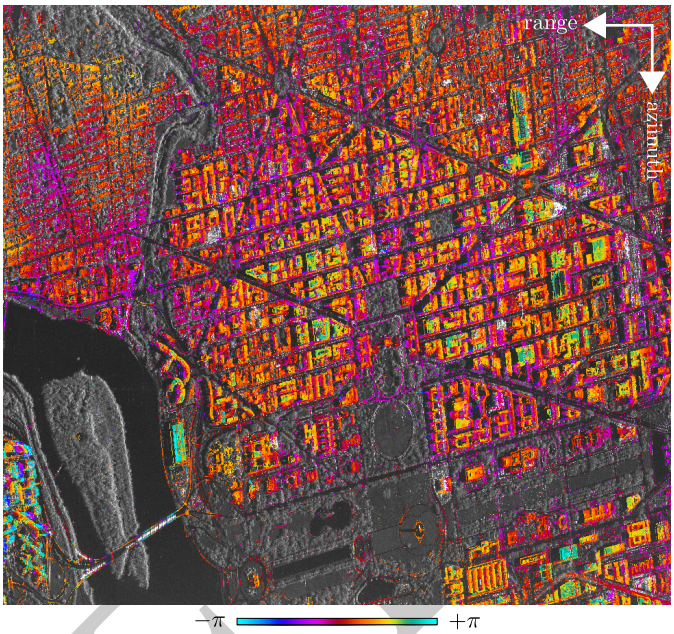

Fig. 3. Staring spotlight differential interferogram of Washington, D.C. with a spatial perpendicular baseline of approximately −71 m and a temporal baseline of −22 days.

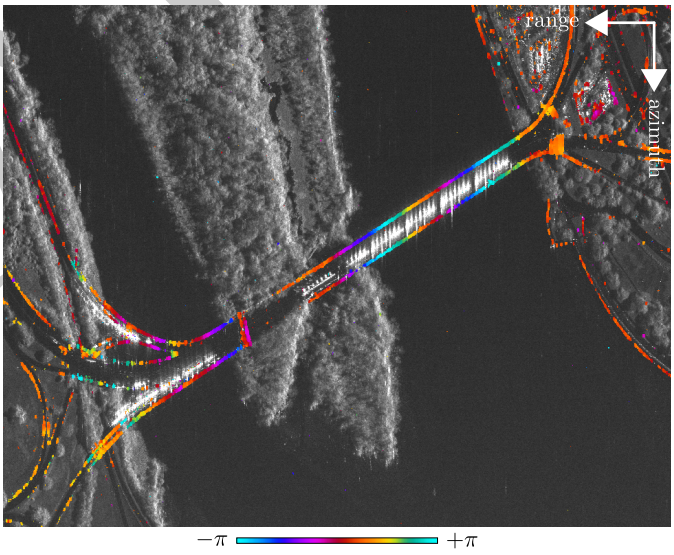

Fig. 4. Zoomed-in view of Fig. 3 on the Theodore Roosevelt Bridge (lower left).

III. TOMOSAR PRINCIPLES

Due to the common side-looking geometry of spaceborne SAR sensors, echoes of the chirp signal from equidistant targets within an elevation extent Δs in the far field sum to give one measurement for each azimuth-range pixel in the focused image, as illustrated in Fig. 5. The 3-D azimuth-range-elevation (x-r-s) reflectivity profile is thus embedded in 2-D, i.e., information regarding elevation is encoded during imaging. TomoSAR is a technique to reconstruct the elevation axis from multibaseline measurements [16]–[18]. For spaceborne SAR, this multibaseline configuration is usually

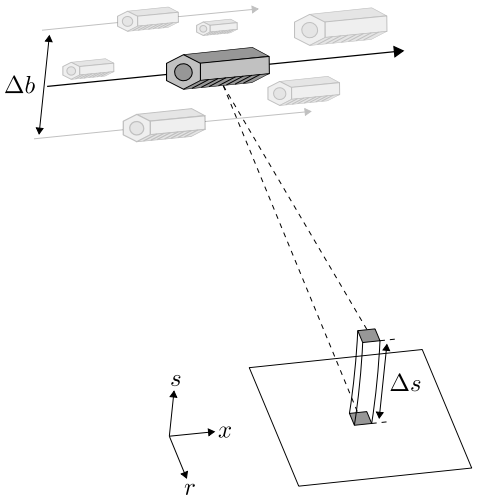

Fig. 5. Layover phenomenon in side-looking SAR imaging. x, r and s represent respectively azimuth, range, and elevation axes that form a local 3-D Cartesian coordinate system. An elevation aperture Δb is built by means of repeat-pass measurements to resolve multiple scatterers in the far-field toroid segment with elevation extent Δs.

achieved by repeat-pass measurements (depicted as semi-transparent satellite models in Fig. 5), in which scatterers' motion in the course of time often needs to be taken into account. A well-established theory models the complex InSAR measurement g_n of a specific pixel in the n-th interferogram as the integration of a phase-modulated elevation-dependent complex reflectivity profile $\gamma(s)$ over Δs [19]–[21]:

$$g_n \approx \int_{\Delta s} \gamma(s) \exp\big(-i\,2\pi(\xi_n s + 2d(s,t_n)/\lambda)\big)\mathrm{d}s, \quad (2)$$

where $\xi_n \coloneqq 2b_n/(\lambda r)$ is the elevation frequency that is proportional to the effective baseline b_n (λ and r are respectively the radar wavelength and the range between sensor and target in the master image), and $d(s,t_n)$ is the line-of-sight displacement of the scatterer at elevation position s and temporal baseline t_n. In order to reduce the number of unknowns, $d(s,t_n)$ could be modeled as a linear combination of basis functions. It can be shown that (2) is equivalent to a multidimensional spectral estimation problem [21]. After discretizing s and displacement parameters, and subsequently replacing integration by finite sum, a linear model for all N InSAR measurements can be formulated as

$$\mathbf{g} \approx \mathbf{R}\boldsymbol{\gamma}, \quad (3)$$

where $\mathbf{g} \coloneqq (g_1, \ldots, g_N) \in \mathbb{C}^N$ is the complex InSAR measurement vector, $\mathbf{R} \in \mathbb{C}^{N\times L}$ is the TomoSAR dictionary, and $\boldsymbol{\gamma} \in \mathbb{C}^L$ is the discrete elevation-motion reflectivity profile (or spectrum).

Various algorithms were proposed to estimate $\boldsymbol{\gamma}$ with given $\mathbf{R}$ and $\mathbf{g}$. A common approach is to use Tikhonov regularization [4]

$$\underset{\boldsymbol{\gamma}}{\text{minimize}}\, \|\mathbf{R}\boldsymbol{\gamma} - \mathbf{g}\|_2^2 + \delta\|\boldsymbol{\gamma}\|_2^2, \quad (4)$$

where $\delta > 0$ is a regularization constant. Note that (4) is equivalent to the maximum a posteriori estimator of $\boldsymbol{\gamma}$ provided that the measurement noise is additive and white with variance δ, and $\boldsymbol{\gamma}$ is white with variance 1.

If one is primarily concerned with man-made objects in high-resolution spotlight images acquired over urban areas, it is deemed reasonable to assume that radar echoes in the far field are dominated by those from merely few point-like scatterers within the toroid segment in Fig. 5, i.e., $\boldsymbol{\gamma}$ is presumed to be compressible and thus $\mathbf{g}$ could be sufficiently approximated by a linear combination of few atoms (columns) of $\mathbf{R}$. This hypothesis gave rise to approaches with sparsity-driven ℓ_1 regularization [22], [23]:

$$\underset{\boldsymbol{\gamma}}{\text{minimize}}\, \|\mathbf{R}\boldsymbol{\gamma} - \mathbf{g}\|_2^2 + \epsilon\|\boldsymbol{\gamma}\|_1, \quad (5)$$

where $\epsilon > 0$ is another regularization constant.

In terms of the capability to resolve multiple point-like scatterers, conventional methods such as Tikhonov regularization (4) are limited by the elevation resolution $\rho_s \coloneqq \lambda r/(2\Delta b)$, where Δb is the elevation aperture as shown in Fig. 5. For TerraSAR-X, ρ_s is in the order of several tens of meters (typically 20–30 m given a sufficiently large stack), as a consequence of the satellite being confined to a 250-m orbit tube [24]. Given one single scatterer within the resolution cell, a lower bound on the errors of elevation estimates $\hat{s}$ can be derived as [9]

$$\sigma_{\hat{s}} \coloneqq \frac{\lambda r}{4\pi\sqrt{N}\sqrt{2SNR}\,\sigma_b}, \quad (6)$$

where SNR is the scatterer's signal-to-noise ratio, and σ_b is the standard deviation of effective baselines. In case of double scatterers, their mutual interference could be modeled as a scaling factor which depends primarily on their elevation distance and phase difference [25]. For TerraSAR-X, this lower bound is approximately one order smaller than ρ_s and could be approached by means of ℓ_1 regularization (5). In other words, (5) could achieve superresolution [26].

As an overview, a top-down model of the processing chain is illustrated in Fig. 6 and consists primarily of the following parts:

1) *Preprocessing* (via IWAP), which takes focused single-look slant-range complex (SSC) images as input and performs
   a) *InSAR processing*, which provides raster images of calibrated amplitude and differential phase, and subsequently
   b) *PSI processing*, which estimates atmospheric phase screen (APS) from single point-like targets and a sidelobe risk map [14], [27], [28].

   Note that the use of a DEM is optional if the concerned terrain is relatively flat.
2) *TomoSAR processing.*
   a) *Sidelobe detection*. A simple hypothesis test (thresholding) is applied to the sidelobe risk map from 1b).
   b) *APS compensation*. The estimated APS is compensated in differential phase, if the corresponding pixel concerned is, with high probability, not dominated by a sidelobe.

c) *Spectrum estimation*. The elevation-motion spectrum is estimated with, for example, (4) or (5).

d) *Model selection*. By minimizing the penalized negative log-likelihood, the number of scatterers is estimated to reduce false positive rate [25]. If ℓ_1 regularization is employed in 2c), the underestimated amplitude is hereby corrected as a byproduct.

e) *Off-grid correction*. In order to ameliorate the off-grid problem as a consequence of discretizing elevation and motion parameters, the estimated elevation-motion spectrum from 2c) is oversampled in a neighborhood of each statistically significant scatterer. A local maximum is detected in the oversampled high-dimensional signal, which allows better quantization.

f) *Outlier rejection*. As a natural extension of the complex ensemble coherence for single point-like scatterers [29], we define for the multiple-scatterer case

$$\eta \coloneqq \frac{1}{N}\sum_{n=1}^{N}\exp\big(-i\left(\angle \mathbf{r}^n\boldsymbol{\gamma} - \angle g_n\right)\big), \qquad (7)$$

where $\angle : \mathbb{C} \to \mathbb{R}$ returns the phase of a complex number, and $\mathbf{r}^n$ denotes the n-th row of the TomoSAR dictionary $\mathbf{R}$. We reject outliers, i.e., scatterers whose phase history deviates significantly from the adopted model, by thresholding of $|\eta|$.

3) *Postprocessing*, which couples the updated topography and its deformation parameters to produce a 4-D geocoded point cloud.

In the next section, we demonstrate for the first time TerraSAR-X staring spotlight TomoSAR results produced with the abovementioned processing chain. Based on a sufficient number of acquisitions, the demonstration is given not only for individual urban infrastructures, but also on the scale of a city.

IV. First Practical Demonstration of Staring Spotlight TomoSAR

Forty-one staring spotlight images were acquired by TerraSAR-X from July 4, 2014 to November 30, 2016 with a constant repeat interval of 22 days, i.e., every second orbit. The image from October 31, 2015 with an incidence angle of $40.7°$ at scene center was chosen as the master due to its central position in the spatial-temporal baseline plot and relatively small atmospheric delays. Fig. 7 shows the distribution of effective baselines b_n with respect to the master scene, which are indeed confined to ± 250 m. The elevation aperture Δb is approximately 417 m, which leads to an elevation resolution ρ_s of approximately 24.6 m at scene center. Given an SNR of 2 dB, the lower bound for single point-like scatterers $\sigma_{\hat{s}}$ is merely 1.44 m, i.e., less than 6% of ρ_s.

As previously mentioned in section III, the preprocessing (i.e., InSAR and PSI processing) was accomplished by IWAP. In order to decrease the computational cost, we exclusively considered the pixels with SCR ≥ 1.7 dB as candidates for TomoSAR processing, i.e., heavily vegetated areas and water bodies were likely masked out. The number of candidates was further reduced by eliminating those pixels, each of which has

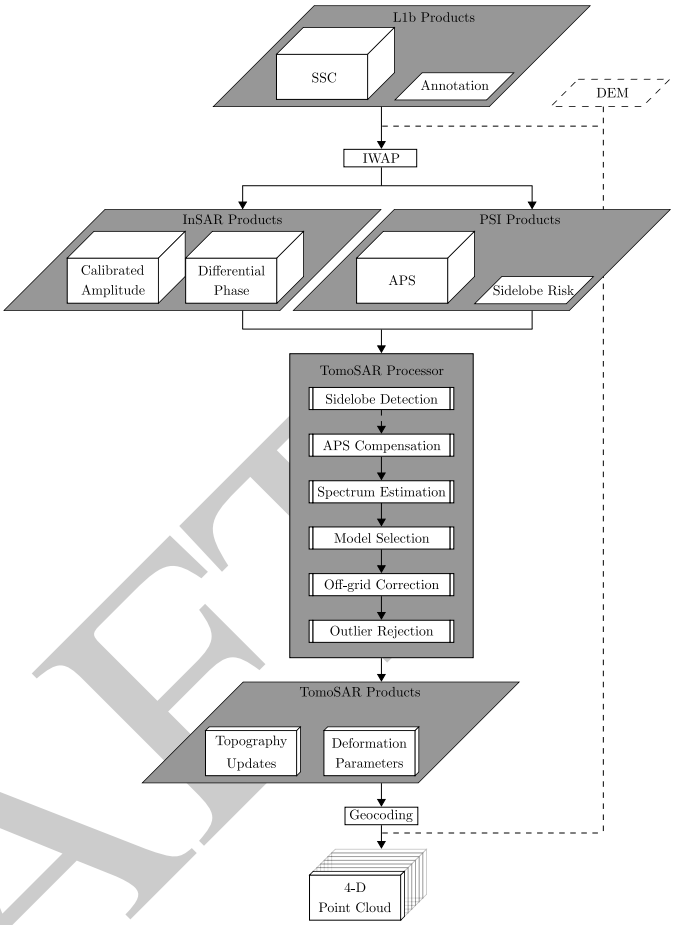

Fig. 6. Top-down model of the processing chain. Modified from [30].

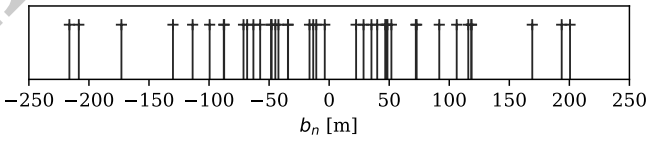

Fig. 7. Distribution of effective baselines b_n.

an estimated likelihood of being a sidelobe larger than 0.45. As a result, we only processed approximately 12% of the original raster data. Scatterers' motion was modeled with a coupled linear and sinusoidal model with the latter having a period of one year. The elevation-motion spectrum was estimated either with Tikhonov regularization (4) for the whole scene, or with ℓ_1 regularization (5) for certain regions of interest. The maximum number of point-like scatterers within each resolution cell was set to 2 and the model selector was trained such that the false positive rate for double scatterers, i.e., the empirical probability that two scatterers are detected whereas there is at most one, is below $1‰$. A neighborhood of each selected scatterer in its 3-D elevation-motion (s-v-a, where v is the linear deformation rate and a is the periodical deformation amplitude) spectrum was oversampled with a factor of 10 to alleviate the off-grid problem. Scatterers with an ensemble coherence (7) lower than 0.6 were considered as outliers and

excluded from postprocessing.

The updated topography h, linear deformation rate v and periodical deformation amplitude a are shown in Fig. 8a, 8b and 8c, respectively. On the Potomac River (lower left), scarcely any point-like scatterers could be detected, except for those from the National Memorial on the Theodore Roosevelt Island (cf. Fig. 3), and those on the Theodore Roosevelt Bridge (cf. Fig. 4). The National Mall in the lower part is in general void of point-like scatterers due to its vegetation.

Most of the buildings in the scene appear to be flat with the exception of several high-rise ones in Rosslyn, Virginia (lower left, to the west of the Theodore Roosevelt Bridge). Zoomed-in views of the Watergate complex and the John F. Kennedy Center for the Performing Arts are provided as Fig. 9 and 10, respectively. Due to the limitations of Google Earth merely 6% of the original point cloud was used for visualization.

Bridges and overpasses are in general subject to periodical deformation as a result of temperature changes, i.e., dilation between piers or fixed bearings in summer and contraction in winter. The estimated periodical deformation amplitude of the Theodore Roosevelt Bridge is shown in Fig. 11. As an example, Fig. 12 demonstrates the phase history of two scatterers within a resolution cell. The higher scatterer (depicted as red dot) is located on the bridge, while the lower (blue) resides at one of the piers. The estimated height difference of these two scatterers is approximately 8.3 m, which lies in the super-resolution regime. As the upper right plot of Fig 12 suggests, the lower scatterer on the pier undergoes little deformation, whereas the periodical deformation amplitude of the higher scatterer on the bridge was estimated to be approximately 2.9 mm. The topography and deformation model of double scatterers fits quite well to the InSAR measurements (see the lower right plot of Fig 12) and the ensemble coherence amounts to approximately 0.97.

The Washington Marriott Marquis hotel (opened on May 1, 2014) beside the Walter E. Washington Convention Center appears to suffer from subsidence that is presumably due to the building weight (see Fig. 13a). In addition, it undergoes thermal dilation and contraction which are more significant on roof than on facade, as can be observed in Fig. 13b. Fig. 14 shows the resolved layover effect of two scatterers, which is a typical case of roof-facade interaction. The higher and lower scatterers subside with a linear rate of -1.1 and -1.0 mm/year, respectively. The scatterer on the roof moves periodically with an amplitude of approximately 3.0 mm, while on the contrary the one on the facade is subject to little such deformation. Similar to the previous example in Fig. 12, the TomoSAR model could describe the phase history sufficiently well with an ensemble coherence of approximately 0.97.

As one last example, Fig. 15a and 15b show the updated topography and periodical deformation amplitude of the Rosslyn Twin Towers, respectively. Clearly the amplitude of thermal dilation and contraction is highly correlated with building height. Note that the tower on the left has smaller point density on the left-hand side of the facade due to its convex shape as seen from the radar wavefront. Fig. 16 demonstrates another typical case of layover effect in urban areas which is the facade-ground (or facade-lower-infrastructure) interaction. The periodical deformation amplitude of the higher and lower scatterers were estimated to be approximately 5.0 and 2.0 mm, respectively.

The next section reports a preliminary comparison of sliding and staring spotlight TomoSAR using TerraSAR-X data. The comparison is based on a limited number of acquisitions and therefore restricted to two small typical urban areas.

V. Preliminary Comparison of Sliding and Staring Spotlight TomoSAR

Due to data unavailability, a direct comparative study of both modes was not possible for Washington D.C. Instead, we drew the comparison with two small descending interferometric stacks of the City of Las Vegas. Each stack contains 12 images which were acquired alternately from October, 2014 to February, 2015 during the TanDEM-X Science Phase [31]. For each mode, 11 interferograms were generated with a similar baseline distribution as in Fig. 7.

Two small areas were selected for the comparison of sliding and staring spotlight TomoSAR. One of them is a relatively flat area of approximately 0.01 km^2. The same area of interest was cropped in both datasets using ground control points. Fig. 17 shows the mean intensity map in each mode. In the staring spotlight case, point-like targets appear more focused, which indicates an increase of SCR. As a result, the contrast between areas of different degrees of smoothness becomes larger, i.e., the boundaries of the rectangular surfaces in the middle of the image are much easier to recognize. The reconstructed TomoSAR point cloud is shown in Fig. 18. An increase in the number of points in the staring spotlight mode is obvious. Indeed, the point density in the staring spotlight case is approximately 5.5 times as high, see Tab. II.

The assessment of the relative height accuracy is explained as follows. Since this area is relatively flat (as confirmed by Fig. 18), we fitted a plane with robust measure through each point cloud and considered it as partial ground truth. Note that this also took the local slope into account. Subsequently, we calculated the distance of each scatterer to the fitted plane and projected it into the vertical direction. In this context, we refer to the median absolute deviation of height estimate errors relative to this fitted plane as relative height accuracy.

Let us denote the vectors containing the geographic coordinates of all m scatterers as $\tilde{\mathbf{x}}, \tilde{\mathbf{y}}, \tilde{\mathbf{z}} \in \mathbb{R}^m$, respectively. We seek a plane parametrized by $\tilde{a}, \tilde{b}, \tilde{c}, \tilde{d} \in \mathbb{R}$ such that,

$$\tilde{a}\tilde{x} + \tilde{b}\tilde{y} + \tilde{c}\tilde{z} + \tilde{d} \approx 0, \tag{8}$$

for each scatterer at the coordinates $\tilde{x} \in \tilde{\mathbf{x}}$, $\tilde{y} \in \tilde{\mathbf{y}}$, $\tilde{z} \in \tilde{\mathbf{z}}$. Without loss of generality, let us assume that $\tilde{c} = 1$. The plane fitting problem can be formulated as

$$\underset{\mathbf{x}}{\text{minimize}} \, \|\mathbf{A}\mathbf{x} - \mathbf{b}\|_1, \tag{9}$$

where $\mathbf{A} \coloneqq \begin{pmatrix} \tilde{\mathbf{x}} & \tilde{\mathbf{y}} & \mathbf{1} \end{pmatrix} \in \mathbb{R}^{m \times 3}$, $\mathbf{1}$ is an m-dimensional vector of ones, $\mathbf{x} \coloneqq \begin{pmatrix} \tilde{a} & \tilde{b} & \tilde{d} \end{pmatrix}^{\mathrm{T}} \in \mathbb{R}^3$, and $\mathbf{b} \coloneqq -\tilde{\mathbf{z}}$. The ℓ_1 loss function is known for its robustness against outliers [32]. Let $\mathbf{x}^*$ denote an optimal solution and $\mathbf{n} \coloneqq \begin{pmatrix} x_1^* & x_2^* & 1 \end{pmatrix}^{\mathrm{T}}$ be a corresponding plane normal, the signed distance of scatterers

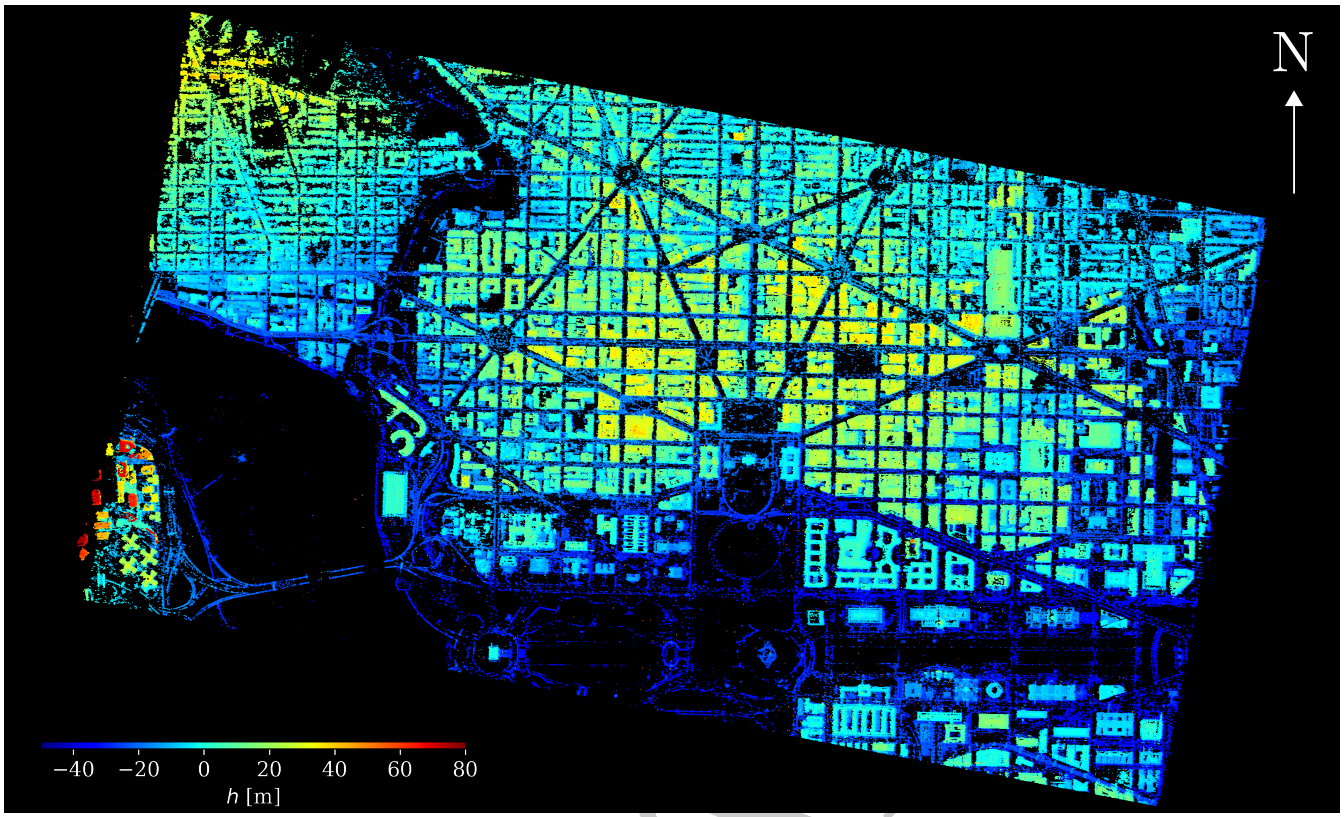

(a) Updated topography h [m]

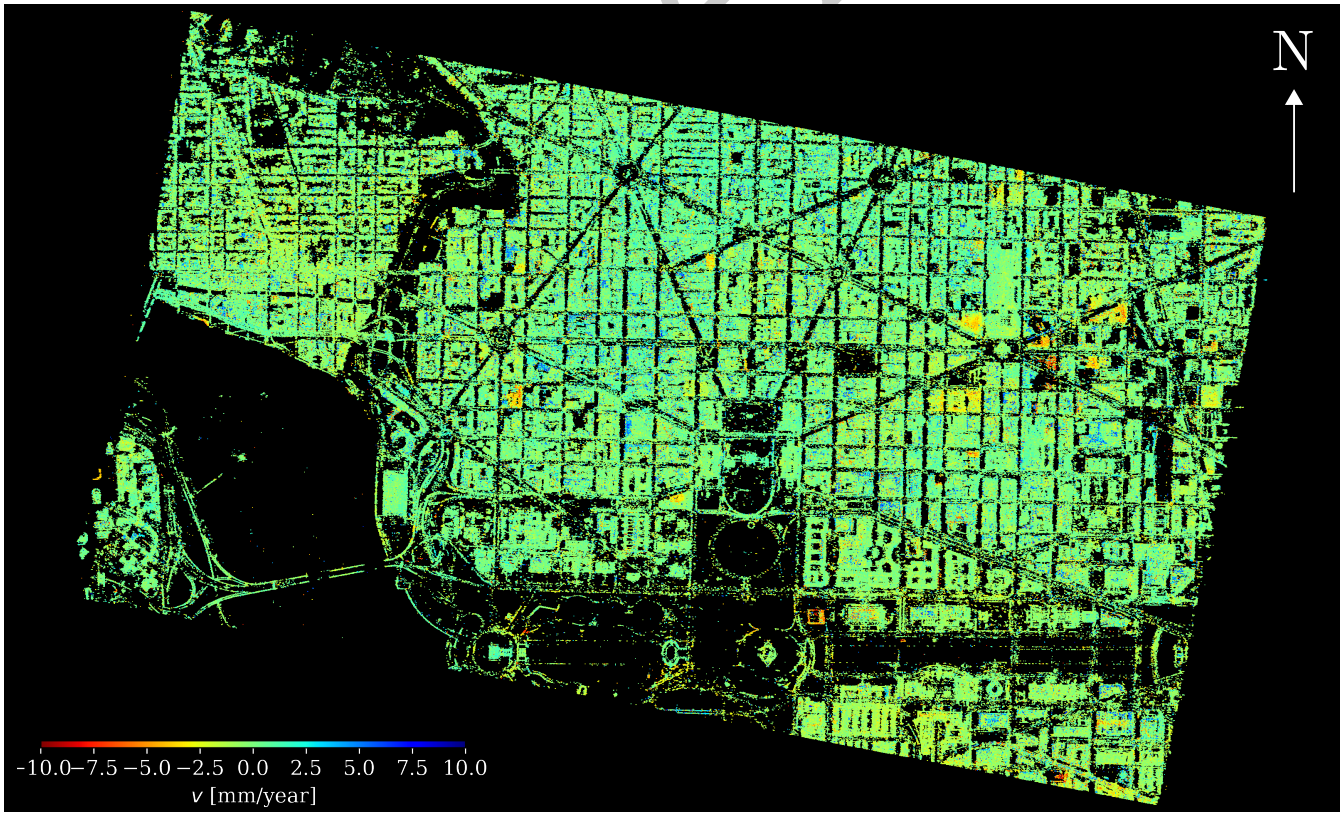

(b) Linear deformation rate v [mm/year]

Fig. 8. TomoSAR results of Washington, D.C. with 41 TerraSAR-X staring spotlight acquisitions.

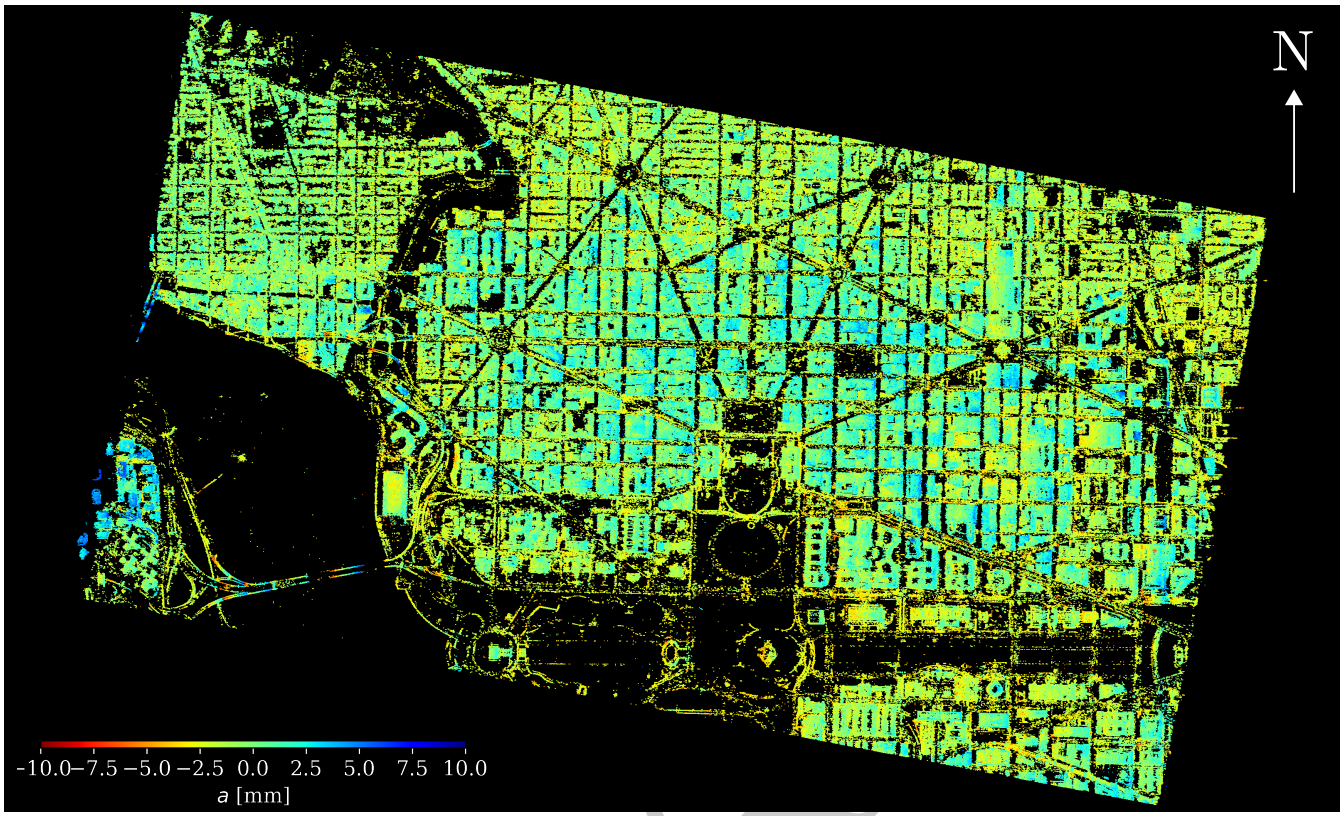

(c) Periodical deformation amplitude a [mm]

Fig. 8. TomoSAR results of Washington, D.C. with 41 TerraSAR-X staring spotlight acquisitions (continued).

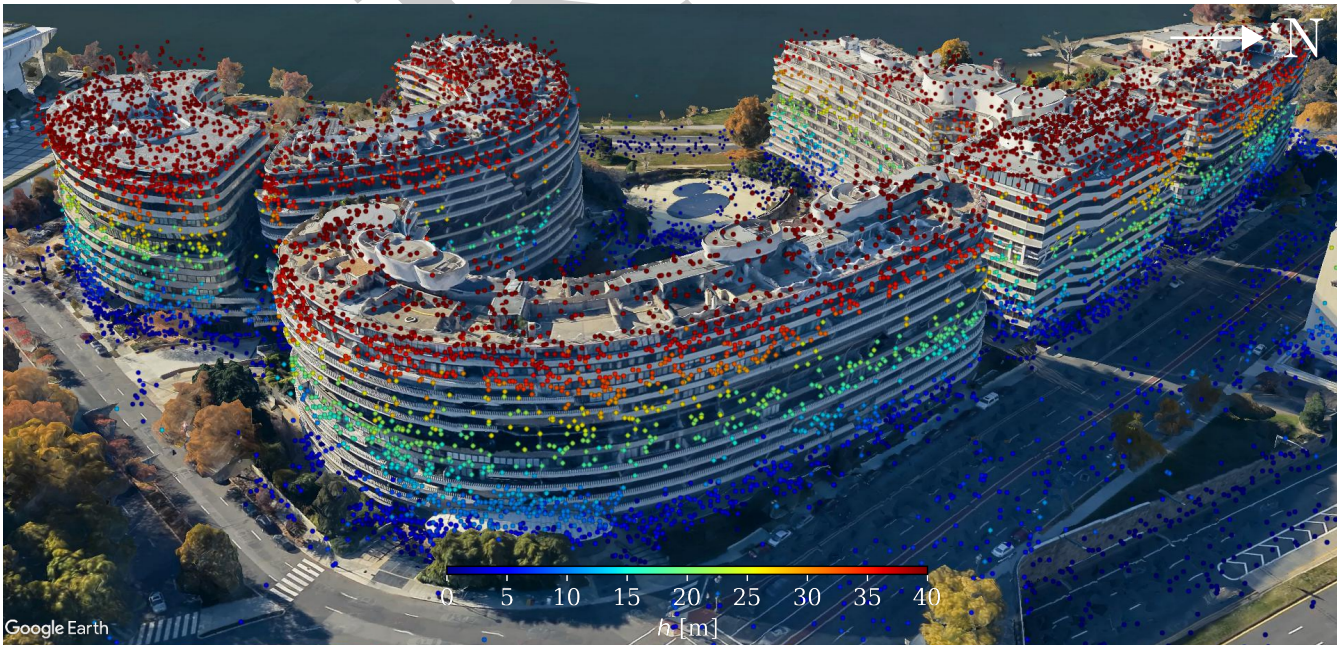

Fig. 9. 6% of the original point cloud of the Watergate complex that is overlaid on Google Earth 3-D photo-realistic building model and color-coded by updated topography h [m].

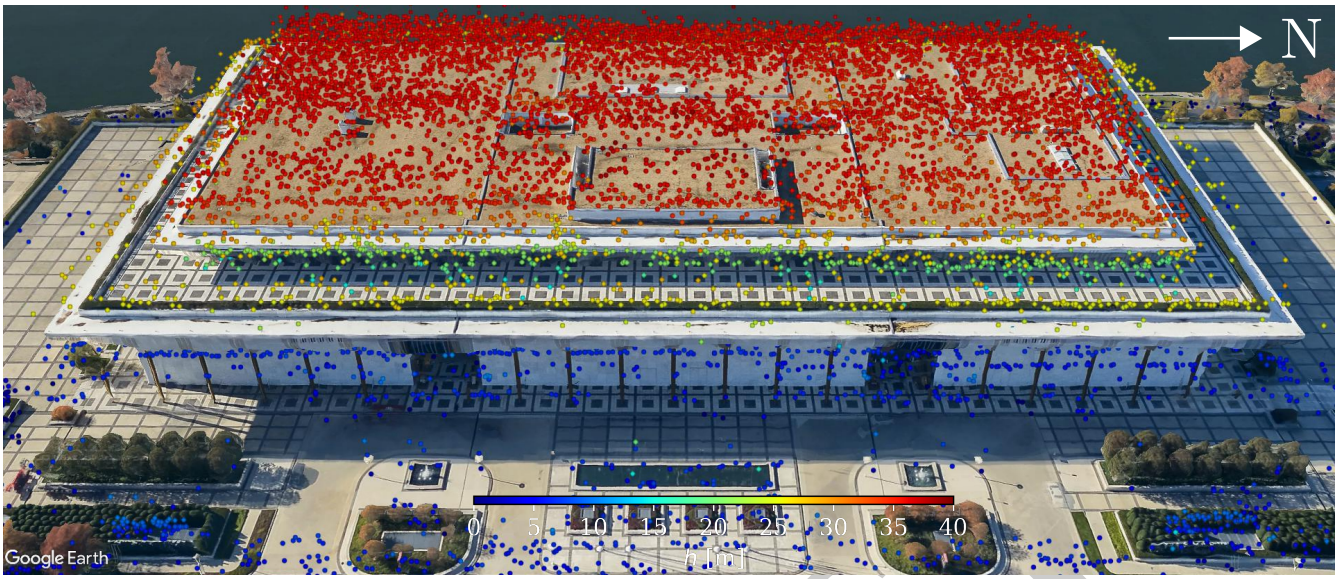

Fig. 10. 6% of the original point cloud of the John F. Kennedy Center for the Performing Arts that is overlaid on Google Earth 3-D photo-realistic building model and color-coded by updated topography h [m].

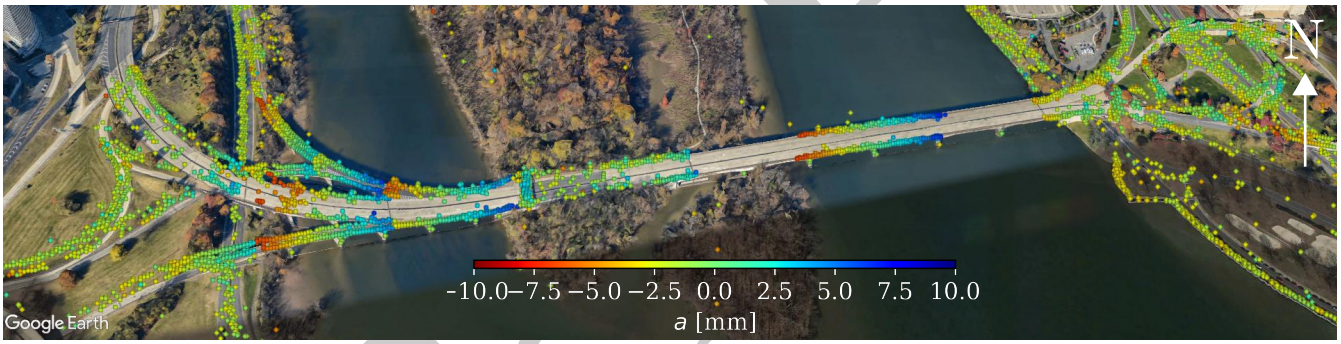

Fig. 11. 6% of the original point cloud of the Theodore Roosevelt Bridge that is overlaid on Google Earth 3-D photo-realistic building model and color-coded by periodical deformation amplitude a [mm].

to the fitted plane is given by $(\mathbf{A}\mathbf{x}^*+\tilde{\mathbf{z}})/\|\mathbf{n}\|_2$. Due to the large scale of problem (9), i.e., $m > 10^5$ as shown in Tab. II, generic conic solvers may not be able to solve it efficiently. Based on the alternating direction method of multipliers (ADMM) [33], we developed a fast solver with super-linear convergence rate, see Algorithm 1, where $\mathbf{z}$ and $\mathbf{y}$ are respectively auxiliary primal and dual variables, $\rho > 0$ is a penalty parameter for a smoothness term in the augmented Lagrangian (fixed to 1 in this paper), and $\mathrm{prox}_{\ell_1,\lambda}(\mathbf{w}) \coloneqq (\mathbf{w}-\lambda)_+ - (-\mathbf{w}-\lambda)_+$ is the elementwise soft thresholding operator [34], where $(\mathbf{u})_+ \coloneqq \max(\mathbf{u}, 0)$ replaces the negative entries with zeros.

Algorithm 1 ADMM-based algorithm for solving (9)

1: **Input:** $\mathbf{A}$, $\mathbf{b}$, ρ
2: **Initialize** $\mathbf{z} \leftarrow \mathbf{0}$, $\mathbf{y} \leftarrow \mathbf{0}$
3: **Until** stopping criterion is satisfied, **Do**
4: $\quad \mathbf{x} \leftarrow (\mathbf{A}^{\mathrm{T}}\mathbf{A})^{-1}\big(\mathbf{A}^{\mathrm{T}}(\mathbf{b}+\mathbf{z}-\frac{1}{\rho}\mathbf{y})\big)$
5: $\quad \mathbf{z} \leftarrow \mathrm{prox}_{\ell_1,1/\rho}(\mathbf{A}\mathbf{x}-\mathbf{b}+\frac{1}{\rho}\mathbf{y})$
6: $\quad \mathbf{y} \leftarrow \mathbf{y}+\mathbf{A}\mathbf{x}-\mathbf{b}-\mathbf{z}$
7: **Output:** $\mathbf{x}$

Fig. 19 depicts the errors of height estimates relative to the fitted plane. Although both normalized histograms are centered around zero, the height estimate errors in the staring spotlight mode exhibit less deviation. According to Tab. III, the relative height accuracy (defined as the median absolute deviation of height estimate errors) in the sliding spotlight case is approximately 1.7 times as high.

The other area of approximately 0.11 km^2 contains two high-rise buildings and its surroundings. The regular patterns of building facades appear sharper in the staring spotlight mode (see Fig. 20). The reconstructed point clouds are illustrated in Fig. 21 for single and double scatterers, respectively. As expected, the staring spotlight mode densified the corresponding point cloud in both single- and double-scatterer cases. In total, the point density in the staring spotlight case is approximately 5.1 times as high, see Tab. IV. With respect to the ratio of the number of single scatterers to the number of double scatterers, we recorded a slight decrease approximately from 6.9 (sliding) to 6.0 (staring), i.e., no significant difference was observed.

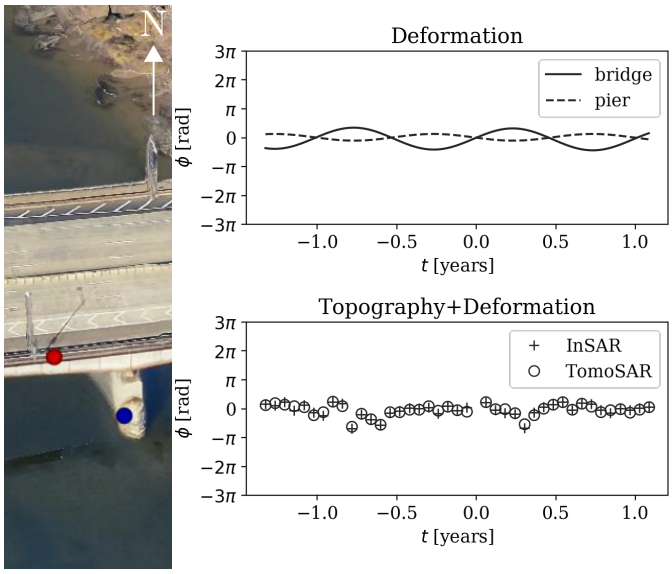

Fig. 12. Phase history of InSAR measurements and TomoSAR reconstruction of double scatterers subject to layover in Fig. 11. The higher and lower scatterers are marked as red and blue, respectively.

TABLE II
STATISTICS OF THE POINT CLOUDS IN FIG. 18

	Sliding	Staring	Ratio[2]
Total no. of scatterers	26037	142085	5.46
Scatterer density [million/km^2]	2.47	13.46	5.46

TABLE III
STATISTICS OF THE HEIGHT ESTIMATE ERRORS IN FIG. 19

	Sliding	Staring	Ratio[2]
Median [m]	0.00	0.00	n.a.
Mean [m]	0.01	0.01	n.a.
Median absolute deviation [m]	0.94	0.54	1.74
Standard deviation [m]	1.12	0.76	1.47

TABLE IV
STATISTICS OF THE POINT CLOUDS IN FIG. 21

	Sliding	Staring	Ratio[2]
No. of single scatterers	148646	740656	4.98
No. of double scatterers	21576	124546	5.77
Total no. of scatterers	170222	865202	5.08
Single-to-double-scatterer ratio	6.89	5.95	1.16
Scatterer density [million/km^2]	1.56	7.91	5.08

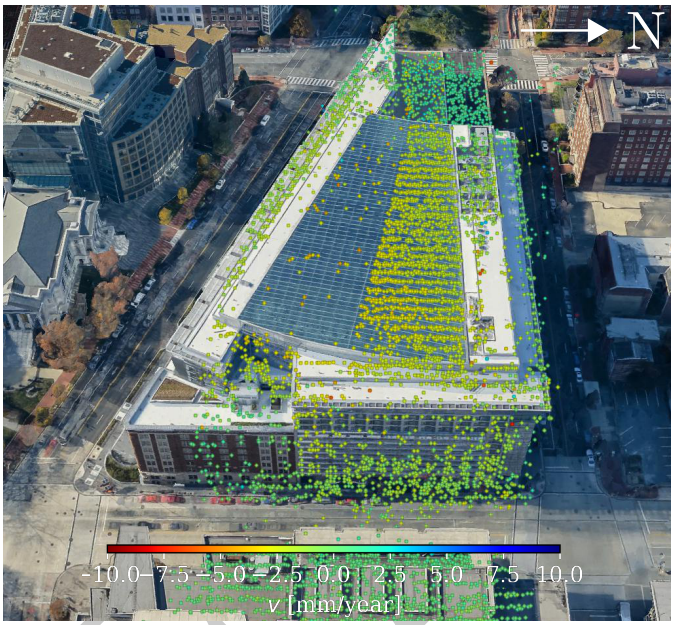

(a) Linear deformation rate v [mm/year]

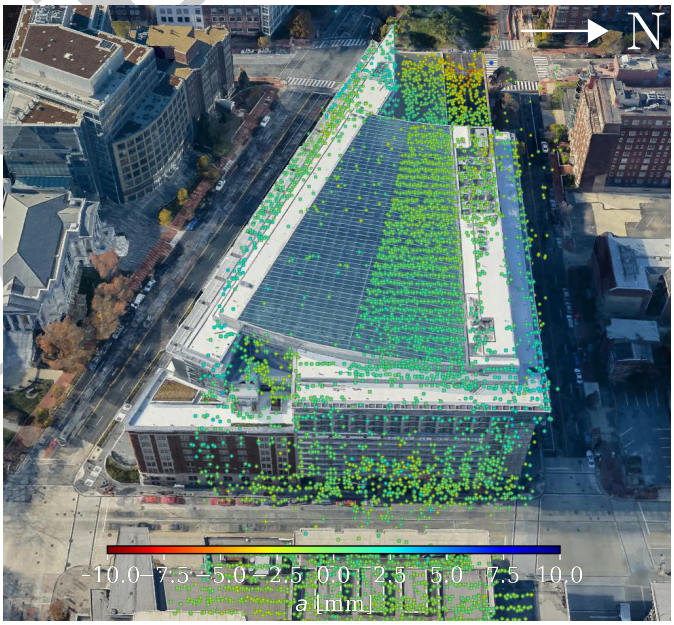

(b) Periodical deformation amplitude a [mm]

Fig. 13. 4% of the original point cloud of the Washington Marriott Marquis hotel that is overlaid on Google Earth 3-D photo-realistic building model.

VI. CONCLUSION

In this paper, we studied the characteristics of the TerraSAR-X staring spotlight mode and its impact on multi-baseline InSAR techniques, in particular, PSI and TomoSAR. The difference in the time-variant Doppler spectra of the sliding and staring spotlight modes was analyzed in concept in order to demonstrate the azimuth resolution versus scene extent trade-off. The usage of the TerraSAR-X annotation component containing the Doppler centroid in focused image time was proposed to skirt the time conversion issue. The TomoSAR processing chain was revised in order to incorporate sidelobe detection, off-grid correction and outlier rejection. A first practical demonstration was made with an interferometric stack of 41 images of Washington, D.C. The whole scene extent was processed to estimate topography update of point-like scatterers and their deformation parameters. Besides, the results of several typical urban areas were visualized and interpreted. A preliminary comparison between sliding and staring spotlight TomoSAR was drawn in the end with two

[2]The ratio was calculated by dividing the larger by the smaller value.

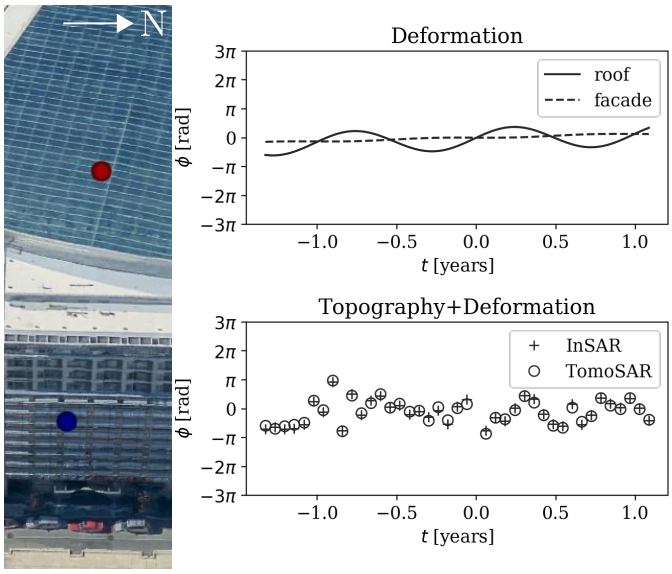

Fig. 14. Phase history of InSAR measurements and TomoSAR reconstruction of double scatterers subject to layover in Fig. 13. The higher and lower scatterers are marked as red and blue, respectively.

small interferometric stacks of the City of Las Vegas.

In section I, we argued that by means of the staring spotlight mode, 1) more point-like targets would be separable in the azimuth-range plane; 2) each target would have a higher SCR. As a result, the 4-D point cloud would be not only denser but also more accurate. In this work, we observed that, 1) the density of the *staring* spotlight point cloud is approximately 5.1–5.5 times as high; 2) the relative height accuracy of the *staring* spotlight point cloud is approximately 1.7 times as high.

Multiple-snapshot TomoSAR approaches, e.g., using an adaptive neighborhood identified within a spatial search window [35], [36], or incorporating additional geospatial information of building footprints [37], could also benefit from the staring spotlight mode. In the former case, the enhanced azimuth resolution would increase the number of pixels in the homogeneous area; in the latter, the iso-height clusters of a facade to be jointly reconstructed would expand. On the whole, it would lead to a larger number of snapshots and in turn to a better estimation accuracy.

Appendix

As previously mentioned in section II, f_{DC} is provided in t_{image} on a 3-by-3 grid as a TerraSAR-X annotation component [13]. This grid is defined as the Cartesian product of the sets $\{\text{start } t_{\mathrm{image}}, \text{ center } t_{\mathrm{image}}, \text{ stop } t_{\mathrm{image}}\}$ and $\{\text{near range}, \text{ mid range}, \text{ far range}\}$, as depicted in Fig. 22. This information could be employed to bypass time conversion from t_{raw} to t_{image}, and to consider second-order variations of f_{DC} along range. Note that this grid is also provided for each burst of any ScanSAR SSC product.

Acknowledgment

TerraSAR-X data was provided by the German Aerospace Center (DLR) under the TerraSAR-X New Modes AO Project

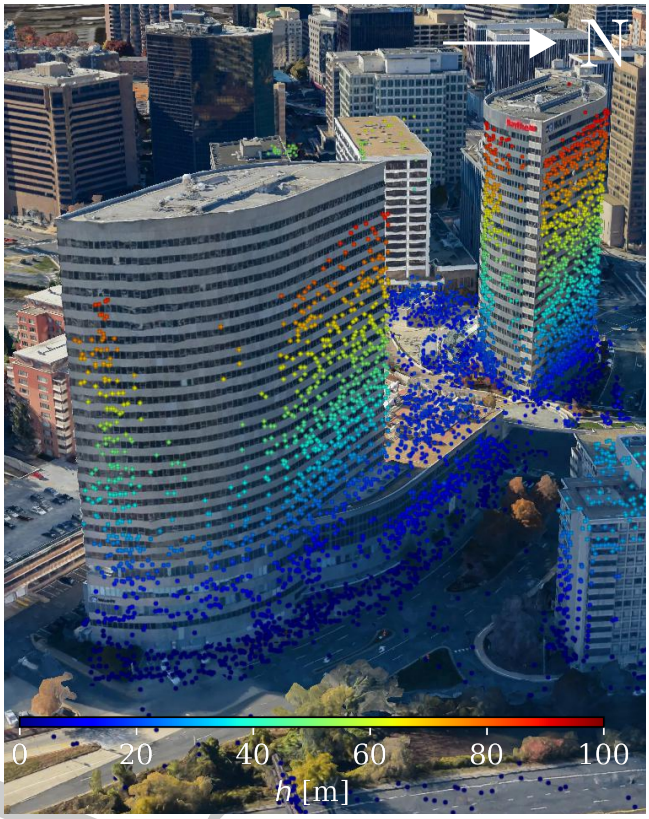

(a) Updated topography h [m]

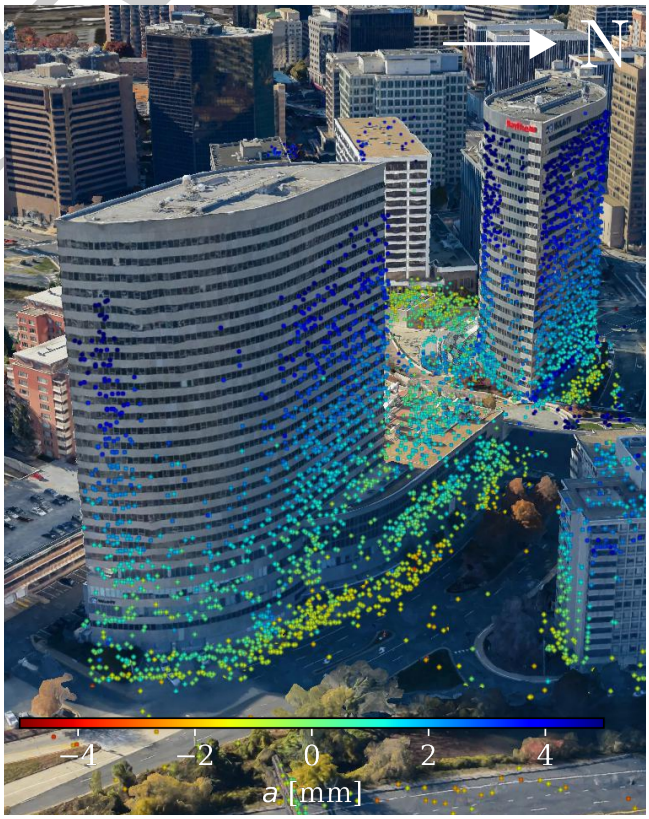

(b) Periodical deformation amplitude a [mm]

Fig. 15. 5% of the original point cloud of the Rosslyn Twin Towers that is overlaid on Google Earth 3-D photo-realistic building model.

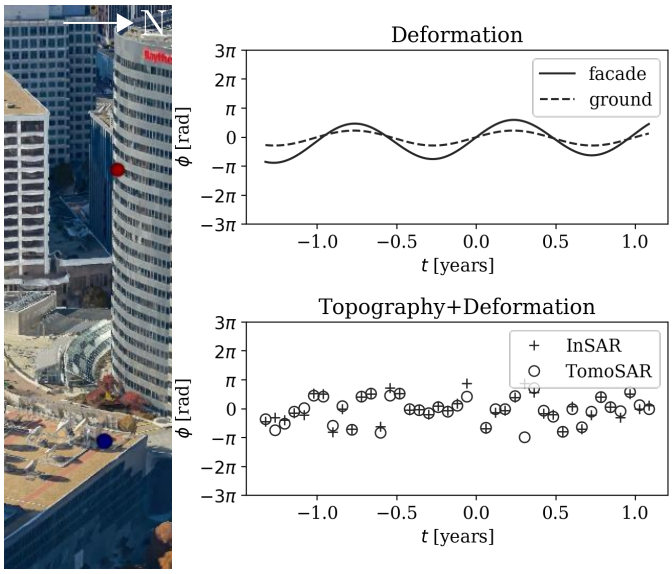

Fig. 16. Phase history of InSAR measurements and TomoSAR reconstruction of double scatterers subject to layover in Fig. 15. The higher and lower scatterers are marked as red and blue, respectively.

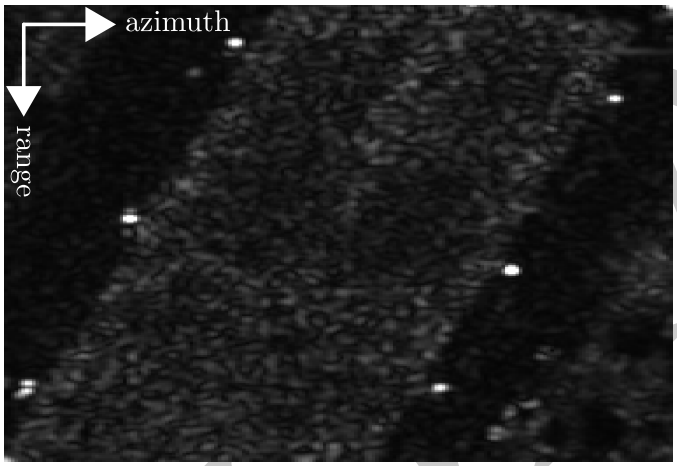

(a) Sliding

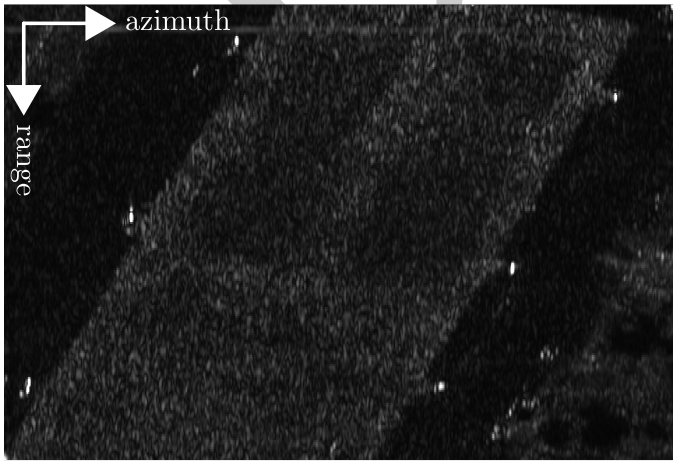

(b) Staring

Fig. 17. Mean intensity map of a relatively flat area in the (a) sliding and (b) staring spotlight modes.

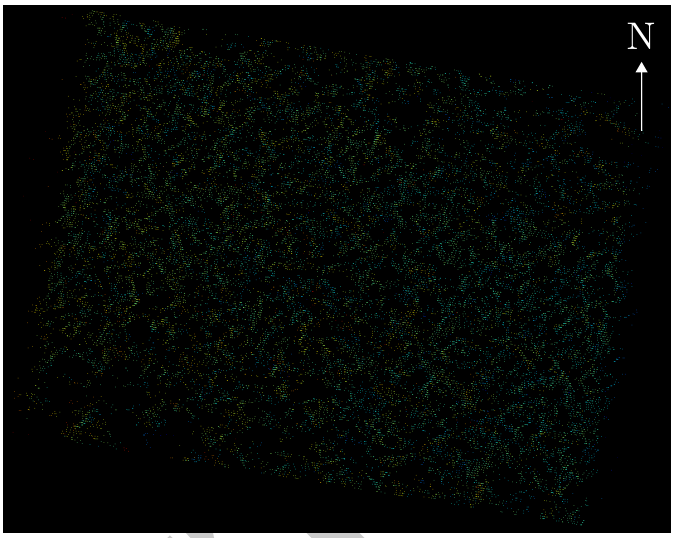

(a) Sliding

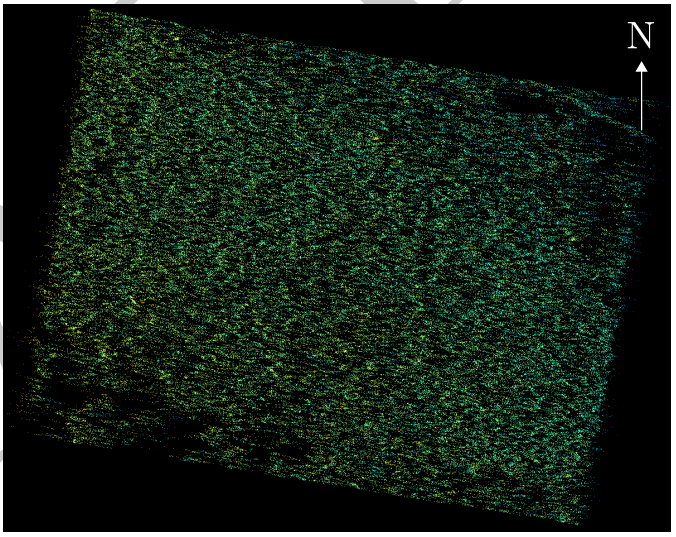

(b) Staring

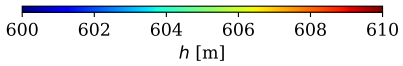

Fig. 18. Updated topography h [m] of the area in Fig. 17 with 12 TerraSAR-X images in the (a) sliding and (b) staring spotlight modes, respectively.

LAN2188 and the TanDEM-X Science Phase AO Project NTI_INSA6729. The authors would like to express their gratitude to TerraSAR-X science coordinator Ursula Marschalk for her kind support. The authors would also like to thank Helko Breit and Dr. Thomas Fritz for their advice about TerraSAR-X annotation components, Nico Adam for his comment on the relation between spatial resolution and the density of double scatterers, Sina Montazeri for sharing his experience of sliding spotlight TomoSAR, Dr. Marie Lachaise for the discussion about vertical accuracy, Alessandro Parizzi for explaining the principles of sidelobe detection, and the reviewers for their constructive and insightful comments.

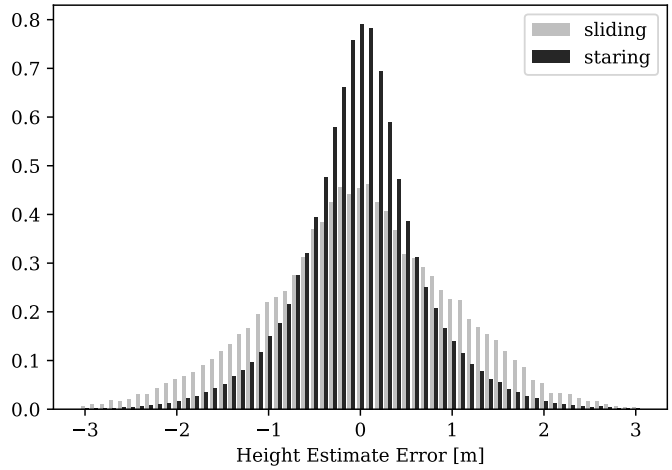

Fig. 19. Normalized histogram of height estimate errors of the point clouds in Fig. 18 relative to a fitted plane.

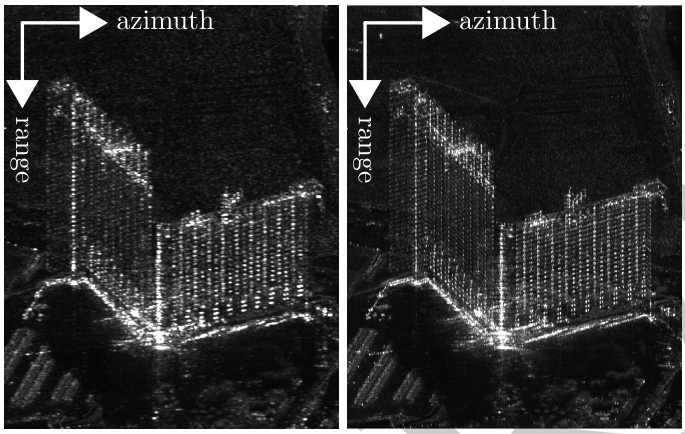

(a) Sliding (b) Staring

Fig. 20. Mean intensity map of Hilton Grand Vacations on the Las Vegas Strip and its surroundings in the (a) sliding and (b) staring spotlight modes.

REFERENCES

[1] M. Eineder, N. Adam, R. Bamler, N. Yague-Martinez, and H. Breit, "Spaceborne spotlight SAR interferometry with TerraSAR-X," *IEEE Transactions on Geoscience and Remote Sensing*, vol. 47, no. 5, pp. 1524–1535, 2009.

[2] S. Gernhardt, N. Adam, M. Eineder, and R. Bamler, "Potential of very high resolution SAR for persistent scatterer interferometry in urban areas," *Annals of GIS*, vol. 16, no. 2, pp. 103–111, 2010.

[3] X. Cong, M. Eineder, and T. Fritz, "Atmospheric delay compensation in differential SAR interferometry for volcanic deformation monitoring-study case: El hierro," in *Geoscience and Remote Sensing Symposium (IGARSS), 2012 IEEE International*. IEEE, 2012, pp. 3887–3890.

[4] X. X. Zhu and R. Bamler, "Very high resolution spaceborne SAR tomography in urban environment," *IEEE Transactions on Geoscience and Remote Sensing*, vol. 48, no. 12, pp. 4296–4308, 2010.

[5] D. Reale, G. Fornaro, A. Pauciullo, X. Zhu, and R. Bamler, "Tomographic imaging and monitoring of buildings with very high resolution sar data," *IEEE Geoscience and Remote Sensing Letters*, vol. 8, no. 4, pp. 661–665, July 2011.

[6] M. Bartusch, "HRWS high resolution wide swath: the next national X-band SAR mission," in *TerraSAR-X/TanDEM-X Science Team Meeting, DLR, Oberpfaffenhofen, Germany, October 17–20*, 2016.

[7] J. Mittermayer, S. Wollstadt, P. Prats-Iraola, and R. Scheiber, "The TerraSAR-X staring spotlight mode concept," *IEEE Transactions on Geoscience and Remote Sensing*, vol. 52, no. 6, pp. 3695–3706, 2014.

[8] P. Prats-Iraola, R. Scheiber, M. Rodriguez-Cassola, J. Mittermayer, S. Wollstadt, F. De Zan, B. Bräutigam, M. Schwerdt, A. Reigber, and A. Moreira, "On the processing of very high resolution spaceborne SAR data," *IEEE Transactions on Geoscience and Remote Sensing*, vol. 52, no. 10, pp. 6003–6016, 2014.

[9] R. Bamler, M. Eineder, N. Adam, X. Zhu, and S. Gernhardt, "Interferometric potential of high resolution spaceborne SAR," *Photogrammetrie-Fernerkundung-Geoinformation*, vol. 2009, no. 5, pp. 407–419, 2009.

[10] M. Eineder and T. Fritz, "TerraSAR-X basic product specification document," TX-GS-DD-3302, Tech. Rep., 2013.

[11] H. Breit, T. Fritz, U. Balss, M. Lachaise, A. Niedermeier, and M. Vonavka, "TerraSAR-X SAR processing and products," *IEEE Transactions on Geoscience and Remote Sensing*, vol. 48, no. 2, pp. 727–740, 2010.

[12] S. Duque, H. Breit, U. Balss, and A. Parizzi, "Absolute height estimation using a single TerraSAR-X staring spotlight acquisition," *IEEE Geoscience and Remote Sensing Letters*, vol. 12, no. 8, pp. 1735–1739, 2015.

[13] T. Fritz and R. Werninghaus, "TerraSAR-X ground segment level 1b product format specification," TX-GS-DD-3307, Tech. Rep., 2007.

[14] N. Adam, F. R. Gonzalez, A. Parizzi, and R. Brcic, "Wide area persistent scatterer interferometry: current developments, algorithms and examples," in *Geoscience and Remote Sensing Symposium (IGARSS), 2013 IEEE International*. IEEE, 2013, pp. 1857–1860.

[15] F. Rodriguez Gonzalez, N. Adam, A. Parizzi, and R. Brcic, "The integrated wide area processor (IWAP): A processor for wide area persistent scatterer interferometry," in *Proceedings of ESA Living Planet Symposium 2013*, 2013.

[16] A. Reigber and A. Moreira, "First demonstration of airborne SAR tomography using multibaseline L-band data," *IEEE Transactions on Geoscience and Remote Sensing*, vol. 38, no. 5, pp. 2142–2152, 2000.

[17] F. Gini, F. Lombardini, and M. Montanari, "Layover solution in multibaseline SAR interferometry," *IEEE Transactions on Aerospace and Electronic Systems*, vol. 38, no. 4, pp. 1344–1356, 2002.

[18] G. Fornaro, F. Lombardini, and F. Serafino, "Three-dimensional multipass SAR focusing: Experiments with long-term spaceborne data," *IEEE Transactions on Geoscience and Remote Sensing*, vol. 43, no. 4, pp. 702–714, 2005.

[19] F. Lombardini, "Differential tomography: A new framework for SAR interferometry," *IEEE Transactions on Geoscience and Remote Sensing*, vol. 43, no. 1, pp. 37–44, 2005.

[20] G. Fornaro, D. Reale, and F. Serafino, "Four-dimensional SAR imaging for height estimation and monitoring of single and double scatterers," *IEEE Transactions on Geoscience and Remote Sensing*, vol. 47, no. 1, pp. 224–237, 2009.

[21] X. X. Zhu and R. Bamler, "Let's do the time warp: Multicomponent nonlinear motion estimation in differential SAR tomography," *IEEE Geoscience and Remote Sensing Letters*, vol. 8, no. 4, pp. 735–739, 2011.

[22] ——, "Tomographic SAR inversion by L_1-norm regularization–the compressive sensing approach," *IEEE Transactions on Geoscience and Remote Sensing*, vol. 48, no. 10, pp. 3839–3846, 2010.

[23] A. Budillon, A. Evangelista, and G. Schirinzi, "Three-dimensional SAR focusing from multipass signals using compressive sampling," *IEEE Transactions on Geoscience and Remote Sensing*, vol. 49, no. 1, pp. 488–499, 2011.

[24] Y. T. Yoon, M. Eineder, N. Yague-Martinez, and O. Montenbruck, "TerraSAR-X precise trajectory estimation and quality assessment," *IEEE Transactions on Geoscience and Remote Sensing*, vol. 47, no. 6, pp. 1859–1868, 2009.

[25] X. X. Zhu and R. Bamler, "Super-resolution power and robustness of compressive sensing for spectral estimation with application to spaceborne tomographic SAR," *IEEE Transactions on Geoscience and Remote Sensing*, vol. 50, no. 1, pp. 247–258, 2012.

[26] ——, "Superresolving SAR tomography for multidimensional imaging of urban areas: Compressive sensing-based TomoSAR inversion," *IEEE Signal Processing Magazine*, vol. 31, no. 4, pp. 51–58, 2014.

[27] N. Adam, A. Parizzi, M. Eineder, and M. Crosetto, "Practical persistent scatterer processing validation in the course of the Terrafirma project," *Journal of Applied Geophysics*, vol. 69, no. 1, pp. 59–65, 2009.

[28] R. Iglesias and J. J. Mallorqui, "Side-lobe cancelation in DInSAR pixel selection with SVA," *IEEE Geoscience and Remote Sensing Letters*, vol. 10, no. 4, pp. 667–671, 2013.

[29] A. Ferretti, C. Prati, and F. Rocca, "Permanent scatterers in SAR interferometry," *IEEE Transactions on geoscience and remote sensing*, vol. 39, no. 1, pp. 8–20, 2001.

[30] Y. Wang, X. X. Zhu, and R. Bamler, "An efficient tomographic inversion approach for urban mapping using meter resolution SAR image stacks,"

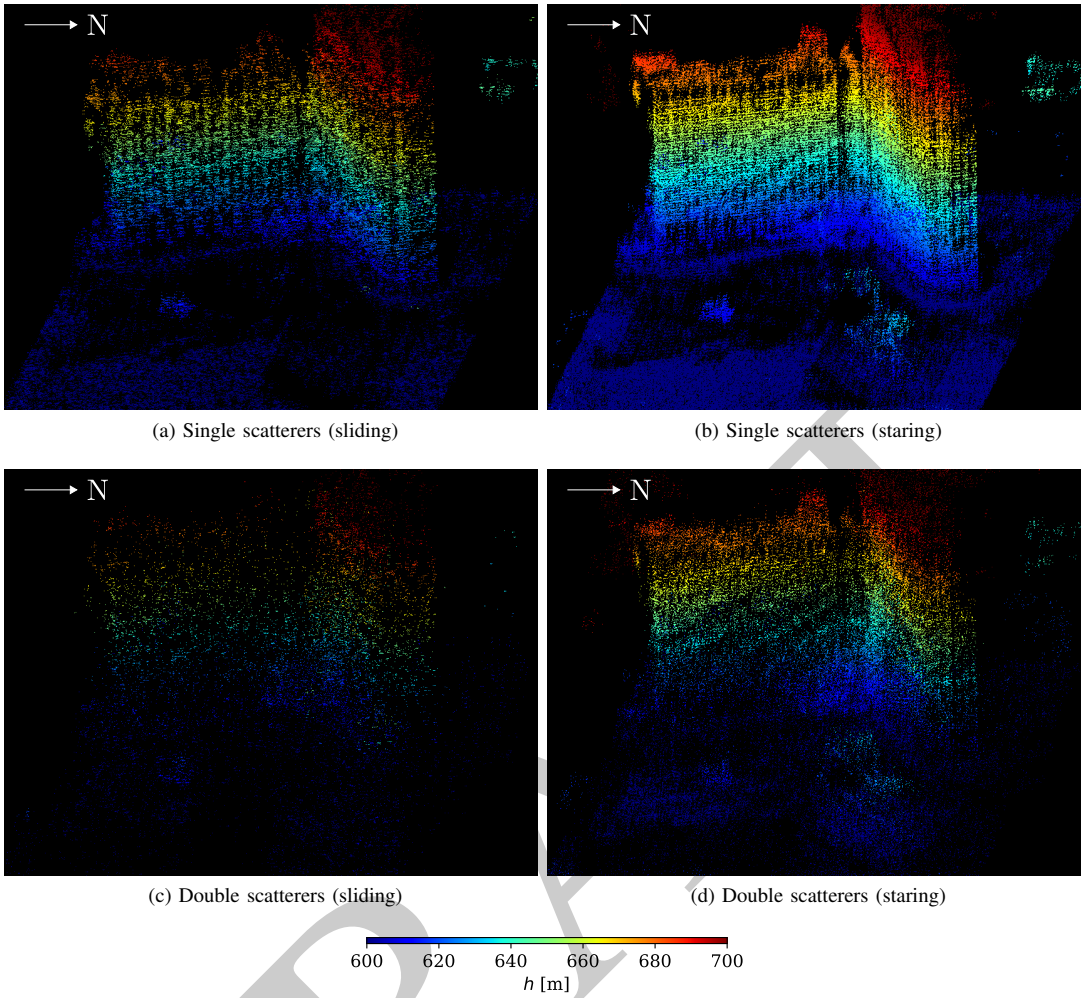

(a) Single scatterers (sliding)

(b) Single scatterers (staring)

(c) Double scatterers (sliding)

(d) Double scatterers (staring)

Fig. 21. Updated topography h [m] of the area in Fig. 20 with 12 TerraSAR-X images in the sliding (left column) and staring (right column) spotlight modes, respectively. The upper and lower rows show single and double scatterers, respectively.

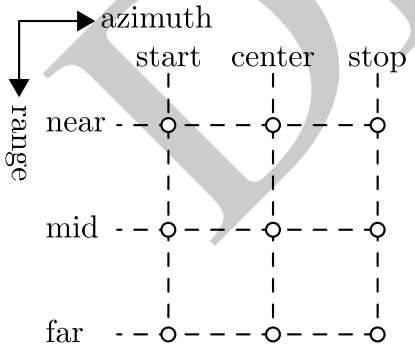

Fig. 22. 3-by-3 grid of Doppler centroid frequency f_{DC} in focused image time t_{image}.

IEEE Geoscience and Remote Sensing Letters, vol. 11, no. 7, pp. 1250–1254, 2014.

[31] I. Hajnsek, T. Busche, G. Krieger, M. Zink, and A. Moreira, "Announcement of opportunity: TanDEM-X science phase," *DLR Public Document TD-PD-PL-0032*, no. 10, 2014.

[32] S. Boyd and L. Vandenberghe, *Convex optimization*. Cambridge university press, 2004.

[33] S. Boyd, N. Parikh, E. Chu, B. Peleato, J. Eckstein *et al.*, "Distributed optimization and statistical learning via the alternating direction method of multipliers," *Foundations and Trends® in Machine learning*, vol. 3, no. 1, pp. 1–122, 2011.

[34] N. Parikh, S. Boyd *et al.*, "Proximal algorithms," *Foundations and Trends® in Optimization*, vol. 1, no. 3, pp. 127–239, 2014.

[35] G. Fornaro, S. Verde, D. Reale, and A. Pauciullo, "CAESAR: An approach based on covariance matrix decomposition to improve multibaseline–multitemporal interferometric SAR processing," *IEEE Transactions on Geoscience and Remote Sensing*, vol. 53, no. 4, pp. 2050–2065, 2015.

[36] M. Schmitt and U. Stilla, "Compressive sensing based layover separation in airborne single-pass multi-baseline InSAR data," *IEEE Geoscience and Remote Sensing Letters*, vol. 10, no. 2, pp. 313–317, 2013.

[37] X. X. Zhu, N. Ge, and M. Shahzad, "Joint sparsity in SAR tomography for urban mapping," *IEEE Journal of Selected Topics in Signal Processing*, vol. 9, no. 8, pp. 1498–1509, 2015.